

INFORMATION TO USERS

This manuscript has been reproduced from the microfilm master. UMI films the text directly from the original or copy submitted. Thus, some thesis and dissertation copies are in typewriter face, while others may be from any type of computer printer.

The quality of this reproduction is dependent upon the quality of the copy submitted. Broken or indistinct print, colored or poor quality illustrations and photographs, print bleedthrough, substandard margins, and improper alignment can adversely affect reproduction.

In the unlikely event that the author did not send UMI a complete manuscript and there are missing pages, these will be noted. Also, if unauthorized copyright material had to be removed, a note will indicate the deletion.

Oversize materials (e.g., maps, drawings, charts) are reproduced by sectioning the original, beginning at the upper left-hand corner and continuing from left to right in equal sections with small overlaps.

Photographs included in the original manuscript have been reproduced xerographically in this copy. Higher quality 6" x 9" black and white photographic prints are available for any photographs or illustrations appearing in this copy for an additional charge. Contact UMI directly to order.

**Bell & Howell Information and Learning
300 North Zeeb Road, Ann Arbor, MI 48106-1346 USA
800-521-0600**

UMI[®]

NOTE TO USERS

This reproduction is the best copy available.

UMI

UNIVERSITY OF OKLAHOMA

GRADUATE COLLEGE

**TUNING THE FRONTIER ORBITAL CHARACTER
OF IRON-THIOLATE COMPLEXES**

A Dissertation

SUBMITTED TO THE GRADUATE FACULTY

in partial fulfillment of the requirements for the

degree of

Doctor of Philosophy

**By
DANNY GORDON MCGUIRE
Norman, Oklahoma
2000**

UMI Number: 9975799

UMI[®]

UMI Microform 9975799

Copyright 2000 by Bell & Howell Information and Learning Company.

**All rights reserved. This microform edition is protected against
unauthorized copying under Title 17, United States Code.**

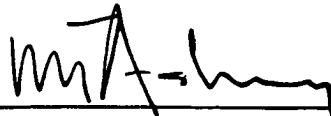
**Bell & Howell Information and Learning Company
300 North Zeeb Road
P.O. Box 1346
Ann Arbor, MI 48106-1346**

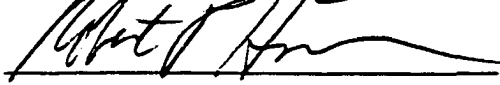
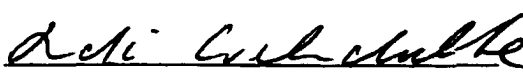
**© Copyright by Danny McGuire 2000
All Rights Reserved.**

TUNING THE FRONTIER ORBITAL CHARACTER
OF IRON-THIOLATE COMPLEXES

A Dissertation APPROVED FOR THE
DEPARTMENT OF CHEMISTRY AND BIOCHEMISTRY

BY

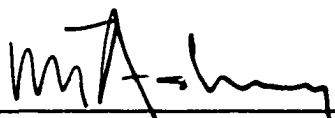


TUNING THE FRONTIER ORBITAL CHARACTER
OF IRON-THIOLATE COMPLEXES

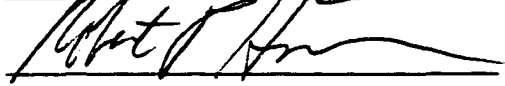
A Dissertation APPROVED FOR THE
DEPARTMENT OF CHEMISTRY AND BIOCHEMISTRY

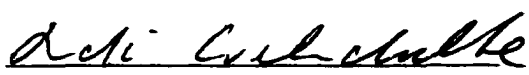
BY











Acknowledgments

I would like to express my sincere gratitude to my parents, Denver and Jayne McGuire, for their unwavering confidence, guidance, and love. Thanks for instilling in me the desire to learn and to always give everything my best shot. I have been privileged to have you as parents. I would also like to thank my father-in-law and mother-in-law Vernon and Clara Ferguson. Their words of encouragement and support have meant a great deal to me over the years.

A special thanks goes to my major professor, Dr. Michael Ashby, for his guidance, support, inspiration, and patience. When projects were not working out, we worked together to solve the problems. Long hours have been spent together. He and his family opened their home and hospitality to me when I really needed it. Thank you so much.

I would like to thank Drs. Goerge Richter-Addo, Ken Nicholas, Ralph Wheeler, Daniel Resasco, Bob Houser, and Rudi Welmschulte for serving as my advisory committee members. Their guidance and instruction contributed much to my success throughout my graduate studies.

I would like to thank all my co-workers present and past in Dr. Michael Ashby's group: Sam Asirvatham, Susan Alguindigue, John Lilly, Angela Kowalski, Justin Schwane, and Dominique Moore. I would also like to thank other fellow Inorganic Division graduate students and post-docs: Li Chen, Kris Wise, Shelly Hodge, Geun-Bae Yi, Jonghyuk Lee, and Li-Sheng Wang.

I would like to express my deepest appreciation to Calvary Baptist Church for their prayers and allowing me to share my concerns with them.

Finally, and most significantly, I wish to thank my wife Leslie for her unfeigning love, undying friendship and eternal devotion she has given to me for over twenty years. I could not have accomplished any of this work without her. I must also thank my beautiful daughters Amber and Rhyan for their "big" hugs and the confidence they have always had in me. I love you very much.

Table of Contents

	Page
List of Tables	ix
List of Figures	xii
List of Abbreviations	xxii
Abstract	xxiii
CHAPTER 1	
INTRODUCTION	1
CHAPTER 2	
THE USE OF $\text{CpFe}(\text{CO})_2(\text{SC}_6\text{H}_5)$ AS A MODEL SYSTEM FOR THE REGULATORY FUNCTION OF HYDROGEN BONDING IN IRON-THIOLATE PROTEINS	
2.1 Introduction and Background	3
2.2 Experimental Section	6
2.2.1 Alternate Preparation of $[\text{CpFe}(\text{CO})_2(\text{HSC}_6\text{H}_5)]\text{BF}_4$	7
2.2.2 Preparation of $\text{CpFe}(\text{CO})_2(\text{SC}_6\text{H}_5)$ crystal	7
2.2.3 Infrared Measurements	7
2.2.4 Preparation of $\text{CpFe}(\text{CO})_2(\text{SC}_6\text{H}_5)$ and $[\text{CpFe}(\text{CO})_2(\text{HSC}_6\text{H}_5)]\text{BF}_4$ solutions	8
2.2.5 Reactions of $\text{CpFe}(\text{CO})_2(\text{SC}_6\text{H}_5)$ with various concentrations of CCl_3COOH	8
2.2.6 Reactions of $\text{CpFe}(\text{CO})_2(\text{SC}_6\text{H}_5)$ with various Brønsted acids	8
2.2.7 Reactions of $\text{CpFe}(\text{CO})_2(\text{SC}_6\text{H}_5)$ with less than 1 equivalent of $\text{HBF}_4 \cdot \text{O}(\text{CH}_3)_2$	9
2.2.8 Reactions of $\text{CpFe}(\text{CO})_2\text{Cl}$ and $\text{CpFe}(\text{CO})_2\text{I}$ with CF_3COOH	9
2.2.9 Dissolving $\text{CpFe}(\text{CO})_2\text{Cl}$ and $\text{CpFe}(\text{CO})_2(\text{SC}_6\text{H}_5)$ in a salt solution of CH_2Cl_2	9
2.2.10 Reacting $\text{CpFe}(\text{CO})_2(\text{SC}_6\text{H}_5)$ with CCl_3COOH in the presence of $(\text{NBu}_4)(\text{PF}_6)$ in CH_2Cl_2	9
2.2.11 X-ray Crystal Structures	10
2.2.12 Molecular Orbital Calculations	10

	2.3 Results of the Solution Experiments	11
	2.4 Results of the Solid State Experiments	23
	2.5 Results of the Molecular Orbital Calculations	34
	2.6 Discussion	36
	2.7 Conclusions	51
	2.8 References	53
CHAPTER 3	SOLVATOCHROMATIC AND OTHER SOLVENT EFFECTS ON CpFe(CO)₂(SC₆H₅)	
	3.1 Introduction and Background	65
	3.2 Experimental Section	73
	3.2.1 Infrared Measurements.....	73
	3.2.2 Solvation of CpFe(CO)₂(SC₆H₅) in various solvents.....	74
	3.2.3 Solvation of CpFe(CO)₂(SC₆H₄-<i>p</i>-CF₃) in various solvents.....	74
	3.2.4 Solvation of CpFe(CO)₂Cl and CpFe(CO)₂I in various solvents.....	74
	3.3 Results of the Solution Experiments	75
	3.4 Discussion	105
	3.5 Conclusions	112
	3.6 References	115
CHAPTER 4	ELECTRONIC, CHEMICAL, AND STRUCTURAL STUDIES OF CpFe(dppe)(SC₆H₄-<i>p</i>-Z) FOR Z = OCH₃, H, Cl, CF₃, AND NO₂	
	4.1 Introduction and Background	121
	4.2 Experimental Section	131
	4.2.1 Preparation of CpFe(dppe)(SC₆H₄-<i>p</i>-OCH₃).....	132

4.2.2	Preparation of CpFe(dppe)(SC₆H₄-<i>p</i>-Cl).....	133
4.2.3	Preparation of CpFe(dppe)(SC₆H₄-<i>p</i>-CF₃).....	133
4.2.4	Preparation of CpFe(dppe)(SC₆H₄-<i>p</i>-NO₂).....	134
4.2.5	Alternative Preparation of [CpFe(dppe)(SC₆H₅)]BF₄.....	134
4.2.6	Preparation of [CpFe(dppe)(SC₆H₄-<i>p</i>-OCH₃)]BF₄.....	135
4.2.7	Preparation of [CpFe(dppe)(SC₆H₄-<i>p</i>-Cl)]BF₄.....	135
4.2.8	Preparation of [CpFe(dppe)(SC₆H₄-<i>p</i>-CF₃)]BF₄.....	136
4.2.9	Preparation of [CpFe(dppe)(SC₆H₄-<i>p</i>-NO₂)]BF₄.....	136
4.2.10	Preparation of [CpFe(P₂S)]PF₆.....	136
4.2.11	Preparation of CpFe(P₂S).....	137
4.2.12	Preparation of CpFe(dppe)(SC₆H₄-<i>p</i>-Z) crystals where Z = H, NO₂ and [CpFe(dppe)(SC₆H₅)]BF₄.....	138
4.2.13	Preparation of CpFe(dppe)(SC₆H₄-<i>p</i>-OCH₃) crystals...	138
4.2.14	Preparation of [CpFe(P₂S)]PF₆ crystals.....	138
4.2.15	Reaction between CpFe(dppe)(SC₆H₅) with HBF₄ under aerobic and anaerobic conditions.....	138
4.2.16	Kinetic experiments: Reaction of CpFe(dppe)(SC₆H₄-<i>p</i>-Z) (where Z = OCH₃, H, Cl, CF₃, NO₂) with CH₃I.....	139
4.2.17	Reaction of CpFe(P₂S) with HBF₄·O(CH₃)₂.....	140
4.2.18	Reaction of Zinc Powder with HBF₄·O(CH₃)₂.....	141
4.2.19	Cyclic Voltammetry experiments.....	141
4.2.20	Electron Paramagnetic Resonance experiments.....	141
4.2.21	X-ray Crystal Structures.....	142
4.2.22	Molecular Orbital Calculations.....	144
4.3	Results	143
4.3.1	UV-vis Spectra of [CpFe(dppe)(SC₆H₄-<i>p</i>-Z)]BF₄ and [CpFe(P₂S)]PF₆.....	146

4.3.2 Results of the kinetic experiments: Reacting CpFe(dppe)(SC ₆ H ₄ - <i>p</i> -Z) where Z = OCH ₃ , H, Cl, NO ₂ with CH ₃ I.....	147
4.3.3 Results of the Cyclic Voltammetry experiments.....	151
4.3.4 Results of EPR experiments.....	155
4.3.5 Results of the Solid State experiments...	159
4.3.6 Results of the Molecular Orbital Calculations.....	193
4.4 Discussion	193
4.5 Conclusions	207
4.6 References	211
CHAPTER 5	CONCLUSIONS
5.1 Summary of the Results from Chapter 2	220
5.2 Summary of the Results from Chapter 3	223
5.3 Summary of the Results from Chapter 4	225
5.4 Future Work	229
5.5 References	231

List of Tables

	Page	
Table 2.1	Infrared stretching frequencies for a 10 mM $\text{CpFe}(\text{CO})_2(\text{SC}_6\text{H}_5)$ solution with various concentrations of CCl_3COOH in CH_2Cl_2 . A curve fit analysis has been accomplished on the carbonyl stretching frequencies.	12
Table 2.2	The carbonyl stretching frequencies of 10 mM $\text{CpFe}(\text{CO})_2(\text{SC}_6\text{H}_5)$ with 150 mM acid in CH_2Cl_2 .	16
Table 2.3	Infrared data of 10 mM $\text{CpFe}(\text{CO})_2\text{Cl}$ and 10 mM $\text{CpFe}(\text{CO})_2\text{I}$ with and without 150 mM CF_3COOH in CH_2Cl_2 .	20
Table 2.4	Crystal data and structure refinement for $\text{CpFe}(\text{CO})_2(\text{SC}_6\text{H}_5)$.	24
Table 2.5	Atomic Coordinates and Equivalent Isotropic Displacement Parameters for $\text{CpFe}(\text{CO})_2(\text{SC}_6\text{H}_5)$.	25
Table 2.6	Crystal data and structure refinement for $[\text{CpFe}(\text{CO})_2(\text{HSC}_6\text{H}_5)]\text{BF}_4$.	26
Table 2.7	Atomic Coordinates and Equivalent Isotropic Displacement Parameters for $[\text{CpFe}(\text{CO})_2(\text{HSC}_6\text{H}_5)]\text{BF}_4$.	27
Table 2.8	Selected bond lengths (Å) and angles (deg) for $\text{CpFe}(\text{CO})_2(\text{SC}_6\text{H}_5)$.	32
Table 2.9	Selected bond lengths (Å) and angles (deg) for $[\text{CpFe}(\text{CO})_2(\text{HSC}_6\text{H}_5)]\text{BF}_4$.	33
Table 2.10	Experimental ($\text{R}=\text{C}_6\text{H}_5$) and computed ($\text{R}=\text{CH}_3$) bond distances and carbonyl stretching for $\text{CpFe}(\text{CO})_2\text{R}$ and its hydrogen-bonded adducts.	34
Table 2.11	Changes in Fe-S distances and redox potential in a model cytochrome P450 containing NH...S hydrogen bonds.	41
Table 2.12	Fe-S bond lengths (Å) for structurally characterized $[\text{CpFe}(\text{CO})_2]^+$ with S-donor ligands.	48

Table 2.13	Fe-S bond lengths (Å) for structurally characterized Fe(II) phenyl-thiolate complexes.	49
Table 3.1	The carbonyl stretching frequencies of specific metal carbonyls from pressed KBr disks.	70
Table 3.2	A 10 mM CpFe(CO) ₂ (SC ₆ H ₅) solution dissolved in a variety of solvents: list of LMCT bands, carbonyl stretching frequencies, Obs F_{CO} (mdyn/Å), dielectric constants, Gutmann's acceptor numbers, Kosower's Z-scale, and Kamlet-Taft's π^* parameters.	77
Table 3.3	UV/vis and infrared stretching frequency data of a 10 mM CpFe(CO) ₂ (SC ₆ H ₄ - <i>p</i> -CF ₃) solution solvated with a variety of aprotic solvents.	94
Table 3.4	The carbonyl stretching frequencies of 10 mM solutions of CpFe(CO) ₂ Cl and CpFe(CO) ₂ I in six different solvent.	95
Table 4.1	Represents the kinetic data for the reaction between CpFe(dppe)(SC ₆ H ₄ - <i>p</i> -Z) and excess CH ₃ I.	149
Table 4.2	Cyclic voltammetric data for CpFe(dppe)(SC ₆ H ₄ - <i>p</i> -Z) and CpFe(P ₂ S).	154
Table 4.3	EPR spectral data for [CpFe(dppe)(SC ₆ H ₄ - <i>p</i> -Z)]BF ₄ .	157
Table 4.4	Crystal data and structure refinement for CpFe(dppe)(SC ₆ H ₄ - <i>p</i> -OCH ₃).	161
Table 4.5	Atomic Coordinates and Equivalent Isotropic Displacement Parameters for CpFe(dppe)(SC ₆ H ₄ - <i>p</i> -OCH ₃).	162
Table 4.6	Selected bond lengths (Å) and angles (deg) for CpFe(dppe)(SC ₆ H ₄ - <i>p</i> -OCH ₃).	164
Table 4.7	Crystal data and structure refinement for CpFe(dppe)(SC ₆ H ₅).	165
Table 4.8	Atomic Coordinates and Equivalent Isotropic Displacement Parameters for CpFe(dppe)(SC ₆ H ₅).	166
Table 4.9	Selected bond lengths (Å) and angles (deg) for CpFe(dppe)(SC ₆ H ₅).	168

Table 4.10	Crystal data and structure refinement for CpFe(dppe)(SC₆H₄-p-NO₂).	169
Table 4.11	Atomic Coordinates and Equivalent Isotropic Displacement Parameters for CpFe(dppe)(SC₆H₄-p-NO₂).	170
Table 4.12	Selected bond lengths (Å) and angles (deg) for CpFe(dppe)(SC₆H₄-p-NO₂).	172
Table 4.13	Crystal data and structure refinement for [CpFe(dppe)(SC₆H₅)]BF₄.	173
Table 4.14	Atomic Coordinates and Equivalent Isotropic Displacement Parameters for [CpFe(dppe)(SC₆H₅)]BF₄.	174
Table 4.15	Selected bond lengths (Å) and angles (deg) for [CpFe(dppe)(SC₆H₅)]BF₄.	177
Table 4.16	Crystal data and structure refinement for [CpFe(P₂S)]PF₆.	178
Table 4.17	Atomic Coordinates and Equivalent Isotropic Displacement Parameters for [CpFe(P₂S)]PF₆.	179
Table 4.18	Selected bond lengths (Å) and angles (deg) for [CpFe(P₂S)]PF₆.	182
Table 4.19	Density functional calculations of the HOMO and LUMO in the units of hartrees and electron volts for the following compounds: CpFe(CO)₂(SCH₃), [CpFe(CO)₂(SCH₃)]⁺, CpFe(PH₃)₂(SCH₃), and [CpFe(PH₃)₂(SCH₃)]⁺.	193
Table 4.20	Fe-S bond lengths (Å) and angles (deg) for structurally characterized iron(II) aryl thiolate complexes.	202

List of Figures

		Page
Figure 2.1	Rieske fragment from the bovine heart mitochondria.	5
Figure 2.2	Compounds used for density functional calculations.	10
Figure 2.3	IR spectrum of 10 mM $\text{CpFe}(\text{CO})_2(\text{SC}_6\text{H}_5)$ in CH_2Cl_2 .	11
Figure 2.4	IR spectrum of 10 mM $[\text{CpFe}(\text{CO})_2(\text{SC}_6\text{H}_5)]\text{BF}_4$ in CH_2Cl_2 .	11
Figure 2.5	Infrared spectrum of 10 mM $\text{CpFe}(\text{CO})_2(\text{SC}_6\text{H}_5)$ reacting with 50 mM CCl_3COOH in CH_2Cl_2 .	12
Figure 2.6	Infrared spectrum of 10 mM $\text{CpFe}(\text{CO})_2(\text{SC}_6\text{H}_5)$ reacting with 100 mM CCl_3COOH in CH_2Cl_2 .	13
Figure 2.7	Infrared spectrum of 10 mM $\text{CpFe}(\text{CO})_2(\text{SC}_6\text{H}_5)$ reacting with 500 mM CCl_3COOH in CH_2Cl_2 .	13
Figure 2.8	Infrared spectrum of 10 mM $\text{CpFe}(\text{CO})_2(\text{SC}_6\text{H}_5)$ reacting with 1000 mM CCl_3COOH in CH_2Cl_2 .	14
Figure 2.9	Changes in the UV-vis spectra of $\text{CpFe}(\text{CO})_2(\text{SC}_6\text{H}_5)$ upon addition of trichloroacetic acid and corresponding changes in the IR of the same solutions.	15
Figure 2.10	Infrared spectrum of 10 mM $\text{CpFe}(\text{CO})_2(\text{SC}_6\text{H}_5)$ reacting with 150 mM CH_3COOH in CH_2Cl_2 .	16
Figure 2.11	Infrared spectrum of 10 mM $\text{CpFe}(\text{CO})_2(\text{SC}_6\text{H}_5)$ reacting with 150 mM CClH_2COOH in CH_2Cl_2 .	17
Figure 2.12	Infrared spectrum of 10 mM $\text{CpFe}(\text{CO})_2(\text{SC}_6\text{H}_5)$ reacting with 150 mM CCl_2HCOOH in CH_2Cl_2 .	17
Figure 2.13	Infrared spectrum of 10 mM $\text{CpFe}(\text{CO})_2(\text{SC}_6\text{H}_5)$ reacting with 150 mM CCl_3COOH in CH_2Cl_2 .	18
Figure 2.14	Infrared spectrum of 10 mM $\text{CpFe}(\text{CO})_2(\text{SC}_6\text{H}_5)$ reacting with 150 mM CF_3COOH in CH_2Cl_2 .	18

Figure 2.15	Changes in the UV-vis spectra of $\text{CpFe}(\text{CO})_2(\text{SC}_6\text{H}_5)$ in CH_2Cl_2 upon addition of acetic acid, monochloroacetic acid, dichloroacetic acid, trichloroacetic acid, and trifluoroacetic acid and the corresponding changes in the IR spectra.	19
Figure 2.16	IR spectrum of 10 mM $\text{CpFe}(\text{CO})_2(\text{SC}_6\text{H}_5)$ + 5 mM $\text{HBF}_4 \cdot \text{O}(\text{CH}_3)_2$ in CH_2Cl_2.	20
Figure 2.17	IR spectra of 5 mM $\text{CpFe}(\text{CO})_2\text{Cl}$ with 150 mM $(\text{NBu}_4)(\text{PF}_6)$ and without $(\text{NBu}_4)(\text{PF}_6)$ in CH_2Cl_2.	21
Figure 2.18	IR spectra of 10 mM $\text{CpFe}(\text{CO})_2(\text{SC}_6\text{H}_5)$ with $(\text{NBu}_4)(\text{PF}_6)$ and without 1.0 M $(\text{NBu}_4)(\text{PF}_6)$ in CH_2Cl_2.	21
Figure 2.19	Visible spectrum of a 10 mM $\text{CpFe}(\text{CO})_2(\text{SC}_6\text{H}_5)$ with $(\text{NBu}_4)(\text{PF}_6)$ and without 1.0 M $(\text{NBu}_4)(\text{PF}_6)$ in CH_2Cl_2.	22
Figure 2.20	Changes in the infrared spectra of $\text{CpFe}(\text{CO})_2(\text{SC}_6\text{H}_5)$ in CH_2Cl_2 upon addition of an increasing concentration of trichloroacetic acid in the presence of $(\text{NBu}_4)(\text{PF}_6)$.	22
Figure 2.21	Thermal ellipsoid drawing of the crystal structure of $\text{CpFe}(\text{CO})_2(\text{SC}_6\text{H}_5)$ at the 50% level with the labeling scheme.	28
Figure 2.22	The crystal packing diagram of $\text{CpFe}(\text{CO})_2(\text{SC}_6\text{H}_5)$.	29
Figure 2.23	Thermal ellipsoid drawing of the crystal structure of $[\text{CpFe}(\text{CO})_2(\text{HSC}_6\text{H}_5)]^+$ at the 50% level with the labeling scheme.	30
Figure 2.24	The crystal packing diagram of $[\text{CpFe}(\text{CO})_2(\text{HSC}_6\text{H}_5)]\text{BF}_4$.	31
Figure 2.25	Highest Occupied Molecular Orbitals (HOMOs) of Various Brønsted Acid Adducts of $\text{CpFe}(\text{CO})_2\text{SCH}_3$ as calculated by the DFT Method.	35
Figure 2.26	The complex $\text{CpFe}(\text{CO})_2(\text{SR})$ mixed with an increasing acid concentration until protonation takes place.	37
Figure 2.27	Spectroscopic Properties for $\text{CpFe}(\text{CO})_2(\text{SC}_6\text{H}_4\text{-}p\text{-Z})$ where $Z = \text{H}, \text{Cl}, \text{CF}_3, \text{and } \text{NO}_2$.	39

Figure 2.28	A potential product from the reaction between 10 mM CpFe(CO)₂(SC₆H₅) and 5 mM HBF₄·O(CH₃)₂.	42
Figure 3.1	Pyridinium-N-phenoxide betaine dye.	66
Figure 3.2	Solvent effects on the electronic transition energy of dipolar solutes in polar solvents where A represents the dipole moment of the Franck-Condon excited state of the solute that is larger than the ground state ($\mu_g < \mu_e$) and B represents the dipole moment of the Franck-Condon excited state of the solute smaller than the ground state $\mu_g > \mu_e$.	72
Figure 3.3	A visible spectrum of a 10 mM CpFe(CO)₂(SC₆H₅) solution in pentane.	78
Figure 3.4	A visible spectrum of a 10 mM CpFe(CO)₂(SC₆H₅) solution in heptane.	78
Figure 3.5	A visible spectrum of a 10 mM CpFe(CO)₂(SC₆H₅) solution in cyclohexane.	79
Figure 3.6	A visible spectrum of a 10 mM CpFe(CO)₂(SC₆H₅) solution in toluene.	79
Figure 3.7	A visible spectrum of a 10 mM CpFe(CO)₂(SC₆H₅) solution in diethyl ether.	80
Figure 3.8	A visible spectrum of a 10 mM CpFe(CO)₂(SC₆H₅) solution in benzene.	80
Figure 3.9	A visible spectrum of a 10 mM CpFe(CO)₂(SC₆H₅) solution in tetrahydrofuran.	81
Figure 3.10	A visible spectrum of a 10 mM CpFe(CO)₂(SC₆H₅) solution in chloroform.	81
Figure 3.11	A visible spectrum of a 10 mM CpFe(CO)₂(SC₆H₅) solution in dichloromethane.	82
Figure 3.12	A visible spectrum of a 10 mM CpFe(CO)₂(SC₆H₅) solution in acetone.	82

Figure 3.13	A visible spectrum of a 10 mM $\text{CpFe}(\text{CO})_2(\text{SC}_6\text{H}_5)$ solution in acetonitrile.	83
Figure 3.14	A visible spectrum of a 10 mM $\text{CpFe}(\text{CO})_2(\text{SC}_6\text{H}_5)$ solution in 1-butanol.	83
Figure 3.15	A visible spectrum of a 10 mM $\text{CpFe}(\text{CO})_2(\text{SC}_6\text{H}_5)$ solution in 1-pentanol.	84
Figure 3.16	A visible spectrum of a 10 mM $\text{CpFe}(\text{CO})_2(\text{SC}_6\text{H}_5)$ solution in methanol.	84
Figure 3.17	A visible spectrum of a 10 mM $\text{CpFe}(\text{CO})_2(\text{SC}_6\text{H}_5)$ solution in 2,2,2-trifluoroethanol.	85
Figure 3.18	An infrared spectrum of the carbonyl stretching frequencies of a 10 mM $\text{CpFe}(\text{CO})_2(\text{SC}_6\text{H}_5)$ solution in heptane.	86
Figure 3.19	An infrared spectrum of the carbonyl stretching frequencies of a 10 mM $\text{CpFe}(\text{CO})_2(\text{SC}_6\text{H}_5)$ solution in cyclohexane.	86
Figure 3.20	An infrared spectrum of the carbonyl stretching frequencies of a 10 mM $\text{CpFe}(\text{CO})_2(\text{SC}_6\text{H}_5)$ solution in pentane.	87
Figure 3.21	An infrared spectrum of the carbonyl stretching frequencies of a 10 mM $\text{CpFe}(\text{CO})_2(\text{SC}_6\text{H}_5)$ solution in toluene.	87
Figure 3.22	An infrared spectrum of the carbonyl stretching frequencies of a 10 mM $\text{CpFe}(\text{CO})_2(\text{SC}_6\text{H}_5)$ solution in diethyl ether.	88
Figure 3.23	An infrared spectrum of the carbonyl stretching frequencies of a 10 mM $\text{CpFe}(\text{CO})_2(\text{SC}_6\text{H}_5)$ solution in chloroform.	88
Figure 3.24	An infrared spectrum of the carbonyl stretching frequencies of a 10 mM $\text{CpFe}(\text{CO})_2(\text{SC}_6\text{H}_5)$ solution in dichloromethane.	89

Figure 3.25	An infrared spectrum of the carbonyl stretching frequencies of a 10 mM $\text{CpFe}(\text{CO})_2(\text{SC}_6\text{H}_5)$ solution in benzene.	89
Figure 3.26	An infrared spectrum of the carbonyl stretching frequencies of a 10 mM $\text{CpFe}(\text{CO})_2(\text{SC}_6\text{H}_5)$ solution in acetonitrile.	90
Figure 3.27	An infrared spectrum of the carbonyl stretching frequencies of a 10 mM $\text{CpFe}(\text{CO})_2(\text{SC}_6\text{H}_5)$ solution in acetone.	90
Figure 3.28	An infrared spectrum of the carbonyl stretching frequencies of a 10 mM $\text{CpFe}(\text{CO})_2(\text{SC}_6\text{H}_5)$ solution in tetrahydrofuran.	91
Figure 3.29	An infrared spectrum of the carbonyl stretching frequencies of a 10 mM $\text{CpFe}(\text{CO})_2(\text{SC}_6\text{H}_5)$ solution in methanol.	91
Figure 3.30	An infrared spectrum of the carbonyl stretching frequencies of a 10 mM $\text{CpFe}(\text{CO})_2(\text{SC}_6\text{H}_5)$ solution in 1-pentanol.	92
Figure 3.31	An infrared spectrum of the carbonyl stretching frequencies of a 10 mM $\text{CpFe}(\text{CO})_2(\text{SC}_6\text{H}_5)$ solution in 1-butanol.	92
Figure 3.32	An infrared spectrum of the carbonyl stretching frequencies of a 10 mM $\text{CpFe}(\text{CO})_2(\text{SC}_6\text{H}_5)$ solution in 2,2,2-trifluoroethanol.	93
Figure 3.33	An infrared spectrum of the carbonyl stretching frequencies of a 5 mM $\text{CpFe}(\text{CO})_2\text{Cl}$ solution in pentane.	96
Figure 3.34	An infrared spectrum of the carbonyl stretching frequencies of a 5 mM $\text{CpFe}(\text{CO})_2\text{Cl}$ solution in diethyl ether.	96
Figure 3.35	An infrared spectrum of the carbonyl stretching frequencies of a 5 mM $\text{CpFe}(\text{CO})_2\text{Cl}$ solution in tetrahydrofuran.	97

Figure 3.36	An infrared spectrum of the carbonyl stretching frequencies of a 5 mM CpFe(CO) ₂ Cl solution in acetone.	97
Figure 3.37	An infrared spectrum of the carbonyl stretching frequencies of a 5 mM CpFe(CO) ₂ Cl solution in acetonitrile.	98
Figure 3.38	An infrared spectrum of the carbonyl stretching frequencies of a 5 mM CpFe(CO) ₂ Cl solution in dichloromethane.	98
Figure 3.39	An infrared spectrum of the carbonyl stretching frequencies of a 5 mM CpFe(CO) ₂ I solution in pentane.	99
Figure 3.40	An infrared spectrum of the carbonyl stretching frequencies of a 5 mM CpFe(CO) ₂ I solution in diethyl ether.	99
Figure 3.41	An infrared spectrum of the carbonyl stretching frequencies of a 5 mM CpFe(CO) ₂ I solution in tetrahydrofuran.	100
Figure 3.42	An infrared spectrum of the carbonyl stretching frequencies of a 5 mM CpFe(CO) ₂ I solution in acetone.	100
Figure 3.43	An infrared spectrum of the carbonyl stretching frequencies of a 5 mM CpFe(CO) ₂ I solution in acetonitrile.	101
Figure 3.44	An infrared spectrum of the carbonyl stretching frequencies of a 5 mM CpFe(CO) ₂ I solution in dichloromethane.	101
Figure 3.45	Plot of wavelength vs. the Dimroth-Reichardt's normalized energy of transition scale of solvents of a 10 mM CpFe(CO) ₂ (SC ₆ H ₅) solution.	102
Figure 3.46	Plot of wavelength vs. the Dimroth-Reichardt's normalized energy of transition scale of solvents of a 10 mM CpFe(CO) ₂ (SC ₆ H ₅) solution and a 10 mM CpFe(CO) ₂ (SC ₆ H ₄ -p-CF ₃).	102
Figure 3.47	Plot of wavelength vs. Gutmann's Acceptor Number of a 10 mM CpFe(CO) ₂ (SC ₆ H ₅) solution.	103

Figure 3.48	Plot of wavelength vs. Kosower's Z-scale of solvents of a 10 mM CpFe(CO) ₂ (SC ₆ H ₅) solution.	103
Figure 3.49	Plot of wavelength vs. the Kamlet and Taft's π* polarity scale of solvents of a 10 mM CpFe(CO) ₂ (SC ₆ H ₅) solution.	104
Figure 3.50	A plot of the antisymmetric vs. symmetric stretching frequencies of a 10 mM CpFe(CO) ₂ (SC ₆ H ₅) solution in various solvents.	104
Figure 3.51	A plot of the force constants based on the observed infrared carbonyl stretching frequencies of CpFe(CO) ₂ Cl, CpFe(CO) ₂ I, and CpFe(CO) ₂ (SC ₆ H ₅) vs. Gutmann's Acceptor Number.	105
Figure 3.52	Streck <i>et al.</i> used the P=O stretching frequency of trimethyl phosphate to determine solvent effects.	108
Figure 3.53	The two isomers of [η ⁵ -CpMo(CO) ₂ (PPh ₃ C ₆ H ₆ O)] ⁺ .	111
Figure 3.54	Infrared spectrum of the solvent (THF) and a 10 mM CpFe(CO) ₂ (SC ₆ H ₅) solution in THF showing the overlap of a solvent stretching frequency and the asymmetric carbonyl stretching frequency.	112
Figure 4.1	Proposed FeMo-cofactor structure in nitrogenase MoFe-proteins where Y is most likely sulfur.	122
Figure 4.2	End-on metal-dinitrogen bonding.	122
Figure 4.3	The bimetallic center of the [NiFe] hydrogenase <i>Desulfovibrio gigas</i> . where Y is possibly oxo or hydroxo ligand, L1 and L2 could be cyanides and L3 is possibly carbon monoxide.	125
Figure 4.4	The active-site of the Fe-only hydrogenase which contains two subclusters. L represents possible CO and CN ligands.	126
Figure 4.5	Structure of [Fe(PS ₃)(CO)(CN)] ²⁻ synthesized by Hsu <i>et al.</i> as a model system for hydrogenase.	128

Figure 4.6	The first nickel complex with predominantly sulfur ligands, which serves as a model for [FeNi] hydrogenase, that undergoes H ₂ /D ⁺ exchange at the nitrogen site.	130
Figure 4.7	Schlenk glassware used for hydrogenation experiments.	140
Figure 4.8	UV-vis spectra of [CpFe(dppe)(SC ₆ H ₄ - <i>p</i> -Z)]BF ₄ in CH ₂ Cl ₂ .	146
Figure 4.9	UV-vis data that was collected over a period of 120 seconds of the reaction between 1.0 mM CpFe(dppe)(SC ₆ H ₅) and 0.1 M CH ₃ I in dry degassed acetone.	147
Figure 4.10	UV-vis spectrum of 1.0 mM CpFe(dppe)I in acetone and the product of the reaction between 1.0 mM CpFe(dppe)(SC ₆ H ₅) and 0.1 M CH ₃ I in acetone after 120 seconds.	148
Figure 4.11	Beer's Law plot of 0.5 mM CpFe(dppe)(SC ₆ H ₄ - <i>p</i> -OCH ₃) and 50 mM CH ₃ I in acetone at 340 nm.	148
Figure 4.12	The plot of absorbance vs. time of a pseudo-first order reaction of 0.5 mM CpFe(dppe)(SC ₆ H ₄ - <i>p</i> -OCH ₃) and 50 mM CH ₃ I in acetone. Residual plot of reaction A.	149
Figure 4.13	The plot of absorbance vs. time of a pseudo-first order reaction of 1.0 mM CpFe(dppe)(SC ₆ H ₄ - <i>p</i> -NO ₂) and 100 mM CH ₃ I in acetone. Residual plot of reaction A.	150
Figure 4.14	Hammett relationship between the rate of reaction of CpFe(dppe)(SC ₆ H ₄ - <i>p</i> -Z) with iodomethane and the Hammett substituent constant (σ).	150
Figure 4.15	Cyclic Voltagram of a 0.5 mM solution of CpFe(P ₂ S).	151
Figure 4.16	Cyclic Voltagram of a 0.5 mM solution of CpFe(dppe)(SC ₆ H ₄ - <i>p</i> -OCH ₃).	151
Figure 4.17	Cyclic Voltagram of a 0.5 mM solution of CpFe(dppe)(SC ₆ H ₅).	152
Figure 4.18	Cyclic Voltagram of a 0.5 mM solution of CpFe(dppe)(SC ₆ H ₄ - <i>p</i> -Cl).	152

Figure 4.19	Cyclic Voltagram of a 0.5 mM solution of CpFe(dppe)(SC ₆ H ₄ - <i>p</i> -CF ₃).	153
Figure 4.20	Cyclic Voltagram of a 0.5 mM solution of CpFe(dppe)(SC ₆ H ₄ - <i>p</i> -NO ₂).	153
Figure 4.21	Hammett relationship between the half-wave potential of CpFe(dppe)(SC ₆ H ₄ - <i>p</i> -Z) and sigma (σ).	154
Figure 4.22	EPR spectrum of a 3.1 mM [CpFe(dppe)(SC ₆ H ₄ - <i>p</i> -OCH ₃)]BF ₄ .	155
Figure 4.23	EPR spectrum of a 1.1 mM [CpFe(dppe)(SC ₆ H ₅)]BF ₄ .	155
Figure 4.24	EPR spectrum of a 2.1 mM [CpFe(dppe)(SC ₆ H ₄ - <i>p</i> -Cl)]BF ₄ .	156
Figure 4.25	EPR spectrum of a 1.5 mM [CpFe(dppe)(SC ₆ H ₄ - <i>p</i> -CF ₃)]BF ₄ .	156
Figure 4.26	EPR spectrum of a 3.3 mM [CpFe(dppe)(SC ₆ H ₄ - <i>p</i> -NO ₂)]BF ₄ .	157
Figure 4.27	Hammett relationship between the g-values of CpFe(dppe)(SC ₆ H ₄ - <i>p</i> -Z) in CH ₂ Cl ₂ at 298K and sigma (σ).	158
Figure 4.28	Hammett relationship between the half width half maximum (HWHM) values of CpFe(dppe)(SC ₆ H ₄ - <i>p</i> -Z) in CH ₂ Cl ₂ at 298K and sigma (σ).	158
Figure 4.29	Thermal ellipsoid drawings of the crystal structure of CpFe(dppe)(SC ₆ H ₄ - <i>p</i> -OCH ₃) at the 50% level with the labeling scheme.	183
Figure 4.30	Packing diagram of CpFe(dppe)(SC ₆ H ₄ - <i>p</i> -OCH ₃) at the 25% level.	184
Figure 4.31	Thermal ellipsoid drawings of the crystal structure of CpFe(dppe)(SC ₆ H ₅) at the 50% level with the labeling scheme.	185

Figure 4.32	Packing diagram of $\text{CpFe(dppe)(SC}_6\text{H}_5)$ at the 25% level.	186
Figure 4.33	Thermal ellipsoid drawing of the crystal structure of $\text{CpFe(dppe)(SC}_6\text{H}_4\text{-}i>p\text{-NO}_2)$ at the 40% level with the labeling scheme.	187
Figure 4.34	Packing diagram of $\text{CpFe(dppe)(SC}_6\text{H}_4\text{-}i>p\text{-NO}_2)$ at the 20% level.	188
Figure 4.35	Thermal ellipsoid drawing of the crystal structure of $[\text{CpFe(dppe)(SC}_6\text{H}_5)]\text{BF}_4$ at the 40% level with the labeling scheme.	189
Figure 4.36	Packing diagram of $\text{CpFe(dppe)(SC}_6\text{H}_5)]\text{BF}_4$ at the 20% level.	190
Figure 4.37	Thermal ellipsoid drawing of the crystal structure of $[\text{CpFe(P}_2\text{S)}]\text{PF}_6$ at the 50% level with the labeling scheme.	191
Figure 4.38	Packing diagram of $[\text{CpFe(P}_2\text{S)}]\text{PF}_6$ at the 20% level.	192
Figure 4.39	Dinuclear model for hydrogenase.	194
Figure 4.40	Proposed mechanism for ligand-ligand activation for the liberation of dihydrogen.	195
Figure 4.41	The compound, $\text{CpFe(P}_2\text{S)}$, which was synthesized as a potential model system for hydrogenase.	197
Figure 4.42	Methylation and ligand exchange reaction between $[\text{4Fe-4S}]$ -cluster and $(\text{CH}_3\text{O})_3\text{PO}$.	198
Figure 4.43	Substitution effect on the HOMO's energy (hartrees) in going from carbonyl to phosphine ligands.	205

List of Abbreviations

bipy	2,2'-bipyridine
<i>t</i> -Bu	<i>tert</i> -Butyl
Cp	Cyclopentadiene
Cp*	Pentamethylcyclopentadiene
Cys	Cysteine
DFT	Density Functional Theory
Dppe	1,2-Bis(diphenylphosphino)ethane
Fc	Ferrocene
Fp	CpFe(CO) ₂
HOMO	Highest Occupied Molecular Orbital
HWHH	Half Width at Half Height
IR	Infrared
IP	Ionization Potential
LMCT	Ligand to Metal Charge Transfer
LUMO	Lowest Unoccupied Molecular Orbital
Me	Methyl
NBu ₄	<i>t</i> -Butyl ammonium
Phen	Phenanthroline
PES	Photoelectron Spectroscopy
Ph	Phenyl
P ₂ S	2,2-Bis(diphenylphosphinomethyl)-1-phenylthiopropene
Py	Pyridine
TBAHFP	<i>t</i> -Butyl ammonium hexafluorophosphate
UV-vis	Ultraviolet-visible

Abstract

A portion of this work describes intermolecular hydrogen bonding studies using the compound $\text{CpFe}(\text{CO})_2(\text{SC}_6\text{H}_5)$ as a model system for iron-thiolate proteins. A nonpolar aprotic solvent, CH_2Cl_2 , was used to promote hydrogen bonding while using various Brønsted acids. The acids were added to a CH_2Cl_2 solution of $\text{CpFe}(\text{CO})_2(\text{SC}_6\text{H}_5)$ and then infrared spectroscopy was used to assess the hydrogen bonding effects by observing the changes in the carbonyl stretching frequencies. UV-vis spectroscopy was also used to observe the changes in the ligand to metal charge transfer band (LMCT) as the Brønsted acids were added to the solutions of $\text{CpFe}(\text{CO})_2(\text{SC}_6\text{H}_5)$. The IR and UV-vis experiments were accomplished using the same solutions. A correlation between the half-wave potential, $E_{1/2}$, and the force constant, F_{CO} , was determined. Based upon the empirical formula $\Delta E_{1/2} = \lambda \Delta F_{\text{CO}}$, it has been calculated that there is a substantially smaller effect on the half-wave potential for hydrogen bonding compared with protonation, (about 30%). Density functional calculations on $\text{CpFe}(\text{CO})_2(\text{SCH}_3)$ and $[\text{CpFe}(\text{CO})_2(\text{SCH}_3)]^+$ corroborate the experimental spectral values.

The solid-state structures of $\text{CpFe}(\text{CO})_2(\text{SC}_6\text{H}_5)$ and $[\text{CpFe}(\text{CO})_2(\text{HSC}_6\text{H}_5)]\text{BF}_4$, which were determined by single crystal X-ray crystallography, show that protonation produces a shorter Fe-S bond. This indicates a stabilization of the Fe-S bond due to a weakening of the HOMO $\text{Fe}(d\pi)\text{-S}(p\pi)$ antibonding orbital.

Another part of this work describes the solvatochromatic effect of $\text{CpFe}(\text{CO})_2(\text{SC}_6\text{H}_5)$ dissolved in different solvents. The polarity of the solvents that were used varied from the non-polar (pentane) to polar (2,2,2-trifluoroethanol). The changes in the metal to ligand charge transfer band

were monitored by UV-vis spectroscopy and the CO stretching frequencies were monitored by IR spectroscopy. The wavelength of the ligand to metal charge transfer band was correlated to several solvent polarity scales. The best correlations were obtained by using the Dimroth-Reichardt's normalized energy of transition scale, Gutmann's Acceptor Number scale, and Kosower's Z-scale. A blue shift in the UV-vis spectra occurs as $\text{CpFe}(\text{CO})_2(\text{SC}_6\text{H}_5)$ is solvated in more polar solvents, which is evidence that the ground-state dipole moment is greater than the excited-state dipole moment, $\mu_g > \mu_e$.

The infrared spectral data show a complex solvent effect. Since the compound $\text{CpFe}(\text{CO})_2(\text{SC}_6\text{H}_5)$ contains two separate polar sites, this complicates the prediction of the solvent shifts. There is a competition for solvent interaction between the π accepting carbonyl ligands and the π donor phenyl thiolate ligand that determines whether the carbonyl stretching frequency will increase or decrease.

Another part of this work describes the use of $\text{CpFe}(\text{dppe})(\text{SC}_6\text{H}_5)$ and $\text{CpFe}(\text{P}_2\text{S})$ as a potential model systems for the hydrogenase enzyme. The P_2S ligand (2,2-bis[(diphenylphosphanyl)methyl]-1-propanethiolate) is a tripodal ligand with two phosphorus groups and a thiolate group that coordinates to the iron. These compounds were tested by reacting them with excess $\text{HBF}_4 \cdot \text{O}(\text{CH}_3)_2$ under inert conditions and it was determine that molecular hydrogen is not produced as has been previously suggested in the literature (for $\text{CpFe}(\text{dppe})(\text{SC}_6\text{H}_5)$).

The synthesis and characterization of $\text{CpFe}(\text{dppe})(\text{SC}_6\text{H}_4\text{-}p\text{-Z})$ where $Z = \text{OCH}_3, \text{H}, \text{Cl}, \text{NO}_2,$ and CF_3 are described. A comparative reactivity study between $\text{CpFe}(\text{CO})_2(\text{SC}_6\text{H}_4\text{-}p\text{-Z})$ and the more electron rich $\text{CpFe}(\text{dppe})(\text{SC}_6\text{H}_4\text{-}p\text{-Z})$ is presented. This study involved observing the kinetics of the pseudo-first order methylation of $\text{CpFe}(\text{dppe})(\text{SC}_6\text{H}_4\text{-}p\text{-Z})$ by CH_3I in

acetone to form the products $\text{CpFe}(\text{dppe})\text{I}$ and $\text{CH}_3\text{S}(\text{C}_6\text{H}_5)$. It was determined that the reaction was first order in CH_3I , as expected, and that a correlation exists between the relative donor ability of the aryl substituent and the reaction rate. From a Hammett plot, a value of $\rho = -2.14$ was calculated which indicates a developing positive charge on the sulfur center during the course of the reaction.

Cyclic voltammetry of $\text{CpFe}(\text{dppe})(\text{SC}_6\text{H}_4\text{-}p\text{-Z})$ in THF was used to measure the redox potential. According to the CV data, the ratio of anodic to cathodic currents (i_{pa}/i_{pc}) are near unity indicating a chemically reversible process with no decomposition of oxidized product; however, $E_{pc} - E_{pa}$ are slightly greater than 59 mV and vary with a sweep rate which is typical of a quasi-reversible electron transfer process. The required potentials for oxidation vary from -577 mV for the OCH_3 derivative to -357 mV for the NO_2 derivative versus the Ag/AgNO_3 reference electrode. A linear free energy relationship is observed in this electrochemical study between the relative donor ability of the aryl substituent and the half-wave potential of the compounds $\text{CpFe}(\text{dppe})(\text{SC}_6\text{H}_4\text{-}p\text{-Z})$. Apparently, the NO_2 substituent best stabilizes the complex by withdrawing electron density from the HOMO which is the $d\pi\text{-}p\pi$ antibonding orbital.

The solid state evidence is also consistent with the CV data. Single-crystal X-ray crystallographic analysis of $\text{CpFe}(\text{dppe})(\text{SC}_6\text{H}_4\text{-}p\text{-OCH}_3)$, $\text{CpFe}(\text{dppe})(\text{SC}_6\text{H}_5)$ and $\text{CpFe}(\text{dppe})(\text{SC}_6\text{H}_4\text{-}p\text{-NO}_2)$ shows that the Fe-S bond distances decrease in the order of the derivatives: $\text{OCH}_3 > \text{H} > \text{NO}_2$. Their bond distances are 2.332(2), 2.3289(8), and 2.2933(7) Å, respectively. Another comparison is the Fe-S bond distance between $\text{CpFe}(\text{dppe})(\text{SC}_6\text{H}_5)$ and $[\text{CpFe}(\text{dppe})(\text{SC}_6\text{H}_5)]\text{BF}_4$ which shows that the Fe(II) derivative has the greater bond length of 2.3289(8) Å while the Fe(III) has a bond length of 2.1899(10) Å. This result is due to the removal of an electron from the iron-sulfur π -antibonding

HOMO of the Fe(II) species which causes stabilization of the bond.

The HOMO energies from density functional calculations on the oxidized species $[\text{CpFe}(\text{CO})_2(\text{SCH}_3)]^+$ and $[\text{CpFe}(\text{dppe})(\text{SCH}_3)]^+$ also show that the HOMO of the carbonyl derivative is more stable than the phosphine derivative; however, the calculations also indicate that the HOMO in the carbonyl derivative is predominantly sulfur in character while in the phosphine derivative, the HOMO is predominantly metal in character.

There is also indication that the HOMO of the compound $[\text{CpFe}(\text{dppe})(\text{SC}_6\text{H}_4\text{-}p\text{-Z})]\text{BF}_4$, where $Z = \text{OCH}_3, \text{H}, \text{Cl}, \text{NO}_2, \text{and } \text{CF}_3$, is primarily metal in character as determined from the data collected from electron paramagnetic resonance (EPR) experiments. The g -values range from 2.0716 for the OCH_3 derivative to 2.0753 for the NO_2 derivative. A linear free energy relationship is observed relative to the g -values and the relative donor ability of the aryl substituent. Apparently, when the aryl substituent becomes more electron withdrawing and the g -values increase the HOMO becomes more metal in character.

The HOMO on the compounds, $\text{CpFe}(\text{CO})_2(\text{SC}_6\text{H}_4\text{-}p\text{-Z})$ and $\text{CpFe}(\text{dppe})(\text{SC}_6\text{H}_5\text{-}p\text{-Z})$, are primarily sulfur in character. Many of the experiments in this work were designed to perturb the HOMO located on the sulfur (e.g., hydrogen bonding experiments) to determine how such perturbations influence the redox potential of the metal center. The perturbation of the HOMO influences the reactivity of the Fe(II) complexes towards methylation and also influences the Fe-S bond distances.

Chapter 1 INTRODUCTION

This dissertation concerns the study of electron rich iron-thiolate complexes. In an effort to explore the electronic behavior about the metal and sulfur sites in these complexes, three projects were developed which are explained in detail in chapters 2 through 4. The results of these studies are summarized in chapter 5. An extensive background is included in chapters 2 through 4 to explain various ideas and to give examples to illustrate concepts related to each project. The following is a preview of the chapters to follow.

Chapter 2 describes the study of intermolecular hydrogen bonding using $\text{CpFe}(\text{CO})_2(\text{SC}_6\text{H}_5)$ as a model system for iron-thiolate proteins and a number of Brønsted acids (i.e., CCl_3COOH and CCF_3COOH). The carbonyl ligands are probes that are easily detected by infrared spectroscopy and are sensitive to the changes in the electronic environment of the metal center. The compound, $\text{CpFe}(\text{CO})_2(\text{SC}_6\text{H}_5)$, is also highly colored and changes in the ligand to metal charge transfer (LMCT) band are detected by UV-vis spectroscopy.

Chapter 3 describes the study of the solvatochromic effects in the UV-vis and IR spectra. Such effects are probes to the influence of solvent (dipolar environment) on the ground-state and electronic excited-state electronic structures of $\text{CpFe}(\text{CO})_2(\text{SR})$ complexes. For example, by observing the shifts in the visible region of $\text{CpFe}(\text{CO})_2(\text{SC}_6\text{H}_5)$ dissolved in various solvents, a conclusion may be drawn as to whether the dipole moment of the ground-state is greater than or less than that of the Franck-Condon excited-state.

In Chapter 4, three goals were established to investigate possible mechanisms for $\text{H}_2(\text{g})$ production from model systems of hydrogenase and also to study the electronic effects on the iron and sulfur atoms upon perturbing the

sulfur site in electron rich iron-thiolate complexes. The first goal is to determine whether $\text{H}_2(\text{g})$ evolution takes place when the compounds $\text{CpFe}(\text{dppe})(\text{SC}_6\text{H}_5)$ or $\text{CpFe}(\text{P}_2\text{S})$ react with $\text{HBF}_4\text{-O}(\text{CH}_3)_2$ and then determine possible mechanisms. The second goal contains two parts. The first is to determine the oxidation potentials of the compounds, $\text{CpFe}(\text{dppe})(\text{SC}_6\text{H}_4\text{-}p\text{-Z})$ where $Z = \text{OCH}_3, \text{H}, \text{Cl}, \text{CF}_3,$ and NO_2 , using cyclic voltammetry. The second is to study the reaction between $\text{CpFe}(\text{dppe})(\text{SC}_6\text{H}_5\text{-}p\text{-Z})$ with CH_3I to determine how Z affects the rate of methylation. A correlation is then established between the redox potentials and the rates of reaction from the kinetic studies. The third goal is to determine whether the lone electron in the HOMO of $[\text{CpFe}(\text{dppe})(\text{C}_6\text{H}_4\text{-}p\text{-Z})]\text{BF}_4$ resides primarily on the metal or sulfur by using electron paramagnetic resonance spectroscopy and running density functional calculations on the following compounds: $\text{CpFe}(\text{PH}_3)_2(\text{SCH}_3)$ and $[\text{CpFe}(\text{PH}_3)_2(\text{SCH}_3)]^+$.

Chapter 5 summarizes the investigations and results from chapters 2 through 4 and it also presents possible directions of future work.

Chapter 2 THE USE OF $\text{CpFe}(\text{CO})_2(\text{SC}_6\text{H}_5)$ AS A MODEL SYSTEM FOR THE REGULATORY FUNCTION OF HYDROGEN BONDING IN IRON-THIOLATE PROTEINS

2.1 Introduction and Background

Hydrogen bonding plays a significant role in biological systems. In particular, it has an essential function in regulating the redox potential of the metal center in iron-sulfur proteins and enzymes.^{1,2} Apparently, hydrogen bonds can drive redox potentials in positive directions, compared to non-hydrogen bound analogs, making reduction of proteins easier.^{3,4}

The redox potentials of certain iron-sulfur proteins are not only affected by hydrogen bonding but by protonation as well. Some iron-sulfur clusters $[\text{3Fe-4S}]$ will undergo redox-linked protonation.⁵ It is proposed that the site of protonation is an inorganic sulfur to form a $\text{H}^+[\text{3Fe-4S}]^0$ cluster with a sulfhydryl (SH^-) ligand.⁶ Far less is known about the $[\text{3Fe-4S}]$ cluster's atom transfer properties than their abilities as an electron transfer agent.⁷

Rubredoxin, which is the simplest non-heme iron-sulfur proteins, includes a single $\text{Fe}(\text{S-Cys})_4$ site that is involved in electron transport. The crystal structures of rubredoxin from *Desulfovibrio vulgaris* and *Desulfovibrio gigas* indicate that the iron-sulfur clusters within these proteins contain hydrogen bonds to the cysteinyl sulfur atoms and some even have two $\text{NH}\dots\text{S}$ bonds.^{8,9} These $\text{NH}\dots\text{S}$ hydrogen bonding interactions apparently tune the potential of a given metal center.^{10,11}

Ferredoxins and High-Potential Iron Proteins (HiPIP) are also non-heme iron-sulfur proteins that contain $[\text{4Fe-4S}]$ clusters. The sulfur centers typically originate from cysteinates and they contain hydrogen bonds which have been observed in ferredoxin from the crystal structures of *Peptococcus aerogenes*, *Bacillus thermoproteolyticus*, and *Azotobacter vinelandii* and in HiPIP from the

crystal structures of *Chromatium*, *Rhodocyclus*, *Rhodopila*, and *Ectothiorhodospira*.^{12,13}

The iron-sulfur cluster [2Fe-2S] ferredoxin from the cyanobacterium *Anabaena* has been studied by Vidakovic *et al.* and it was determined through site-directed mutagenesis that hydrogen bonding from the side chain hydroxyl group of serine 45 to the ligand sulfur atom of cysteine 41 tunes the redox potential of the iron-sulfur cluster.¹⁴ The amino acid alanine is typically in position 45 in wild type (WT) *Anabaena* but it was replaced with serine. The overall structure was not disturbed by the replacement. It was determined by the spectrophotometric redox titration method that the midpoint potential of Ala45Ser *Anabaena* ferredoxin is higher (-382 mV) than the potential of WT *Anabaena* ferredoxin (-406 mV). Hence, the redox potentials of iron-sulfur clusters are affected by hydrogen bonding.

Another [2Fe-2S] protein that exhibits hydrogen bonding with sulfur atoms is the Rieske protein.¹⁵⁻¹⁷ Figure 2.1 shows the water soluble fragment from the bovine heart mitochondria but the residue numbering corresponds to the *Paracoccus* sequence.¹⁸ After removing specific hydrogen bonds to the sulfur atoms via site-directed mutagenesis, structural integrity is maintained but the redox potential is greatly affected which, in turn, causes a decrease in the rate of electron transfer.¹⁵

The influence of a hydrogen bond to a bridging sulfur center seems to be greater than that of a hydrogen bond to a terminal cysteine residue. By removing the hydrogen bond from the bridging sulfur, the redox potential drops 95 mV but removing the hydrogen bond from the terminal sulfur, the redox potential drops 44 mV. This was explained by the higher amount of electron density around the bridging sulfurs than the terminal sulfurs¹⁹; however, not all hydrogen bonds are equal in strength. Calculations by Datta *et al.* using the CNDO/2 method have

determined that the HOMOs and the LUMOs of the model Rieske iron-sulfur complex $[\text{Fe}_2\text{S}_2\text{-pr}]$, which has two histidine and two cysteine residues coordinated to the iron, contain large contributions from the orbitals of the sulfur atoms.¹⁹ The effect of delocalizing the electron density from the iron-sulfur cluster through hydrogen bonding would be greater for the bridging sulfurs than the terminal sulfurs.¹⁸ In either case, hydrogen bonding affects are instrumental in tuning the iron-sulfur complex in Rieske proteins.

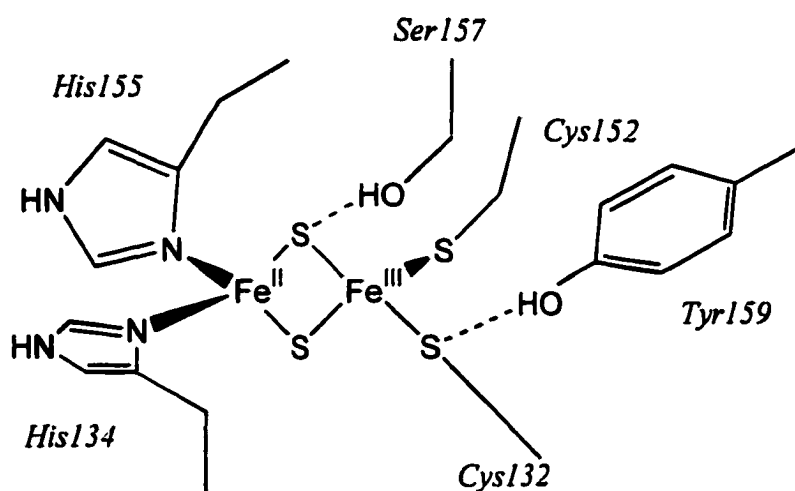


Figure 2.1. Rieske fragment from the bovine heart mitochondria.¹⁸

Cytochrome P450 is a heme-type oxo transfer protein that bears an axial cysteinate ligand²⁰ in which the sulfur is hydrogen bound.^{21,22} The presence of $\text{NH}\dots\text{S}$ in the active site of cytochrome P450cam has been determined by X-ray crystallography.^{23,24} However, not much has been published on the redox effect of the $\text{NH}\dots\text{S}$ hydrogen bond where the sulfur is coordinated to the iron in the cytochrome P450 complexes.²⁵

A common way to study the effects of hydrogen bonding and protonation is by the use of model systems.²⁶⁻²⁸ Ueyama *et al.* have synthesized a number

of model systems for both cytochrome P450 and the iron-sulfur clusters.^{25,29,30} In each case, the NH...S hydrogen bonding shifts the redox potential to the positive side with respect to the non-hydrogen bound analog. Each of the models by Ueyama involves intramolecular hydrogen bonding so there is at least a minimal chelation effect. Ueyama also typically employs a low dielectric solvent to improve the environment for hydrogen bonding to take place.^{31,32}

Although many models exist for iron-sulfur clusters that exhibit intramolecular hydrogen bonding, this work provides a small molecular model, CpFe(CO)₂(SC₆H₅), that undergoes both intermolecular hydrogen bonding and protonation. The reasons for choosing this compound to study are: 1) it is easily synthesized, 2) it contains carbonyl probes that are easily detected by infrared spectroscopy, 3) it is highly colored 4) it is soluble in a wide range of solvents 5) it contains a sulfur that is accessible for hydrogen bonding and 6) much is already known about the electronics and reactivity of the compound.³³⁻³⁵

2.2 Experimental Section

All reactions were performed under an atmosphere of prepurified nitrogen or argon using Schlenk technique or a MO-40M VAC Dry Box unless stated otherwise. Solvents were distilled from appropriate drying agents under nitrogen and degassed by freeze pump thawing three times prior to use unless stated otherwise: CH₂Cl₂ (CaH₂), pentane (Na). CpFe(CO)₂(SC₆H₅), CpFe(CO)₂Cl and CpFe(CO)₂I were prepared by literature methods.³⁶⁻³⁸ CH₃COOH, CClH₂COOH, CCl₂HCOOH, CCl₃COOH, CF₃COOH and HBF₄·O(CH₃)₂ were purchased from Aldrich Chemical Company and used as received. Infrared spectra were recorded on a Bruker IFS 66/S FTIR spectrometer. ¹H NMR spectra were obtained on a Varian 400MHz spectrometer. UV-vis spectra were recorded on a Hewlett-Packard HP8453 Diode Array instrument.

2.2.1 Alternate Preparation of [CpFe(CO)₂(HSC₆H₅)]BF₄.³⁹

To a CH₂Cl₂ (50mL) solution of CpFe(CO)₂(SC₆H₅) (150 mg, 0.53 mmol) was added HBF₄·O(CH₃)₂ (64 μL, 0.53 mmol). The color of the solution immediately changed from red to yellow. The mixture stirred for 5 minutes. Then it was transferred to another 100 mL Schlenk flask using a filter canula. Pentane was added to the yellow solution and the [CpFe(CO)₂(HSC₆H₅)]BF₄ precipitated. The solution was filtered off using a Schlenk filter frit and the yellow compound dried *in vacuo* for 4 hours to give [CpFe(CO)₂(HSC₆H₅)]BF₄ (170 mg, 0.46 mmol, 87% yield). It was stored in a dry box under nitrogen. IR (CH₂Cl₂, cm⁻¹): ν_{CO} = 2067, 2025. ¹H NMR (CD₂Cl₂): δ 7.58 - 7.40 (m, C₆H₅), 5.38 (s, SH), 5.34 (s, Cp).

The identity of the product was confirmed by a single-crystal X-ray crystallographic analysis. A suitable crystal for structure determination was obtained by evaporation of a saturated CH₂Cl₂ solution under nitrogen overnight.

2.2.2 Preparation of CpFe(CO)₂(SC₆H₅) crystal.

The crystal for structure determination was obtained by evaporation of a saturated pentane solution under nitrogen.

2.2.3 Infrared Measurements.

Sodium chloride salt plates and a 0.5 mm teflon spacer were used in all of the following infrared spectroscopy experiments. A 0.2 mm quartz cell was utilized in the UV-vis spectroscopy experiments. All infrared spectra were analyzed by taking the second derivative of each spectrum and then fitted by a Gaussian Amplitude curve fit method⁴⁰ using the Peakfit computer program. In the figures that show infrared spectra, the CO stretching frequencies that were determined from the curve fit analysis are located in the legend of each spectrum and the CO stretching frequencies that were determined before the curve fit analysis are located in the graphs.

2.2.4 Preparation of $\text{CpFe}(\text{CO})_2(\text{SC}_6\text{H}_5)$ and $[\text{CpFe}(\text{CO})_2(\text{HSC}_6\text{H}_5)]\text{BF}_4$ solutions.

A 10 mM solution of $\text{CpFe}(\text{CO})_2(\text{SC}_6\text{H}_5)$ and $[\text{CpFe}(\text{CO})_2(\text{HSC}_6\text{H}_5)]\text{BF}_4$ were each prepared in CH_2Cl_2 under nitrogen. Figures 2.4 and 2.5 show the IR spectra and a comparison between the values of the CO stretching frequencies before a curve fit analysis and after the curve fit analysis.

2.2.5 Reactions of $\text{CpFe}(\text{CO})_2(\text{SC}_6\text{H}_5)$ with various concentrations of CCl_3COOH .

Six solutions of 10 mM $\text{CpFe}(\text{CO})_2(\text{SC}_6\text{H}_5)$ with each of 0 mM, 10mM, 50 mM, 100 mM, 500 mM, and 1000 mM CCl_3COOH in CH_2Cl_2 were prepared under nitrogen. These solutions were examined by infrared and UV-vis spectroscopy. Table 2.1 shows the results of the infrared experiments which compares the CO stretching frequencies before a curve fit analysis and after the curve fit analysis. The individual infrared spectra showing the CO stretching frequencies are shown in Figures 2.5 – 2.8. An overlay of selected spectra from the UV-vis and infrared experiments are shown in Figure 2.9.

2.3.6 Reactions of $\text{CpFe}(\text{CO})_2(\text{SC}_6\text{H}_5)$ with various Brønsted acids.

Six solutions of 10 mM $\text{CpFe}(\text{CO})_2(\text{SC}_6\text{H}_5)$ with 150 mM acid in CH_2Cl_2 were prepared under nitrogen. The acids include CH_3COOH , CClH_2COOH , CCl_2HCOOH , CCl_3COOH , CF_3COOH , and $\text{HBF}_4 \cdot \text{O}(\text{CH}_3)_2$. Table 2.2 shows the results of the infrared experiments which compares the CO stretching frequencies before a curve fit and after a curve fit. Figures 2.10 – 2.14 show the individual infrared spectra of each mixture and the the results of the curve fit analysis. An overlay of the spectra from the UV-vis and infrared experiments are shown in Figure 2.15.

2.2.7 Reactions of $\text{CpFe}(\text{CO})_2(\text{SC}_6\text{H}_5)$ with less than 1 equivalent of $\text{HBF}_4 \cdot \text{O}(\text{CH}_3)_2$.

A solution of 10 mM $\text{CpFe}(\text{CO})_2(\text{SC}_6\text{H}_5)$ with 5 mM $\text{HBF}_4 \cdot \text{O}(\text{CH}_3)_2$ in CH_2Cl_2 was prepared under nitrogen. Infrared spectroscopy was used to locate the carbonyl stretching frequencies of the solution (Figure 2.16).

2.2.8 Reactions of $\text{CpFe}(\text{CO})_2\text{Cl}$ and $\text{CpFe}(\text{CO})_2\text{I}$ with CF_3COOH .

Solutions of a 10 mM $\text{CpFe}(\text{CO})_2\text{Cl}$ and a 10 mM $\text{CpFe}(\text{CO})_2\text{I}$ in CH_2Cl_2 were prepared under nitrogen. Then a 10 mM $\text{CpFe}(\text{CO})_2\text{Cl}$ and a 10 mM $\text{CpFe}(\text{CO})_2\text{I}$ each with 150 mM CF_3COOH in CH_2Cl_2 were prepared under nitrogen. All solutions were examined by infrared spectroscopy. Table 2.3 contains the results of these experiments.

2.2.9 Dissolving $\text{CpFe}(\text{CO})_2\text{Cl}$ and $\text{CpFe}(\text{CO})_2(\text{SC}_6\text{H}_5)$ in a salt solution of CH_2Cl_2 .

A solution of 5 mM $\text{CpFe}(\text{CO})_2\text{Cl}$ with and without 150 mM $(\text{NBu}_4)(\text{PF}_6)$ and a 10 mM $\text{CpFe}(\text{CO})_2(\text{SC}_6\text{H}_5)$ with and without 1 M $(\text{NBu}_4)(\text{PF}_6)$ in CH_2Cl_2 were each prepared. These solutions were examined by infrared and UV-vis spectroscopy. Figures 2.17 and 2.18 show the infrared spectra of the $\text{CpFe}(\text{CO})_2\text{Cl}$ and $\text{CpFe}(\text{CO})_2(\text{SC}_6\text{H}_5)$ solutions, respectively and Figure 2.19 shows the change in the visible spectrum of the $\text{CpFe}(\text{CO})_2(\text{SC}_6\text{H}_5)$ solutions.

2.2.10 Reacting $\text{CpFe}(\text{CO})_2(\text{SC}_6\text{H}_5)$ with CCl_3COOH in the presence of $(\text{NBu}_4)(\text{PF}_6)$ in CH_2Cl_2 .

A 10 mM solution of $\text{CpFe}(\text{CO})_2(\text{SC}_6\text{H}_5)$ was reacted with each of 0 mM, 50 mM, 100 mM, and 250 mM CCl_3COOH in CH_2Cl_2 . The 0 M acid solution was also 1 M in $(\text{NBu}_4)(\text{PF}_6)$. The 50 mM acid solution was 0.95 M in $(\text{NBu}_4)(\text{PF}_6)$. The 100 mM acid solution was 0.90 M in $(\text{NBu}_4)(\text{PF}_6)$ and the 250 mM acid solution was 0.75 M in $(\text{NBu}_4)(\text{PF}_6)$. These solutions were examined by infrared spectroscopy. The results of these experiments are shown in Figure 2.20.

2.2.11 X-ray Crystal Structures. Data for the crystal structures of $\text{CpFe(CO)}_2(\text{SC}_6\text{H}_5)$ and $[\text{CpFe(CO)}_2(\text{HSC}_6\text{H}_5)]\text{BF}_4$ were collected at $-85\text{ }^\circ\text{C}$ on a Siemens P4 diffractometer using $\text{MoK}\alpha$ ($\lambda=0.71073\text{ \AA}$) radiation. The data were corrected for Lorentz and polarization effects; and an empirical absorption correction based on psi-scans was applied.

The structure was solved by the direct method using SHELXTL (Siemens) system, and refinement by full-matrix least-squares on F^2 using all reflections.⁴¹ The hydrogen atom on the sulfur in $[\text{CpFe(CO)}_2(\text{HSC}_6\text{H}_5)]\text{BF}_4$ was located in the difference map and refined isotropically. All the other hydrogen atoms were included with idealized parameters.

2.2.12 Molecular Orbital Calculations. Density functional calculations using the DN* basis set, which is a numerical polarization basis set that includes d-type functions on heavy atoms, were carried out using the program SPARTAN 5.0⁴² running on a Silicon Graphics IRIS Indigo 2 Solid Impact with a R10000 processor. The compounds used for the calculations are shown in Figure 2.2. A comparison between the calculated CO stretching frequencies, and the Fe-S bond distances of species A through D are listed in Table 2.12.

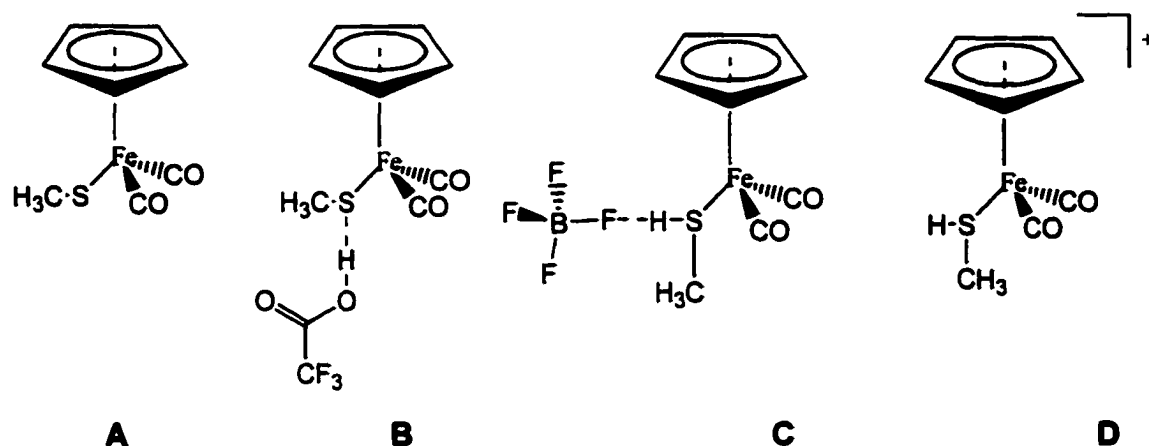


Figure 2.2. Compounds used for density functional calculations.

2.3 Results of the Solution Experiments

A 10 mM solution of $\text{Fp}(\text{SC}_6\text{H}_5)$ and $[\text{Fp}(\text{HSC}_6\text{H}_5)]\text{BF}_4$ ($\text{Fp} = \text{CpFe}(\text{CO})_2$) were each prepared in CH_2Cl_2 under nitrogen. Two carbonyl stretching frequencies for each compound were found from their infrared spectra (Figures 2.4 and 2.5). Note that the stretching frequencies match the curve fit analysis for each compound due to the symmetry of the peaks.

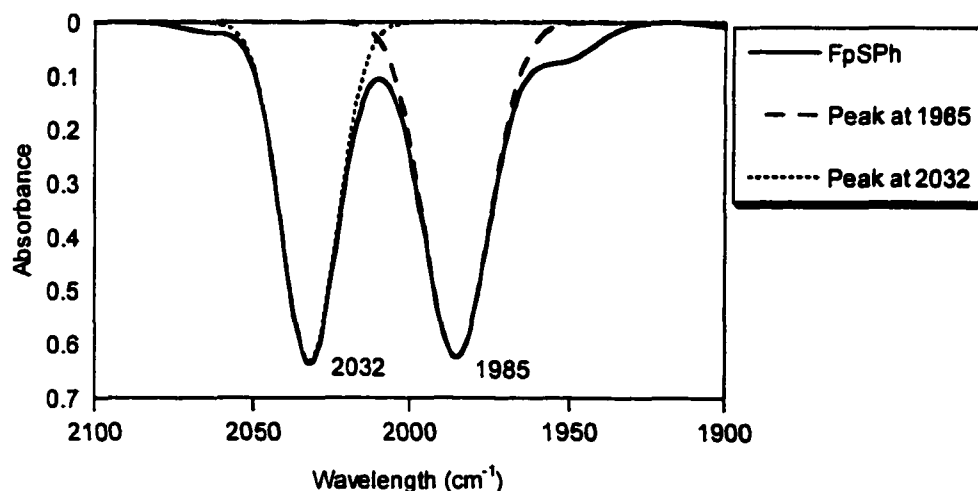


Figure 2.3. IR spectrum of 10 mM $\text{CpFe}(\text{CO})_2(\text{SC}_6\text{H}_5)$ in CH_2Cl_2 .

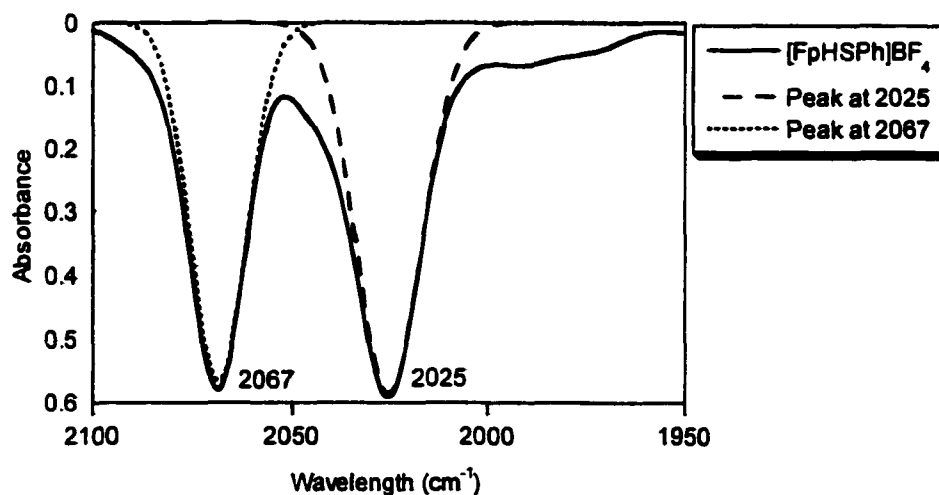


Figure 2.4. IR spectrum of 10 mM $[\text{CpFe}(\text{CO})_2(\text{HSC}_6\text{H}_5)]\text{BF}_4$ in CH_2Cl_2 .

Table 2.1. Infrared stretching frequencies for a 10 mM $\text{CpFe}(\text{CO})_2(\text{SC}_6\text{H}_5)$ solution reacting with various concentrations of CCl_3COOH in CH_2Cl_2 . A curve fit analysis has been accomplished on the carbonyl stretching frequencies.

[CCl_3COOH]	ν_{CO} (cm^{-1})					
0 mM			2032			1985
50 mM ^a		2037			1991	
50 mM ^b	2066	2042	2031	2014	1998	1983
100 mM ^a	2068	2038			1994	
100 mM ^b	2067	2042	2031	2013	1997	1984
500 mM ^a	2068	2040			1995	
500 mM ^b	2068	2042	2027	2006	1995	1984
1000 mM ^a	2068	2040			1996	
1000 mM ^b	2069	2045	2037	2025	2003	1992

- a. The experimental CO stretching frequencies before a curve fit analysis.
 b. The experimental CO stretching frequencies after a curve fit analysis.

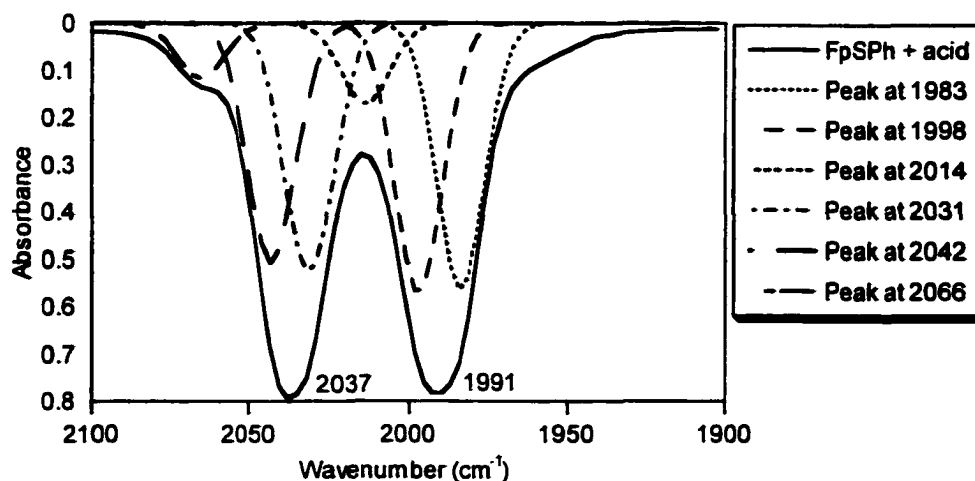


Figure 2.5. Infrared Spectrum of 10 mM $\text{CpFe}(\text{CO})_2(\text{SC}_6\text{H}_5)$ reacting with 50 mM CCl_3COOH in CH_2Cl_2 .

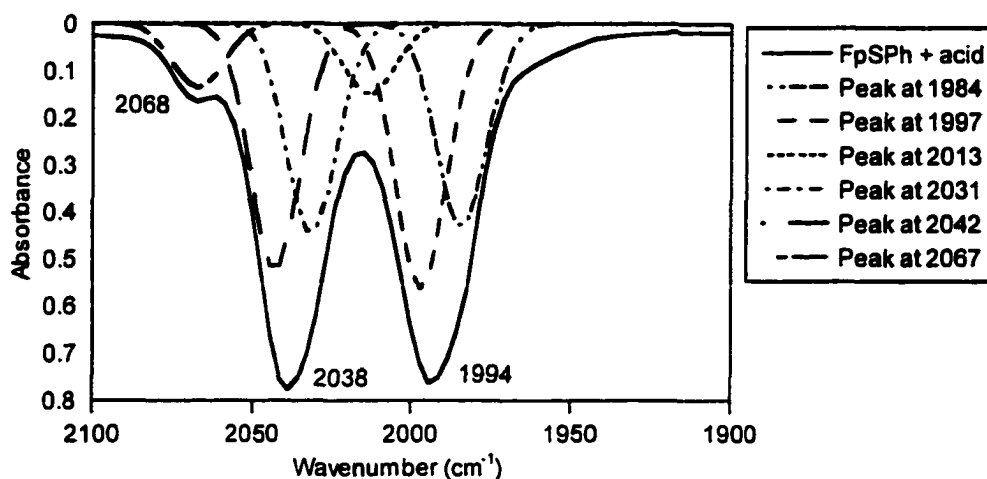


Figure 2.6. Infrared Spectrum of 10 mM $\text{CpFe}(\text{CO})_2(\text{SC}_6\text{H}_5)$ reacting with 100 mM CCl_3COOH in CH_2Cl_2 .

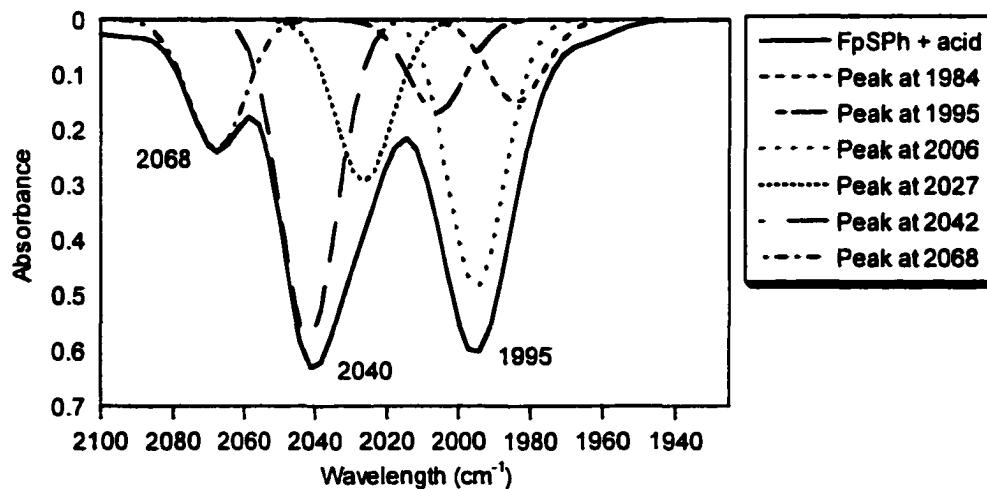


Figure 2.7. Infrared Spectrum of 10 mM $\text{CpFe}(\text{CO})_2(\text{SC}_6\text{H}_5)$ reacting with 500 mM CCl_3COOH in CH_2Cl_2 .

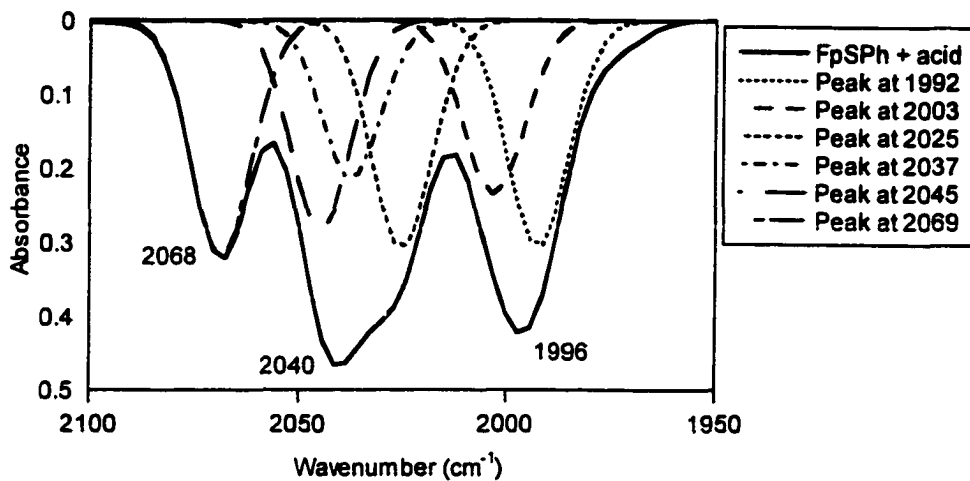
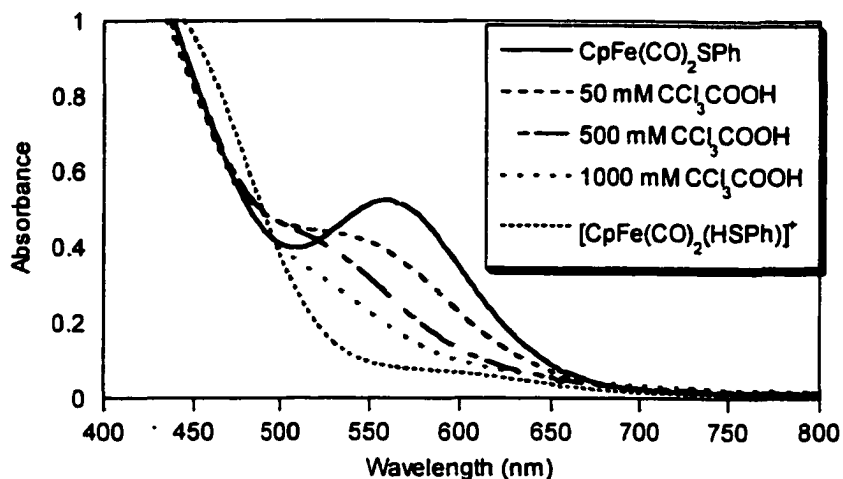
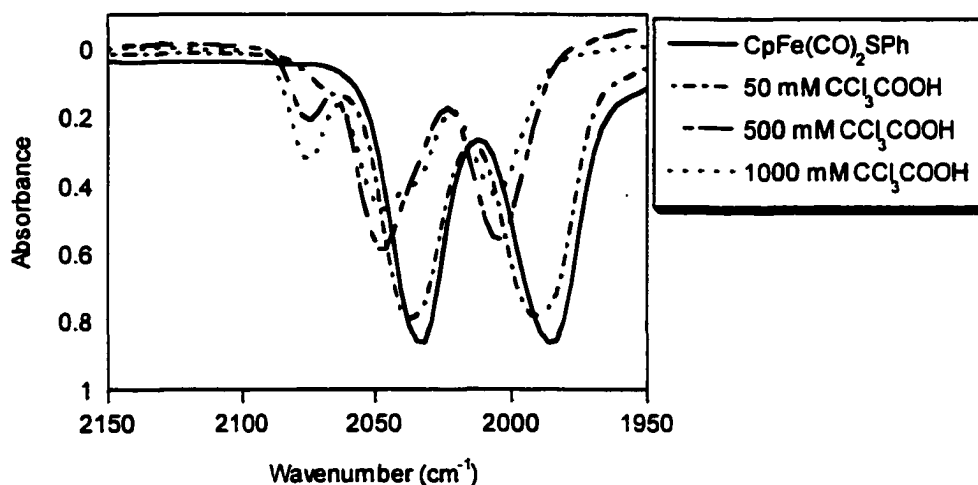


Figure 2.8. Infrared Spectrum of 10 mM $\text{CpFe}(\text{CO})_2(\text{SC}_6\text{H}_5)$ reacting with 1000 mM CCl_3COOH in CH_2Cl_2 .



a.



b.

Figure 2.9. a) Changes in the UV-visible spectra of **1** in CH_2Cl_2 upon addition of trichloroacetic acid. Note the lack of isosbestic points. The spectrum of $[\text{CpFe}(\text{CO})_2(\text{HSC}_6\text{H}_5)]^+$ is shown for comparison. b) Corresponding changes in the IR of the same solutions that were used to collect the UV-visible spectra.

Table 2.2. The carbonyl stretching frequencies of 10 mM CpFe(CO)₂(SC₆H₅) with 150 mM acid in CH₂Cl₂.

150 mM Acid	pKa	$\nu_{\text{CO}} \text{ cm}^{-1}$					
CF ₃ COOH ^a	<0.5	2072		2038		1993	
CF ₃ COOH ^b		2071	2041	2029	2012	1997	1986
CCl ₃ COOH ^a	0.70	2069		2038		1992	
CCl ₃ COOH ^b		2069	2041	2028	2011	1997	1984
CCl ₂ HCOOH ^a	1.48	2066		2035			1989
CCl ₂ HCOOH ^b		2067	2040	2029	2011	1995	1983
CClH ₂ COOH ^a	2.85			2033			1986
CClH ₂ COOH ^b			2038	2030		1993	1982
CH ₃ COOH ^a	4.75			2032			1985
CH ₃ COOH ^b				2032			1985

- a. The experimental CO stretching frequencies before a curve fit analysis.
 b. The experimental CO stretching frequencies after a curve fit analysis.

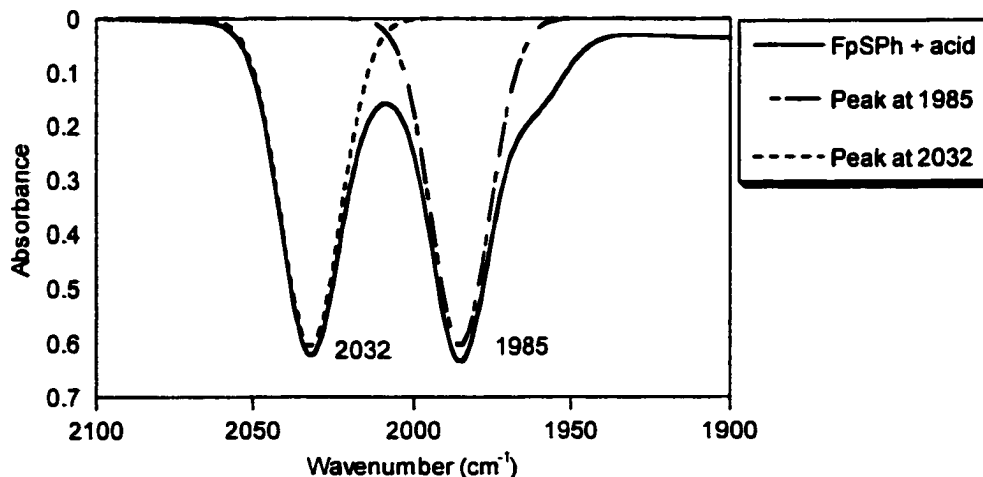


Figure 2.10. Infrared spectrum of 10 mM CpFe(CO)₂(SC₆H₅) reacting with 150 mM CH₃COOH in CH₂Cl₂. Note that the curve fit stretching frequency values match the experimental values.

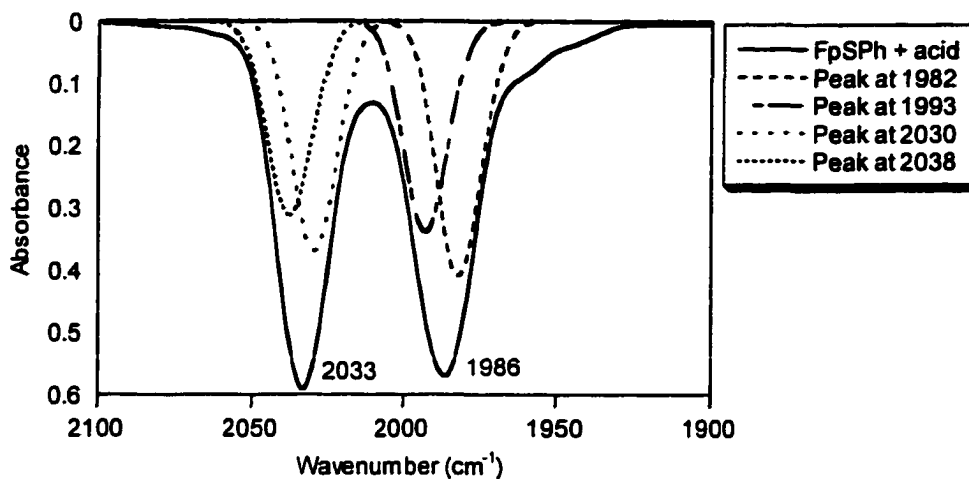


Figure 2.11. Infrared spectrum of 10 mM $\text{CpFe}(\text{CO})_2(\text{SC}_6\text{H}_5)$ reacting with 150 mM CClH_2COOH in CH_2Cl_2 .

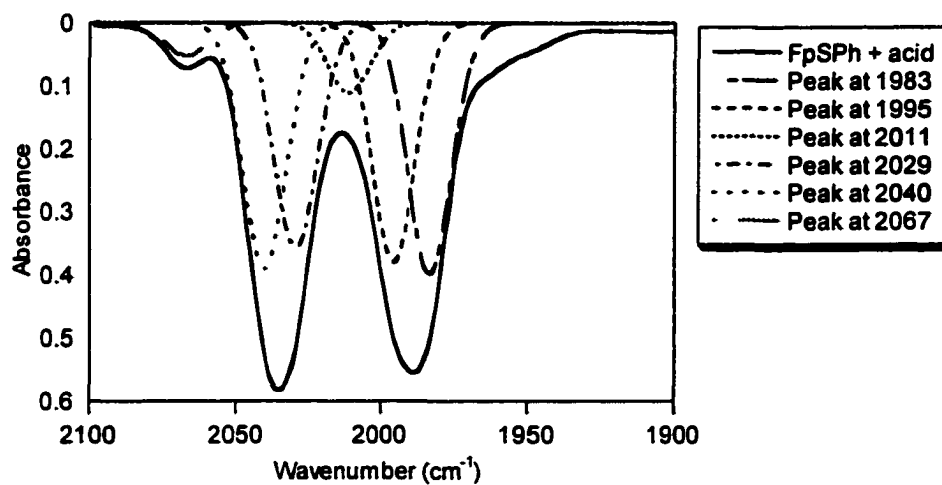


Figure 2.12. Infrared spectrum of 10 mM $\text{CpFe}(\text{CO})_2(\text{SC}_6\text{H}_5)$ reacting with 150 mM CCl_2HCOOH in CH_2Cl_2 .

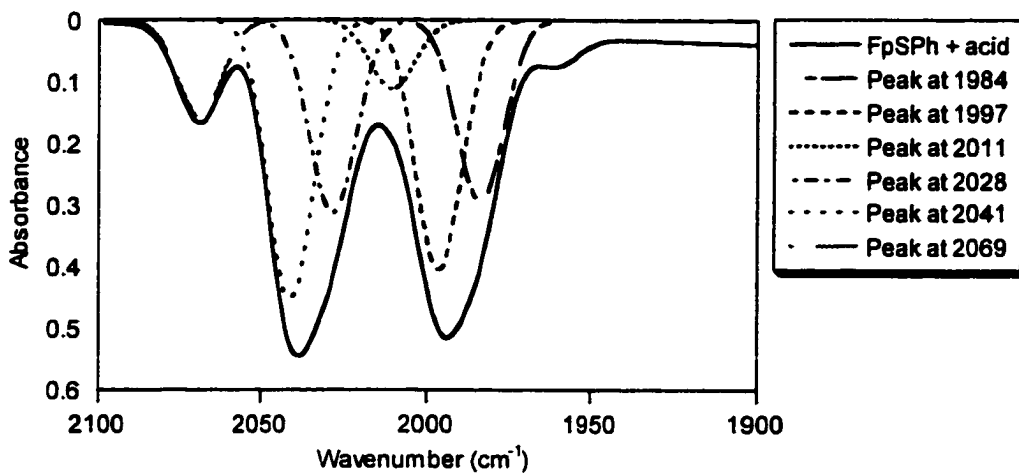


Figure 2.13. Infrared spectrum of 10 mM $\text{CpFe}(\text{CO})_2(\text{SC}_6\text{H}_5)$ reacting with 150 mM CCl_3COOH in CH_2Cl_2 .

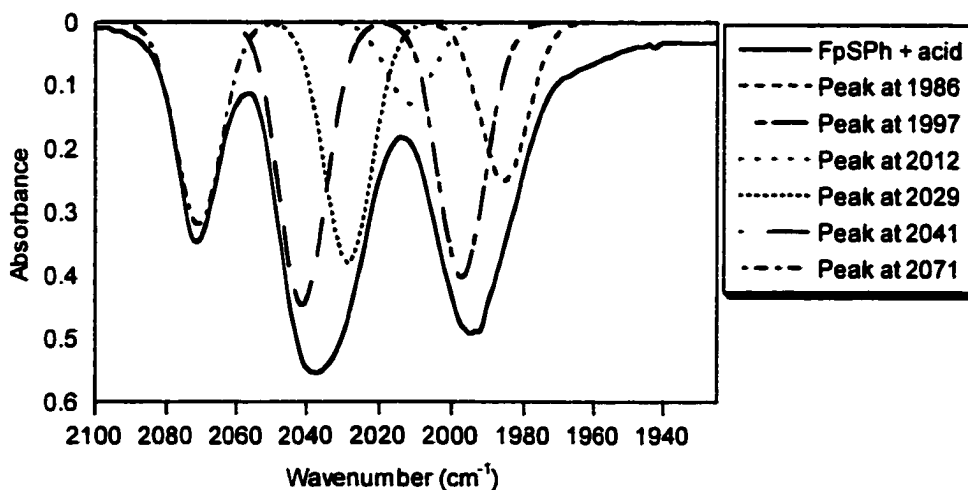


Figure 2.14. Infrared spectrum of 10 mM $\text{CpFe}(\text{CO})_2(\text{SC}_6\text{H}_5)$ reacting with 150 mM CF_3COOH in CH_2Cl_2 .

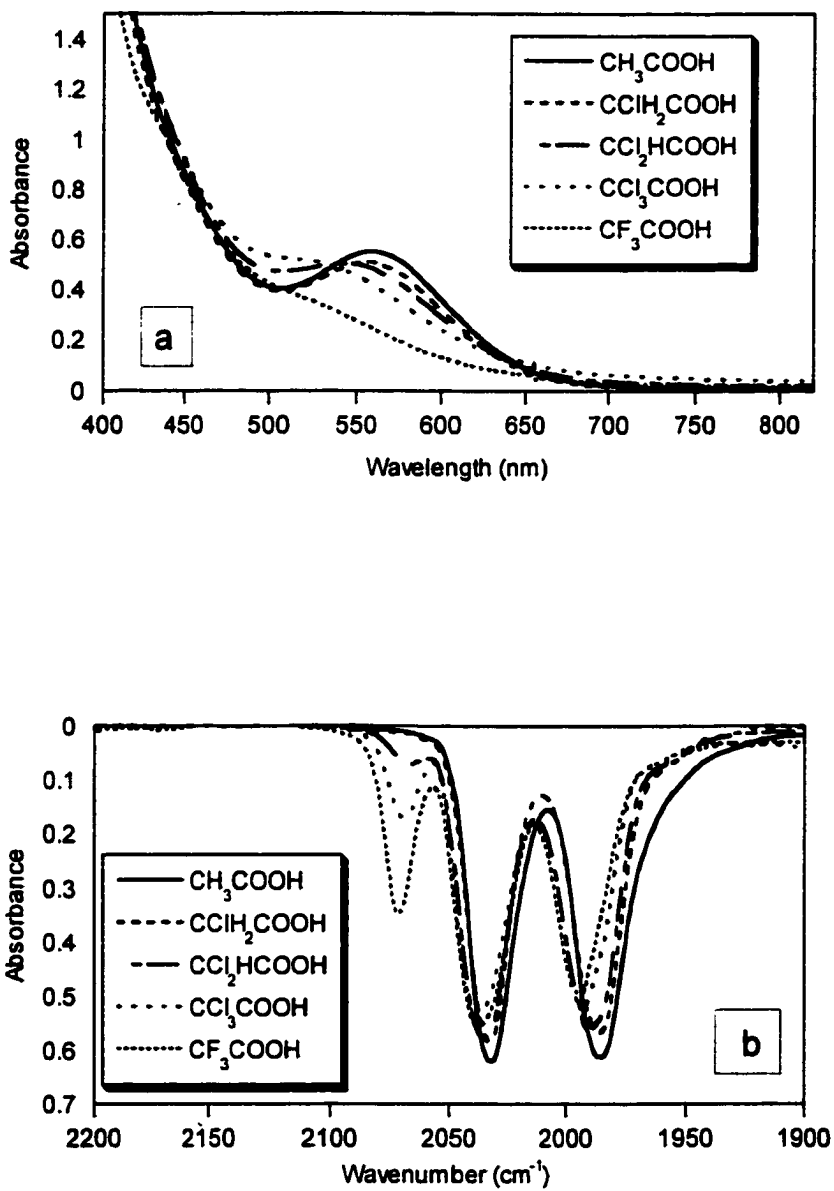


Figure 2.15. a) Changes in the UV-visible spectra of $\text{CpFe}(\text{CO})_2(\text{SC}_6\text{H}_5)$ in CH_2Cl_2 upon addition of acetic acid, monochloroacetic acid, dichloroacetic acid, trichloroacetic acid, and trifluoroacetic acid. Note the lack of isosbestic points. b) Corresponding changes in the IR of the same solutions that were used to collect the UV-visible spectra.

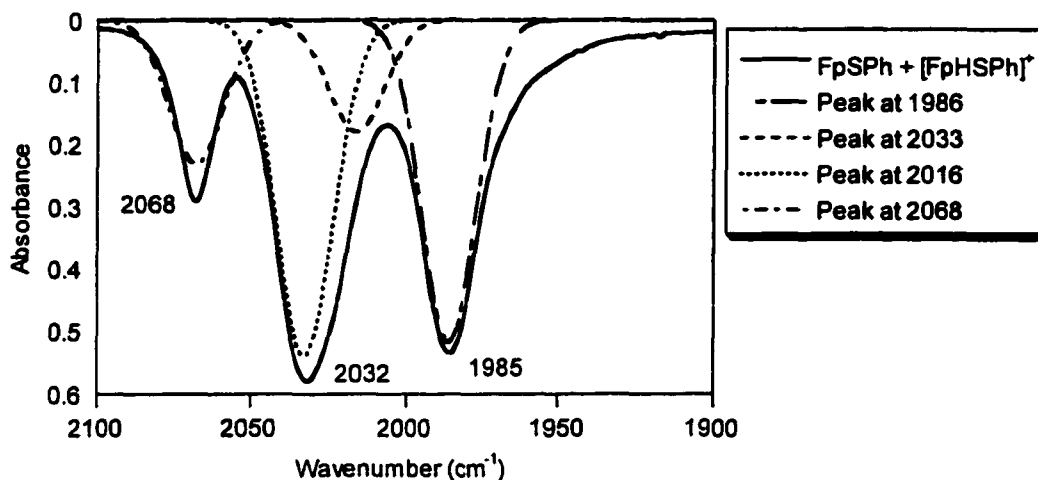


Figure 2.16. IR spectrum of 10 mM $\text{CpFe}(\text{CO})_2(\text{SC}_6\text{H}_5) + 5 \text{ mM HBF}_4 \cdot \text{O}(\text{CH}_3)_2$ in CH_2Cl_2 .

Table 2.3. Infrared data of 10 mM $\text{CpFe}(\text{CO})_2\text{Cl}$ and 10 mM $\text{CpFe}(\text{CO})_2\text{I}$ with and without 150 mM CF_3COOH in CH_2Cl_2 .

10 mM $\text{CpFe}(\text{CO})_2\text{X}^{\text{a}}$	$\nu_{\text{CO}} (\text{cm}^{-1})$			
$\text{CpFe}(\text{CO})_2\text{Cl}^{\text{b}}$	2052		2007	
$\text{CpFe}(\text{CO})_2\text{Cl}^{\text{c}}$	2060		2015	
$\text{CpFe}(\text{CO})_2\text{I}^{\text{b}}$		2041		1996
$\text{CpFe}(\text{CO})_2\text{I}^{\text{c}}$		2041		1996

a. X is Chloride or Iodide

b. Compound $\text{CpFe}(\text{CO})_2\text{X}$ without CF_3COOH .

c. Compound $\text{CpFe}(\text{CO})_2\text{X}$ with CF_3COOH .

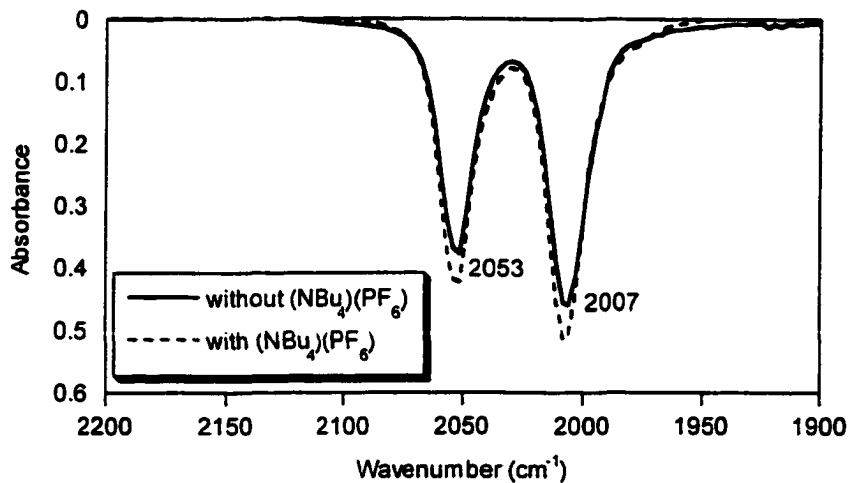


Figure 2.17. IR spectra of 5 mM CpFe(CO)₂Cl with (NBu₄)(PF₆) and without 150 mM (NBu₄)(PF₆) in CH₂Cl₂. Note that the stretching frequencies for both solutions are the same.

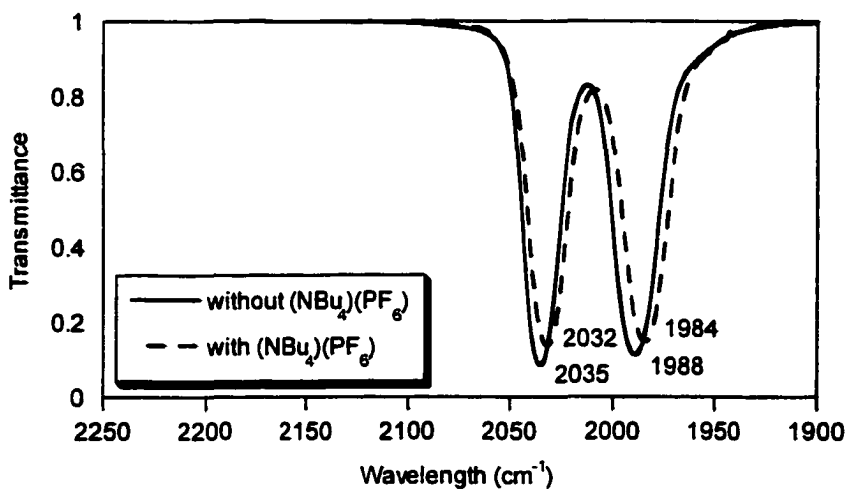


Figure 2.18. Infrared spectrum of a 10 mM CpFe(CO)₂(SC₆H₅) with and without 1.0 M (NBu₄)(PF₆) in CH₂Cl₂.

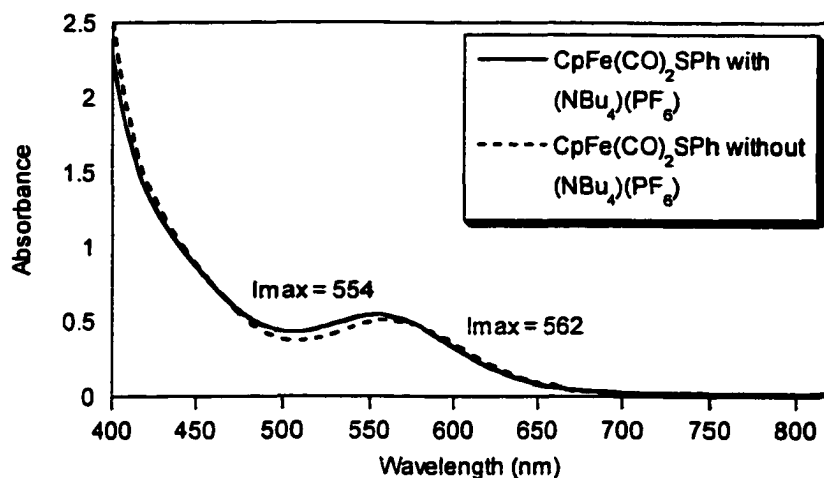


Figure 2.19. Visible spectrum of a 10 mM $\text{CpFe}(\text{CO})_2(\text{SC}_6\text{H}_5)$ with and without 1.0 M $(\text{NBu}_4)(\text{PF}_6)$ in CH_2Cl_2 .

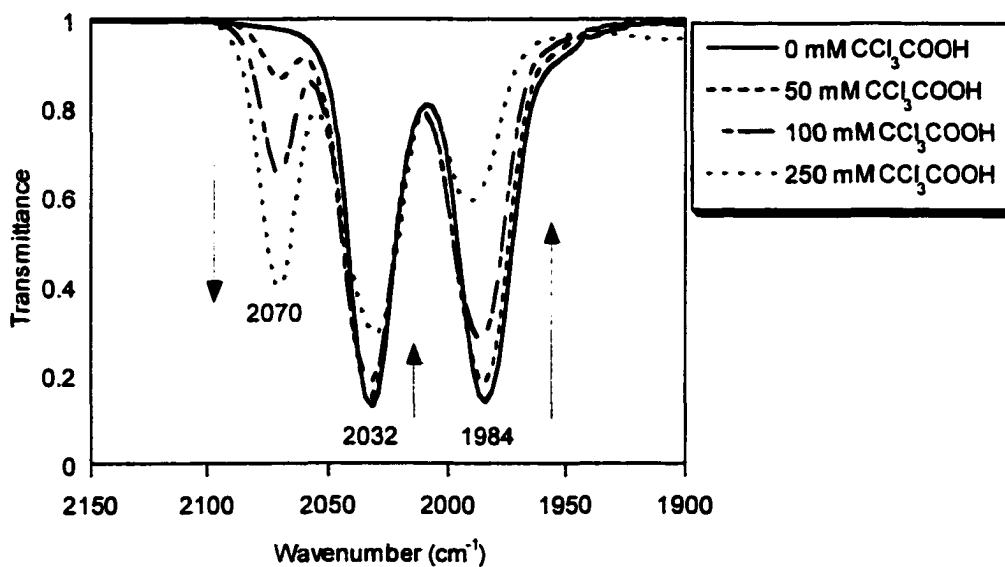


Figure 2.20. Changes in the infrared spectra of $\text{CpFe}(\text{CO})_2(\text{SC}_6\text{H}_5)$ in CH_2Cl_2 upon addition of an increasing concentration of trichloroacetic acid in the presence of $(\text{NBu}_4)(\text{PF}_6)$.

2.4 Results of the Solid State Experiments

The crystal data and structure refinement for $\text{CpFe(CO)}_2(\text{SC}_6\text{H}_5)$ and $[\text{CpFe(CO)}_2(\text{HSC}_6\text{H}_5)]\text{BF}_4$ are located in Tables 2.4 and 2.6 respectively. The atomic coordinates ($\times 10^4$) and equivalent isotropic displacement parameters ($\text{\AA}^2 \times 10^3$) for $\text{CpFe(CO)}_2(\text{SC}_6\text{H}_5)$ and $[\text{CpFe(CO)}_2(\text{HSC}_6\text{H}_5)]\text{BF}_4$ are located in Tables 2.5 and 2.7 respectively. The thermal ellipsoid drawings of $\text{CpFe(CO)}_2(\text{SC}_6\text{H}_5)$ and $[\text{CpFe(CO)}_2(\text{HSC}_6\text{H}_5)]\text{BF}_4$ are shown in Figures 2.21 and 2.23 respectively. The crystal packing of $\text{CpFe(CO)}_2(\text{SC}_6\text{H}_5)$ and $[\text{CpFe(CO)}_2(\text{HSC}_6\text{H}_5)]\text{BF}_4$ are also shown in Figures 2.21 and 2.23 respectively.

Table 2.4. Crystal Data and Structure Refinement for $\text{CpFe}(\text{CO})_2(\text{SC}_6\text{H}_5)$.

Empirical formula	$\text{C}_{13}\text{H}_{10}\text{FeO}_2\text{S}$
Formula weight	286.12
Temperature	188(2) K
Wavelength	0.71073 Å
Crystal system	Monoclinic
Space group	$P2_1/n$
Unit cell dimensions	$a = 6.147(2)$ Å $\alpha = 90$ deg. $b = 15.933(3)$ Å $\beta = 97.92(3)$ deg. $c = 12.711(3)$ Å $\gamma = 90$ deg.
Volume, Z	$1233.1(5)$ Å ³ , 4
Density (calculated)	1.541 mg/m ³
Absorption coefficient	1.376 mm ⁻¹
F(000)	584
Crystal size	0.12 x 0.30 x 0.16 mm
Theta range for data collection	2.06 to 24.98 deg.
Limiting indices	$0 \leq h \leq 7$, $-18 \leq k \leq 0$, $-15 \leq l \leq 14$
Reflections collected	2351
Independent reflections	2137 [R(int) = 0.0271]
Absorption correction	Semi-empirical from psi-scans
Max. and min. transmission	0.3646 and 0.3250
Refinement method	Full-matrix least-squares on F ²
Data/restraints/parameters	2135/0/154
Goodness-of-fit on F ²	1.122
Final R indices [$I > 2\sigma(I)$]	R1 = 0.0536, wR2 = 0.1437
R indices (all data)	R1 = 0.0657, wR2 = 0.1558
Largest diff. Peak and hole	1.089 and -0.391 e. Å ⁻³

Table 2.5. Atomic coordinates ($\times 10^4$) and equivalent isotropic displacement parameters ($\text{\AA}^2 \times 10^3$) for $\text{CpFe}(\text{CO})_2(\text{SC}_6\text{H}_5)$. $U(\text{eq})$ is defined as one third of the trace of the orthogonalized U_{ij} tensor.

	x	y	z	U(eq)
Fe(1)	2126(1)	2998(1)	5036(1)	25(1)
S(1)	-830(2)	3578(1)	4008(1)	29(1)
O(1)	-498(9)	1490(3)	5129(4)	68(2)
O(2)	3902(7)	2488(3)	3119(3)	50(1)
C(1)	1848(9)	3605(3)	6481(4)	33(1)
C(2)	2842(9)	4156(3)	5815(4)	32(1)
C(3)	4793(9)	3784(4)	5586(4)	39(1)
C(4)	5024(10)	2995(4)	6108(5)	44(2)
C(5)	3207(11)	2895(4)	6668(4)	43(1)
C(6)	-105(8)	4239(3)	2990(4)	28(1)
C(7)	-1783(9)	4432(3)	2170(4)	34(1)
C(8)	-1414(10)	4983(4)	1371(4)	42(1)
C(9)	636(11)	5333(4)	1356(4)	42(1)
C(10)	2325(10)	5131(4)	2149(5)	40(1)
C(11)	1960(9)	4586(3)	2959(4)	32(1)
C(12)	529(10)	2081(4)	5077(5)	39(1)
C(13)	3235(9)	2687(3)	3883(4)	34(1)

Table 2.6. Crystal data and structure refinement for [CpFe(CO)₂(HSC₆H₅)]BF₄.

Empirical formula	C ₁₃ H ₁₁ BF ₄ FeO ₂ S
Formula weight	373.94
Temperature	188(2) K
Wavelength	0.71073 Å
Crystal system	Monoclinic
Space group	P2 ₁ /c
Unit cell dimensions	a = 6.3987(10) Å alpha = 90 deg. b = 7.4616(14) Å beta = 95.206(12) c = 31.177(5) Å gamma = 90 deg.
Volume, Z	1482.4(4) Å ³ , 4
Density (calculated)	1.675 mg/m ³
Absorption coefficient	1.202 mm ⁻¹
F(000)	752
Crystal size	0.06 x 0.38 x 0.28 mm
Theta range for data collection	2.62 to 26.00 deg.
Limiting indices	0 ≤ h ≤ 7, 0 ≤ k ≤ 9, -38 ≤ l ≤ 38
Reflections collected	3179
Independent reflections	2897 [R(int) = 0.0329]
Absorption correction	Semi-empirical from psi-scans
Max. and min. transmission	0.4488 and 0.3755
Refinement method	Full-matrix least-squares on F ²
Data/restraints/parameters	2889/0/197
Goodness-of-fit on F ²	1.092
Final R indices [I > 2σ(I)]	R1 = 0.0543, wR2 = 0.1330
R indices (all data)	R1 = 0.0785, wR2 = 0.1637
Largest diff. Peak and hole	0.660 and -0.472 e. Å ⁻³

Table 2.7. Atomic coordinates ($\times 10^4$) and equivalent isotropic displacement parameters ($\text{\AA}^2 \times 10^3$) for $[\text{CpFe}(\text{CO})_2(\text{HSC}_6\text{H}_5)]\text{BF}_4$. $U(\text{eq})$ is defined as one third of the trace of the orthogonalized U_{ij} tensor.

	x	y	z	U(eq)
Fe(1)	2761(1)	2332(1)	4036(1)	25(1)
S(1)	3780(2)	4663(2)	3642(1)	39(1)
O(1)	-1558(5)	2318(6)	3641(1)	54(1)
O(2)	3972(7)	-509(6)	3568(1)	60(1)
C(1)	3988(9)	3799(7)	4578(1)	44(1)
C(2)	5232(8)	2240(8)	4519(2)	46(1)
C(3)	3927(8)	733(7)	4549(1)	40(1)
C(4)	1907(8)	1341(7)	4619(1)	39(1)
C(5)	1959(8)	3228(7)	4639(1)	40(1)
C(6)	3023(7)	4342(6)	3085(1)	34(1)
C(7)	1147(8)	5037(7)	2898(2)	45(1)
C(8)	665(10)	4849(8)	2454(2)	54(1)
C(9)	2053(10)	3991(7)	2206(2)	54(1)
C(10)	3884(10)	3282(8)	2401(2)	53(1)
C(11)	4397(4)	3457(4)	2838(1)	45(1)
C(12)	3573(4)	587(4)	3679(1)	31(1)
C(13)	117(4)	2350(4)	3794(1)	34(1)
B(1)	-968(10)	7269(8)	4194(2)	46(1)
F(1)	-620(10)	7114(8)	3775(1)	126(2)
F(2)	932(6)	7314(5)	4442(2)	81(1)
F(3)	-2050(6)	8825(5)	4256(2)	84(1)
F(4)	-2040(6)	5822(5)	4317(1)	78(1)

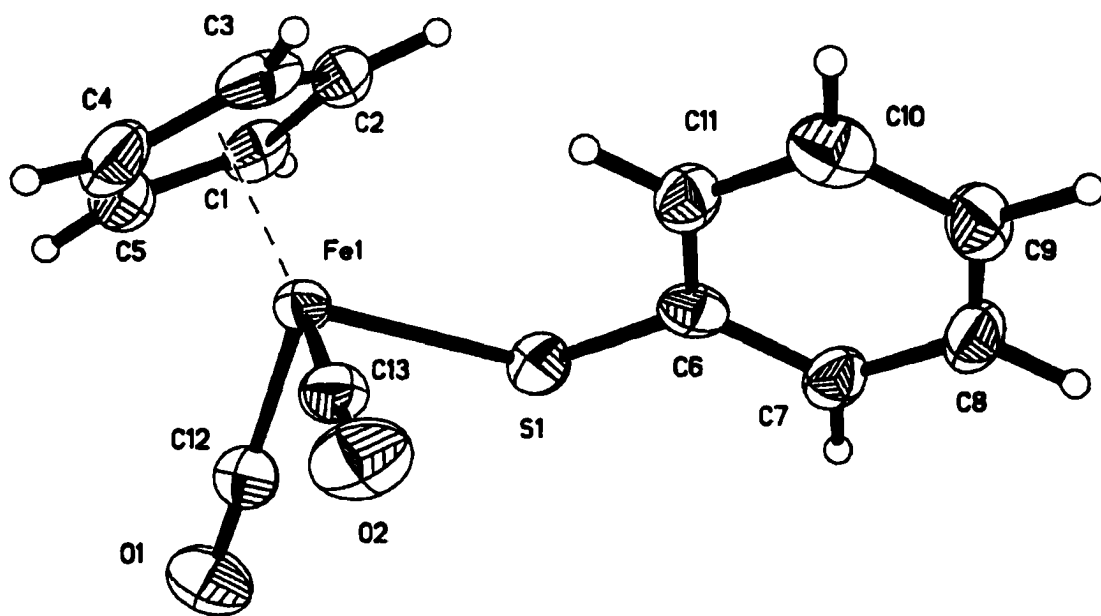


Figure 2.21. Thermal ellipsoid drawing of the crystal structure of $\text{CpFe(CO)}_2(\text{SC}_6\text{H}_5)$ at the 50% level with the labeling scheme. The hydrogen atoms were included with idealized parameters.

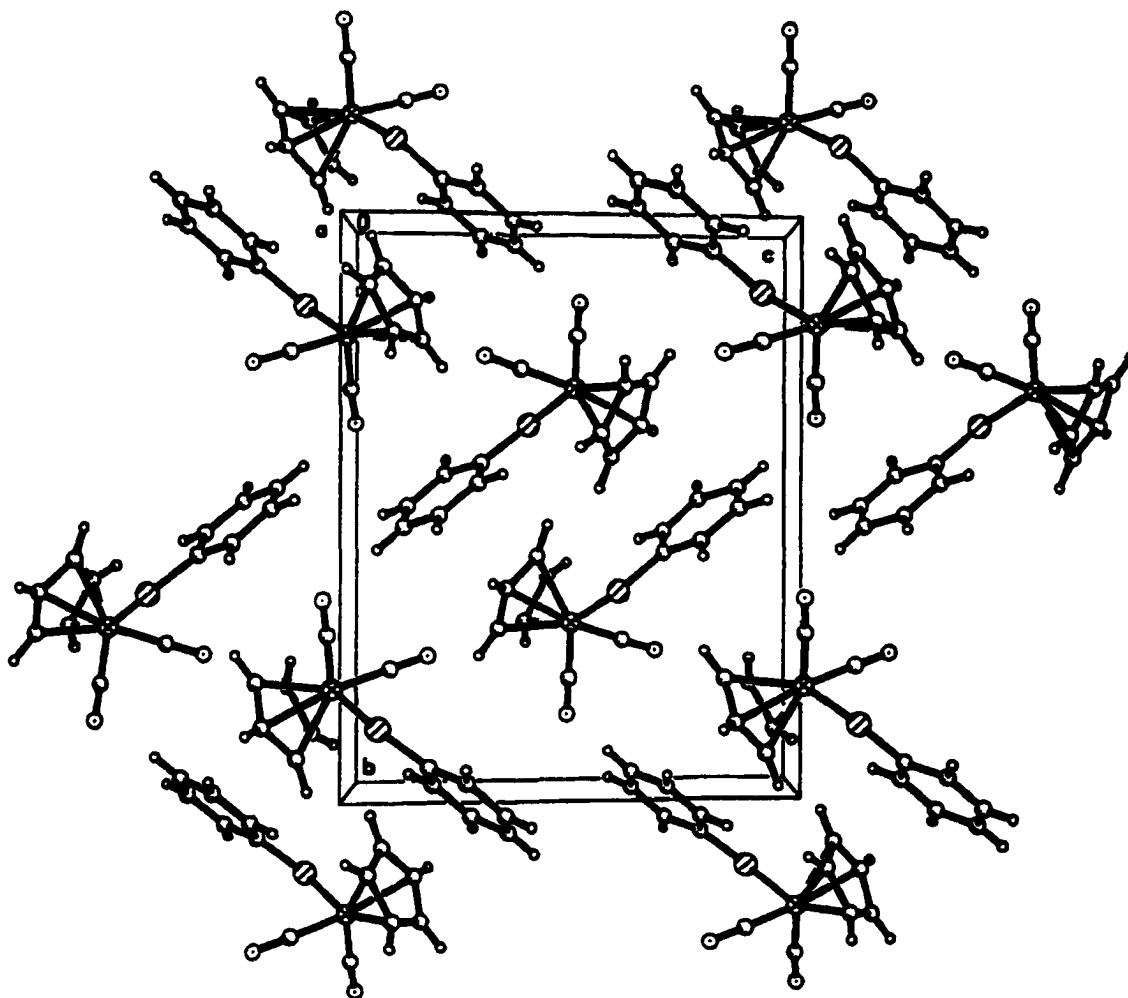


Figure 2.22. The crystal packing diagram of $\text{CpFe}(\text{CO})_2(\text{SC}_6\text{H}_5)$. The hydrogen atoms were included with idealized parameters.

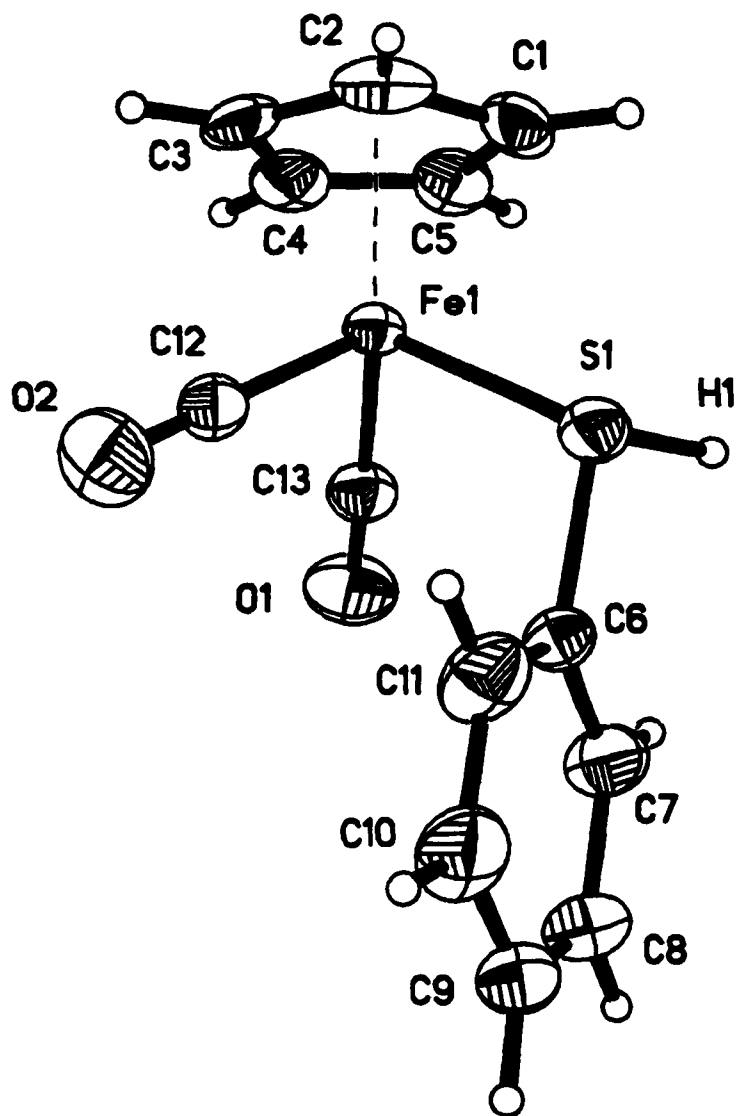


Figure 2.23. Thermal ellipsoid drawing of the crystal structure of $[\text{CpFe}(\text{CO})_2(\text{HSC}_6\text{H}_5)]^+$ at the 50% level with the labeling scheme. The hydrogen atom on the sulfur atom was located in the difference map and refined isotropically. All the other hydrogen atoms were included with idealized parameters.

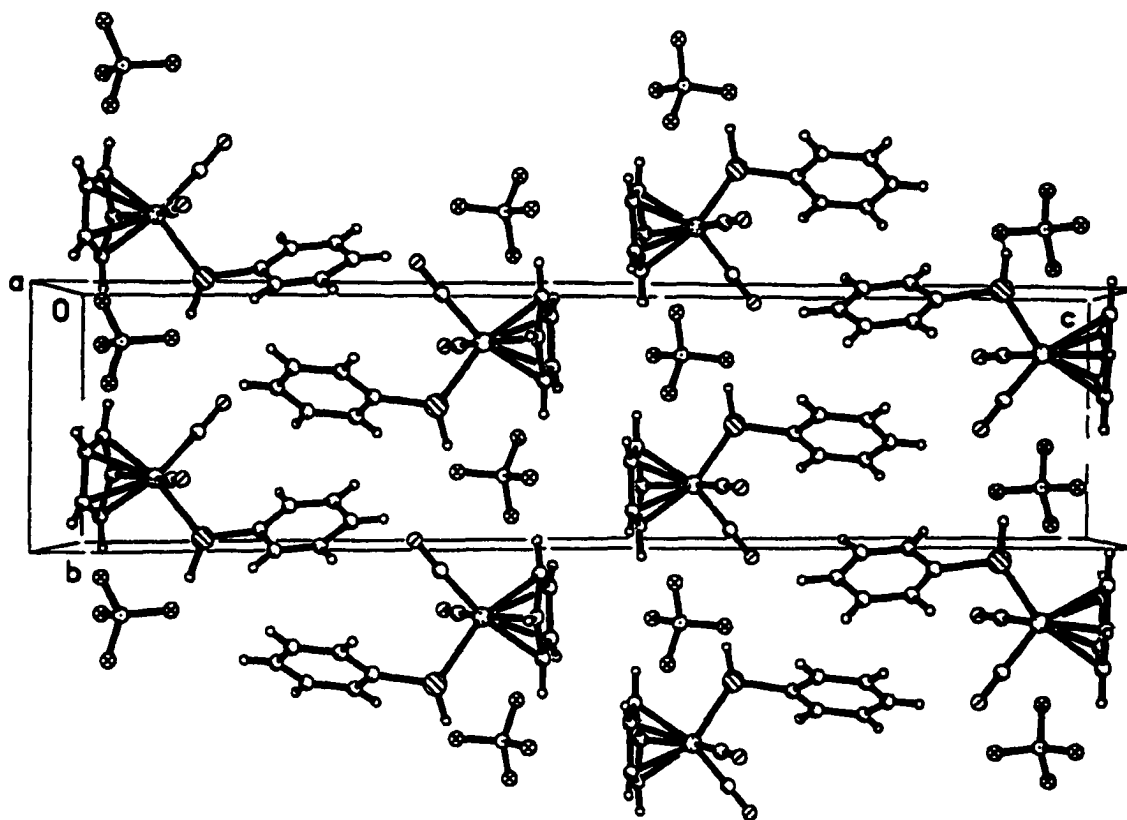


Figure 2.24. The crystal packing diagram of $[\text{CpFe}(\text{CO})_2(\text{HSC}_6\text{H}_5)]\text{BF}_4$. The hydrogen atoms were included with idealized parameters.

Table 2.8. Selected bond lengths (Å) and angles (deg) for CpFe(CO)₂(SC₆H₅).

Fe(1) - C(12)	1.766(6)
Fe(1) - C(13)	1.770(6)
Fe(1) - S(1)	2.283(2)
Fe(1) - X(1)	1.724(6)
C(12) - Fe(1) - C(13)	94.1(3)
C(12) - Fe(1) - S(1)	87.1(2)
C(13) - Fe(1) - S(1)	90.4(2)
X(1) - Fe(1) - S(1)	123.6(3)
X(1) - Fe(1) - C(12)	124.8(4)
X(1) - Fe(1) - C(13)	125.9(4)

X represents the centroid of Cp.

Table 2.9. Selected bond lengths (Å) and angles (deg) for
[CpFe(CO)₂(HSC₆H₅)]BF₄.

Fe(1) - C(13)	1.789(3)
Fe(1) - C(12)	1.819(3)
Fe(1) - S(1)	2.2590(13)
Fe(1) - X(1)	1.711(3)
S(1) - H(1)	1.35(7)
C(13) - Fe(1) - C(12)	93.34(13)
C(13) - Fe(1) - S(1)	94.19(9)
C(12) - Fe(1) - S(1)	96.04(9)
X(1) - Fe(1) - S(1)	120.4(1)
X(1) - Fe(1) - C(12)	122.1(1)
X(1) - Fe(1) - C(13)	123.5(1)
H(1) - S(1) - Fe(1)	108(3)
H(1) - S(1) - C(6)	100(3)

X represents the centroid of Cp.

2.5 Results of the Molecular Orbital Calculations

Some results of the density functional calculations are presented in Table 2.10 along with selected results from the crystal structures and solution studies. A comparison of bond lengths, bond angles, and carbonyl stretching frequencies are listed.

The Highest Occupied Molecular Orbitals (HOMOs) of the various Brønsted acid adducts of CpFe(CO)₂SCH₃ were calculated by the DFT method. The pictorial representations are located in Figure 2.25.

Table 2.10. Experimental (R=C₆H₅)^a and Computed (R=CH₃)^b Bond Distances and Carbonyl Stretching for CpFe(CO)₂SR and Its Hydrogen-Bonded Adducts.

FpS-R ^c compounds	Fe-S bond dist. (Å)	S-H bond dist. (Å)	Obs ν_{CO} (cm ⁻¹)	Obs F_{CO} (k _i) (mdyn/ Å)	Cald ν_{CO} (cm ⁻¹)
FpSR	2.331	N/A	1985, 2032	16.29 ₂ (0.38 ₁)	1980, 2024
FpSR-AcOH ^d	2.331	2.227	1985, 2032	16.29 ₂ (0.38 ₁)	1990, 2032
FpSR-CAA ^e			1986, 2033	16.30 ₉ (0.38 ₁)	
FpSR-DCA ^f			1988, 2035	16.34 ₁ (0.38 ₁)	
FpSR-TCA ^g			1992, 2038	16.39 ₈ (0.37 ₄)	
FpSR-TFA ^h	2.332	2.126	1995, 2038	16.42 ₂ (0.35 ₀)	1993, 2035
FpSR-HBF ₄ ⁱ	2.301	1.471			1998, 2043
FpHSR ⁺	2.284	1.372	2025, 2067	16.90 ₆ (0.34 ₇)	2031, 2068

^a10 mM CpFe(CO)₂(SC₆H₅) in CH₂Cl₂. ^bCalculated at the pDF/BP* level for the Brønsted Acid Adducts of CpFe(CO)₂SCH₃ using Spartan 5.0. ^cFp represents CpFe(CO)₂. ^dAcetic acid. ^eChloroacetic acid. ^fDichloroacetic acid. ^gTrichloroacetic acid. ^hTrifluoroacetic acid. ⁱHydrogen bound tetrafluoroboric acid.

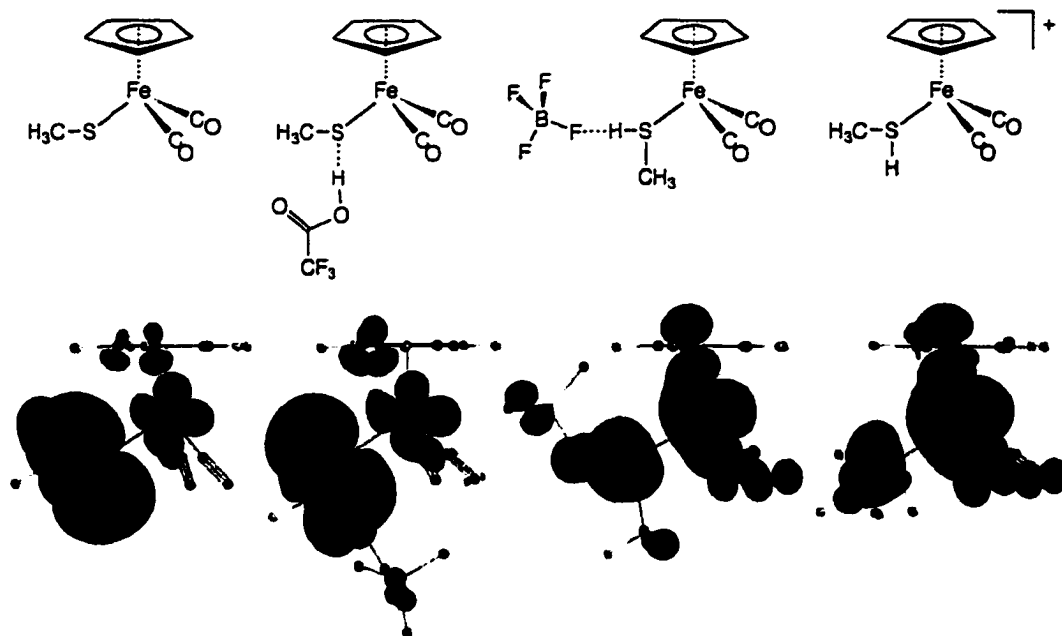
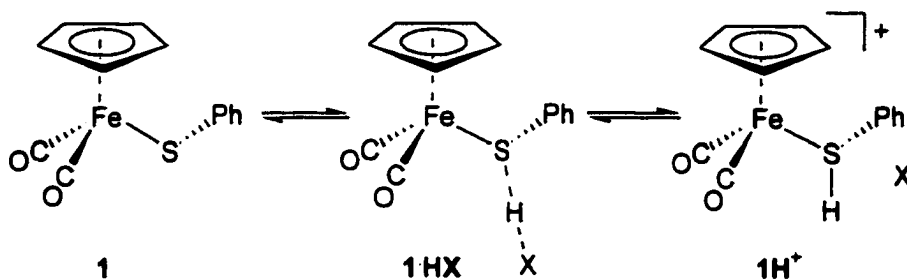


Figure 2.25. Highest Occupied Molecular Orbitals (HOMOs) of Various Brønsted Acid Adducts of CpFe(CO)₂SCH₃ as calculated by the DFT Method.

Note the HOMO is largely S in character until the H-bond is polarized toward S, at which time the HOMO becomes largely Fe in character (with concomitant increase in Cp character).

2.6 Discussion

In this chapter, we presented spectroscopic, solid state, and MO calculations as evidence in support of the equilibrium process as outlined in Scheme 2.1. These studies corroborate one another very well.



Scheme 2.1

The spectroscopic studies focused on analyses of the carbonyl stretching frequencies in the infrared region and observation of the changes in the ligand to metal charge transfer band (LMCT) in the visible region as compound **1** is dissolved in an aprotic, low dielectric solvent such as CH₂Cl₂ and a Brønsted acid is added to the solution. As the acid concentration increases, the equilibrium is shifted to the right as is indicated by an increase in the carbonyl stretching frequencies and a shift to shorter wavelength of the LMCT band. The carbonyl stretching frequencies and, in turn, force constants (F_{CO}) have been determined to be related to ionization potentials. There is a significant difference in the half wave potential, $E_{1/2}$, between the non-protonated **1** and the protonated species **1H⁺** as will be presented in this discussion.

Compounds **1** and **1H⁺** are isolable but **1·HX** is not. The **1·HX** complex appears to be a hydrogen bonded species and is formed by the acidic hydrogen

from a carboxylic acid group bonding to the sulfur. As the acid concentration increases, multiple hydrogen bonds are expected at the sulfur. Also under these conditions, the dielectric constant of the solvent is increasing and hydrogen bonding is probably occurring between the proton donors as shown in Figure 2.27. Complex $1 \cdot HX$ would then appear to be part of a continuum with minimal hydrogen bonding at low acid concentrations to multiple hydrogen bonds at higher concentrations. As the acid concentration continues to increase, the polarity of the solvent promotes ionization of the acid and protonation of compound 1 occurs to form compound $1H^+$.

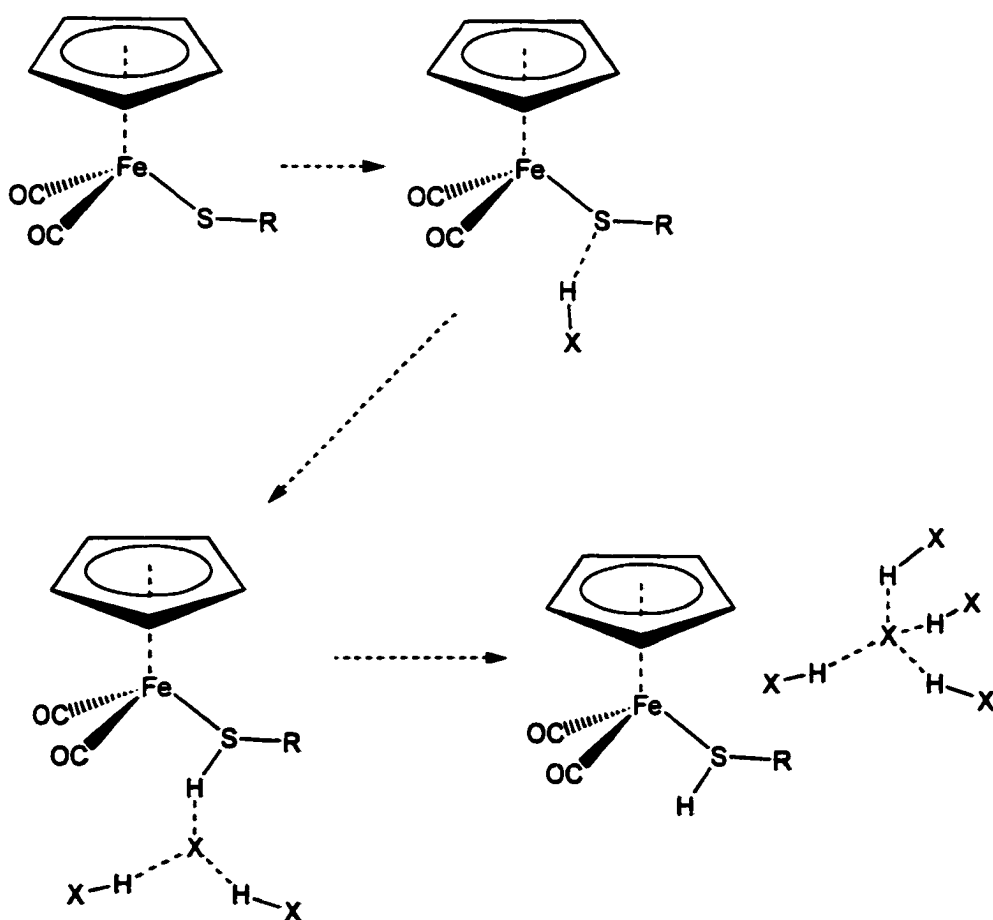


Figure 2.26. The complex $CpFe(CO)_2(SR)$ mixed with an increasing acid concentration until protonation takes place.

The highest occupied molecular orbital (HOMO) of compound **1** is an Fe($d\pi$)-S($p\pi$) anti-bonding orbital and is largely sulfur in character.^{33,35} The sulfur, as expected, is the point of attack by a proton donor. The donor properties of the thiolate ligand toward the metal are affected by hydrogen bonding; however, we propose that a substantially greater effect occurs due to protonation. We can observe, indirectly, the changing electronic effects that are occurring at the metal center as compound **1** is titrated with various weak and strong acids. By using infrared spectroscopy to observe the changes in CO stretching frequencies and UV-vis spectroscopy to observe the change in the ligand to metal charge transfer band, the electronic effects can be accurately monitored during titration. For example, to test if hydrogen bonding may be occurring at oxygen site on the carbonyls of CpFe(CO)₂(SC₆H₅), 150 mM CF₃COOH was added to a CH₂Cl₂ solution of CpFe(CO)₂Cl (10.62 mg, 5 mM). The results are listed in Table 2.3. The CO stretching frequencies are 2053 and 2007 cm⁻¹ without CF₃COOH added to the solution and 2058 and 2014 cm⁻¹ with CF₃COOH. Apparently, hydrogen bonding may be occurring on the chloride ligand.⁵⁹ To test this, CpFe(CO)₂I was substituted for the chloride compound since the iodide ligand is softer in character than the chloride ligand. No effect was observed on the carbonyl stretching frequencies when 150 mM CF₃COOH was added to a CH₂Cl₂ solution of CpFe(CO)₂I (15.2 mg, 5 mM). The results in this case indicate that no hydrogen bonding is occurring on the carbonyls since no change in the CO stretching frequencies are observed. Based on these experiments, we suggest the hydrogen bonding that occurs to CpFe(CO)₂(SC₆H₅) happens mostly at the sulfur.

In a previous study by Ashby *et al.*, the CO stretching frequencies of the compound CpFe(CO)₂SC₆H₄-p-Z where Z = H, Cl, CF₃, and NO₂, were correlated to the HOMO ionization potential (as determined by gas-phase PES) of each

compound.³⁵ Figure 2.26 represents the correlation between the symmetric and antisymmetric stretching frequencies and the first ionization potentials as determined from previous PES studies.³⁵

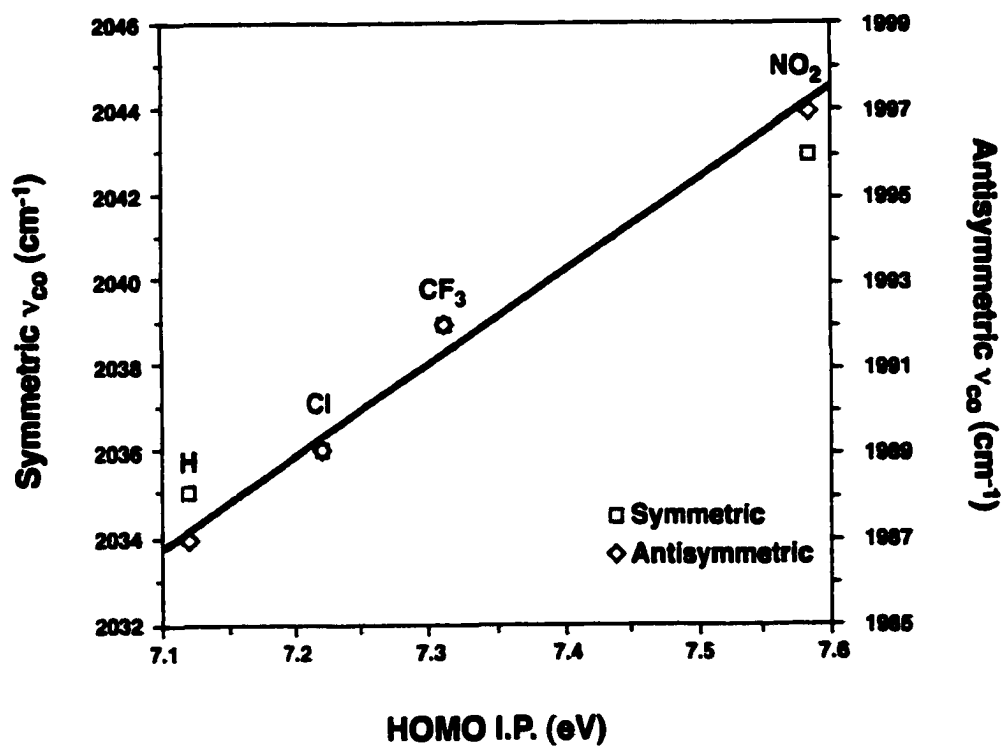


Figure 2.27. Spectroscopic Properties for $CpFe(CO)_2SC_6H_4-p-Z$ where $Z = H, Cl, CF_3,$ and NO_2 .

As Z becomes more electron withdrawing, the carbonyl stretching frequencies increase as well as the ionization potential which establishes a linear relationship. This relationship in terms of the force constant, F_{co} , and the first ionization potential can be described in the following equation:³⁵

$$\text{IP} = 2.68F_{\text{co}} - 36.6$$

A correlation between electrochemical and photoionization data generally yield empirical relationships of the form:⁶⁰⁻⁶⁴

$$E_{1/2} = (0.6 \text{ to } 0.8)\text{IP} - (3.5 \text{ to } 4.5)$$

By using the empirical formula:

$$\Delta E_{1/2} = \lambda \Delta F_{\text{co}} \text{ (i.e., for } 1.6 \leq \lambda \leq 2.1 \text{ and the observed } \Delta F_{\text{co}} = 0.65 \text{ mdyn/\AA)}$$

we predict a shift of the oxidation potential of **1** by 1.0 – 1.3 V upon protonation. This range can be compared with the 500 – 700 mV positive shift that has been observed for model Ni^{65,66} and Fe⁶⁵ complexes. Using the value of $F_{\text{co}} = 16.42$ mdyn/\AA that is observed for the hydrogen bound species **1.TFA** (TFA is trifluoroacetic acid), we estimate a maximal effect of $300 \leq \Delta E_{1/2} \leq 400$ mV for H-bonding to **1**. Based on this information, there is a substantially smaller effect for hydrogen bonding, which is about 30% of that observed upon protonation. Shubina *et al.* has demonstrated that sometimes hydrogen bonding is the first stage of protonation.⁶⁷ Perhaps this is what is occurring in the iron-sulfur clusters [3Fe-4S] of certain proteins in which protonation does occur.⁷

Ueyama *et al.* has described the effects of a double and single hydrogen bond on a cytochrome P450 model in terms of potential (eV) and the Fe-S bond distance (Table 2.11).⁶⁸ The compound is an iron(III) complex so the Fe-S bond distance increases due primarily to the weakening of the sigma bond as the hydrogen bonding influence increases. Naturally, the thiolate becomes a weaker base. Notice that the decreased changes in bond distance between the Fe-S has a great influence in the redox potential in that the compounds are more easily reducible.

Table 2.11. Changes in Fe-S distances and Redox potential in a model Cytochrome P450 containing NH...S hydrogen bonds.

Number of NH...S bonds	Fe-S distance (Å)	Redox potential (eV)
0	2.29	-0.68
1	2.32	-0.52
2	2.36	-0.35

Using infrared spectroscopy to observe changes in stretching frequencies in biologically relevant model systems is not new, however the NH stretching frequency is typically the frequency of interest and that is to see if hydrogen bonding is taking place.^{26,68,69} The C=O stretching frequencies in amide groups have also been used to detect hydrogen bonding or the lack of it in model systems.⁷⁰ The S-H stretching frequency of cysteine has also been used as a good indicator of hydrogen bonding inside proteins.⁷¹

The carbonyl stretching frequencies can be used as great indicators as to whether hydrogen bonding is taking place at the ligand or metal. The carbonyl stretching frequencies (ν_{CO}) shifting to higher wavenumbers is an indirect

indication of the existence of a hydrogen bond to a ligand or metal as demonstrated by Kazarian *et al.*⁷² and Peris *et al.*⁷³ As electron density is decreased at the metal center as a result of hydrogen bonding to the metal or a ligand, there is less back donation from the metal to the CO π^* antibonding orbitals.^{35,74}

By adding less than one equivalent of $\text{HBF}_4 \cdot \text{O}(\text{CH}_3)_2$ to $\text{CpFe}(\text{CO})_2(\text{SC}_6\text{H}_5)$, a mixture of **1** and 1H^+ is produced instead of the compound $[\text{CpFe}(\text{CO})_2(\text{SC}_6\text{H}_5)]_2\text{HBF}_4$ as shown in Figure 2.28. The carbonyl stretching frequencies for each species in solution are unperturbed (Figure 2.16). Using the fitting program PeakFit, the center peak can be fitted into two peaks which are representative of the protonated and nonprotonated species. Before protonation, the carbonyl stretching frequencies occur at 1985 and 2032 cm^{-1} (Figure 2.3). By adding one equivalent or greater of $\text{HBF}_4 \cdot \text{O}(\text{CH}_3)_2$ to $\text{CpFe}(\text{CO})_2(\text{SC}_6\text{H}_5)$, complete protonation occurs to form the product 1H^+ . Upon protonation, the color immediately changes from red to yellow, which corresponds to loss of the Fe-S LMCT band in the visible spectrum. (Figure 2.9) There is also an increase in the carbonyl stretching frequencies as expected (Figure 2.4).

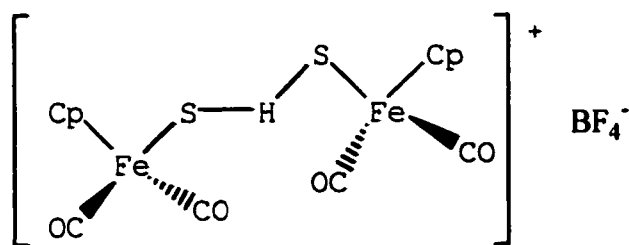


Figure 2.28. A potential product from the reaction between 10 mM $\text{CpFe}(\text{CO})_2(\text{C}_6\text{H}_5)$ and 5 mM $\text{HBF}_4 \cdot \text{O}(\text{CH}_3)_2$.

A continuum of change in the UV-visible and infrared spectra is observed when less strong acids are added to $\text{CpFe}(\text{CO})_2(\text{SC}_6\text{H}_5)$ in a nonpolar solvent. This is explained by the equilibrium that is shown in Scheme 2.1. For example, by increasing the concentration of CCl_3COOH to a 10 mL CH_2Cl_2 solution of $\text{CpFe}(\text{CO})_2(\text{SC}_6\text{H}_5)$ (28.6 mg, 10 mM), the ligand to metal charge transfer band in the visible region is undergoing a blue shift due to an increase in hydrogen bonding and at the same time, the CO stretching frequencies in the infrared region are shifting to a higher frequency (Figure 2.9). There are no isosbestic points in the visible region, which indicates that there is not a discrete $1\cdot\text{HX}$ species. As the acid concentration increases, more than one hydrogen bond can be associated with the sulfur until the dielectric of the solvent becomes such that ionization of the acid occurs with concomitant solvation of the conjugate base and protonation of the thiolate takes place. A peak at approximately 2068 cm^{-1} in the infrared region is growing in as the acid concentration increases, which is indicative of the protonated species.

A curve fit analysis on the carbonyl stretching frequencies indicates at least three species in solution when 50 mM CCl_3COOH is reacted with 10 mM $\text{CpFe}(\text{CO})_2(\text{SC}_6\text{H}_5)$. A broad peak at 1991 cm^{-1} and a peak at 2037 cm^{-1} with a shoulder appears in the infrared spectrum (Figure 2.5). According to the curve fit analysis, six individual peaks could be found within these peaks. Two of the peaks, 1983 cm^{-1} and 2031 cm^{-1} are from compound **1** and the smaller peaks at 2066 and 2014 are from compound 1H^+ . Presumably, the strong peaks that are showing up at 2042 cm^{-1} and 1998 cm^{-1} are indicative of a predominant hydrogen bound species. Of course, the equilibrium (Scheme 2.1) is still shifted more to the left since the protonated species is showing up at one-fifth the intensity as the parent compound and the hydrogen bound species. When 1000 mM CCl_3COOH

is reacted with 10 mM $\text{CpFe}(\text{CO})_2(\text{SC}_6\text{H}_5)$, three fairly broad peaks representing the carbonyl stretching frequencies appear in the infrared spectrum (Figure 2.9). The peaks are located at 1996, 2040, and 2068 cm^{-1} . Once again, according to the curve fit analysis, six peaks could be found; however, species **1** has completely reacted to form either the hydrogen bond complex or the protonated species. The two potential hydrogen bonded species have stretching frequencies at 1992 and 2045 cm^{-1} and at 2003 and 2037 cm^{-1} . The frequencies of the protonated species are at 2025 cm^{-1} and 2069 cm^{-1} as expected. By observing the curve fitted values in Table 2.1, it appears that there is a predominant hydrogen bound species which exhibits frequencies at about 1998 cm^{-1} and the other is about 2042 cm^{-1} . The shift of the LMCT to higher energy and the increase in the CO stretching frequencies indicates a shift to the right in the equilibrium (Scheme 2.1).

Reacting various concentrations of CCl_3COOH with 10 mM $\text{CpFe}(\text{CO})_2(\text{SC}_6\text{H}_5)$ in the presence of an inert salt, $(\text{NBu}_4)(\text{PF}_6)$, shows the equilibrium shifts to the right more quickly at significantly lower acid concentrations (Figure 2.20). This certainly is not unexpected since dissociation of an acid is easier in more polar solvents than in less polar solvents and therefore, protonation can take place at lower concentrations. As 250 mM CCl_3COOH reacts with compound **1** in the presence of $(\text{NBu}_4)(\text{PF}_6)$, the absorbance is 0.40 at 2069 cm^{-1} , which is the stretching frequency for the protonated species, and reacting 1000 mM CCl_3COOH with compound **1** excluding $(\text{NBu}_4)(\text{PF}_6)$, the absorbance is only 0.31 at 2069 cm^{-1} which is significantly less considering the concentration difference. This is one of the reasons for studying the affects of hydrogen bonding in less polar solvents.

Not only is hydrogen bonding dependent upon the concentration of a specific acid and solvent polarity, but it is also dependent upon the strength of an

acid. A series of experiments were carried out using CH_3COOH , CH_2ClCOOH , CHCl_2COOH , CCl_3COOH , and CF_3COOH at the same concentration (150 mM in CH_2Cl_2). To each acid solution was added enough $\text{CpFe}(\text{CO})_2(\text{SC}_6\text{H}_5)$ to form a 10 mM solution. The wavelength of the MLCT band decreased and the CO stretching frequencies increased as the strength of the acid increased (Figure 2.8) as expected for a shift in equilibrium to the right with the effective pK_a of the acid (Figure 2.9, Table 2.5).^{63,64} When reacting compound **1** with CH_3COOH , only a slight decrease in the LMCT band was observed (Figure 2.16) and no significant change occurred in the carbonyl stretching frequencies. According to the curve fit analysis, the peaks found were at the same frequencies (2032 and 1985 cm^{-1}) as the experimentally determined frequencies (Figure 2.10).

When reacting compound **1** with CClH_2COOH , a more significant blue shift in the LMCT band than with the acetic acid occurred, and a slight shift in the carbonyl stretching frequencies was also observed (Figure 2.11). The stretching frequencies at 2033 and 1986 cm^{-1} were fitted and the results indicate that four major peaks are present. The frequencies are 1982 and 2030 cm^{-1} representing compound **1** and the others are at 1993 and 2038 cm^{-1} representing a hydrogen bound species. Apparently, the monochloroacetic acid is not a strong enough acid under these conditions to protonate compound **1**. A protoned species begins to appear together with the parent compound and a hydrogen bound species in the infrared spectrum when the dichloroacetic acid is reacted with compound **1** (Figure 2.12).

The dielectric constant of the solvent has increased since the monochloroacetic acid is obviously polar and a substantial amount was added. This could be the reason why the peaks of the compound **1** are now at 1982 and 2030 cm^{-1} instead of 1984 and 2032 cm^{-1} . By making up a solution containing 10 mM $\text{CpFe}(\text{CO})_2(\text{SC}_6\text{H}_5)$ and an inert salt, $(\text{NBu}_4)(\text{PF}_6)$, to increase the dielectric

affect of the solvent, a slight decrease by several wavenumbers in the carbonyl stretching frequencies was observed (Figure 2.18) as well as a slight blue shift in the visible region (Figure 2.19) indicating a solvatochromic effect. Of course, hydrogen bonding increases the CO stretching frequency of compound **1** so there is a distinguishing feature between solvent polarity and hydrogen bonding affects. Another set of solutions were prepared using 10 mM CpFe(CO)₂Cl, instead of compound **1**, with and without (NBu₄)(PF₆). No change occurred in the infrared stretching frequencies (Figure 2.17). So apparently the solvatochromic effect has to do with the type of ligand coordinated to the metal in this case.

When CF₃COOH is reacted with compound **1**, three strong bands show up in the infrared spectrum and a significant loss in the LMCT band in the visible region is observed (Figure 2.16). The bands at 2038 and 1993 cm⁻¹ are broad indicating overlapping bands (Figure 2.15). A curve fit analysis shows large peaks at 2029 and 2071 cm⁻¹ which represents the protonated species. The peaks at 1997 and 2041 cm⁻¹ probably represents the predominant hydrogen bound species; however, the peaks at 1984 and 2011 cm⁻¹ are at much different intensities which indicates a more complex solution involving perhaps two other hydrogen bound species which are at much lower concentrations. As mentioned before, sulfur can have more than a single hydrogen bond.

A comparison of the bond distances and angles of **1** and **1H⁺** was accomplished by single-crystal X-ray crystallographic analysis of a suitable crystal of each compound. The thiolate compound was grown by evaporation of a saturated pentane solution under nitrogen over eight hours and the thiol crystal was obtained by evaporation of a saturated CH₂Cl₂ solution under nitrogen overnight.

Apparently, the X-ray structure of **1H⁺** is the first Fe(II)-thiol compound to be published. There are a limited number of Fe(III)-thiol compounds and all of

them are iron-porphyrin complexes.⁷⁵ An interesting point is that Collman *et al.* have shown in the crystal structure of Fe(TPP)(C₆H₅S)(C₆H₅SH) is that the Fe-S bond distance between the Fe(III)-benzenethiolate is shorter (2.27 Å) than the Fe(III)-benzenethiol (2.43 Å).⁷⁶ This is not unexpected since the thiol is a weaker Lewis base than the thiolate. However, it is also interesting that the Fe-S bond distance for complex **1H**⁺ (2.2590 Å) is shorter than the Fe-S bond distance for **1** complex (2.283 Å). This can be attributed to a reduction of energy of the 4-electron Fe-S dπ-pπ anti-bonding orbital upon protonation of the thiolate ligand.³⁵ The molecular structures of the thiolate and thiol are shown in Figures 2.21 and 2.23 respectively. The selected bond lengths and bond angles are listed in Tables 2.8 and 2.9. The Fe-S bond length for compound **1** is comparable with those of other structurally characterized Fp S-donor complexes (Table 2.12); however, it seems it is one of the shortest bonds that has been observed for Fe(II)-phenylthiolate derivatives (Table 2.13).

The crystal packing diagrams of CpFe(CO)₂(SC₆H₅) and [CpFe(CO)₂(HC₆H₅)]BF₄ are also shown for comparison (Figures 2.23 and 2.25). Notice the apparent hydrogen bonding in the crystal packing diagram for [CpFe(CO)₂(HSC₆H₅)]BF₄ that is taking place between a fluorine from the BF₄⁻ anion and the hydrogen from the sulfur. However, the bond distance from the fluorine to the hydrogen on the sulfur is 2.196 Å, which is too far for any significant hydrogen bonding.⁷⁷

Calculations using a variety of methods such as the Extended Hückel Molecular Orbital method (EHMO), Molecular Dynamic simulations (MD), the Semi-empirical Spin-Restricted Open Shell method, and the Density Functional method (DFT) have been previously carried out to study hydrogen bonding effects in metal-thiolate complexes.^{78,79} The present MO calculations using DFT

were carried out using SPARTAN 5.0⁴² running on a Silicon Graphics IRIS Indigo 2 Solid Impact with a R10000 processor.

Table 2.12. Fe-S Bond Lengths (Å) for Structurally Characterized [CpFe(CO)₂]⁺ with S-Donor Ligands

Fe(II) Compounds	Fe-S Å	Ref.
CpFe(CO) ₂ SC(S)CH ₃	2.256(2)	43
CpFe(CO) ₂ SCO(2-NO ₂ C ₆ H ₄)	2.266(1)	44
W(CO) ₅ {C(SFe[CO]Cp)(Ph)=C(OCH ₂ CH ₃)Ph}	2.269(5)	45
Cp(CO) ₂ FeC(=S)SFe(Cp(CO) ₂ W(CO) ₅)	2.273(1)	46
CpFe(CO) ₂ (η ¹ -SC(S)OCH ₂ CH ₃)	2.274(4)	47
(μ-S ₄)[CpFe(CO) ₂] ₂	2.276(2)	48
(μ-S ₃)[CpFe(CO) ₂] ₂	2.283(2)	48
CpFe(CO) ₂ (SC ₆ H ₅)	2.283(2)	this study
CpFe(CO) ₂ (SCH ₂ CH ₃)	2.296(2)	49
CpFe(C ₄ H ₁₀ O ₂ PS ₂)(CO) ₂ ⁺	2.304(1)	50
[CpFe(C ₆ H ₁₄ O ₂ PS ₂)(CO) ₂] ⁺	2.322(2)	51

Table 2.13. Fe-S Bond Lengths (Å) for Structurally Characterized Fe(II) Phenyl Thiolate Complexes

Compound	Fe-S Å	Fe-S Å (av)	Ref.
$[P(C_6H_5)_4]_2[Fe(SC_6H_5)_4]$	2.359(2), 2.360(2), 2.338(2), 2.355(2)	2.353	52
$(C_6H_5S)Fe(H)(CO)_2(P(OC_6H_5)_3)_2$	2.343(3)	2.342	53
<i>cis, cis, cis</i> - $Fe(CO)_2(dppe)(SC_6H_5)_2$	2.339(5), 2.343(4)	2.341	54
<i>fac</i> - $[Na(15\text{-crown-}5)][Fe(CO)_3(SC_6H_5)_3]$	2.341(3), 2.337(3), 2.345(3)	2.341	55
$Fe(SC_6H_5)_2(H_2NC_2H_4NH_2)(CO)_2$	2.326(1), 2.338(1)	2.332	56
$((CH_3CH_2)_4N)_2[S_2MoS_2Fe(SC_6H_5)_2]$	2.299(2), 2.315(2)	2.307	57
$[(C_6H_5)_4P]_2[(C_6H_5S)_2FeS_2MoS_2]$	2.292(2), 2.303(2)	2.298	58
$C_5H_5Fe(CO)_2(SC_6H_5)$	2.283(2)	2.283	this study

Calculations were carried out on $CpFe(CO)_2(SCH_3)$, two hydrogen bound species with CF_3COOH and HBF_4 as the hydrogen bound donors, and the protonated species $[CpFe(CO)_2HSCH_3]^+$ as shown in Figure 2.2. Compounds **A** and **D** are analogous to $CpFe(CO)_2(SC_6H_5)$ and $[CpFe(CO)_2(HSC_6H_5)]BF_4$ respectively, which were used in the solution studies. Compounds **B** and **C** are models of the hydrogen bound species where **B** uses the weaker acid, CF_3COOH , as the hydrogen donor and **C** uses the stronger acid, HBF_4 . These calculations allow us to see the change in the HOMO characters as compound **A** is hydrogen bound by acids in **B** and **C** and then protonated in compound **D**.

The data from the calculations for $\text{CpFe}(\text{CO})_2\text{SCH}_3$ show that the HOMO is primarily sulfur in character, as expected, but upon protonation, becomes primarily metal in character (Figure 2.24). The complex that contains the weaker acid, CF_3COOH , that is hydrogen bound to $\text{CpFe}(\text{CO})_2\text{SCH}_3$ shows more of the HOMO as primarily sulfur in character but the complex that contains the stronger acid, HBF_4 , hydrogen bound to $\text{CpFe}(\text{CO})_2\text{SCH}_3$ shows a decrease in sulfur character and an increase in metal character.

Bond distances, bond angles and carbonyl stretching frequencies were also calculated for each complex as shown in Table 2.12. Of course, the methyl group of $\text{CpFe}(\text{CO})_2\text{SCH}_3$ is more of an electron donor than the phenyl group that it replaced for calculation purposes so there should be some slight differences in bond distances and stretching frequencies but the overall trends should be basically the same.

The bond distances for Fe-S in FpSCH_3 , and $\text{FpSCH}_3\text{-TFA}$, where Fp is $\text{CpFe}(\text{CO})_2$, are 2.331 and 2.332 Å respectively, so they are basically the same. However, the Fe-S bond distances for $\text{FpSCH}_3\text{-HBF}_4$ and FpHSCH_3^+ are 2.301 and 2.284 Å respectively. The trend for the Fe-S bond distance as the parent compound FpSCH_3 undergoes hydrogen bonding and then protonation is that it gets shorter. This trend matches the crystallographic data. The shortening of Fe-S bond reflects increasing stability due to the decreasing filled-filled interaction between the $\text{Fe}d\pi\text{-Sp}\pi$ antibonding orbital.

The computed carbonyl stretching frequencies also exhibit an interesting trend. The stretching frequencies for FpSCH_3 are 1980 and 2024 cm^{-1} and the frequencies for $\text{FpSCH}_3\text{-HBF}_4$ and FpHSCH_3^+ are 1998, 2043 cm^{-1} and 2042, 2078 cm^{-1} respectively. The trend is an increase in carbonyl stretching frequencies as FpSCH_3 undergoes hydrogen bonding and then protonation. Again, this reflects the decreased electron density backbonding from the metal to

the CO π^* antibonding orbitals. The overall trend for the calculated stretching frequencies matches the trend encountered in the solution studies. The intriguing values of 1998 and 2043 cm^{-1} that were calculated for the hydrogen bonded complex matches very closely to the carbonyl stretching frequencies found for the predominant hydrogen bound species in much of the solution studies.

2.7 Conclusions.

In summary, we have provided spectroscopic, solid state, and density functional calculations as evidence to show that protonation can significantly change the reduction/oxidation properties of the metal center as compared to hydrogen bonding. Infrared and UV-vis spectroscopy data support the idea that **1.HX** is not a discrete hydrogen bound species (Scheme 2.1). There are no isosbestic points in the visible spectra (Figures 2.10 and 2.16) and the curve fit analysis indicated that perhaps there are more than one type of hydrogen bound species in solution at higher concentrations of acid. The hydrogen bound species is part of a continuum, which means that at low concentrations of weak protic acids, little hydrogen bonding can be detected but as the concentrations or strengths of the protic acids increase, hydrogen bonding becomes stronger. The continuum reflects the combined influences of the polarity of the solvent environment and the ability of the acid to hydrogen bond to the thiolate ligand. As the concentration of a protic acid (e.g., CCl_3COOH) continues to increase, the pK_b of the Lewis base (sulfur site of $\text{CpFe}(\text{CO})_2(\text{SC}_6\text{H}_5)$) is reached and protonation occurs (Scheme 2.1).

Upon protonation, there is a considerable increase in the CO stretching frequencies. This implies a significant change in the redox properties of the iron center. The crystal structures of **1** and **1H⁺** show that protonation produces a

shorter Fe-S bond. This indicates a stabilization of the Fe-S bond due to the weakening of the HOMO Fe-S $d\pi-p\pi$ antibonding orbital. The HOMO of compound **1** is mostly sulfur in character (Figure 2.24). Calculations suggest even the **1.HX** complex contains significant sulfur character in the HOMO; however, when protonation of compound **1** takes place, the HOMO is mostly metal in character. Protonation presumably influences the redox potential in a significant way as compared to the hydrogen bound complexes. Based on the free-energy relationships that relate redox potentials and ν_{CO} , there is a substantially smaller affect for hydrogen bonding, which is about 30% of that observed upon protonation.

The carbonyl stretching frequencies that were calculated using the density functional method follows the same trend as those that were observed experimentally. An increase in the stretching frequencies occurs as hydrogen bonding to compound **1** takes place and even more so when protonation occurs. These results indicate only a small perturbation of the donor ability of the thiolate ligand during hydrogen bonding as compared with the more significant change that results from protonation.

2.8 References.

- 1) Chakrabarti, P. and Pal, D. "An Electrophile-Nucleophile Interaction in Metalloprotein Structures", *Protein Sci.* **1997**, *6*, 851-859.
- 2) Sweeney, W. V. and Rabinowitz, J. C. "Proteins Containing 4Fe-4S Clusters : an Overview", *Annu. Rev. Biochem.* **1980**, *49*, 139-161.
- 3) Adman, E. T. "Comparison of the Structures of Electron-Transfer Proteins", *Biochim. Biophys. Acta* **1979**, *549*, 107-144.
- 4) Maskiewicz, R. and Bruice, T. C. "Solvation as the Determining Factor for the Redox Potential of $\text{Fe}_4\text{S}_4[\text{S}-(\text{CH}_2)_n(\text{CO})_2]^{6-}$ Cluster Ions", *J. Chem. Soc., Chem. Commun.* **1978**, 703-704.
- 5) Breton, J. L., Duff, J. L. C., Butt, J. N., Armstrong, F. A., George, S. J., Petillot, Y., Forest, E., Schafer, G. and Thomson, A. J. "Identification of the Iron-Sulfur Clusters in a Ferredoxin From the Archaeon *Sulfolobus Acidocaldarius* : Evidence For a Reduced [3Fe-4S] Cluster With PH-Dependent Electronic-Properties", *Eur. J. Biochem.* **1995**, *233*, 937-946.
- 6) Butt, J. N., Sucheta, A., Martin, L. L., Shen, B. H., Burgess, B. K. and Armstrong, F. A. "Voltammetric Study of Proton-Gated Electron-Transfer in a Mutant Ferredoxin : Altering Aspartate to Asparagine Blocks Oxidation of the [3Fe-4S] Cluster of *Azotobacter-Vinelandii* Ferredoxin-I", *J. Am. Chem. Soc.* **1993**, *115*, 12587-12588.
- 7) Armstrong, F. A., Heering, H. A. and Hirst, J. "Reactions of Complex Metalloproteins Studied By Protein-Film Voltammetry", *Chem. Soc. Rev.* **1997**, *26*, 169-179.
- 8) Adman, E. T., Sieker, L. C. and Jensen, L. H. "Structure of Rubredoxin From *Desulfovibrio-Vulgaris* At 1.5-Å Resolution", *J. Mol. Biol.* **1991**, *217*, 337-352.

- 9) Frey, M., Sieker, L., Payan, F., Haser, R., Bruschi, M., Pepe, G. and Legall, J. "Rubredoxin From *Desulfovibrio-Gigas* : a Molecular-Model of the Oxidized Form At 1.4 Å Resolution", *J. Mol. Biol.* **1987**, *197*, 525-541.
- 10) Xiao, Z. G., Lavery, M. J., Ayhan, M., Scrofani, S. D. B., Wilce, M. C. J., Guss, J. M., Tregloan, P. A., George, G. N. and Wedd, A. G. "The Rubredoxin From *Clostridium-Pasteurianum* : Mutation of the Iron Cysteinyl Ligands to Serine : Crystal and Molecular-Structures of Oxidized and Dithionite-Treated Forms of the Cys42Ser Mutant", *J. Am. Chem. Soc.* **1998**, *120*, 4135-4150.
- 11) Low, D. W. and Hill, M. G. "Rational Fine-Tuning of the Redox Potentials in Chemically Synthesized Rubredoxins", *J. Am. Chem. Soc.* **1998**, *120*, 11536-11537.
- 12) Backes, G., Mino, Y., Loehr, T. M., Meyer, T. E., Cusanovich, M. A., Sweeney, W. V., Adman, E. T. and Sandersloehr, J. "The Environment of Fe₄S₄ Clusters in Ferredoxins and High-Potential Iron Proteins : New Information From X-Ray Crystallography and Resonance Raman-Spectroscopy", *J. Am. Chem. Soc.* **1991**, *113*, 2055-2064.
- 13) Cowan, J. A. and Lui, S. M. "Structure-Function Correlations in High-Potential Iron Proteins", *Adv. Inorg. Chem.* **1998**, *45*, 313-350.
- 14) Vidakovic, M., Fraczkiewicz, G., Dave, B., Czernuszewicz, R. and Germanas, J. "The Environment of [2Fe-2S] Clusters in Ferredoxins : The Role of Residue-45 Probed by Site-Directed Mutagenesis", *Biochemistry* **1995**, *34*, 13906-13913.
- 15) Link, T. A. "The Structures of Rieske and Rieske-type Proteins", *Advances in Inorg. Chem.* **1999**, *47*, 83-157.

- 16) Iwata, S., Saynovits, M., Link, T. A. and Michel, H. "Structure of a Water Soluble Fragment of the 'Rieske' Iron Sulfur Protein of the Bovine Heart Mitochondrial Cytochrome bc(1) Complex Determined by MAD Phasing at 1.5 Å resolution", *Structure* **1996**, *4*, 567-579.
- 17) Link, T. A., Saynovits, M., Assmann, C., Iwata, S., Ohnishi, T. and vonJagow, G. "Isolation ; Characterisation and Crystallisation of a Water-Soluble Fragment of the Rieske Iron-Sulfur Protein of Bovine Heart Mitochondrial bc(1) Complex", *Eur. J. Biochem.* **1996**, *237*, 71-75.
- 18) Schroter, T., Hatzfeld, O. M., Gemeinhardt, S., Korn, M., Friedrich, T., Ludwig, B. and Link, T. A. "Mutational Analysis of Residues Forming Hydrogen Bonds in the Rieske [2Fe-2S] Cluster of the Cytochrome bc(1) Complex in *Paracoccus Denitrificans*", *Eur. J. Bioch.* **1998**, *255*, 100-106.
- 19) Datta, S. N., Nehra, V. and Jha, A. "Electronic Structure of a Rieske Iron-Sulfur Complex and the Calculation of Its Reduction Potential", *J. Phys. Chem. B* **1999**, *103*, 8768-8772.
- 20) Dawson, J. H. and Sono, M. "Cytochrome P-450 and Chloroperoxidase : Thiolate-Ligated Heme Enzymes : Spectroscopic Determination of Their Active-Site Structures and Mechanistic Implications of Thiolate Ligation", *Chem. Rev.* **1987**, *87*, 1255-1276.
- 21) Ullrich, V. "Dioxygen Activation by Heme-Sulfur Proteins", *J. Mol. Catal.* **1980**, *7*, 159-167.
- 22) Montanari, F. and Casella, L. *Metalloporphyrins Catalyzed Oxidations*; Kluwer Academic Publishers: Norwell, MA, 1994; Vol. 17.
- 23) Poulos, T. L., Finzel, B. C. and Howard, A. J. "High-Resolution Crystal-Structure of Cytochrome-P450cam", *J. Mol. Biol.* **1987**, *195*, 687-700.
- 24) Poulos, T. L. "The Role of the Proximal Ligand in Heme Enzymes", *J. Biol. Inorg. Chem.* **1996**, *1*, 356-359.

- 25) Ueyama, N., Nishikawa, N., Yamada, Y., Okamura, T., Oka, S., Sakurai, H. and Nakamura, A. "Synthesis and Properties of Octaethylporphinato(Arenethiolato)Iron(III) Complexes With Intramolecular NH...S Hydrogen-Bond : Chemical Function of the Hydrogen-Bond", *Inorg. Chem.* **1998**, *37*, 2415-2421.
- 26) Huang, J., Ostrander, R. L., Rheingold, A. L., Leung, Y. C. and Walters, M. A. "Hydrogen-Bonding and Polar Group Effects on Redox Potentials in $\text{Mo}[\text{HB}(\text{Me}_2\text{pz})_3](\text{NO})(\text{SR})_2$ ", *J. Am. Chem. Soc.* **1994**, *116*, 6769-6776.
- 27) Huang, J. O., Ostrander, R. L., Rheingold, A. L. and Walters, M. A. "Synthesis and Electrochemistry of $\text{Mo}[\text{BH}(\text{Me}_2\text{pz})_3](\text{NO})[\text{S}(\text{CH}_2)_2\text{-CoNH}(\text{CH}_2)_2\text{S}]$ As a Probe of the Effects of N-H...S Hydrogen-Bonding On Redox Potentials", *Inorg. Chem.* **1995**, *34*, 1090-1093.
- 28) Huang, J., Dewan, J. C. and Walters, M. A. "Structural ; Spectroscopic and Redox Characterization of the Soluble Complexes $[\text{M}(\text{SC}_6\text{H}_4\text{NR}_2)_4]^{2-}$ and the Effects of N-H...S Hydrogen-Bonds", *Inorg. Chim. Acta* **1995**, *228*, 199-206.
- 29) Okamura, T., Takamizawa, S., Ueyama, N. and Nakamura, A. "Novel Rubredoxin Model Tetrathiolato Iron(II) and Cobalt(II) Complexes Containing Intramolecular Single and Double NH...S Hydrogen-Bonds", *Inorg. Chem.* **1998**, *37*, 18-28.
- 30) Ueyama, N., Kajiwara, A., Terakawa, T., Ueno, S. and Nakamura, A. "Redox Potentials of Oligopeptide/ $\text{Fe}_4\text{S}_4^{2+}$ Complexes : Remarkable Positive Shift of the Redox Potential with (Benzyloxycarbonyl)-L-Cys-Gly-L-Ala-L-Cys-OMe as Chelating Ligands", *Inorg. Chem.* **1985**, *24*, 4700-4704.
- 31) Ueyama, N., Okamura, T. A. and Nakamura, A. "Intramolecular NH...S Hydrogen-Bond in O-Acylamino Substituted Benzenethiolate Iron(II) and

- Cobalt(II) Complexes", *J. Chem. Soc., Chem. Commun.* **1992**, 1019-1020.
- 32) Ueyama, N., Terakawa, T., Nakata, M. and Nakamura, A. "Positive Shift of Redox Potential of $[\text{Fe}_4\text{S}_4(\text{Z-Cys-Gly-Ala-OMe})_4]^{2-}$ in Dichloromethane", *J. Am. Chem. Soc.* **1983**, *105*, 7098-7102.
- 33) Treichel, P. M., Schmidt, M. S. and Koehler, S. D. "Alkylation of Organoiron Thiolate Complexes", *J. Organomet. Chem.* **1983**, *258*, 209-216.
- 34) Ashby, M. T. and Enemark, J. H. "Control of the Reactivity and Coordination-Number of a 16-Electron Complex By Pi-Donating Thiolate Ligands", *J. Am. Chem. Soc.* **1986**, *108*, 730-733.
- 35) Ashby, M. T., Enemark, J. H. and Lichtenberger, D. L. "Destabilizing $d\pi-p\pi$ Orbital Interactions and the Alkylation Reactions of Iron(II) Thiolate Complexes", *Inorg. Chem.* **1988**, *27*, 191-197.
- 36) Mushtaq, A., Bruce, R. and Knox, G. R. "Hydrocarbon Metal Sulphide Complexes I. Cyclopentadienylcarbonyliron Mercaptides", *J. Organometal. Chem.* **1966**, *6*, 1-10.
- 37) Piper, T. S., Cotton, F. A. and Wilkinson, G. "Cyclopentadienyl-Carbon Monoxide and Related Compounds of Some Transitional Metals", *J. Inorg. Nucl. Chem.* **1955**, *1*, 165.
- 38) Piper, T. S., Cotton, F. A. and Wilkinson, G. "Alkyl and Aryl Derivatives of π -Cyclopentadienyl Compounds of Chromium, Molybdenum, Tungsten, and Iron", *J. Inorg. Nucl. Chem.* **1956**, *3*, 104.
- 39) Treichel, P. M. and Rosenhein, L. D. "Synthesis of a Metal-Complex of Benzenethiol ; $[\text{Fe}(\text{C}_5\text{H}_5)(\text{CO})_2(\text{PhSH})]\text{BF}_4$; and Its Characterization as a Strong Acid", *Inorg. Chem.* **1981**, *20*, 942-944.

- 40) Smith, B. C. *Fundamentals of Fourier Transform Infrared Spectroscopy*, CRC Press: New York, 1996.
- 41) Siemens *SHELXTL*; 5.03 ed.; Siemens Analytical X-ray Instruments Inc.: Madison, WI, 1994.
- 42) Wavefunction, I. *SPARTAN*; 5.0 ed.; Wavefunction, Inc.: Irvine, CA, 1997.
- 43) Busetto, L., Palazzi, A., Serantoni, E. F. and Disanseverino, L. R. "Use of Phosphorus and Boron Sulfides As Sulfurizing Agents : General Route to Dithiocarboxylate Complexes", *J. Organomet. Chem.* **1977**, *129*, C55-C58.
- 44) Elhinnawi, M. A., Alajlouni, A. M., Abunasser, J. S., Powell, A. K. and Vahrenkamp, H. "Synthesis and Characterization of Cyclopentadienyldicarbonyl-Iron S-Bonded Monothiocarboxylates; FeCp(CO)₂(SCOR): Crystal-Structure of FeCp(CO)₂SCO(2-NO₂C₆H₄)", *J. Organomet. Chem.* **1989**, *359*, 79-86.
- 45) Raubenheimer, H. G., Kruger, G. J., Marais, C. F., Hattingh, J. T. Z., Linford, L. and Vanrooyen, P. H. "Distinctive Chemo-Selective and Stereo-Selective Reactions of [Fe(CO)₂Cp]⁺ and [AuPPh₃]⁺ With the Anionic Thioketene Complex; [W(CO)₅(C(OEt)(Ph)C(Ph)=C=S)]⁻: Crystal-Structures of Z-[W(CO)₅(C(SFe[CO]₂Cp)C(Ph)=C(OEt)Ph)] and E-[W(CO)₅(S=C(AuPPh₃)C(Ph)=C(OEt)Ph)]", *J. Organomet. Chem.* **1988**, *355*, 337-349.
- 46) Busetto, L., Monari, M., Palazzi, A., Albano, V. and Demartin, F. "Novel Hetero Trinuclear Complexes Triply Bridged By Carbon-Disulfide : X-Ray Crystal-Structure of the Complex [(OC)₂(η⁵-C₅H₅)FeC(=S)S-Fe(η⁵-C₅H₅)(CO)₂W(CO)₅]", *J. Chem. Soc., Dalton Trans.* **1983**, 1849-1855.

- 47) Moran, M., Cuadrado, I., Masaguer, J. R., Losada, J., Focesfoces, C. and Cano, F. H. "Cyclopentadienyl Iron Xanthate Complexes : Crystal and Molecular-Structure and Electrochemical Reduction of $\eta\text{-C}_5\text{R}_5\text{Fe}(\text{CO})_2(\eta^1\text{-SC}(\text{S})\text{OEt})$ (R = H or CH_3)", *Inorg. Chim. Acta* **1988**, *143*, 59-70.
- 48) Elhinnawi, M. A., Aruffo, A. A., Santarsiero, B. D., McAlister, D. R. and Schomaker, V. "Organometallic Sulfur Complexes .1. Syntheses; Structures; and Characterizations of Organoiron Sulfane Complexes ($\mu\text{-Sx})[(\eta^5\text{-C}_5\text{H}_5)\text{Fe}(\text{CO})_2]_2(\text{X}=1\text{-}4)$ ", *Inorg. Chem.* **1983**, *22*, 1585-1590.
- 49) English, R. B., Nassimbeni, L. R. and Haines, R. J. "Reactions of Metal-Carbonyl Derivatives .22. Crystal and Molecular-Structures of Dicarbonyl($\eta\text{-Cyclopentadienyl}$)(Ethylthio)Iron and $\mu\text{-Ethylthio-Bis}$ [Dicarbonyl($\eta\text{-Cyclopentadienyl}$)Iron] Tetrafluoroborate; and a Comparison of Their Molecular-Parameter", *J. Chem. Soc., Dalton Trans.* **1978**, *1978*, 1379-1385.
- 50) Sanzaparicio, J., Martinezcarrera, S. and Garciablanco, S. "Structure of Dicarbonyl($\eta^5\text{-Cyclopentadienyl}$)(O;O'-DiethylDithiophosphato)Iron(II)", *Acta Crystallogr., Sect. C* **1987**, *43*, 2009-2011.
- 51) Sanzaparicio, J., Martinezcarrera, S. and Garciablanco, S. "Structure of ($\eta^5\text{-Cyclopentadienyl}$) (Dicarbonyl) (O;O'-Diisopropyl Dithiophosphato)-Iron(II)", *Acta Crystallogr. Sect. C* **1986**, *42*, 1121-1123.
- 52) Coucouvanis, D., Swenson, D., Baenziger, N. C., Holah, D. G., Kostikas, A., Simopoulos, A. and Petrouleas, V. "Crystal and Molecular-Structures of $[(\text{C}_6\text{H}_5)\text{P}_4]_2\text{Fe}(\text{S}_2\text{C}_4\text{O}_2)_2$ and $[(\text{C}_6\text{H}_5)\text{P}_4]_2\text{Fe}(\text{SC}_6\text{H}_5)_4$; a Structural Analog of Reduced Rubredoxin", *J. Am. Chem. Soc.* **1976**, *98*, 5721-5723.

- 53) Wander, S. A., Reibenspies, J. H., Kim, J. S. and Darensbourg, M. Y. "Synthesis and Characterization of a Stable Iron(II) Hydride Thiolate Complex : $(\text{PhS})\text{Fe}(\text{H})(\text{CO})_2(\text{P}(\text{OPh})_3)_2$ ", *Inorg. Chem.* **1994**, *33*, 1421-1426.
- 54) Takacs, J., Marko, L. and Parkanyi, L. "Synthesis and Some Reactions of $\text{Fe}(\text{CO})_2(\text{dppe})(\text{SR})_2$ and $\text{Fe}_3(\text{CO})_6(\text{SR})_6$ Complexes : the Crystal-Structure of $\text{Cis} ; \text{Cis} ; \text{Cis-Fe}(\text{CO})_2(\text{dppe})(\text{SPh})_2$ ", *J. Organomet. Chem.* **1989**, *361*, 109-116.
- 55) Nagymagos, Z., Marko, L., Szakacsschmidt, A., Gervasio, G., Belluso, E. and Kettle, S. F. "Reaction of Carbon-Monoxide With Iron(II) Thiolates : Preparation and Structure of $\text{Fac-}[\text{Na}(15\text{-Crown-5})][\text{Fe}(\text{CO})_3(\text{SPh})_3]$ and $\text{Fac-}[\text{K}(18\text{-Crown-6})][\text{Fe}(\text{CO})_3(\text{SPh})_3]$ ", *Bulletin Des Societes Chimiques Belges* **1991**, *100*, 445-458.
- 56) Takacs, J., Soos, E., Nagymagos, Z., Marko, L., Gervasio, G. and Hoffmann, T. "Synthesis and Molecular-Structure of Carbonyl Derivatives of Iron(II) Thiolates Containing Nitrogen-Donor Ligands", *Inorg. Chim. Acta* **1989**, *166*, 39-46.
- 57) Tieckelmann, R. H., Silvis, H. C., Kent, T. A., Huynh, B. H., Waszczak, J. V., Teo, B. K. and Averill, B. A. "Synthetic Molybdenum-Iron-Sulfur Clusters : Preparation ; Structures ; and Properties of the $[\text{S}_2\text{MoS}_2\text{Fe}(\text{SC}_6\text{H}_5)_2]^{2-}$ and $[\text{S}_2\text{MoS}_2\text{FeCl}_2]^{2-}$ Ions", *J. Am. Chem. Soc.* **1980**, *102*, 5550-5559.
- 58) Coucouvanis, D., Stremple, P., Simhon, E. D., Swenson, D., Baenziger, N. C., Draganjac, M., Chan, L. T., Simopoulos, A., Papaefthymiou, V., Kostikas, A. and Petrouleas, V. "Dinuclear Fe-Mo-S Complexes Containing the FeS_2Mo Core: Syntheses; Ground-State Electronic-Structures; and Crystal and Molecular-Structures of the

$[(C_6H_5)_4P]_2[(C_6H_5S)_2FeS_2MoS_2]$; $[(C_2H_5)_4N]_2[(C_6H_5S)_2FeS_2WS_2]$;
and $[(C_6H_5)_4P]_2[(S_5)FeS_2MoS_2]$; $[(C_6H_5)_4P]_2[(S_5)FeS_2WS_2]$
Complexes", *Inorg. Chem.* **1983**, *22*, 293-308.

- 59) Yandulov, D. V., Caulton, K. G., Belkova, N. V., Shubina, E. S., Epstein, L. M., Khoroshun, D. V., Musaev, D. G. and Morokuma, K. "Diminishing Pi-Stabilization of an Unsaturated Metal Center: Hydrogen-Bonding to $OsHCl(CO)((P^tBu_2Me)_2)$ ", *J. Am. Chem. Soc.* **1998**, *120*, 12553-12563.
- 60) Byers, B. P. and Hall, M. B. "Comparison of Isolobal Fragments: Photoelectron-Spectra and Molecular-Orbital Calculations of (Arene)Tricarbonylchromium; (arene)Tricarbonylmolybdenum; and (arene)Tricarbonyltungsten complexes", *Organometallics* **1987**, *6*, 2319-2325.
- 61) Gower, M., Kane-Maguire, L. A., Maier, J. P. and Sweigart, D. A. "Ultraviolet Photoelectron-Spectra of Cyclohepta-1; 3; 5-Triene and Msitylene Tricarbonyl Complexes of Group-6A Metals", *J. Chem. Soc., Dalton Trans.* **1977**, 316-318.
- 62) Hubbard, J. L. and Lichtenberger, D. L. "The Jahn-Teller Effect in the Photoelectron-Spectrum of Iron Pentacarbonyl", *J. Chem. Phys.* **1981**, *75*, 2560-2568.
- 63) Lichtenberger, D. L., Sellmann, D. and Fenske, R. F. "He (I) Photoelectron-Spectra and Valence Electronic-Structures of $\eta^5-C_5H_5Mn(CO)_2N_2$ and $\eta^5-C_5H_5Mn(CO)_2NH_3$ ", *J. Organomet. Chem.* **1976**, *117*, 253-264.
- 64) Lichtenberger, D. L., Elkadi, Y., Gruhn, N. E., Hughers, R. P., Curnow, O. J. and Zheng, X. M. "Electronic Structure Perturbations of Substituted Ruthenocenes: The First Photoelectron Spectra of Perchloro- and

- Perfluorocyclopentadienyl Complexes", *Organometallics* **1997**, *16*, 5209-5217.
- 65) Sellmann, D., Becker, T. and Knoch, F. "Transition metal complexes with sulfur ligands .120. Protonation and alkylation of the thiolato donors in [Fe(CO)(NHS₄)]: Effects on the structural; electronic; and redox properties of metal-sulfur complexes", *Chemistry* **1996**, *2*, 1092-1098.
- 66) Allan, C. B., Davidson, G., Choudhury, S. B., Gu, Z. J., Bose, K., Day, R. O. and Maroney, M. "Protonation and Alkylation of a Dinuclear Nickel Thiolate Complex", *Inorg. Chem.* **1998**, *37*, 4166-4167.
- 67) Shubina, E. S., Krylov, A. N., Kreindlin, A. Z., Rybinskaya, M. I. and Epstein, L. M. "Hydrogen-Bonded Complexes Involving the Metal Atom and Protonation of Metallocenes of the Iron Subgroup", *J. Organomet. Chem.* **1994**, *465*, 259-262.
- 68) Ueyama, N., Nishikawa, N., Yamada, Y., Okamura, T. and Nakamura, A. "Cytochrome-P-450 Model (Porphinato)(Thiolato)Iron(III) Complexes With Single and Double NH...S Hydrogen-Bonds At the Thiolate Site", *J. Am. Chem. Soc.* **1996**, *118*, 12826-12827.
- 69) Ohno, R., Ueyama, N. and Nakamura, A. "Influence of the Distal Para Substituent Through NH...S Hydrogen-Bonds On the Positive Shift of the Reduction Potentials of [Fe₄S₄(Z-Cys-Gly-NHC₆H₄-P-X)₄]²⁻ (X = H ; OMe ; F ; Cl ; CN) Complexes", *Inorg. Chem.* **1991**, *30*, 4887-4891.
- 70) Ueyama, N., Yamada, Y., Okamura, T., Kimura, S. and Nakamura, A. "Structure and Properties of [Fe₄S₄{2 ;6-bis(acylamino)benzenethiolato-S}₄]²⁻ and [Fe₂S₂{2 ;6-bis(acylamino)benzenethiolato-S}₄]²⁻ : Protection of the Fe-S Bond by Double NH...S Hydrogen-Bonds", *Inorg. Chem.* **1996**, *35*, 6473-6484.

- 71) Kandori, H., Kinoshita, N., Shichida, Y., Maeda, A., Needleman, R. and Lanyi, J. K. "Cysteine S-H as a Hydrogen-Bonding Probe in Proteins", *J. Am. Chem. Soc.* **1998**, *120*, 5828-5829.
- 72) Kazarian, S. G., Hamley, P. A. and Poliakoff, M. "Is Intermolecular Hydrogen-Bonding to Uncharged Metal Centers of Organometallic Compounds Widespread in Solution: A Spectroscopic Investigation in Hydrocarbon, Noble-Gas, and Supercritical-Fluid Solutions of the Interaction Between Fluoro Alcohols and $(\eta^5\text{-C}_5\text{R}_5)\text{ML}_2$ (R = H, Me, M = Co, Rh, Ir, L = CO, C₂H₄, N₂, PMe₃) and Its Relevance to Protonation", *J. Am. Chem. Soc.* **1993**, *115*, 9069-9079.
- 73) Peris, E., Mata, J. A. and Moliner, V. "IR Spectroscopic Study of Hydrogen Bonding Using a Metal Carbonyl Probe", *J. Chem. Soc., Dalton Trans.* **1999**, 3893-3898.
- 74) Treichel, P. M. and Rosenhein, L. D. "Radical Coupling of Mercaptide Ligands Upon Oxidation of Organometallic Mercaptide Complexes", *J. Am. Chem. Soc.* **1981**, *103*, 691-692.
- 75) Byrn, M. P., Katz, B. A., Keder, N. L., Levan, K. R., Magurany, C. J., Miller, K. M., Pritt, J. W. and Strouse, C. E. "Low-Spin Ferric Porphyrin Complexes : Analysis of the Electronic-Structure Based On Single-Crystal Electron-Spin Resonance Measurements", *J. Am. Chem. Soc.* **1983**, *105*, 4916-4922.
- 76) Collman, J. P., Sorrell, T. N., Hodgson, K. O., Kulshrestha, A. K. and Strouse, C. E. "Molecular-Dynamics in Solid-State : Dynamic-Model of Low-Spin Iron(III) to High-Spin Iron(III) Transformation in P450 Enzymes", *J. Am. Chem. Soc.* **1977**, *99*, 5180-5181.
- 77) Jeffrey, G. A. *An Introduction to Hydrogen Bonding*; Oxford University Press: New York, 1997.

- 78) Okamura, T., Ueyama, N., Nakamura, A., Ainscough, E. W., Brodie, A. M. and Waters, J. M. "The Effect of Strong NH...S Hydrogen-Bonds in the Copper(I) Thiolate Complex ; $(\text{NEt}_4)_2[\text{Cu}(\text{O-Pabt})_3]$ (O-Pabt = O-Pivaloylaminobenzenethiolato)", *J. Chem. Soc., Chem. Commun.* **1993**, 1658-1660.
- 79) Keseru, G. M., Kolossvary, I. and Szekely, I. "Inhibitors of Cytochrome P450 Catalyzed Insecticide Metabolism: A Rational Approach", *Int. J. Quantum Chem.* **1999**, 73, 123-135.

3.1 Introduction and Background

Solvatochromism is an effect used to describe a change in position and sometimes the intensity of an UV-vis absorption band with a concomitant change in polarity of the medium.¹ This effect can be easily seen in the visible region (400 nm to 700 nm) of the electromagnetic spectrum. A qualitative interpretation of solvent shifts is possible by considering four concepts: 1) the momentary transition dipole moment present during the optical absorption, 2) the difference in permanent dipole moment between ground and excited-state of the solute, 3) the change in ground-state dipole moment of the solute induced by the solvent, and 4) the Franck-Condon principle which states that since the time required for a molecule to execute a vibration (ca. 10^{-12} s) is much longer than that required for an electronic transition (ca. 10^{-15} s), the nuclei of the chromophore (and of the surrounding solvent molecules) do not appreciably alter their positions during an electronic transition.¹ Some Group VIII and carbonyl compounds that exhibit solvatochromism are *cis*- $[\text{Ru}(\text{bpy})_2(\text{CN})_2]^{2,3}$, *cis*- $[\text{Ru}(\text{phen})_2(\text{CN})_2]^{2,3}$, $[\text{Ru}(\text{NH}_3)_5(\text{py})]^{2+2,4,5}$, $[\text{Fe}(\text{bpy})_2(\text{CN})_2]^{2,6}$, $[\text{Mo}(\text{bpy})(\text{CO})_4]^{7}$ and $[\text{W}(\text{bpy})(\text{CO})_4]^{7}$ (bpy = 2,2'-bipyridine, phen = phenanthroline, and py = pyridine).

Typically, the solvatochromic changes occur with some regularity so that the wavelength(s) at which some compounds absorb can be correlated with specific solvent polarity scales. The vibrational changes in the carbonyl stretching frequencies can also be correlated with specific solvent polarity scales; however, they are more complicated. Some examples of solvent polarity scales are: 1) the $E_T(30)$ and E_T^N scales of Dimroth-Reichardt^{6,8,9}, 2) the Donor and Acceptor Number scales of Gutmann,¹⁰ 3) the Z scale of Kosower^{11,12} 4) the π^*

solvent polarity scale by Kamlet and Taft¹³⁻¹⁵ and 5) the Kirkwood-Bauer-Margat formula¹⁶⁻¹⁸ and Buckingham's Equation.¹⁹

The Dimroth-Reichardt scale, $E_T(30)$, is defined as the energy of the lowest charge transfer absorption band for the organic dye 2,6-diphenyl-4-(2,4,6-triphenyl-1-pyridinio)phenolate which is dye number 30 in reference 20 (Figure 3.1.).

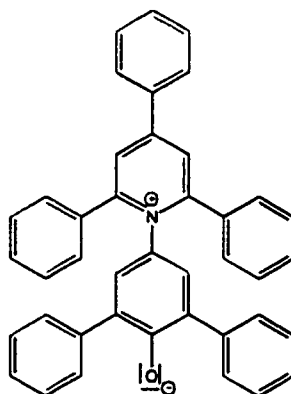


Figure 3.1. Pyridinium-N-phenoxide betaine dye.

This dye contains an extraordinarily large range for the solvatochromic behavior which is $\lambda = 810$ nm in diphenyl ether to $\lambda = 453$ nm in water. The $E_T(30)$ values have the unit kcal/mol which has been abandoned for the unitless normalized scale E_T^N .²⁰ The E_T^N scale ranges from 0.006 for cyclohexane to 1.00 for water.¹

The donor numbers of Gutmann are determined by the molar reaction enthalpy in 1,2-dichloroethane for the formation of a 1:1 adduct between $SbCl_5$ and the added solvent as donor by calorimetry.^{21,22} The acceptor numbers of Gutmann are the relative ^{31}P -NMR chemical shift values δ_{corr} (n-hexane as reference solvent) relative to those of the 1:1 adduct $Et_3PO-SbCl_5$ dissolved in

1,2-dichloroethane. The range is 0.0 for *n*-hexane to 105.3 for trifluoroacetic acid.^{10, 23}

The Z scale of Kosower, which is the transition energies derived from the charge transfer band of the compounds, 1-ethyl-4-carbomethoxypyridinium and pyridine-1-oxide, in various solvents, ranges from 60.1 kcal/mole in isooctane to 94.6 kcal/mole in water.^{11,24} Kosower was the first to systematically use solvatochromism as a probe of solvent polarity.²⁵ Unfortunately, there are not that many solvents for which the Z-values were determined due to solubility problems.

The π^* scale is an index of single-valued solvent polarity-polarizability (SPP) parameters.^{13,14,26} This scale involves seven primary indicator solutes which satisfy four requirements. These requirements are: 1) positions of maxima of symmetrical, reasonably intense bands for $p \rightarrow \pi^*$ or $\pi \rightarrow \pi^*$ transitions should be in experimentally accessible regions of the spectrum, 2) ν_{\max} values in non-hydrogen bonding donor solvents and in hydrogen bonding donor solvents as well, if possible, should show linear regression with high correlation, 3) positions of ν_{\max} should be influenced minimally by band overlap with high intensity higher energy bands, and 4) ν_{\max} values should show adequate responses to changing solvent polarity so that combined uncertainties caused by experimental precision limits and spectral anomalies should have minimal influence on π^* values.¹³ The π^* values range from -0.81 in hexane or heptane to 1.118 in formamide.

The Kirkwood-Bauer-Margat formula¹⁶⁻¹⁸, as shown in Equation 3.1, shows a relationship involved with infrared solvent shifts. ν^g is the vibrational frequency in the gas phase, ν^s is the frequency in the solvent of dielectric constant ϵ_r , and C is a constant depending upon the molecular dimensions and electrical properties of the vibrating solute dipole, and n is the refractive index of the solvent.²⁷

Buckingham's equations¹⁹ are a modification of the Kirkwood-Bauer-Margat formula. Buckingham's equations take into consideration the fact that the influences of solvent dipolarity and solvent polarizability on the solute IR vibrations are two independent effects. The various constants C_1 and $(C_2 + C_3)$ can be determined from the slope and intercept of the plot of the observed relative shifts in Equation 3.3. Instead of using the stretching frequency for compounds in the gas phase as a reference for the formula $\Delta\nu/\nu$, hexane can be used or any extreme value that causes a solvent induced shift.²⁸

Kirkwood-Bauer-Margat formula:

$$\frac{\Delta\nu}{\nu^o} = \frac{\nu^o - \nu^s}{\nu^o} = C \cdot \frac{\epsilon_r - 1}{2\epsilon_r + 1} = C \cdot \frac{n^2 - 1}{2n^2 + 1} \quad (3.1)$$

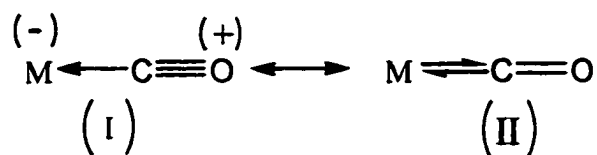
Buckingham's equation for polar solvents:

$$\frac{\Delta\nu}{\nu^o} = C_1 + C_2 \cdot \frac{\epsilon_r - 1}{2\epsilon_r + 1} + C_3 \cdot \frac{n^2 - 1}{2n^2 + 1} \quad (3.2)$$

Buckingham's equation for nonpolar solvents:

$$\frac{\Delta\nu}{\nu^o} = C_1 + \frac{1}{2}(C_2 + C_3) \cdot \frac{\epsilon_r - 1}{2\epsilon_r + 1} \quad (3.3)$$

Solvent effects at the vibrational level can also be observed in the infrared region by observing the shift in the carbonyl stretching frequency. A shift in the carbonyl stretching frequency as well as an increase in the half bandwidth, $\Delta\nu_{1/2}$, occurs as the polarity of the solvent increases provided there is no change in structure on dissolution and no complex formation.²⁹ The polarity of a solvent can influence the π -electron distribution to the M-C-O group in metal carbonyl complexes as illustrated in Scheme 3.1.³⁰



Scheme 3.1. The C-O bond order as higher π -accepting ligands or π -donor ligands are bound to the metal represented by I and II respectively.

An increase in the C-O bond order as represented in structure (I) is favored when higher π -acceptor ligands are bound to the metal and the polarity of the solvent increases. If π -donor ligands are bound to the metal, then the C-O bond order, as represented in structure (II), is favored.^{31,32} The more polar solvents can cause an increase in the formal negative charge towards the oxygen atom through a higher percent of metal to carbonyl back donation, which in turn lowers carbonyl stretching frequency.³⁰ Free carbon monoxide has a polarity that is in the direction $\delta^- \text{C} - \text{O}^{\delta+}$; however, coordination to a transition metal such as iron reverses the polarity to the direction $\delta^+ \text{C} - \text{O}^{\delta-}$. The stronger the back-bonding from the metal to the carbonyl, the stronger the polarity that is in the direction where a stronger partial negative charge will reside on the oxygen. Also, if a solute-solvent interaction (i.e. -C-O-solvent) is involved, the electrons will shift towards the oxygen atom as the strength of this interaction increases.³³ Also, the solvent associated carbonyl ligand has a lower carbonyl stretching frequency due to the increased mass effect of the vibrating species.³⁴

Hales *et al.* have demonstrated that if carbonyls are replaced by ligands of π -donor ability in metal carbonyl compounds, then there is a movement of electrons in the M-CO π -system which results in a decrease in the CO bond order which lowers the carbonyl stretching frequency.³³ Even by changing the

halogen from Cl to Br to I within the same metal carbonyl complex, the carbonyl stretching frequency decreases due to the decreasing polarity of the M—X bond while in the same solvent.^{33,35} This is exemplified by the carbonyl stretching frequencies of $[\text{CpFe}(\text{CO})_3]\text{PF}_6$, $\text{CpFe}(\text{CO})_2\text{Cl}$, $\text{CpFe}(\text{CO})_2\text{Br}$, and $\text{CpFe}(\text{CO})_2\text{I}$ as shown in Table 3.1. Notice the significant decrease in the carbonyl stretching frequency as one of the carbonyls (a strong π acceptor) from $[\text{CpFe}(\text{CO})_3]\text{PF}_6$ is replaced with a fairly weak π donating chloride anion. Also notice, that as the chloride is replaced by a relatively stronger π donating bromide anion and then the iodide anion, the carbonyl stretching frequency continues to decrease as expected.

Table 3.1. The carbonyl stretching frequencies of specific metal carbonyls from pressed KBr disks.

Compound	ν_{CO} stretching frequencies (cm^{-1})	Ref.
$[\text{CpFe}(\text{CO})_3]\text{PF}_6$	2090, 2150	36
$\text{CpFe}(\text{CO})_2\text{Cl}$	2010, 2050	37
$\text{CpFe}(\text{CO})_2\text{Br}$	1995, 2049	38
$\text{CpFe}(\text{CO})_2\text{I}$	1982, 2042	38

Hales *et al.* also demonstrated that as the polarity of the solvent increases, the carbonyl stretching frequencies of the compounds, $\text{Fe}(\text{CO})_4\text{Br}_2$ and $\text{Fe}(\text{CO})_4\text{I}_2$, also increases.³³ Hales states that by increasing the polarity of the solvent, this should better stabilize the polar nature of the metal-halide bond and, therefore, increase the carbonyl stretching frequency concomitantly. However, since the metal carbonyl halides contain two separate polar sites, this can complicate the prediction of the solvent shifts.³³

The compound, $\text{CpFe}(\text{CO})_2(\text{SC}_6\text{H}_5)$, is dipolar and is also solvatochromatic. This compound, as it is dissolved in a variety of solvents, will fit into two of the four limiting cases according to Bayliss and McRae.³⁹ These are a dipolar solute in a nonpolar solvent and a dipolar solute in a polar solvent. In the former case, if the solute dipole moment increases during the electronic transition, the Franck-Condon excited-state is more solvated by dipole-solvent polarization and a red shift is expected. If the solute dipole moment decreases during the electronic transition, the Franck-Condon excited-state is less solvated and a blue shift is expected.^{1,39} In the later case, if the dipole moment of the ground-state is less than the excited-state dipole moment ($\mu_g < \mu_e$), then the Franck-Condon excited-state is formed in a solvent cage of already partly oriented solvent dipoles which results in a better stabilization of the excited-state relative to the ground-state and a bathochromic or red shift occurs (Figure 3.2). If the dipole moment of the ground-state is greater than the excited-state dipole moment ($\mu_g > \mu_e$), then the Franck-Condon excited-state is in a strained solvent cage of oriented dipoles not correctly disposed to efficiently stabilize the excited-state.¹ Thus, with increasing solvent polarity, the energy of the ground-state is less than that of the excited-state which produces a hypsochromic or blue shift (Figure 3.2).¹

By observing the shifts in the visible region of $\text{CpFe}(\text{CO})_2(\text{SC}_6\text{H}_5)$ dissolved in various solutions (Figures 3.3-3.17), a generalization can be determined as to whether the dipole moment of the ground-state is greater than or less than that of the Franck-Condon excited-state. Plots are made from the UV-vis data and the specific solvent polarity scales so that trends may be found which can help to determine more about the electronic behavior of $\text{CpFe}(\text{CO})_2(\text{SC}_6\text{H}_5)$ in solution (Figures 3.43-3.46). Also, a comparison of the UV-vis data is made between $\text{CpFe}(\text{CO})_2(\text{SC}_6\text{H}_5)$ and $\text{CpFe}(\text{CO})_2(\text{SC}_6\text{H}_4\text{-}p\text{-CF}_3)$

in aprotic solvents (Figure 3.46) to see how the electron withdrawing group (CF_3) affects the shift of the LMCT band.

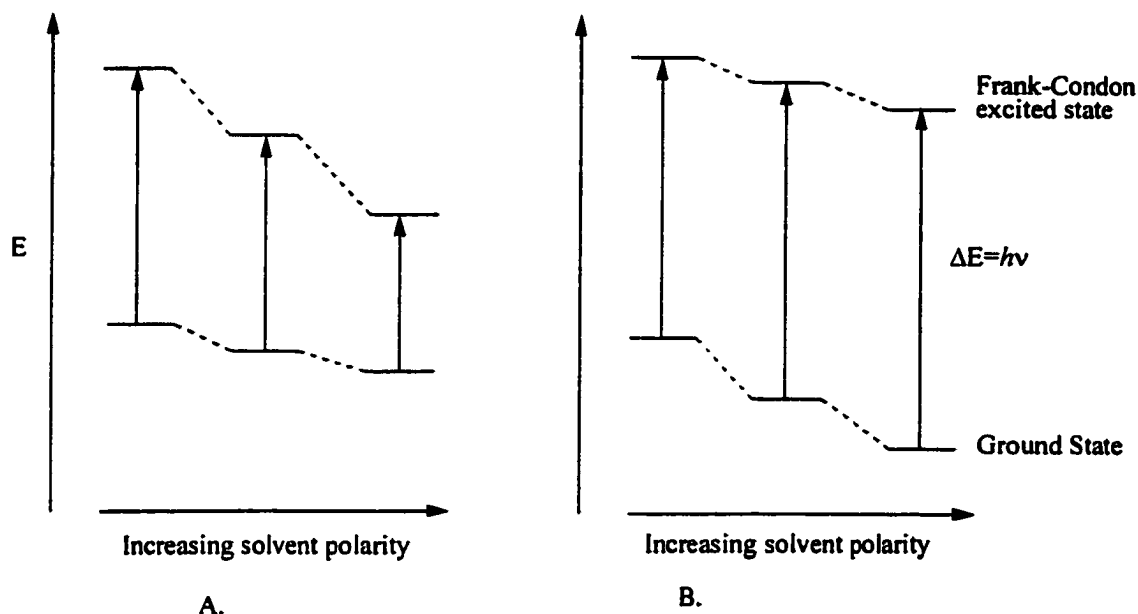


Figure 3.2. Solvent effects on the electronic transition energy of dipolar solutes in polar solvents where A represents the dipole moment of the Franck-Condon excited-state of the solute that is larger than the ground-state ($\mu_g < \mu_e$) and B represents the dipole moment of the Franck-Condon excited-state of the solute smaller than the ground-state $\mu_g > \mu_e$.^{1,39}

Other electronic effects and trends can be generalized by observing the infrared shifts in the carbonyl stretching frequencies of $\text{CpFe}(\text{CO})_2(\text{SC}_6\text{H}_5)$ dissolved in nonpolar and polar solvents; however, the dielectric effect typically does not play a major role in the determination of solvent induced IR shifts.⁴⁰ It is worth noting that the vibrational event is approximately two orders of magnitude slower than the electronic event.⁴¹ The carbonyl stretching frequencies of $\text{CpFe}(\text{CO})_2(\text{SC}_6\text{H}_5)$ in various solvents will be compared to the

infrared shifts in the carbonyl stretching frequencies of the well known compounds, $\text{CpFe(CO)}_2\text{Cl}$ and $\text{CpFe(CO)}_2\text{I}$, which are solvated in some of the same solvents (Figures 3.33-3.42). A plot of the force constants based on the observed carbonyl stretching frequencies versus Gutmann's Acceptor Number will show a correlation between these three compounds (Figure 3.48).

3.2 Experimental Section

All reactions were performed under an atmosphere of prepurified nitrogen or argon using Schlenk technique or a MO-40M VAC Dry Box unless stated otherwise. All solutions were prepared immediately before use. Solvents were distilled from appropriate drying agents under nitrogen and degassed by freeze pump thawing three times prior to use unless stated otherwise: CH_2Cl_2 (CaH_2), pentane (Na), benzene (Na), acetone (CaSO_4), tetrahydrofuran (distilled from P_2O_5 and placed over KOH, then distilled from Na), methanol (Mg), CH_3CN (CaH_2), heptane (Na), toluene (Na), diethyl ether (CaH_2), cyclohexane (Na), 2,2,2-trifluoroethanol, 1-butanol, 1-pentanol. $\text{CpFe(CO)}_2(\text{SC}_6\text{H}_5)$, $\text{CpFe(CO)}_2\text{I}$, and $\text{CpFe(CO)}_2\text{Cl}$ were prepared by literature methods.^{37,38,42} The solvents, 2,2,2-trifluoroethanol, 1-butanol, and 1-pentanol were purchased from Aldrich and used without further purification. Infrared spectra were recorded with a Bruker IFS 66/S FTIR spectrometer. UV-vis spectra were recorded with a Hewlett-Packard HP8453 Diode Array instrument.

3.2.1 Infrared Measurements.

Sodium chloride salt plates and a 0.5 mm teflon spacer were used in all of the following infrared spectroscopy experiments. A 0.2 mm quartz cell was utilized in the UV-vis spectroscopy experiments. Most of the infrared spectra were analyzed by taking the second derivative of each spectrum and then fitted by a Gaussian curve fit method⁴⁰ from the Peakfit computer program. In the

figures that show infrared spectra, the CO stretching frequencies that were determined from the curve fit analysis are located in the legend of each spectrum and the CO stretching frequencies that were determined before the curve fit analysis are located in the graphs.

3.2.2 Solvation of $\text{CpFe}(\text{CO})_2(\text{SC}_6\text{H}_5)$ in various solvents.

Fifteen solutions of 10 mM $\text{CpFe}(\text{CO})_2(\text{SC}_6\text{H}_5)$ were prepared in the following degassed solvents: pentane, heptane, cyclohexane, diethyl ether, benzene, toluene, tetrahydrofuran, chloroform, dichloromethane, acetone, acetonitrile, 1-pentanol, 1-butanol, 2,2,2-trifluoroethanol, and methanol. All of these solutions were analyzed by UV-vis and infrared spectroscopy (Figures 3.3-3.17 and Figures 3.18-3.32, respectively). Plots of the UV-vis data versus specific solvent polarity scales are shown in Figures 3.43-3.46.

3.2.3 Solvation of $\text{CpFe}(\text{CO})_2(\text{SC}_6\text{H}_4\text{-}p\text{-CF}_3)$ in various solvents.

Eight solutions of 10 mM $\text{CpFe}(\text{CO})_2(\text{SC}_6\text{H}_4\text{-}p\text{-CF}_3)$ were prepared in the following degassed aprotic solvents: pentane, diethyl ether, benzene, tetrahydrofuran, chloroform, dichloromethane, acetone, and acetonitrile. All of the solutions were analyzed by UV-vis and infrared spectroscopy (Table 3.3). Plot of the UV-vis data versus E_T^N is located in Figure 3.46. A plot comparing the force constants of $\text{CpFe}(\text{CO})_2\text{Cl}$, $\text{CpFe}(\text{CO})_2\text{I}$, and $\text{CpFe}(\text{CO})_2(\text{SC}_6\text{H}_5)$ versus Gutmann's acceptor number is located in Figure 3.51.

3.2.4 Solvation of $\text{CpFe}(\text{CO})_2\text{Cl}$ and $\text{CpFe}(\text{CO})_2\text{I}$ in various solvents.

Six solutions of 10 mM $\text{CpFe}(\text{CO})_2\text{Cl}$ and 10 mM $\text{CpFe}(\text{CO})_2\text{I}$ were each prepared in the following degassed aprotic solvents: pentane, diethyl ether, tetrahydrofuran, dichloromethane, acetone, and acetonitrile. All of these solutions were analyzed by infrared spectroscopy (Figures 3.33-3.42).

3.3 Results of the Solution Experiments

10 mM solutions of $\text{CpFe}(\text{CO})_2(\text{SC}_6\text{H}_5)$ were each prepared in fifteen different solvents under nitrogen and each was analyzed by UV-vis and infrared spectroscopy. The UV-vis and infrared data, dielectric constants, refractive indices, and various solvent polarity constants are shown in Table 3.2. The UV-vis spectra are shown in Figures 3.3-3.17. Two carbonyl stretching frequencies for each compound were found from their infrared spectra (Figures 3.18-3.32). Note that the stretching frequencies match the curve fit analysis for each compound.

Five plots were made based on the UV-vis data that was collected on the $\text{CpFe}(\text{CO})_2(\text{SC}_6\text{H}_5)$ solutions. The first and second plots, shown in Figures 3.45 and 3.46, use Dimroth-Reichardt's normalized energy transition scale. The third plot, shown in Figure 3.47, uses Gutmann's Acceptor Number. The fourth plot, shown in Figure 3.48, uses Kosower's Z-scale of solvents and the fifth plot, shown in Figure 3.49, uses Kamlet and Taft's π^* solvent polarity scale. No correlation could be found using the Buckingham's equations.

Two plots based on the infrared data that were collected are shown in Figures 3.50 and 3.51. The first of these is a Bellamy plot.³⁴ Bellamy plots, ν_s against ν_{as} , have been used to investigate the infrared stretching vibrations for compounds in a variety of solvents.⁴³ In the case of the $\text{CpFe}(\text{CO})_2(\text{SC}_6\text{H}_5)$ solutions, of which eleven points were plotted, there appears to be two parallel rows. One of the rows contains the less polar solvents, the higher antisymmetric carbonyl stretching frequency, and the lower Gutmann's Acceptor Number. The other row contains the more polar solvents, the lower antisymmetric carbonyl stretching frequency, and the higher Gutmann's Acceptor Number.

The second plot based on the infrared data shows the force constants of the three compounds, $\text{CpFe}(\text{CO})_2\text{Cl}$, $\text{CpFe}(\text{CO})_2\text{I}$, and $\text{CpFe}(\text{CO})_2(\text{SC}_6\text{H}_5)$ versus

Gutmann's Acceptor Number. The force constants and the carbonyl stretching frequencies are located in Table 3.4 for $\text{CpFe}(\text{CO})_2\text{Cl}$ and $\text{CpFe}(\text{CO})_2\text{I}$. Table 3.2 contains the force constants and carbonyl stretching frequencies for $\text{CpFe}(\text{CO})_2(\text{SC}_6\text{H}_5)$.

Table 3.4 also contains the differences, $\Delta\nu_{\text{CO}}$, in the carbonyl stretching frequencies between $\text{CpFe}(\text{CO})_2\text{Cl}$ and $\text{CpFe}(\text{CO})_2\text{I}$ and also between $\text{CpFe}(\text{CO})_2\text{I}$ and $\text{CpFe}(\text{CO})_2(\text{SC}_6\text{H}_5)$ within the same solvents. There is little deviation in the values of $\Delta\nu_{\text{CO}}$ going down the column. This would seem to be a good way to predict where a particular stretching frequency would be located for one of the compounds knowing the stretching frequency for one of the other compounds. For example, the antisymmetric $\Delta\nu_{\text{CO}}$ between $\text{CpFe}(\text{CO})_2\text{Cl}$ and $\text{CpFe}(\text{CO})_2\text{I}$ is about 9 cm^{-1} and the symmetric $\Delta\nu_{\text{CO}}$ is about 12 cm^{-1} . When the compound $\text{CpFe}(\text{CO})_2(\text{SC}_6\text{H}_5)$ was solvated by THF and analyzed by the infrared spectrometer, the antisymmetric peak had a large overlap with the solvent peak and when subtracted made the peak appear at 1988 cm^{-1} . When compared to the $\Delta\nu_{\text{CO}}$ values for the antisymmetric peak, which has an average value of 11 cm^{-1} , it was just a matter of subtracting 11 cm^{-1} from 1990 cm^{-1} , which is the antisymmetric frequency for $\text{CpFe}(\text{CO})_2\text{I}$, to obtain the more reasonable value, 1979 cm^{-1} , for the antisymmetric frequency for $\text{CpFe}(\text{CO})_2(\text{SC}_6\text{H}_5)$ in tetrahydrofuran.

Table 3.2. A 10 mM CpFe(CO)₂(SC₆H₅) solution made with each of the solvents listed below. a) Underlined vibrational frequencies lie below significant solvent features and their values are therefore suspect, b) dielectric constant, c) normalized energy transition values, d) Gutmann's acceptor numbers, e) Kosower's Z-scale, f) Kamlet-Taft's π^* parameters, g) approximate value based on hexane, h) value determined from Table 3.3 and the plot in Figure 3.47

Solvents	UV-vis (nm)	ν_{CO} (cm ⁻¹) _a	Obs F_{CO} (k _i) (mdyn/Å)	ϵ ^b	Refractive Index (<i>n</i>)	E_T^N ^c	AN ^d	Z-scale ^e	π^* ^f
Heptane	584	1990, 2033	16.34 ₁ (0.34 _g)	1.9209	1.388	0.012	N/A	N/A	-0.08
Pentane	582	1991, 2035	16.36 ₆ (0.35 _g)	1.8371	1.357	0.009	(0) ^g	N/A	N/A
Cyclohexane	576	1983, 2029	16.25 ₂ (0.37 ₃)	2.0243	1.426	0.006	N/A	N/A	0.00
Toluene	574	1983, 2029	16.25 ₂ (0.37 ₃)	2.379	1.497	0.099	N/A	N/A	0.54
Benzene	572	<u>1984</u> , 2029	N/A	2.2825	1.501	0.111	8.2	54	0.59
Diethyl Ether	572	1985, 2030	16.27 ₇ (0.36 ₅)	4.2666	1.352	0.117	3.9	N/A	0.27
Tetrahydrofuran	564	(1979) ^h , 2028	16.21 ₂ (0.39 ₆)	7.52	1.407	0.207	8.0	N/A	0.58
Chloroform	562	1989, 2035	16.35 ₀ (0.37 ₄)	4.8069	1.446	0.259	23.1	63.2	0.58
Dichloromethane	560	1985, 2032	16.29 ₃ (0.38 ₁)	8.93	1.424	0.309	20.4	64.2	0.82
Acetone	558	1980, 2029	16.22 ₈ (0.39 ₇)	21.01	1.359	0.355	12.5	65.7	0.71
Acetonitrile	552	1983, 2031	16.26 ₉ (0.38 ₉)	36.64	1.344	0.460	18.9	71.3	0.75
1-Pentanol	550	1987, <u>2032</u>	16.30 ₉ (0.36 ₅)	15.13	1.408	0.568	N/A	N/A	N/A
1-Butanol	550	1990, <u>2033</u>	16.34 ₁ (0.34 _g)	17.84	1.399	0.602	36.8	77.7	N/A
Methanol	542	1985, N/A	N/A	33.0	1.328	0.762	41.5	83.6	0.60
2,2,2-Trifluoro-ethanol	500(sh)	<u>2005</u> , 2045	16.56 ₁ (0.32 ₇)	27.68	1.290	0.898	53.3	N/A	N/A

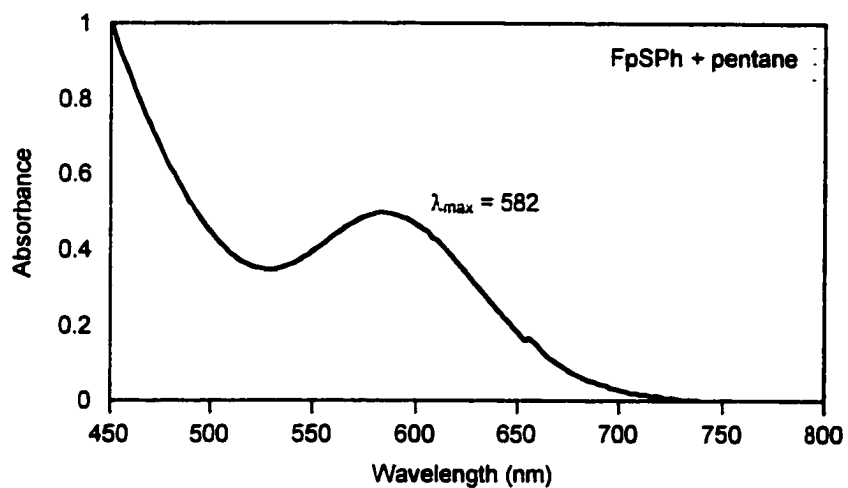


Figure 3.3. A visible spectrum of a 10 mM CpFe(CO)₂(SC₆H₅) solution in pentane.

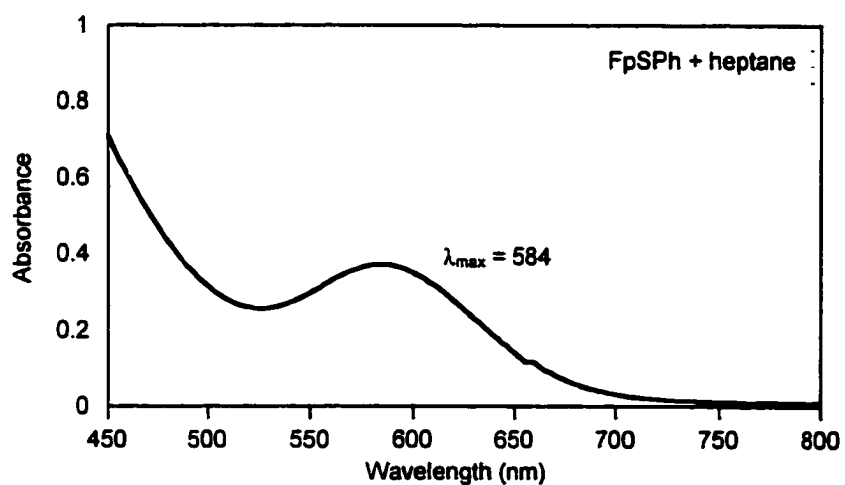


Figure 3.4. A visible spectrum of a 10 mM CpFe(CO)₂(SC₆H₅) solution in heptane.

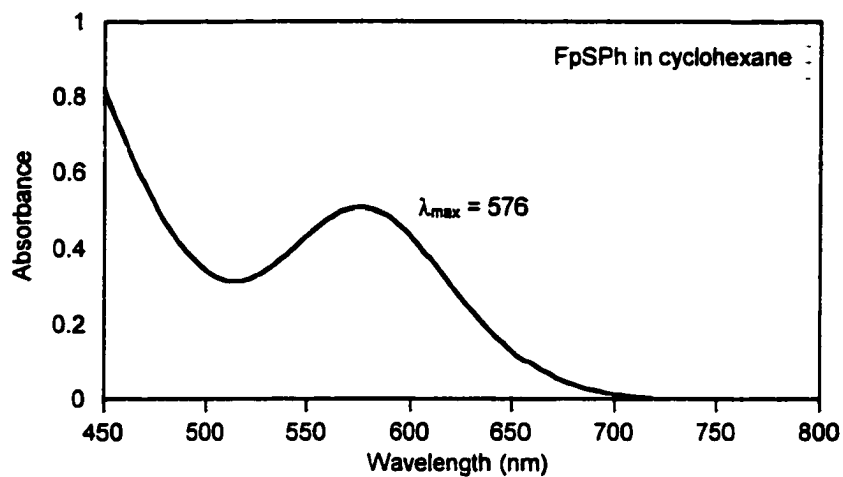


Figure 3.5. A visible spectrum of a 10 mM CpFe(CO)₂(SC₆H₅) solution in cyclohexane.

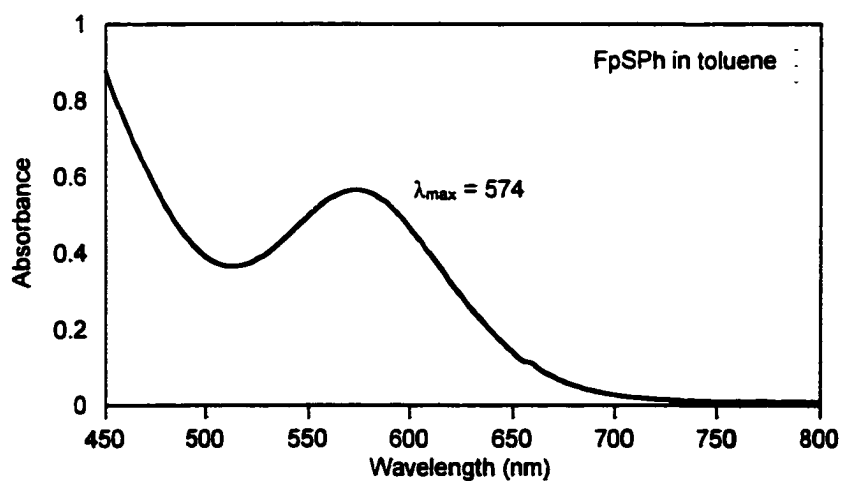


Figure 3.6. A visible spectrum of a 10 mM CpFe(CO)₂(SC₆H₅) solution in toluene.

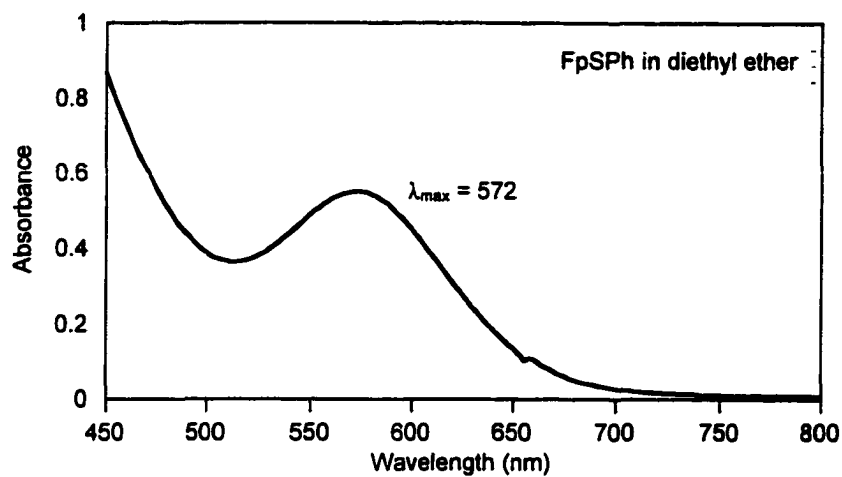


Figure 3.7. A visible spectrum of a 10 mM CpFe(CO)₂(SC₆H₅) solution in diethyl ether.

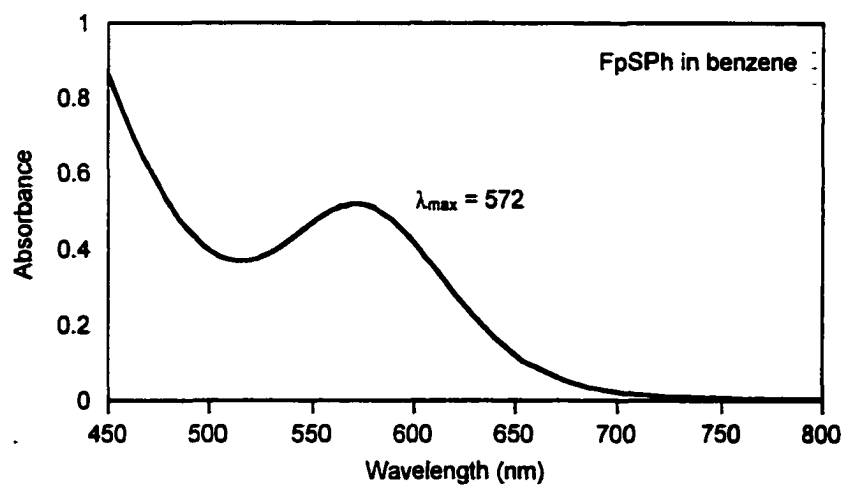


Figure 3.8. A visible spectrum of a 10 mM CpFe(CO)₂(SC₆H₅) solution in benzene.

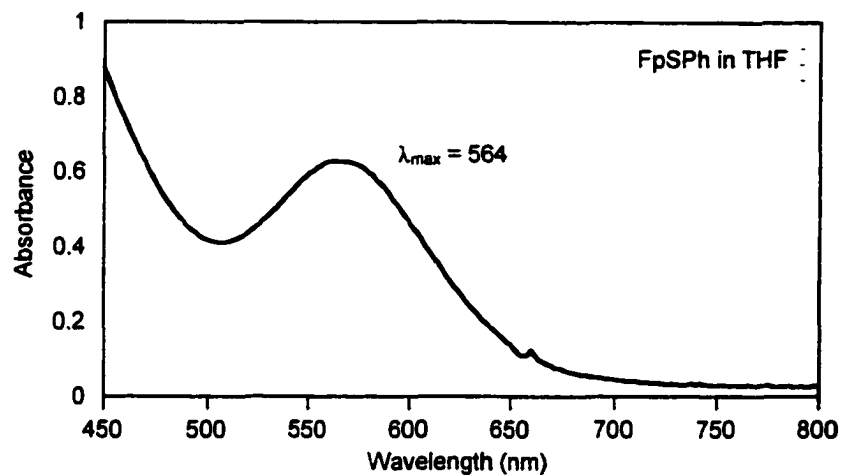


Figure 3.9. A visible spectrum of a 10 mM CpFe(CO)₂(SC₆H₅) solution in tetrahydrofuran.

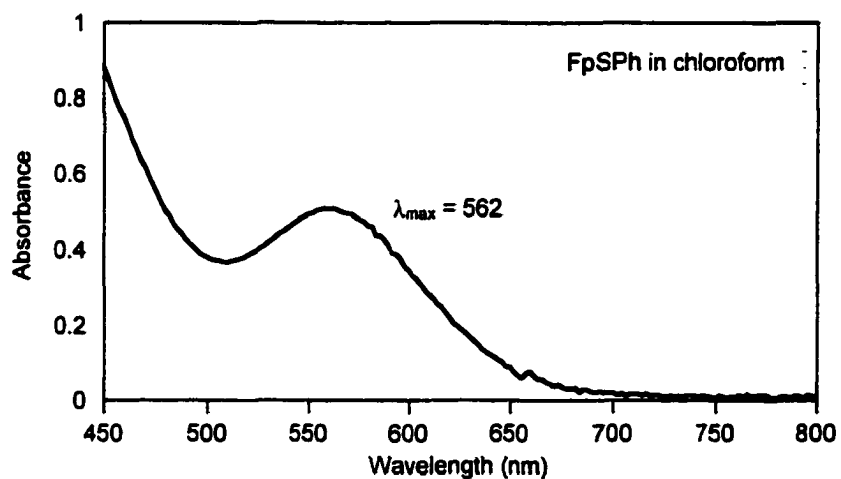


Figure 3.10. A visible spectrum of a 10 mM CpFe(CO)₂(SC₆H₅) solution in chloroform.

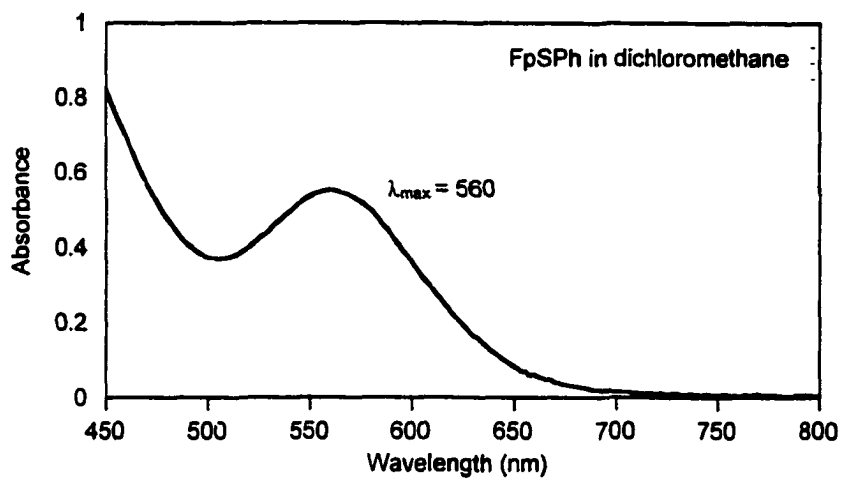


Figure 3.11. A visible spectrum of a 10 mM CpFe(CO)₂(SC₆H₅) solution in dichloromethane.

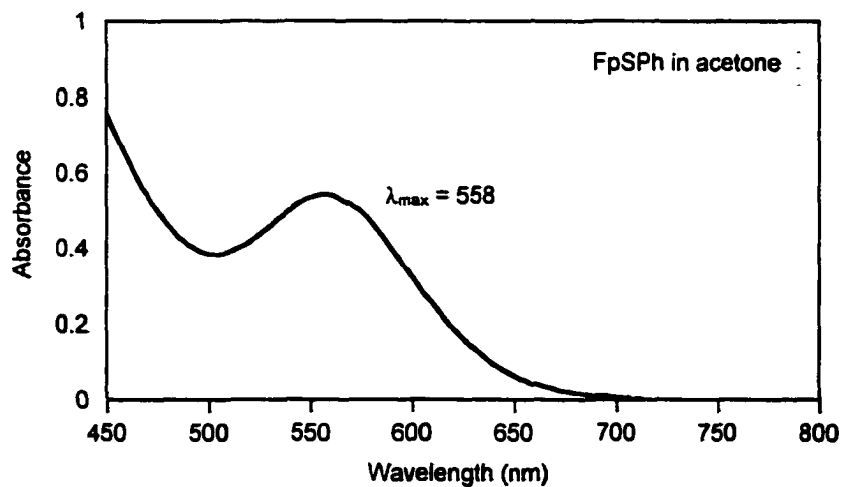


Figure 3.12. A visible spectrum of a 10 mM CpFe(CO)₂(SC₆H₅) solution in acetone.

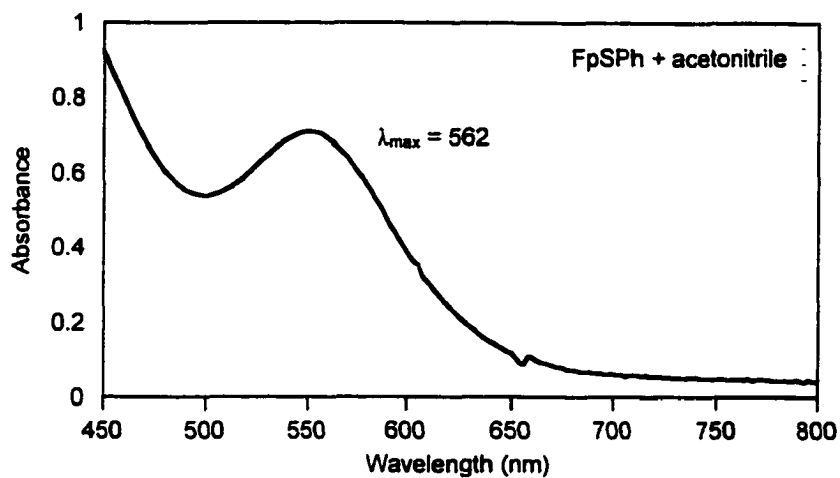


Figure 3.13. A visible spectrum of a 10 mM CpFe(CO)₂(SC₆H₅) solution in acetonitrile.

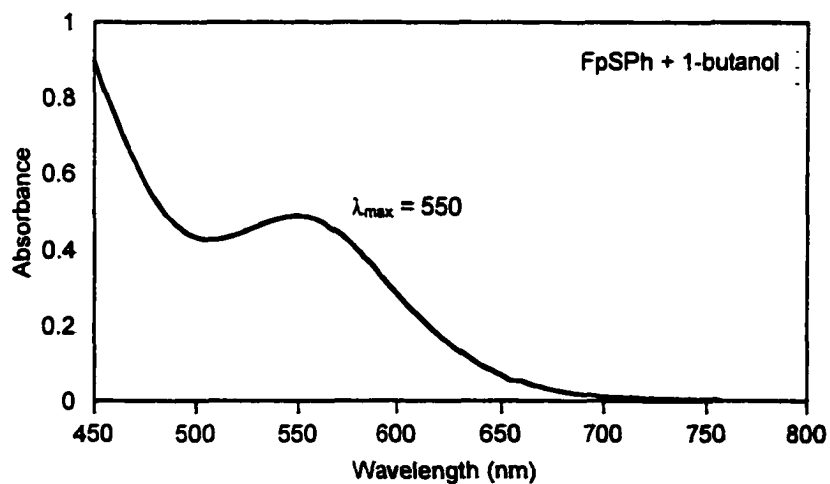


Figure 3.14. A visible spectrum of a 10 mM CpFe(CO)₂(SC₆H₅) solution in 1-butanol.

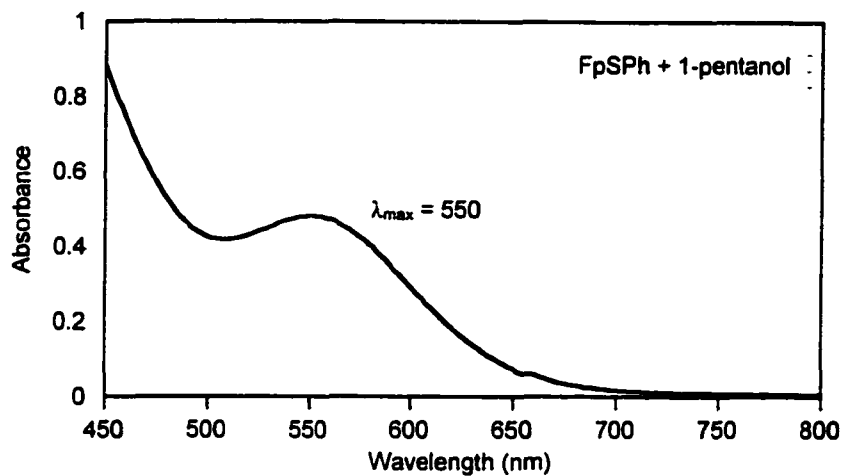


Figure 3.15. A visible spectrum of a 10 mM CpFe(CO)₂(SC₆H₅) solution in 1-pentanol.

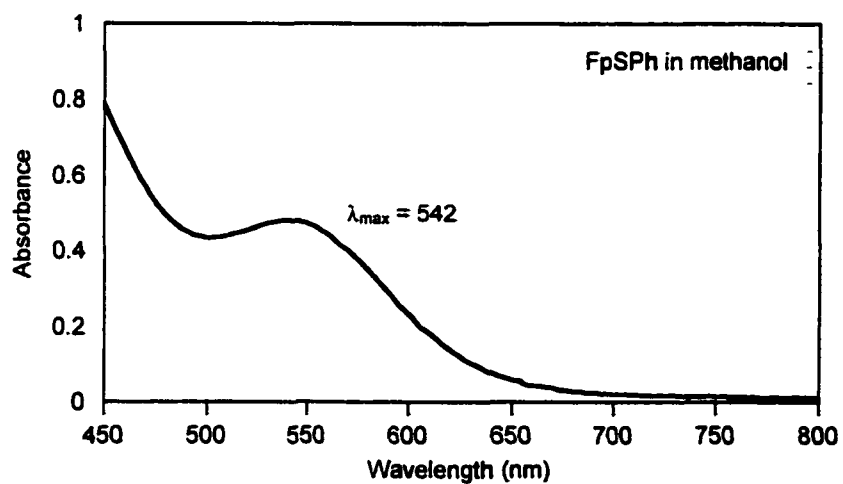


Figure 3.16. A visible spectrum of a 10 mM CpFe(CO)₂(SC₆H₅) solution in methanol.

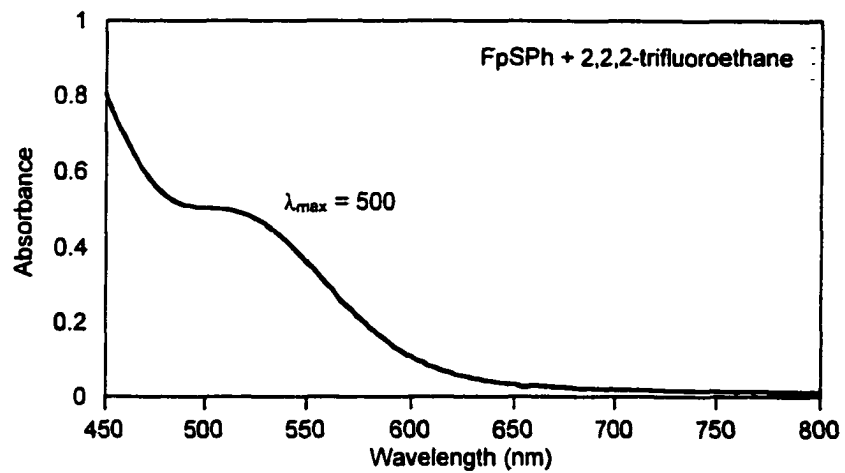


Figure 3.17. A visible spectrum of a 10 mM CpFe(CO)₂(SC₆H₅) solution in 2,2,2-trifluoroethanol.

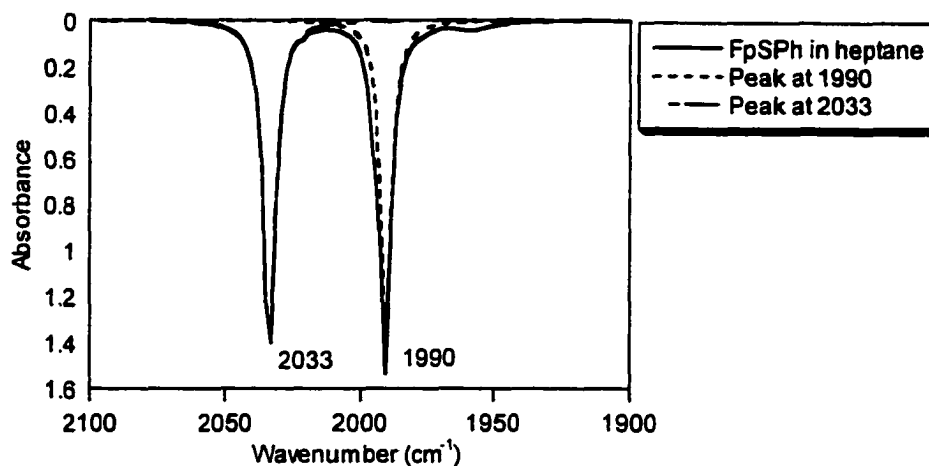


Figure 3.18. An infrared spectrum of the carbonyl stretching frequencies of a 10 mM $\text{CpFe}(\text{CO})_2(\text{SC}_6\text{H}_5)$ solution in heptane.

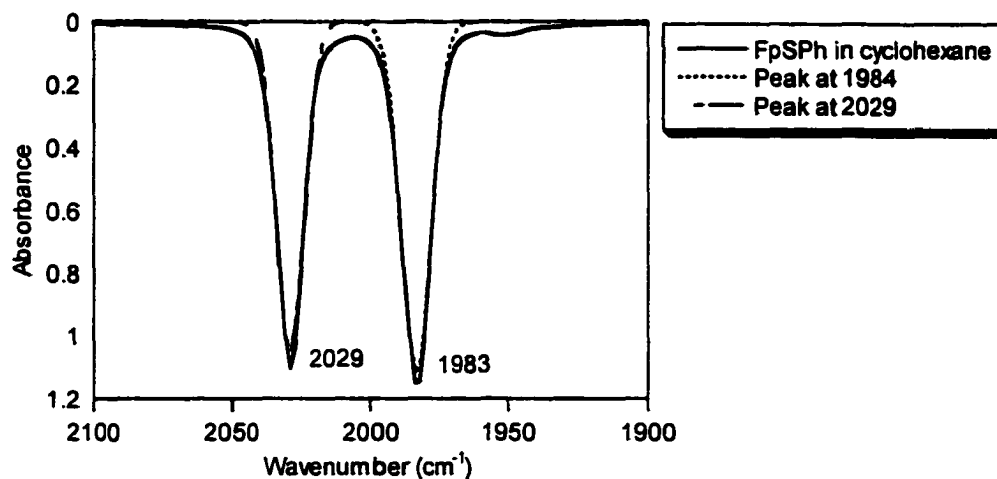


Figure 3.19. An infrared spectrum of the carbonyl stretching frequencies of a 10 mM $\text{CpFe}(\text{CO})_2(\text{SC}_6\text{H}_5)$ solution in cyclohexane.

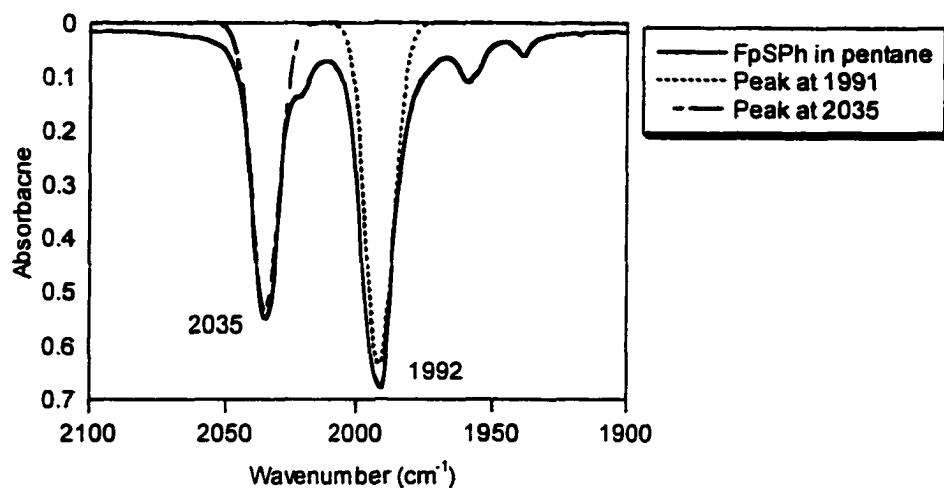


Figure 3.20. An infrared spectrum of the carbonyl stretching frequencies of a 10 mM $\text{CpFe}(\text{CO})_2(\text{SC}_6\text{H}_5)$ solution in pentane.

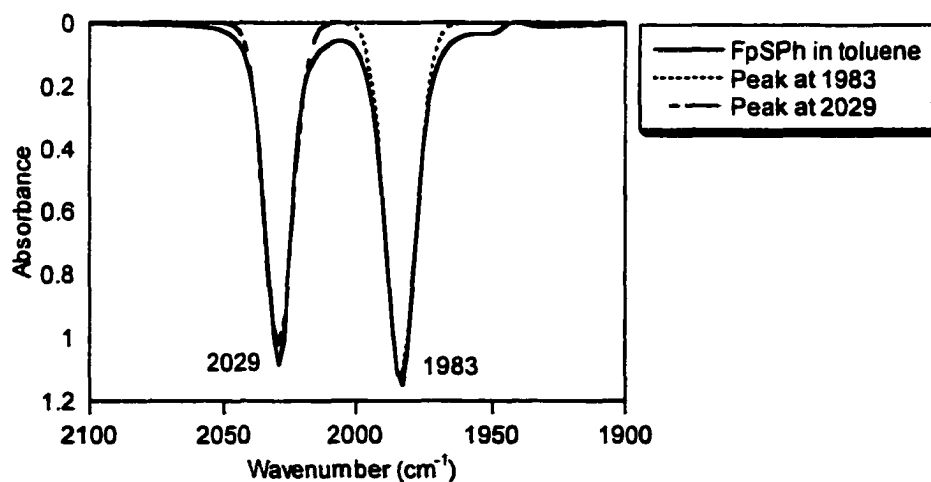


Figure 3.21. An infrared spectrum of the carbonyl stretching frequencies of a 10 mM $\text{CpFe}(\text{CO})_2(\text{SC}_6\text{H}_5)$ solution in toluene.

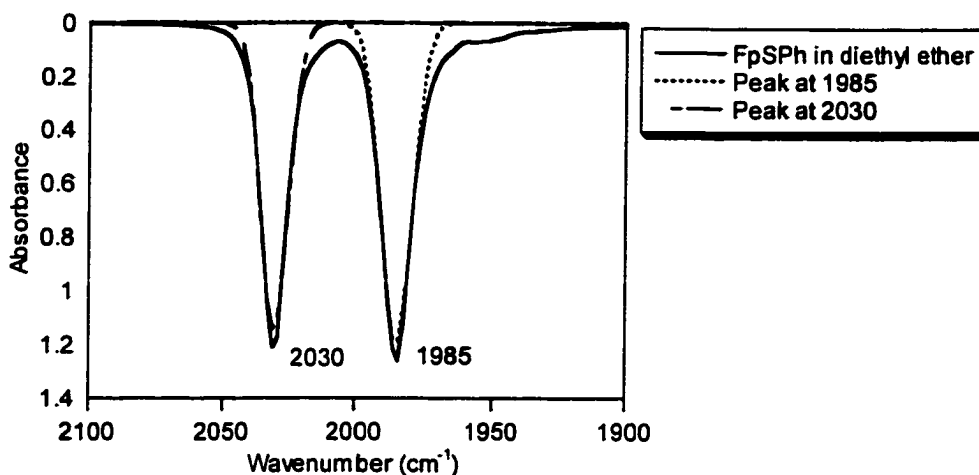


Figure 3.22. An infrared spectrum of the carbonyl stretching frequencies of a 10 mM $\text{CpFe}(\text{CO})_2(\text{SC}_6\text{H}_5)$ solution in diethyl ether.

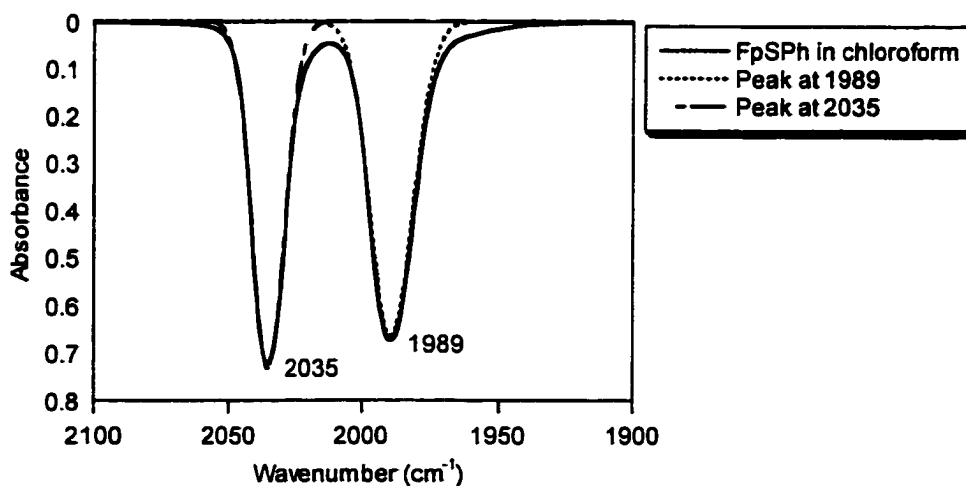


Figure 3.23. An infrared spectrum of the carbonyl stretching frequencies of a 10 mM $\text{CpFe}(\text{CO})_2(\text{SC}_6\text{H}_5)$ solution in chloroform.

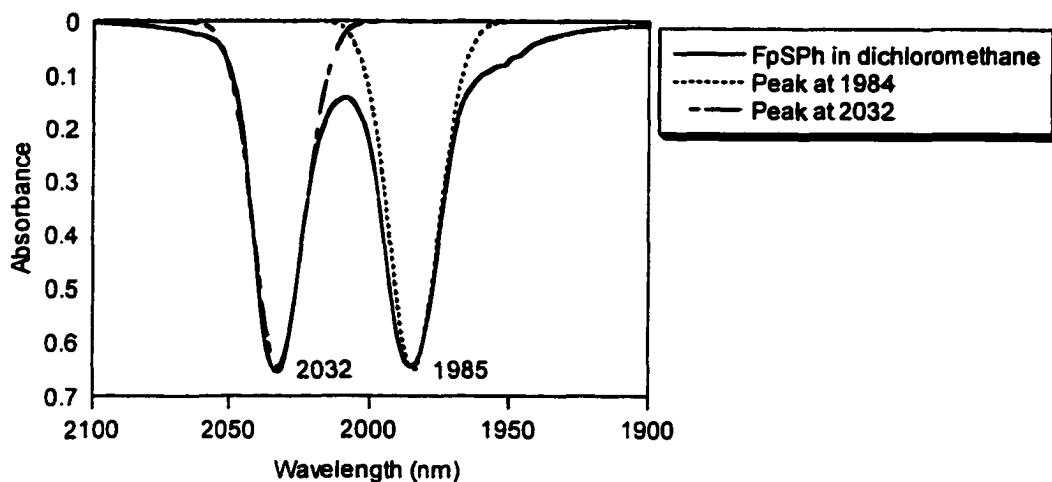


Figure 3.24. An infrared spectrum of the carbonyl stretching frequencies of a 10 mM $\text{CpFe}(\text{CO})_2(\text{SC}_6\text{H}_5)$ solution in dichloromethane.

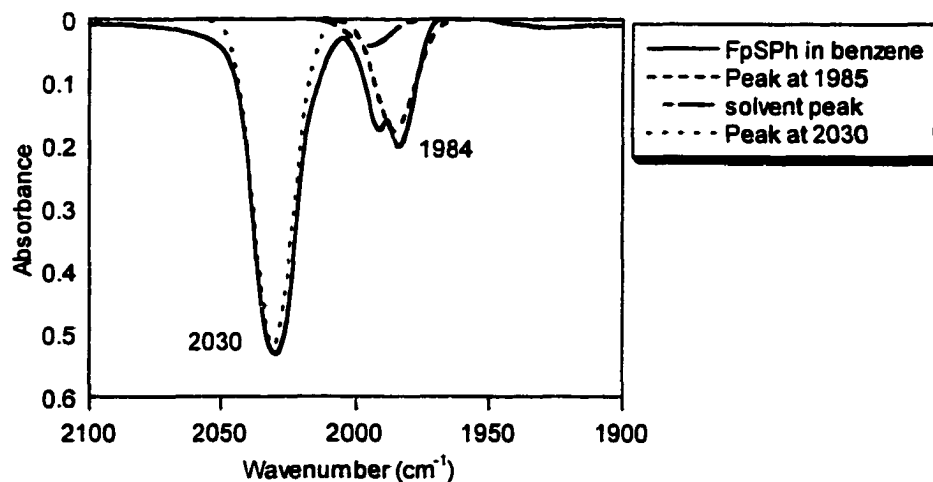


Figure 3.25. An infrared spectrum of the carbonyl stretching frequencies of a 10 mM $\text{CpFe}(\text{CO})_2(\text{SC}_6\text{H}_5)$ solution in benzene. A peak from benzene is interfering with the carbonyl stretching frequency at 1984 cm^{-1} .

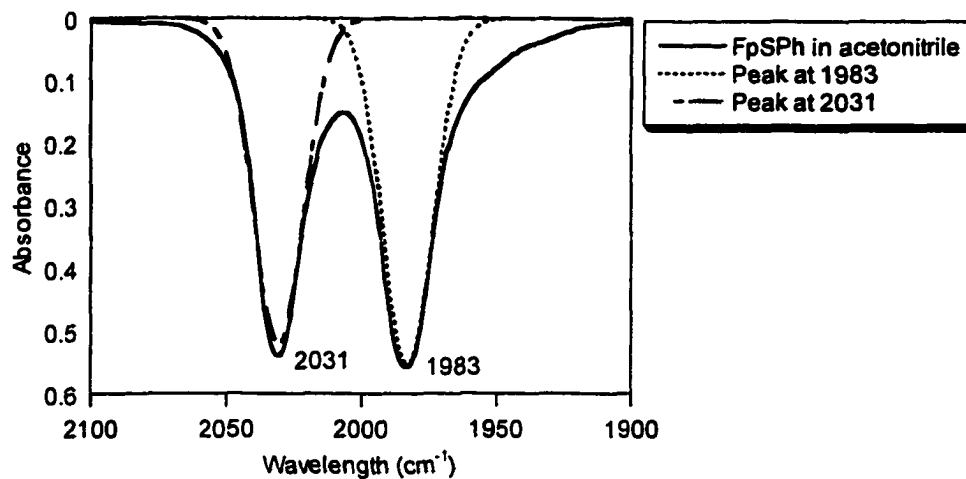


Figure 3.26. An infrared spectrum of the carbonyl stretching frequencies of a 10 mM CpFe(CO)₂(SC₆H₅) solution in acetonitrile.

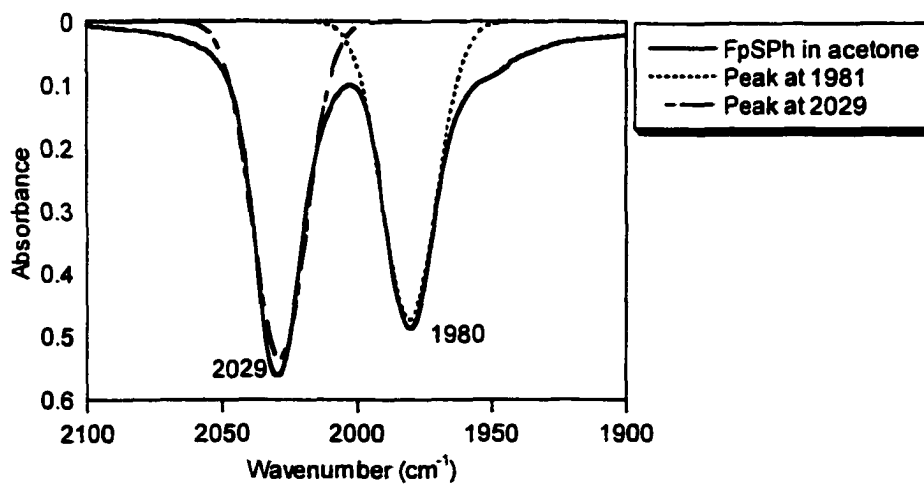


Figure 3.27. An infrared spectrum of the carbonyl stretching frequencies of a 10 mM CpFe(CO)₂(SC₆H₅) solution in acetone.

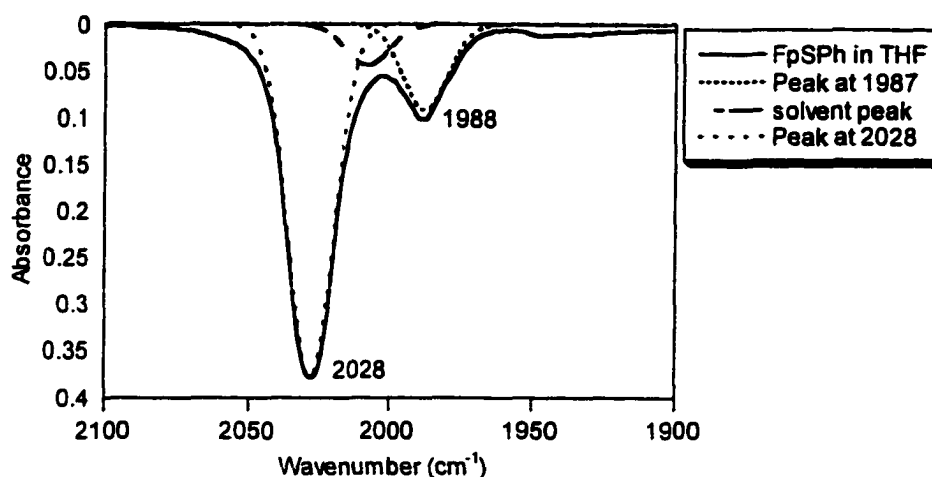


Figure 3.28. An infrared spectrum of the carbonyl stretching frequencies of a 10 mM $\text{CpFe}(\text{CO})_2(\text{SC}_6\text{H}_5)$ solution in tetrahydrofuran. A peak from THF is interfering with the carbonyl stretching frequency at 1988 cm^{-1} .

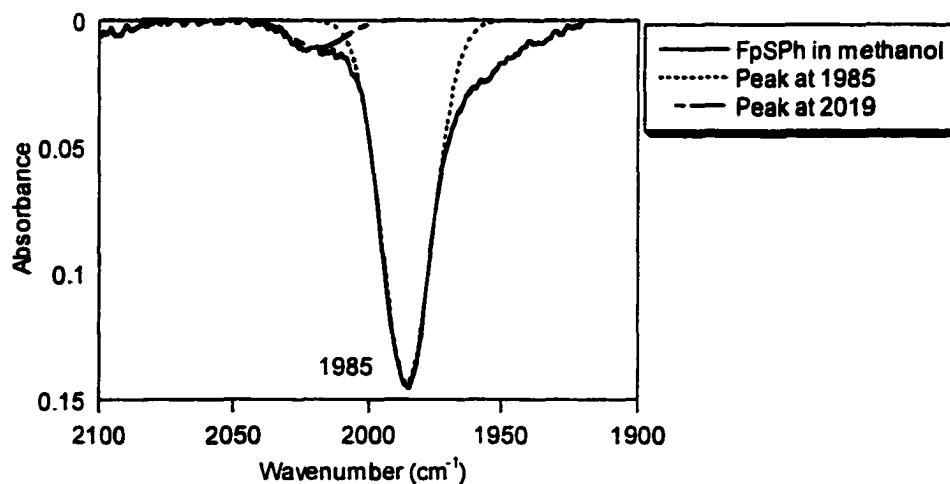


Figure 3.29. An infrared spectrum of the carbonyl stretching frequencies of a 10 mM $\text{CpFe}(\text{CO})_2(\text{SC}_6\text{H}_5)$ solution in methanol. A peak from methanol is interfering with the carbonyl stretching frequency at 2019 cm^{-1} .

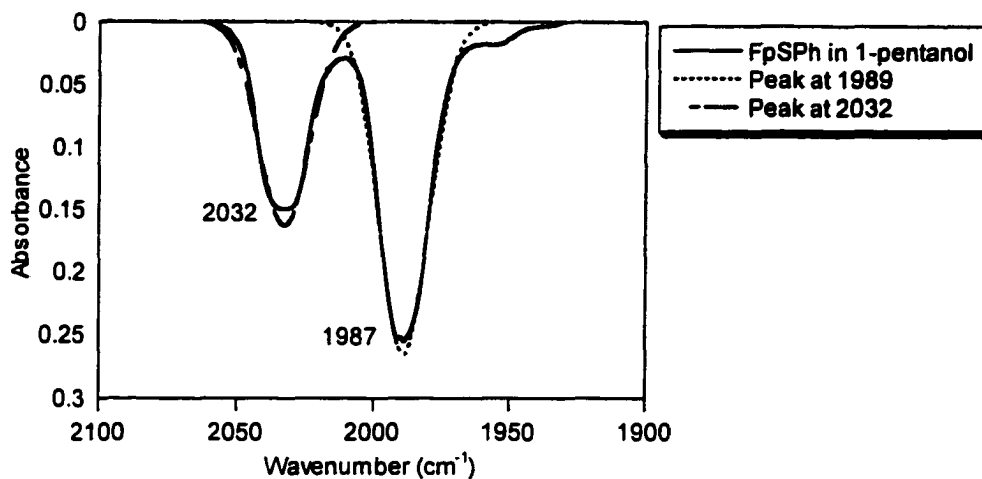


Figure 3.30. An infrared spectrum of the carbonyl stretching frequencies of a 10 mM $\text{CpFe}(\text{CO})_2(\text{SC}_6\text{H}_5)$ solution in 1-pentanol. A peak from 1-pentanol is interfering with the carbonyl stretching frequency at 2032 cm^{-1} .

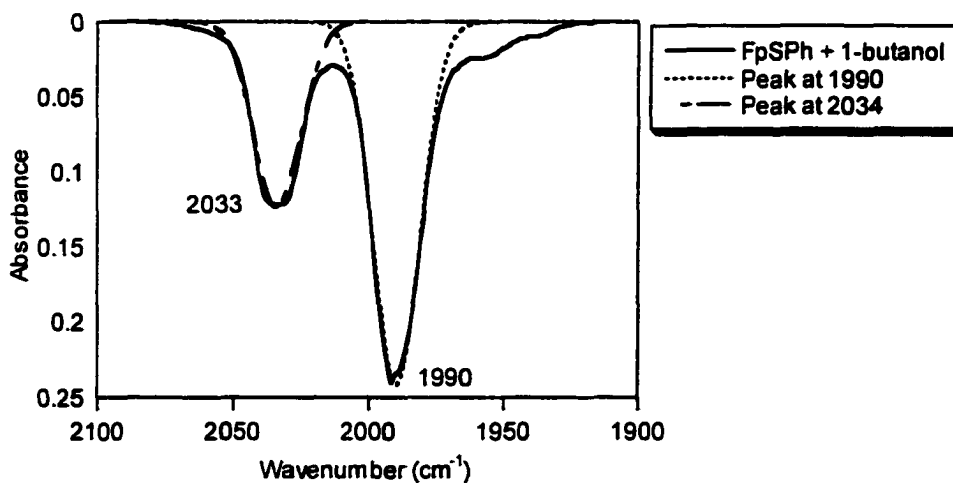


Figure 3.31. An infrared spectrum of the carbonyl stretching frequencies of a 10 mM $\text{CpFe}(\text{CO})_2(\text{SC}_6\text{H}_5)$ solution in 1-butanol. A peak from 1-butanol is interfering with the carbonyl stretching frequency at 2033 cm^{-1} .

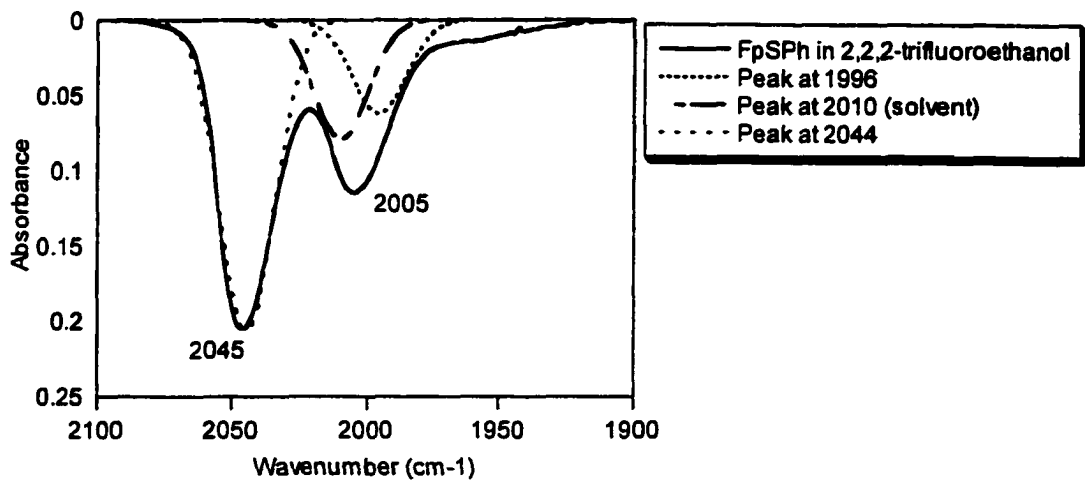


Figure 3.32. An infrared spectrum of the carbonyl stretching frequencies of a 10 mM $\text{CpFe}(\text{CO})_2(\text{SC}_6\text{H}_5)$ solution in 2,2,2-trifluoroethanol. A peak from 2,2,2-trifluoroethanol is interfering with the carbonyl stretching frequency at 2005 cm^{-1} .

Table 3.3. UV-vis and infrared stretching frequency data of a 10 mM $\text{CpFe}(\text{CO})_2(\text{SC}_6\text{H}_4\text{-}p\text{-CF}_3)$ solution solvated with each of the aprotic solvents listed below.

Solvent	UV-vis (nm)	ν_{CO} (cm^{-1})	Obs F_{CO} (k_i) (mdyn/ Å)	E_T^N
Pentane	574	1996, 2039	16.43 ₉ , (0.35 ₀)	0.009
Benzene	558	1988, 2034	16.33 ₃ , (0.37 ₄)	0.111
Diethyl Ether	558	1990, 2035	16.35 ₈ , (0.36 ₆)	0.117
Tetrahydrofuran	548	1986, 2033	16.30 ₉ , (0.38 ₁)	0.207
Chloroform	552	1993, 2039	16.41 ₅ , (0.37 ₄)	0.259
Dichloromethane	550	1990, 2037	16.37 ₄ , (0.38 ₂)	0.309
Acetone	540	1987, 2034	16.32 ₅ , (0.38 ₂)	0.355
Acetonitrile	536	1988, 2035	16.34 ₂ , (0.38 ₂)	0.460

Table 3.4. The carbonyl stretching frequencies of 10 mM solutions of $\text{CpFe}(\text{CO})_2\text{Cl}$ and $\text{CpFe}(\text{CO})_2\text{I}$ in six different solvents. a) Gutmann's Acceptor Number, b) the difference in the antisymmetric stretching frequencies between FpCl and FpI , c) the difference in the symmetric stretching frequencies between FpCl and FpI , d) the difference in the antisymmetric stretching frequencies between FpI and $\text{Fp}(\text{SC}_6\text{H}_5)$ (data from Table 3.2), e) the difference in the symmetric stretching frequencies between FpI and $\text{Fp}(\text{SC}_6\text{H}_5)$ (data from Table 3.2), f) based on the average values of the other differences in the antisymmetric stretching frequencies between FpI and $\text{Fp}(\text{SC}_6\text{H}_5)$

Solvent	AN ^a	$\text{CpFe}(\text{CO})_2\text{Cl}$ $\nu_{\text{CO}} (\text{cm}^{-1})$	Obs $F_{\text{CO}} (k_i)$ (mdyn/Å)	$\text{CpFe}(\text{CO})_2\text{I}$ $\nu_{\text{CO}} (\text{cm}^{-1})$	Obs $F_{\text{CO}} (k_i)$ (mdyn/Å)	$\Delta\nu_{\text{CO}}^b, \Delta\nu_{\text{CO}}^c$ (cm^{-1})	$\Delta\nu_{\text{CO}}^d, \Delta\nu_{\text{CO}}^e$ (cm^{-1})
Pentane	(0)	2013, 2055	16.70 ₉ (0.34 ₄)	2004, 2042	16.52 ₈ (0.31 ₀)	9, 13	13, 7
Diethyl ether	3.9	2004, 2050	16.59 ₄ (0.37 ₇)	1995, 2038	16.42 ₂ (0.35 ₀)	9, 12	10, 8
Tetrahydrofuran	8.0	1998, 2046	16.51 ₃ (0.39 ₂)	1990, 2035	16.35 ₈ (0.36 ₆)	8, 11	(11) ^f , 7
Acetone	12.5	2000, 2048	16.54 ₅ (0.39 ₂)	1991, 2037	16.38 ₂ (0.37 ₄)	9, 11	11, 8
Acetonitrile	18.9	2002, 2050	16.57 ₈ (0.39 ₃)	1993, 2038	16.40 ₆ (0.36 ₆)	9, 12	10, 7
Dichloromethane	20.4	2007, 2052	16.63 ₅ (0.36 ₉)	1996, 2041	16.45 ₆ (0.36 ₇)	11, 11	11, 9

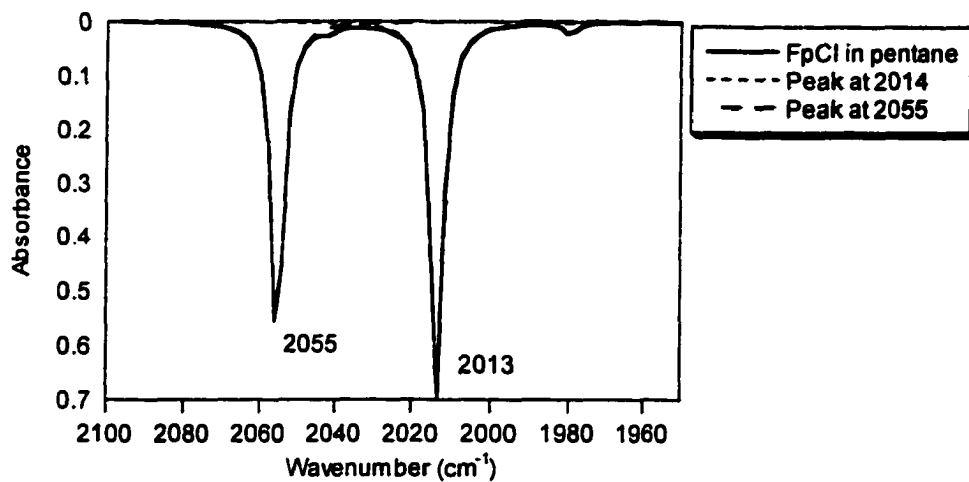


Figure 3.33. An infrared spectrum of the carbonyl stretching frequencies of a 5 mM CpFe(CO)₂Cl solution in pentane.

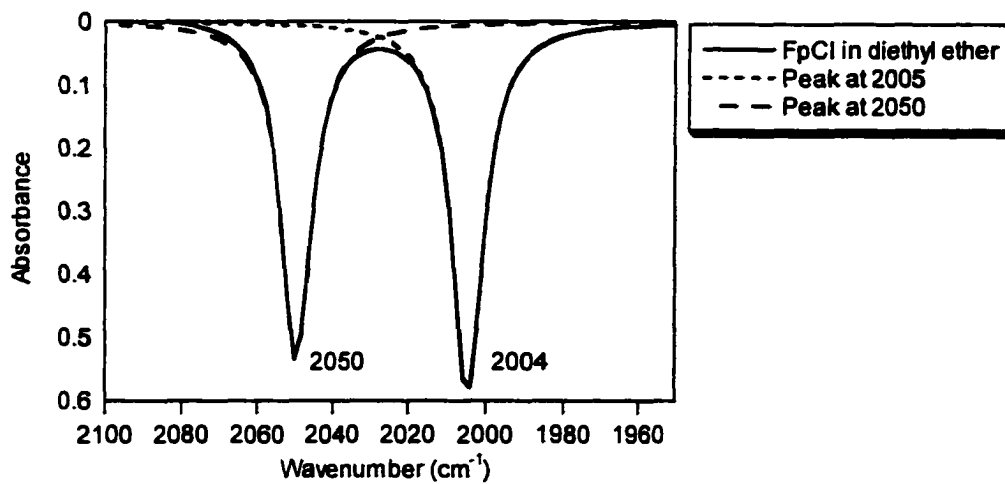


Figure 3.34. An infrared spectrum of the carbonyl stretching frequencies of a 5 mM CpFe(CO)₂Cl solution in diethyl ether.

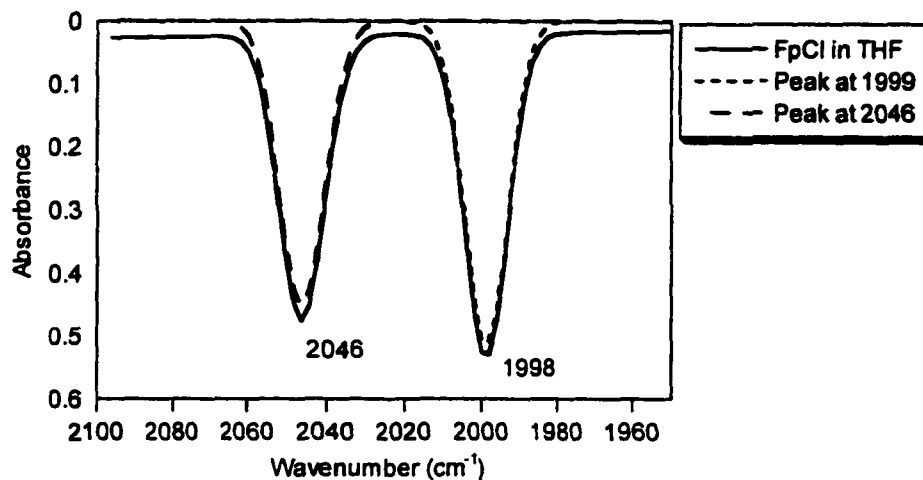


Figure 3.35. An infrared spectrum of the carbonyl stretching frequencies of a 5 mM CpFe(CO)₂Cl solution in tetrahydrofuran.

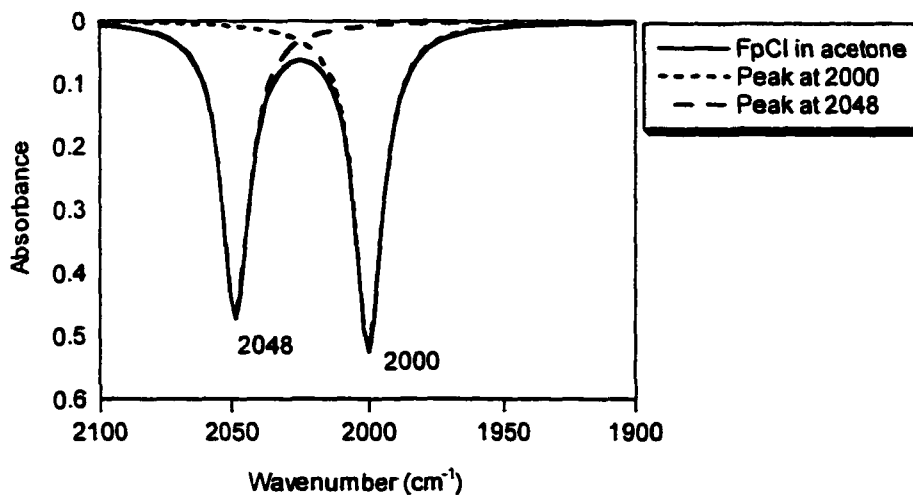


Figure 3.36. An infrared spectrum of the carbonyl stretching frequencies of a 5 mM CpFe(CO)₂Cl solution in acetone.

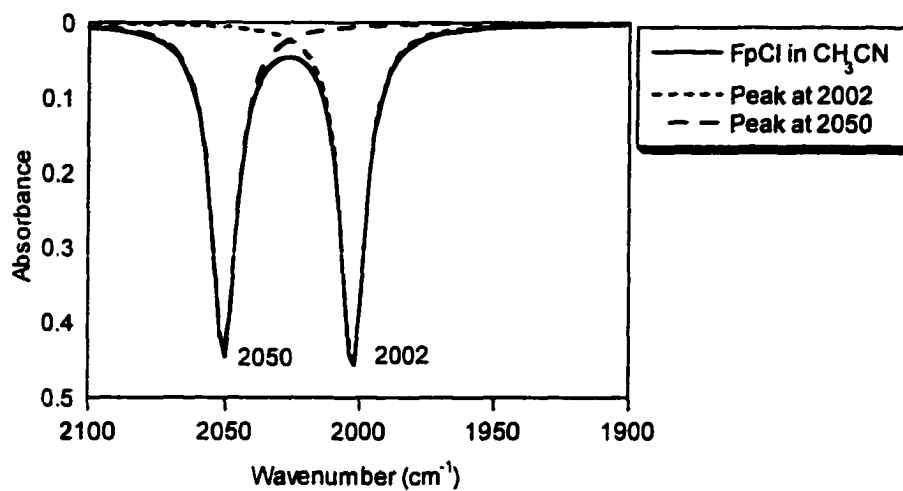


Figure 3.37. An infrared spectrum of the carbonyl stretching frequencies of a 5 mM CpFe(CO)₂Cl solution in acetonitrile.

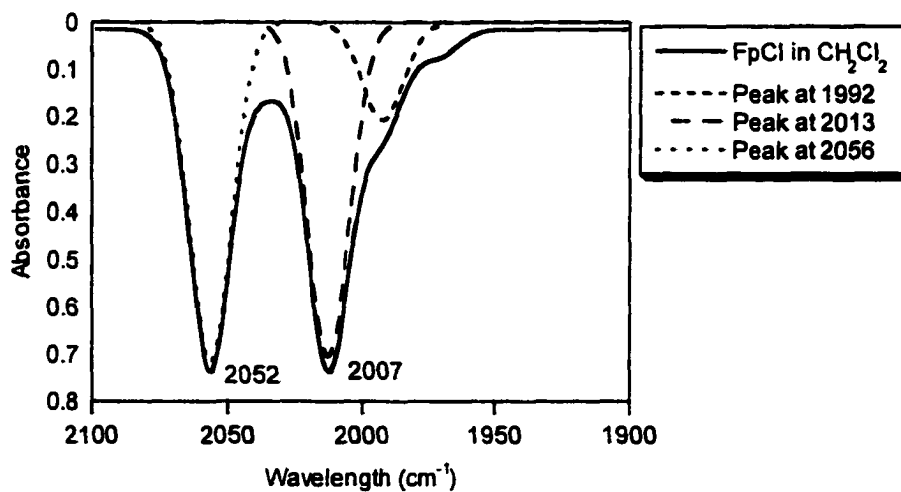


Figure 3.38. An infrared spectrum of the carbonyl stretching frequencies of a 5 mM CpFe(CO)₂Cl solution in dichloromethane.

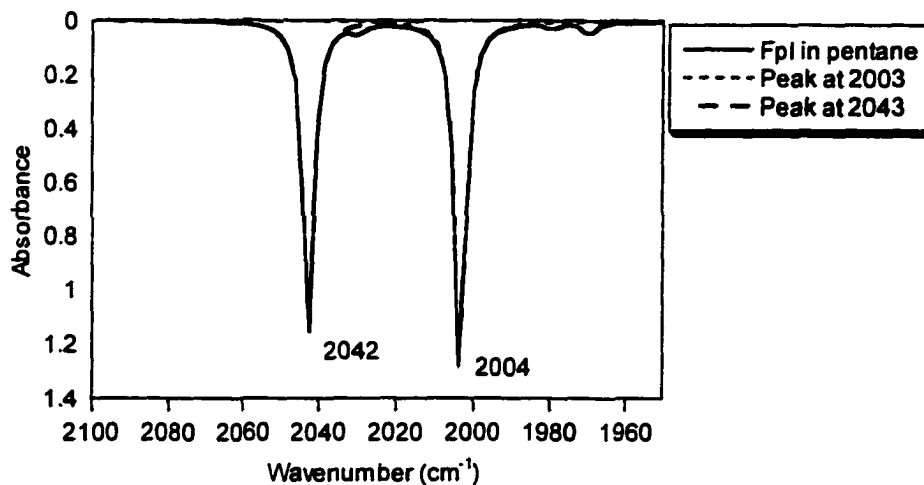


Figure 3.39. An infrared spectrum of the carbonyl stretching frequencies of a 5 mM CpFe(CO)₂I solution in pentane.

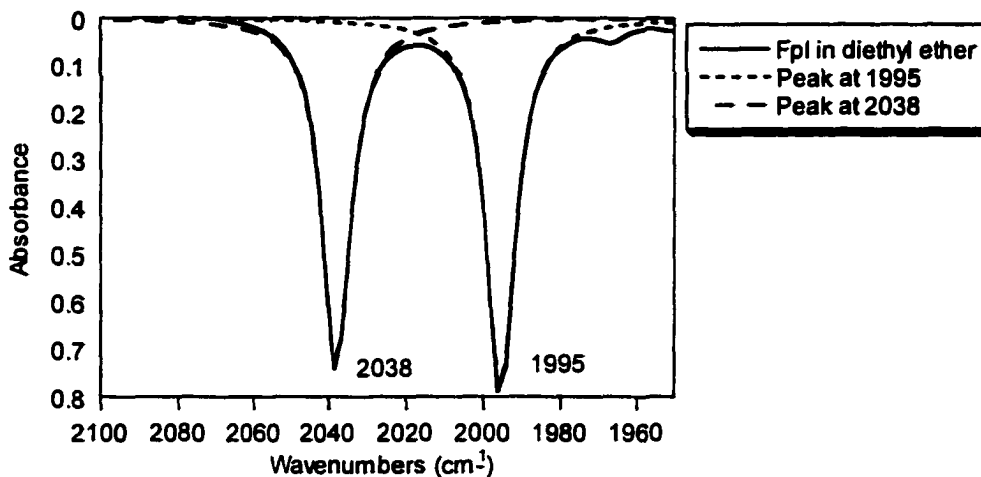


Figure 3.40. An infrared spectrum of the carbonyl stretching frequencies of a 5 mM CpFe(CO)₂I solution in diethyl ether.

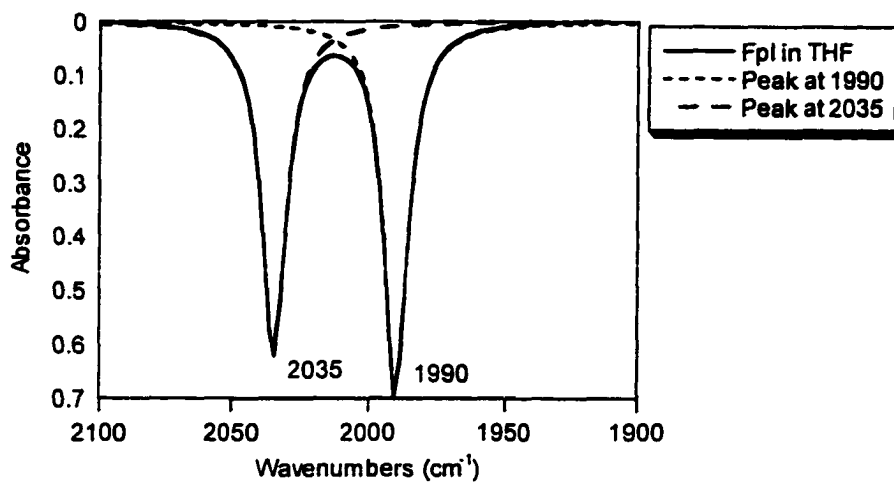


Figure 3.41. An infrared spectrum of the carbonyl stretching frequencies of a 5 mM CpFe(CO)₂I solution in tetrahydrofuran.

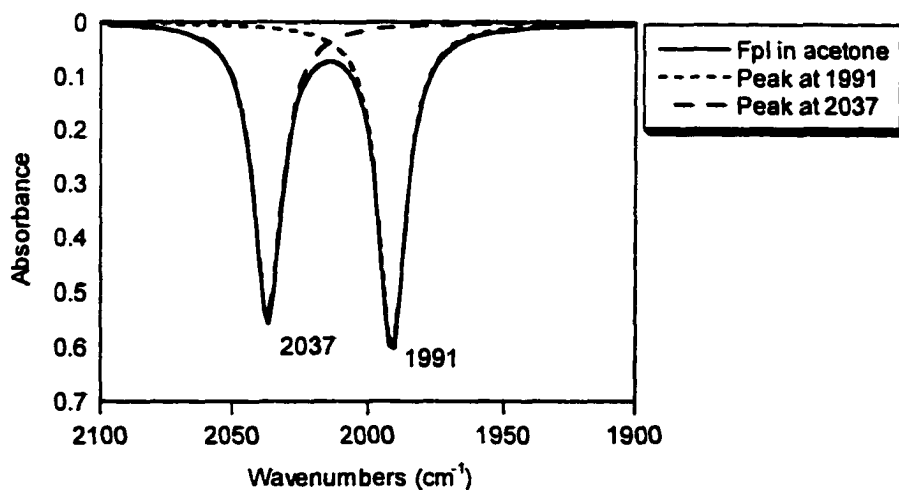


Figure 3.42. An infrared spectrum of the carbonyl stretching frequencies of a 5 mM CpFe(CO)₂I solution in acetone.

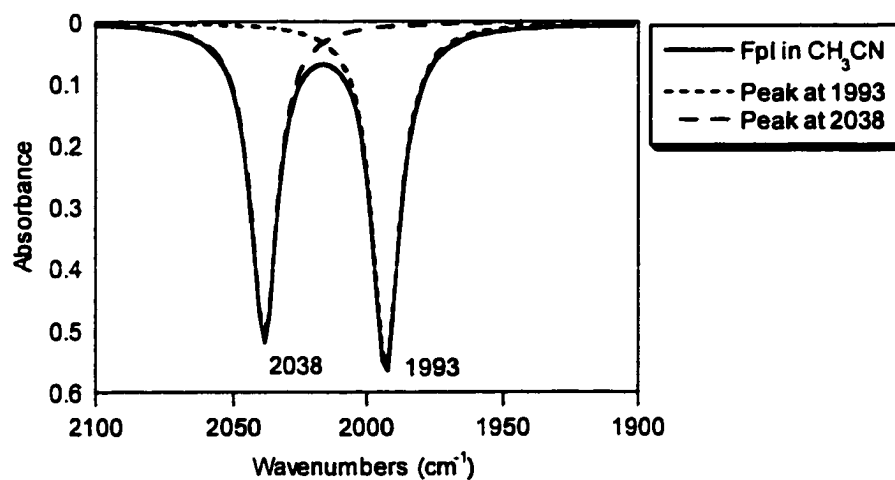


Figure 3.43. An infrared spectrum of the carbonyl stretching frequencies of a 5 mM CpFe(CO)₂I solution in acetonitrile.

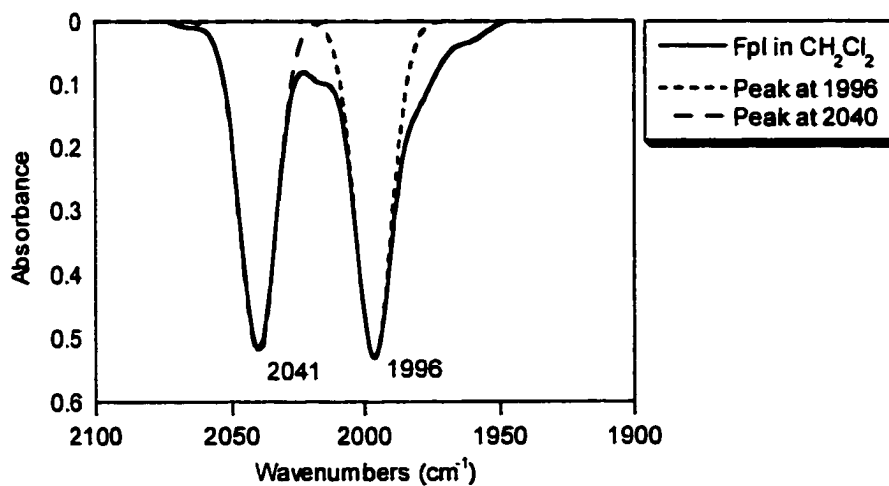


Figure 3.44. An infrared spectrum of the carbonyl stretching frequencies of a 5 mM CpFe(CO)₂I solution in dichloromethane.

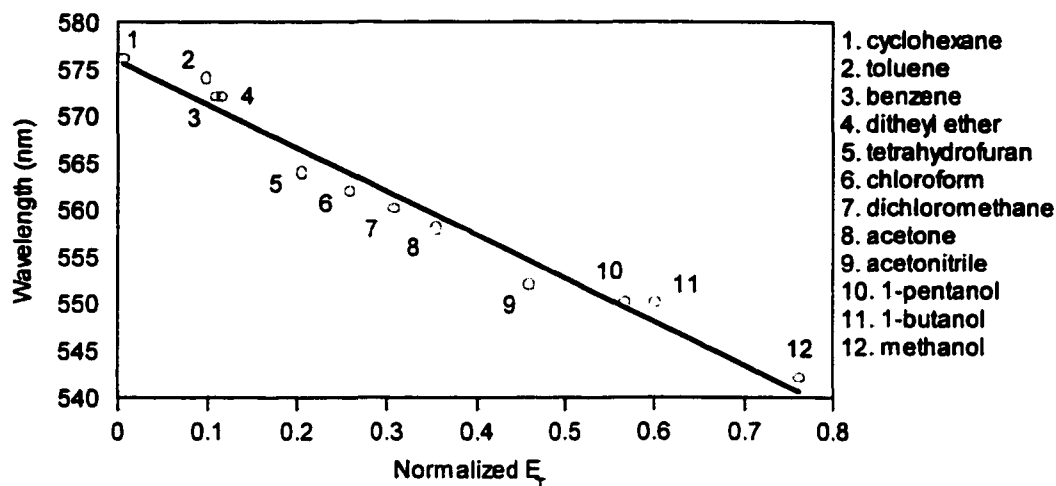


Figure 3.45. Plot of wavelength vs. the Dimroth-Reichardt's normalized energy of transition scale of solvents of a 10 mM $\text{CpFe}(\text{CO})_2(\text{SC}_6\text{H}_5)$ solution.

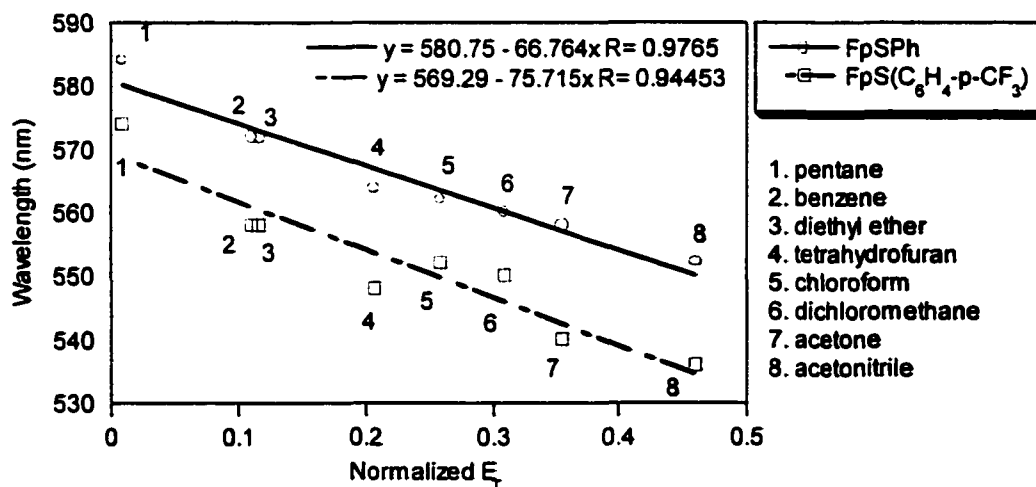


Figure 3.46. Plot of wavelength vs. the Dimroth-Reichardt's normalized energy of transition scale of solvents of a 10 mM $\text{CpFe}(\text{CO})_2(\text{SC}_6\text{H}_5)$ solution and a 10 mM $\text{CpFe}(\text{CO})_2(\text{SC}_6\text{H}_4\text{-}p\text{-CF}_3)$.

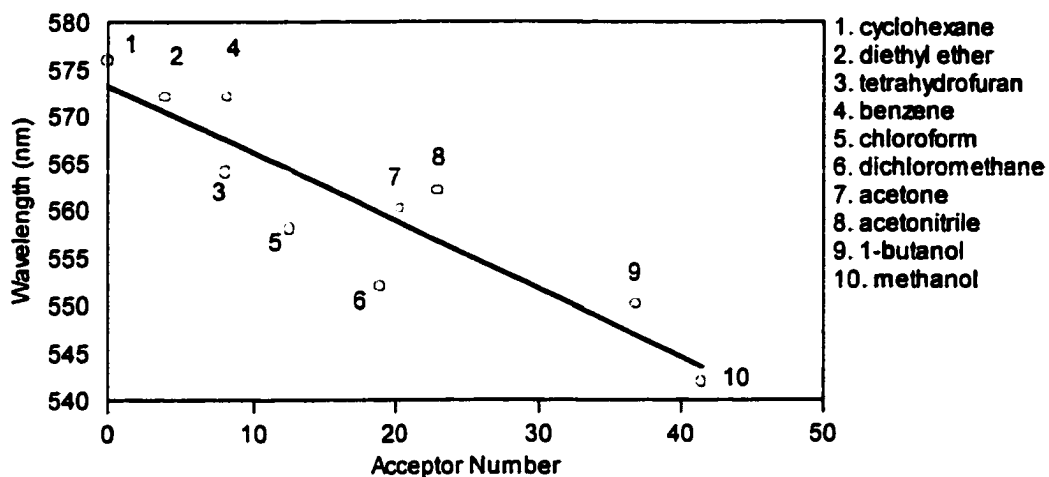


Figure 3.47. Plot of wavelength vs. Gutmann's Acceptor Number of a 10 mM $\text{CpFe}(\text{CO})_2(\text{SC}_6\text{H}_5)$ solution.

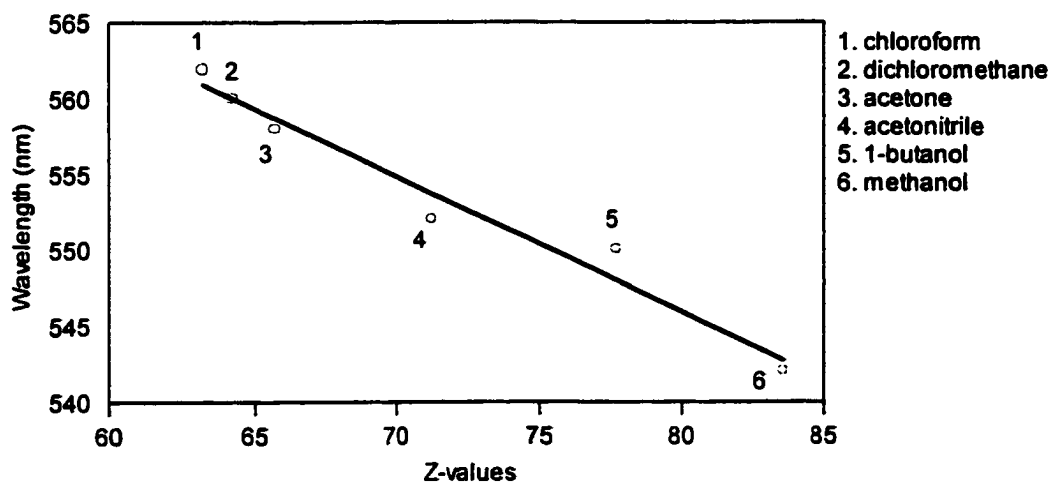


Figure 3.48. Plot of wavelength vs. Kosower's Z-scale of solvents of a 10 mM $\text{CpFe}(\text{CO})_2(\text{SC}_6\text{H}_5)$ solution.

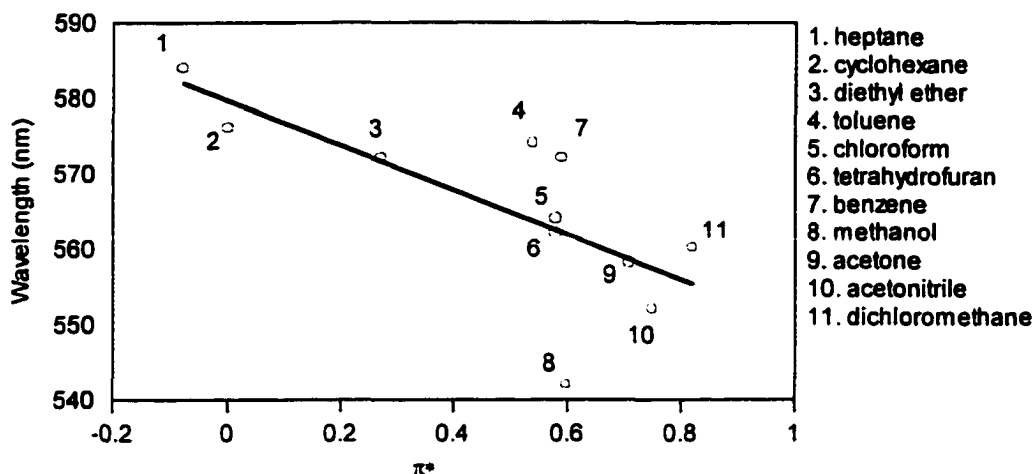


Figure 3.49. Plot of wavelength vs. the Kamlet and Taft's π^* polarity scale of solvents of a 10 mM $\text{CpFe}(\text{CO})_2(\text{SC}_6\text{H}_5)$ solution.

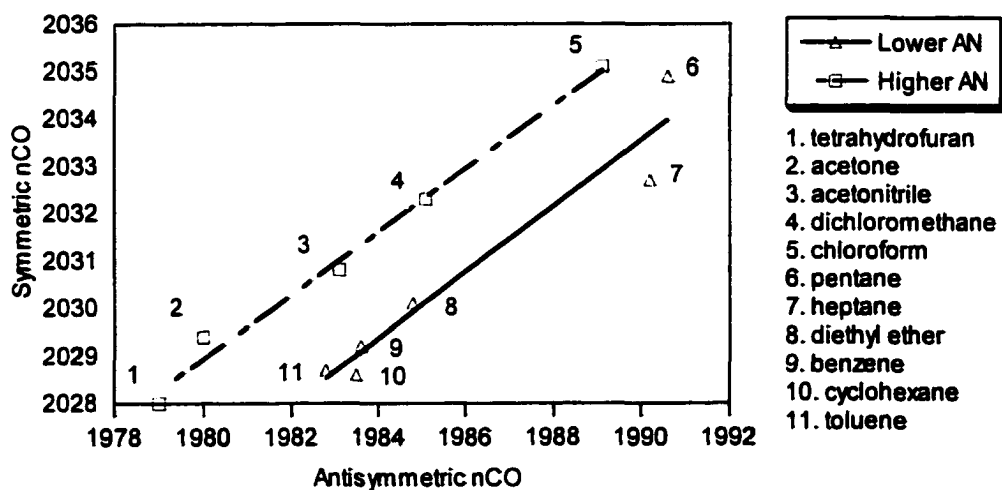


Figure 3.50. A plot of the antisymmetric vs. symmetric stretching frequencies of a 10 mM $\text{CpFe}(\text{CO})_2(\text{SC}_6\text{H}_5)$ solution in various solvents. The triangles represent the solvents with lower Gutmann's acceptor numbers and the squares represent the solvents with higher Gutmann's acceptor numbers.

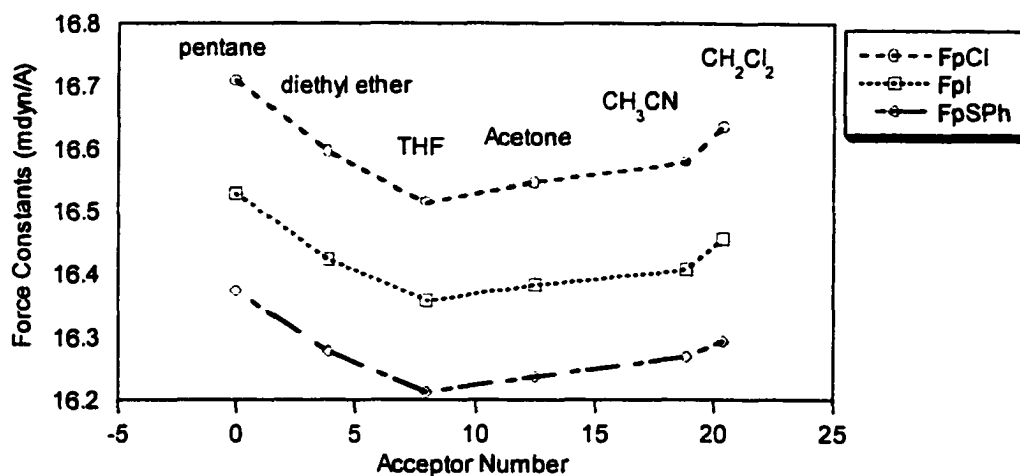


Figure 3.51. A plot of the force constants based on the observed infrared carbonyl stretching frequencies of $\text{CpFe}(\text{CO})_2\text{Cl}$, $\text{CpFe}(\text{CO})_2\text{I}$, and $\text{CpFe}(\text{CO})_2(\text{SC}_6\text{H}_5)$ vs. Gutmann's Acceptor Number.

3.4 Discussion

Empirical solvent scales were used to correlate with the wavelengths from the UV-vis data of $\text{CpFe}(\text{CO})_2(\text{SC}_6\text{H}_5)$ and $\text{CpFe}(\text{CO})_2(\text{SC}_6\text{H}_4\text{-}p\text{-CF}_3)$. The four scales used were Dimroth-Reichardt's solvent parameters (E_T), Gutmann's Acceptor Number (AN), Kosower's Z-scale, and Kamlet and Taft's solvent polarity scale (π^*). Their literature values are incorporated in Table 3.1. The results of correlating the wavelengths of $\text{CpFe}(\text{CO})_2(\text{SC}_6\text{H}_5)$ with E_T , AN, Z-scale and π^* are shown in Figures 3.45-3.49. The two best least squares fit were obtained by using the E_T scale (slope -46.35 , correlation coefficient 0.986) and the Z-values (slope -0.894 , correlation coefficient 0.984). Another one of the better scales was the AN scale (slope -0.72 , correlation coefficient 0.908). One of the poorest scales was the π^* scale (slope -29.655 , correlation coefficient

0.732). Plots of wavelengths vs. dielectric constant (ϵ) and Buckingham's equations were not observed to correlate to the degree of E_T , Z-values or the AN scale and were not further investigated.

The electronic absorption spectra of the compound $\text{CpFe}(\text{CO})_2(\text{SC}_6\text{H}_5)$ exhibits a ligand to metal charge transfer (LMCT). The LMCT band maxima are markedly solvent dependent; for example, solutions of $\text{CpFe}(\text{CO})_2(\text{SC}_6\text{H}_5)$ in pentane, benzene, acetone, are colored green, greenish/brown, and red, respectively. By looking at the UV-vis spectra (Figures 3.3-3.17), it is obvious that $\text{CpFe}(\text{CO})_2(\text{SC}_6\text{H}_5)$ exhibits negative solvatochromism since it undergoes a blue shift as the compound is solvated in more polar solvents. Since a blue shift indicates a lower wavelength or, conversely, a higher frequency and therefore higher energy, then it seems reasonable to assume that the dipole moment in the ground-state, μ_g , is greater than the dipole moment in the excited-state, μ_e , as illustrated by Reichardt (Figure 3.2).¹ This means that the ground-state will become more stable in polar solvents than the excited-state, which will produce a hypsochromic or blue shift.

The analogous compound, $\text{CpFe}(\text{CO})_2(\text{SC}_6\text{H}_4\text{-}p\text{-CF}_3)$, also exhibits a blue shift as it is solvated in more polar solvents. In pentane and acetonitrile, the LMCT band occurs at 574 and 536 nm, respectively. The LMCT band for the parent compound, $\text{CpFe}(\text{CO})_2(\text{SC}_6\text{H}_5)$ in the same solvents are 584 and 552 nm, respectively. Notice the increase in energy in the pentane solutions and even more so in the acetonitrile solutions when the $\text{CpFe}(\text{CO})_2(\text{SC}_6\text{H}_5)$ is replaced by $\text{CpFe}(\text{CO})_2(\text{SC}_6\text{H}_4\text{-}p\text{-CF}_3)$. This is evidence that the ground-state is more stable for the $\text{CpFe}(\text{CO})_2(\text{SC}_6\text{H}_4\text{-}p\text{-CF}_3)$ than the parent compound in solution.

Adding an electron withdrawing substituent in the para position of the phenyl thiolate group makes it a weaker π donating group. Since it has been determined that the HOMO for each of the compounds is a $d\pi\text{-}p\pi$ antibonding

orbital, which is primarily sulfur in character, the electron withdrawing group better stabilizes the compound as demonstrated by PES which is a gas-phase technique.⁴⁴ Apparently, this stability is also demonstrated and supported by the UV-vis data. Figure 3.46 shows the wavelengths of the LMCT bands of the two compounds, $\text{CpFe}(\text{CO})_2(\text{SC}_6\text{H}_5)$ and $\text{CpFe}(\text{CO})_2(\text{SC}_6\text{H}_4\text{-}p\text{-CF}_3)$, solvated in various aprotic solvents. These wavelengths are correlated to Dimroth-Reichardt's normalized transition scale of solvents. As indicated from the plot, both solutions correlate very well with E_T^N . Notice that the line that corresponds to the $\text{CpFe}(\text{CO})_2(\text{SC}_6\text{H}_4\text{-}p\text{-CF}_3)$ solutions has a significantly more negative slope than the line corresponding to the $\text{CpFe}(\text{CO})_2(\text{SC}_6\text{H}_5)$ solutions. Apparently, the relative stability of the ground-state for $\text{CpFe}(\text{CO})_2(\text{SC}_6\text{H}_4\text{-}p\text{-CF}_3)$ in solution as the solvent become more polar achieves greater stability than for $\text{CpFe}(\text{CO})_2(\text{SC}_6\text{H}_5)$ in the same solvents.

An explanation for this could be that the magnitude of the dipole moment in the ground-state is greater for the $\text{CpFe}(\text{CO})_2(\text{SC}_6\text{H}_4\text{-}p\text{-CF}_3)$ than for $\text{CpFe}(\text{CO})_2(\text{SC}_6\text{H}_5)$. If this is the case, then the more polar solvents will better stabilize the ground-state of the $\text{CpFe}(\text{CO})_2(\text{SC}_6\text{H}_4\text{-}p\text{-CF}_3)$ than they would for $\text{CpFe}(\text{CO})_2(\text{SC}_6\text{H}_5)$ and, in effect, a greater increase the ΔE between the ground-state energy and the transition state energy occurs (see Figure 3.2.B.).

Certainly, solvent effects at the vibrational level are observed in the infrared region. It is noteworthy that the vibrational event (10^{-14} s) is much slower than the electronic event (10^{-16} s) by two orders of magnitude (excited-state lifetime).⁴¹ Carbonyl stretching frequencies are some of the most common probes to use to observe solvent effects.^{28,34,45-48} However, silicon-chloride stretching frequencies have been used^{49,50} as well as the cyanide stretching frequencies³. The phosphorus oxygen stretching frequency was used by Streck *et al.* to determine solvent effects on trimethyl phosphate.⁴⁰ The correlation

between the Gutmann's acceptor number and the P=O stretching frequency in the compound shown in Figure 3.52 contains two different slopes.⁴⁰ The line for the aprotic solvents is more negative than the line for the protic solvents. Streck attributes the change in slope to hydrogen bonding to the lone pairs on the doubly bound oxygen atom.

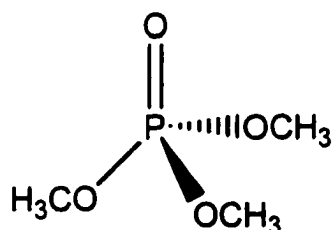


Figure 3.52. Streck *et al.* used the P=O stretching frequency of trimethyl phosphate to determine solvent effects.

Obviously, there are a number of factors that can be involved in the solvent induced shift of a stretching frequency which include: 1) the electrophilicity of the solvent, 2) polarizability of the solute or solvent, and 3) hydrogen bonding.^{34,51} If very little influence is placed upon the solute by the solvent, then the stretching frequencies will tend to be like those of the gas phase stretching frequency, narrow and sharp.⁵² These are illustrated in Figures 3.18, 3.33, and 3.39. Notice how sharp the carbonyl stretching frequencies are for the compound $\text{CpFe}(\text{CO})_2(\text{SC}_6\text{H}_5)$ solvated in heptane and the compounds $\text{CpFe}(\text{CO})_2\text{Cl}$ and $\text{CpFe}(\text{CO})_2\text{I}$ solvated in pentane compared to the other carbonyl stretching frequencies shown in the other figures. As the solute (i.e. carbonyl complex) interacts more strongly with the solvent, then the carbonyl

stretching frequencies broaden and become less intense. A specific correlation between the broadening effect on the carbonyl stretching frequency and any physical properties of the solvent has yet to be found.

Barraclough demonstrated that as metal carbonyls are solvated by more polar solvents, the carbonyl stretching frequencies decrease.⁵³ However, Hales demonstrated that as metal carbonyl halides are solvated by more polar solvents, the carbonyl stretching frequencies increase.³³ Hales states that by increasing the polarity of the solvent, this should better stabilize the polar nature of the metal-halide bond and therefore increase the carbonyl stretching frequency concomitantly. However, since the metal carbonyl halides contain two separate polar sites, this can complicate the prediction of the solvent shifts.³³

Apparently, under certain conditions, the polarity of the solvent can potentially shift the carbonyl frequency of a metal carbonyl halide lower if the solute-solvent interaction on the carbonyl is the predominant influence or the carbonyl frequency can be shifted higher if the solute-solvent interaction on the metal halide is the predominant influence. By looking at the Bellamy plot, Figure 3.50, which is a plot of the antisymmetric stretching versus the symmetric stretching frequencies of $\text{CpFe}(\text{CO})_2(\text{SC}_6\text{H}_5)$ in various solvents, two lines are shown. One line represents the less polar hydrocarbon solvents with the exception of diethyl ether, and the other line represents the more polar solvents.

As indicated in Figure 3.51, there seems to be similar solvent influences on the compounds, $\text{CpFe}(\text{CO})_2\text{Cl}$, $\text{CpFe}(\text{CO})_2\text{I}$, and $\text{CpFe}(\text{CO})_2(\text{SC}_6\text{H}_5)$. The only differences in the compounds are the size and strengths of the π donor ligands. Hales has also demonstrated that a reduction in solvent sensitivity occurs if a stronger π donor replaces a weaker π donor in metal carbonyl halides, i.e. an iodide replacing a chloride.³³ Since the phenyl thiolate ligand is the strongest π donor and certainly the largest of the three ligands, it should be less

sensitive to solvent interactions than the chloride or the iodide ligands. This means that a competition between the carbonyl-solvent interaction and the iron-thiolate-solvent interaction is occurring to determine whether the carbonyl stretching frequency is going to increase or decrease. The Bellamy plot, Figure 3.50, shows that less polar hydrocarbon solvents have less influence on the carbonyl ligands of $\text{CpFe}(\text{CO})_2(\text{SC}_6\text{H}_5)$ and so the carbonyl antisymmetric stretching frequencies, which seem to be more sensitive to the solvent effects³⁰, are higher than in the more polar solvents. In the more polar solvents, tetrahydrofuran seems to effectively interact with the carbonyl ligands enough to significantly lower the carbonyl stretching frequency; however, as the polarity increases, the iron-thiolate-solvent interaction becomes more effective and increases the carbonyl stretching frequency.

In certain cases, there is a significant difference in the relative intensities of the carbonyl stretching frequencies. Cotton *et al.* has attributed these differences to a change in carbonyl-metal-carbonyl bond angles.⁵⁴ Cotton indicates that each CO oscillator can be treated as a dipole vector and the total dipole vector for the entire vibrational mode is taken to be the vector sum of the individual vectors and that the intensities are proportional to the squares of the dipole vectors.⁵⁴ For example, the intensity ratio ($I_{\text{sym}}/I_{\text{asym}}$) for the *cis*- $[\eta^5\text{-CpMo}(\text{CO})_2\text{PPh}_3\text{C}_6\text{H}_6\text{O}]^+$ complex in Figure 3.53 is 1.44 while for the *trans*- $[\eta^5\text{-CpMo}(\text{CO})_2\text{PPh}_3\text{C}_6\text{H}_6\text{O}]^+$ complex is 0.32. Using the equation 3.4, where 2θ is the OC-M-CO bond angle and I_{asym} and I_{sym} are the intensities from the asymmetric and symmetric carbonyl stretching frequencies, gives the OC-Mo-CO bond angles 79 and 121° for the *cis* and *trans* isomers, respectively.⁵⁵ This seems very reasonable since one would expect the *cis* bond angle to be significantly smaller than the *trans* bond angle.

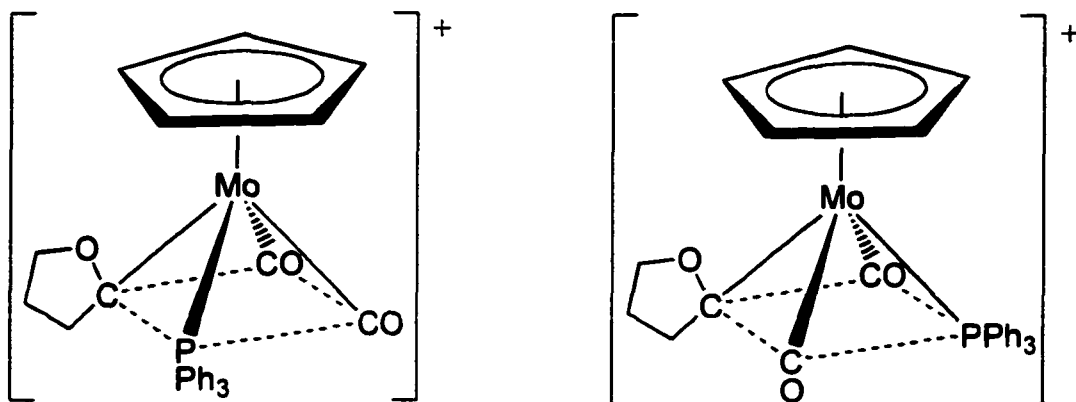


Figure 3.53. The two isomers of $[\eta^5\text{-CpMo(CO)}_2\text{PPh}_3\text{C}_6\text{H}_5\text{O}]^+$.

$$2\theta = \arctan(I_{\text{asym}}/I_{\text{sym}})^{1/2} \quad (3.4)$$

While in some cases the relative intensity of the carbonyl stretching frequencies can be attributed to differences in bond angles, the cases involved in this work where significant differences arise are due to solvent interference. In every case where there is a significant difference in intensities, there is significant overlap between the solvent stretching frequencies and the carbonyl stretching frequencies as shown in an example in Figure 3.54. In this case, a stretching frequency from THF is strongly overlapping the asymmetric carbonyl stretching frequency of $\text{CpFe(CO)}_2(\text{SC}_6\text{H}_5)$.

Another solvent interaction to discuss is the hydrogen bonding between the protic solvents, and $\text{CpFe(CO)}_2(\text{SC}_6\text{H}_5)$. As shown in Figures 3.14-3.17, the UV-vis spectra shows a decrease in intensity and wavelength which is indicative of hydrogen bonding. Another indicator is an increase in the carbonyl stretching frequency. Figures 3.30-3.32 shows a steady increase in the asymmetric stretching frequency going from the less acidic, 1-pentanol, to the more acidic, 2,2,2-trifluoroethanol. The UV-vis and IR data show that a tremendous amount of

hydrogen bonding is occurring with 2,2,2-trifluoroethanol as solvent and in fact may be the predominant species in solution according to data in Chapter 2 of this dissertation. When reacting 10 mM $\text{CpFe}(\text{CO})_2(\text{SC}_6\text{H}_5)$ with 500 mM CCl_3COOH in methylene chloride, the hydrogen bound species is the predominant species in solution with carbonyl stretching frequencies at 1995 and 2040 cm^{-1} . The carbonyl stretching frequencies for $\text{CpFe}(\text{CO})_2(\text{SC}_6\text{H}_5)$ solvated in 2,2,2-trifluoroethanol are 2005 and 2045 cm^{-1} and using Peakfit, the carbonyl stretching frequencies are 1996 and 2044 cm^{-1} .

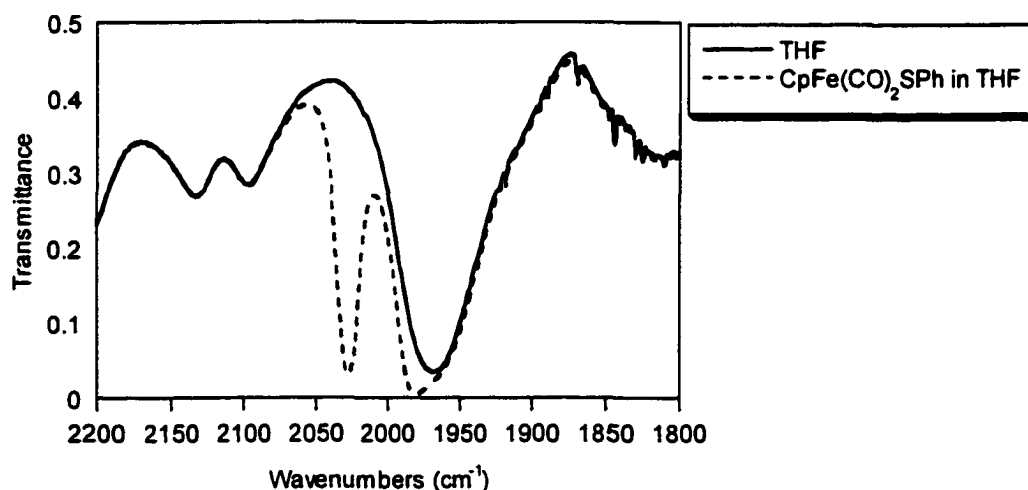


Figure 3.54. Infrared spectrum of the solvent (THF) and a 10 mM $\text{CpFe}(\text{CO})_2(\text{SC}_6\text{H}_5)$ solution in THF showing the overlap of a solvent stretching frequency and the asymmetric carbonyl stretching frequency.

3.5 Conclusions.

In summary, we have provided UV-vis evidence for the solvatochromatic behavior of $\text{CpFe}(\text{CO})_2(\text{SC}_6\text{H}_5)$ and infrared spectral evidence for other solvent effects based on carbonyl stretching frequencies. The wavelength of the LMCT band was correlated to several solvent polarity scales. The best correlations were accomplished by using the Dimroth-Reichardt's normalized energy of

transition scale, Gutmann's Acceptor Number scale, and Kosower's Z-scale (Figures 3.45-3.48).

By observing the UV-vis spectra, Figures 3.3-317, a blue shift occurs as $\text{CpFe}(\text{CO})_2(\text{SC}_6\text{H}_5)$ is solvated in more polar solvents. This is evidence that the ground-state dipole moment is greater than the excited-state dipole moment, $\mu_g > \mu_e$ as illustrated in Figure 3.2. Also, the solvatochromatic behavior of $\text{CpFe}(\text{CO})_2(\text{SC}_6\text{H}_4\text{-}p\text{-CF}_3)$ was also evidenced by UV-vis analysis (Table 3.3). It was shown that the ground-state energy of $\text{CpFe}(\text{CO})_2(\text{SC}_6\text{H}_5)$ is less stable than the ground-state energy of $\text{CpFe}(\text{CO})_2(\text{SC}_6\text{H}_4\text{-}p\text{-CF}_3)$ (Figure 3.46). It was also shown that as the solvent increases in polarity, the stability of the $\text{CpFe}(\text{CO})_2(\text{SC}_6\text{H}_4\text{-}p\text{-CF}_3)$ increases more than the $\text{CpFe}(\text{CO})_2(\text{SC}_6\text{H}_5)$ in solution.

The infrared spectral evidence showed a complex solvent effect. Since the compound, $\text{CpFe}(\text{CO})_2(\text{SC}_6\text{H}_5)$, contains two separate polar sites, this complicated the prediction of the solvent shifts. When the carbonyl ligands are interacting with the solvent, then a decrease in the carbonyl stretching frequencies is expected. However, if the π donor, such as the phenyl thiolate, is interacting with the solvent, then an increase in the carbonyl stretching frequency is expected. So there is a competition between the π accepting carbonyl ligands and the π donor phenyl thiolate ligand as to whether the carbonyl stretching frequency will increase or decrease. In either case, the carbonyl stretching frequency is solvent dependent. While in non-polar hydrocarbon solvent, it appears that the little interaction between the carbonyl ligand and the solvent occurs (Figure 3.50). When this is the case, the asymmetric carbonyl stretching frequency is higher than if polar solvent were used. Tetrahydrofuran appears to be interacting with the carbonyl ligand and therefore a low carbonyl stretching frequency was observed. However, as the solvent increases in polarity, the iron-

thiolate-solvent interaction becomes stronger and an increase in the carbonyl stretching frequency occurs.

As shown in Figure 3.51, the compound $\text{CpFe}(\text{CO})_2(\text{SC}_6\text{H}_5)$ exhibits similar solvent effects as $\text{CpFe}(\text{CO})_2\text{Cl}$ and $\text{CpFe}(\text{CO})_2\text{I}$. The only differences in the compounds are the size and strength of the π donor ligands. The ligand, which is better at π donation, lowers the carbonyl stretching frequencies, which is reflected in the lower force constants. Table 3.4 shows how the differences in the carbonyl stretching frequencies are relatively consistent going down a column. For example, the difference in the antisymmetric carbonyl stretching frequency for $\text{CpFe}(\text{CO})_2\text{Cl}$ and $\text{CpFe}(\text{CO})_2\text{I}$ dissolved in six aprotic solvents is approximately 9 cm^{-1} down the column. Perhaps this correlation can be used as a method to predict where certain carbonyl stretching frequencies should be located knowing the stretching frequency for an analogous compound.

The last solvent interaction to be mentioned is the hydrogen bonding effect between the protic solvents and $\text{CpFe}(\text{CO})_2(\text{SC}_6\text{H}_5)$. Figures 3.14-3.17 show a decrease in intensity and wavelength which is indicative of hydrogen bonding. The solvent, 2,2,2-trifluoroethanol, shows substantial hydrogen bonding according to the UV-vis and infrared spectra. The carbonyl stretching frequencies closely matches those of the hydrogen bound species that was made by reaction 10 mM $\text{CpFe}(\text{CO})_2(\text{SC}_6\text{H}_5)$ with 500 mM CCl_3COOH in methylene chloride which is discussed in Chapter 2 of this dissertation.

3.6 References.

- 1) Reichardt, C. *Solvent and Solvent Effects in Organic Chemistry*, 2nd ed.; VCH Publishers: New York, 1988.
- 2) Chen, P. and Meyer, T. J. "Medium Effects on Charge Transfer in Metal Complexes", *Chem. Rev.* **1998**, *98*, 1439-1477.
- 3) Timpson, C. J., Bignozzi, C. A., Sullivan, B. P., Kober, E. M. and Meyer, T. J. "Influence of Solvent on the Spectroscopic Properties of Cyano Complexes of Ruthenium(II)", *J. Phys. Chem.* **1996**, *100*, 2915.
- 4) Curtis, J. C., Sullivan, B. P. and Meyer, T. J. "Hydrogen-Bonding-Induced Solvatochromism in the Charge-Transfer Transitions of Ruthenium(II) and Ruthenium(III) Ammine Complexes", *Inorg. Chem.* **1983**, *22*, 224-236.
- 5) Doorn, S. K. and Hupp, J. T. "Preresonance Raman Studies of Metal-to-Ligand Charge-Transfer in $(\text{NH}_3)_4\text{Ru}(2,2'\text{-Bpy})^{2+}$: Insitu Bond Length Changes, Force Constants, and Reorganization Energies", *J. Am. Chem. Soc.* **1989**, *111*, 4704.
- 6) Reichardt, C. "Empirical Parameters of Solvent Polarity As Linear Free-Energy Relationships", *Angew. Chem., Int. Ed. Engl.* **1979**, *18*, 98-110.
- 7) Manuta, D. M. and Lees, A. J. "Solvent and Substituent Effects on the Lowest Energy Excited-States of $\text{Cr}(\text{CO})_4(\text{diimine})$; $\text{Mo}(\text{CO})_4(\text{diimine})$; $\text{W}(\text{CO})_4(\text{diimine})$ Complexes", *Inorg. Chem.* **1983**, *22*, 3825-3828.
- 8) Reichardt, C. "Solvatochromic Dyes As Empirical Indicators of Solvent Polarity", *Chimia* **1991**, *45*, 322-324.
- 9) Reichardt, C. "Solvatochromism; Thermochromism; Piezochromism; Halochromism; and Chiro-Solvatochromism of Pyridinium N-Phenoxide Betaine Dyes", *Chem. Soc. Rev.* **1992**, *21*, 147-153.
- 10) Gutmann, V. *The Donor-Acceptor Approach to Molecular Interactions*; Plenum Press: New York, 1978.

- 11) Kosower, E. M. "The Effect of Solvent on Spectra. I. A New Empirical Measure of Solvent Polarity: Z-Values", *J. Am. Chem. Soc.* **1957**, *80*, 3253-3260.
- 12) Kosower, E. M. "The Effect of Solvent on Spectra. II. Correlation of Spectral Absorption Data with Z-Values", *J. Am. Chem. Soc.* **1958**, *80*, 3261-3270.
- 13) Kamlet, M. J., Abboud, J. L. and Taft, R. W. "Solvatochromic Comparison Method .6. Pi-Star Scale of Solvent Polarities", *J. Am. Chem. Soc.* **1977**, *99*, 6027-6038.
- 14) Kamlet, M. J. and Taft, R. W. "Solvatochromic Comparison Method .1. Beta-Scale of Solvent Hydrogen-Bond Acceptor (Hba) Basicities", *J. Am. Chem. Soc.* **1976**, *98*, 377-383.
- 15) Taft, R. W. and Kamlet, M. J. "Solvatochromic Comparison Method .2. Alpha-Scale of Solvent Hydrogen-Bond Donor (Hbd) Acidities", *J. Am. Chem. Soc.* **1976**, *98*, 2886-2894.
- 16) Kirkwood, J. G. "Theory of Solutions of Molecules Containing Widely Separated Charges with Special Application to Zwitterions", *J. Chem. Phys.* **1934**, *2*, 351-361.
- 17) Bauer, E. and Magat, M. "Sur La Deformation Des Molecules En Phase Condensee Et La <<Liaison Hydrogene>>", *Journal De Physique* **1938**, *9*, 319-330.
- 18) West, W. and Edwards, R. T. "The Infrared Absorption Spectrum of Hydrogen Chloride in Solution", *J. Chem. Phys.* **1937**, *5*, 14-22.
- 19) Buckingham, A. D. "Solvent Effects in Vibrational Spectroscopy", *Trans. Faraday Soc.* **1960**, *56*, 753-760.
- 20) Reichardt, C. and Harbusch-Gornert, E. "Pyridinium N-Phenoxide Betaines and Their Application for the Characterization of Solvent Polarities. 10. Extension; Correction; and New Definition of the ET Solvent Polarity Scale by

- Application of a Lipophilic Penta-tert-Butyl -Substituted Pyridinium N-Phenoxide Betaine Dye", *Liebigs Ann. Chem.* **1983**, *5*, 721-743.
- 21) Gutmann, V. *Coordination Chemistry in Non-Aqueous Solvents*; Springer: New York, 1968.
 - 22) Gutmann, V. "Solvent Effects on Reactivities of Organometallic Compounds", *Coord. Chem. Rev.* **1976**, *18*, 225-255.
 - 23) Mayer, U. *NMR-Spectroscopic Studies on Solute-Solvent and Solute-Solute Interactions*; Elsevier: New York, 1983.
 - 24) Kosower, E. M. *An Introduction to Physical Organic Chemistry*; Wiley: New York, 1968.
 - 25) Buncl, E. and Rajagopal, S. "Solvatochromism and Solvent Polarity Scales", *Acc. Chem. Res.* **1990**, *23*, 226-231.
 - 26) Kamlet, M. J. and Taft, R. W. "Linear Solvation Energy Relationships .1. Solvent Polarity : Polarizability Effects On Infrared-Spectra", *J. Chem. Soc., Perkin Trans. 2* **1979**, *1979*, 337-341.
 - 27) Bayliss, N. S., Cole, A. R. H. and Little, L. H. "Solvent effects on the infra-red frequency and intensity of the nitrile vibration in aceto-, propio-, benzo-, and phthalo-nitriles", *Spectrochim. Acta* **1959**, *15*, 12-19.
 - 28) Parker, D. J. and Stiddard, M. H. B. "Vibrational and Electronic Spectra of Transition-metal Carbonyl Complexes. Part V. Solvent Effects on the Infrared Spectra of the Complexes $(\eta\text{-C}_5\text{H}_5)\text{Mn}(\text{CO})_3$ and $(\pi\text{-C}_6\text{Me}_6)\text{Cr}(\text{CO})_3$ ", *J. Chem. Soc. A* **1968**, 2263-2264.
 - 29) Adams, D. M. *Metal-Ligand and Related Vibrations*; St. Martins Press: New York, 1968.
 - 30) Foffani, A., Poletti, A. and Cataliotti, R. "Solvent effect on C-O and N-O stretching modes of different symmetry in transition-metal carbonyl-nitrosyls", *Spectrochim. Acta* **1968**, *24A*, 1437-1447.

- 31) Gutmann, V. "Empirical Approach to Molecular Interactions", *Coordination Chem. Rev.* **1975**, *15*, 207-237.
- 32) Horrocks Jr., W. D. and Mann, R. H. "Solvent effects on the infrared frequency of inorganic carbonyl and nitrosyl bands", *Spectrochim. Acta* **1965**, *21*, 399-408.
- 33) Hales, L. A. and Irving, R. J. "Solvent effects in the infra-red for some osmium carbonyl halide compounds", *Spectrochim. Acta* **1967**, *23A*, 2981-2987.
- 34) Bellamy, L. J. and Williams, R. L. "Infra-red Spectra and Solvent Effects", *Trans. Faraday Soc.* **1958**, *55*, 14-18.
- 35) El-Sayed, M. A. and Kaesz, H. D. "Infrared Spectra and Structure of the Tetracarbonyl Halide Dimers of Manganese, Technetium, and Rhenium", *Inorg. Chem.* **1962**, *2*, 158-162.
- 36) King, R. B. "A Novel Synthesis of the Hexafluorophosphate of the Cyclopentadienyliron Tricarbonyl Cation", *Inorg. Chem.* **1962**, *1*, 964-965.
- 37) Piper, T. S., Cotton, F. A. and Wilkinson, G. "Cyclopentadienyl-Carbon Monoxide and Related Compounds of Some Transitional Metals", *J. Inorg. Nucl. Chem.* **1955**, *1*, 165.
- 38) Hallam, B. F. and Pauson, P. L. "Ferrocene Derivatives. Part III. cyclopentadienyliron Carbonyls.", *J. Chem. Soc.* **1956**, *159*, 3030-3037.
- 39) Bayliss, N. S. and McRae, E. G. "Solvent Effects in Organic Spectra: Dipole Forces and the Franck-Condon Principle", *J. Phys. Chem.* **1954**, *58*, 1002.
- 40) Streck, R. and Barnes, A. J. "Solvent effects on infrared ; C-13 and P-31 NMR spectra of trimethyl phosphate : Part 1. Single solvent systems", *Spectrochim. Acta, Part A* **1999**, *55*, 1049-1057.
- 41) Drago, R. S. *Physical Methods for Chemists*; 2nd ed.; Saunders College Publishing: New York, 1992.

- 42) Mushtaq, A., Bruce, R. and Knox, G. R. "Hydrocarbon Metal Sulphide Complexes I. Cyclopentadienylcarbonyliron Mercaptides", *J. Organometal. Chem.* **1966**, *6*, 1-10.
- 43) Creaser, C. S., Fey, M. A. and Stephenson, G. R. "Environment Sensitivity of Ir-Active Metal-Carbonyl Probe Groups", *Spectrochim. Acta Part A* **1994**, *50*, 1295-1299.
- 44) Ashby, M. T., Enemark, J. H. and Lichtenberger, D. L. "Destabilizing $d\pi$ - $p\pi$ Orbital Interactions and the Alkylation Reactions of Iron(II) Thiolate Complexes", *Inorg. Chem.* **1988**, *27*, 191-197.
- 45) Nyquist, R. A. and Luoma, D. A. "Infrared Study of Tetraalkylurea in Carbon-Tetrachloride and or Hexane and in Chloroform and or Hexane 1-Percent Solutions", *Appl. Spectrosc.* **1991**, *45*, 1497-1500.
- 46) Nyquist, R. A. and Luoma, D. A. "Infrared Study of Tetraalkylureas in Dilute-Solutions", *Appl. Spectrosc.* **1991**, *45*, 1491-1496.
- 47) Nyquist, R. A., Luoma, D. A. and Putzig, C. L. "Vibrational Study of Alkyl Isocyanates in Solution", *Appl. Spectrosc.* **1992**, *46*, 972-980.
- 48) Kolling, O. W. "Re-examination of the effect of aprotic solvents upon the fundamental vibrational peak of the carbonyl group in 1; 1; 3; 3-tetramethylurea", *Appl. Spectrosc.* **1999**, *53*, 29-32.
- 49) Ikram, M., Rauf, M. A. and Jabeen, Z. "Solvent Effects On the Si-Cl Stretching Bands of Dimethyldichlorosilane By IR Spectroscopy", *Spectrochim. Acta Part A* **1993**, *49*, 939-945.
- 50) Rauf, M. A., Ikram, M., Bhatti, M. H. and Jabeen, Z. "Solvent effects on Si-Cl stretching vibrations of trimethylchlorosilane methyltrichlorosilane and diphenyldichlorosilane", *J. Chem. Soc. Pakistan* **1996**, *18*, 105-109.
- 51) Wohar, M. M., Seehra, J. K. and Jagodzinski, P. W. "Correlation Between Solvent-Induced Vibrational Frequency-Shifts of the C=O Moiety and Solvent

Electron-Acceptor Numbers : Tetramethylurea", *Spectrochim. Acta Part A* **1988**, *44*, 999-1006.

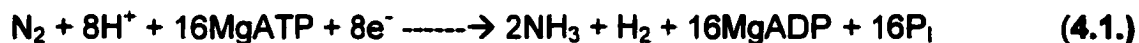
- 52) Bor, G. "Solvent-effect studies on the infra-red spectra of metal carbonyls", *Spectrochim. Acta* **1962**, *18*, 817-822.
- 53) Barraclough, C. C., Lewis, J. and Nyholm, R. S. "Solvent Shifts in the Infrared Spectral of Metal Carbonyls and Their Derivatives", *J. Chem. Soc.* **1961**, 2582-2584.
- 54) Cotton, F. A. and Wilkinson, G. *Advanced Inorganic Chemistry: A Comprehensive Text*, 4th ed.; Wiley: New York, 1980.
- 55) Cotton, F. A. and Lukehart, C. M. "Complexes of Cyclic 2-Oxacarbenes. I. A Spontaneous Cyclization to Form a Complex of 2-Oxacyclopentylidene.", *J. Am. Chem. Soc.* **1971**, *93*, 2672-2676.

**Chapter 4 ELECTRONIC, CHEMICAL, AND STRUCTURAL STUDIES
OF CpFe(dppe)(SC₆H₄-p-Z) WHERE Z = OCH₃, H, Cl, CF₃,
NO₂**

4.1 Introduction and Background

Thiolate ligands are ubiquitous in bioinorganic chemistry. Two vitally important biological enzymes that contain iron-thiolate active centers are nitrogenase and hydrogenase.

Nitrogenase is involved in the net reduction of molecular nitrogen to ammonia as shown in Equation 4.1.1.² Nitrogenase is made up of two proteins, Fe-protein and MoFe-protein.^{3,4} The Fe-protein is a dimer of identical subunits containing one [4Fe-4S]-cluster which binds the subunits and also functions as a one-electron donor. The coordination of the [4Fe-4S] cluster within the protein matrix is through the use of S atoms of cysteines as confirmed by X-ray structural analysis.⁵ The main function of the Fe-protein is the MgATP driven one-electron transfer to the large MoFe-protein.



The MoFe-protein contains the center of substrate binding and reduction.⁶ The MoFe-protein consist of P-clusters which are four [4Fe-4S]-clusters and FeMo (or FeV or Fe-only) -cofactors. A proposed FeMo-cofactor structure in nitrogenase MoFe-proteins is shown in Figure 4.1.⁷

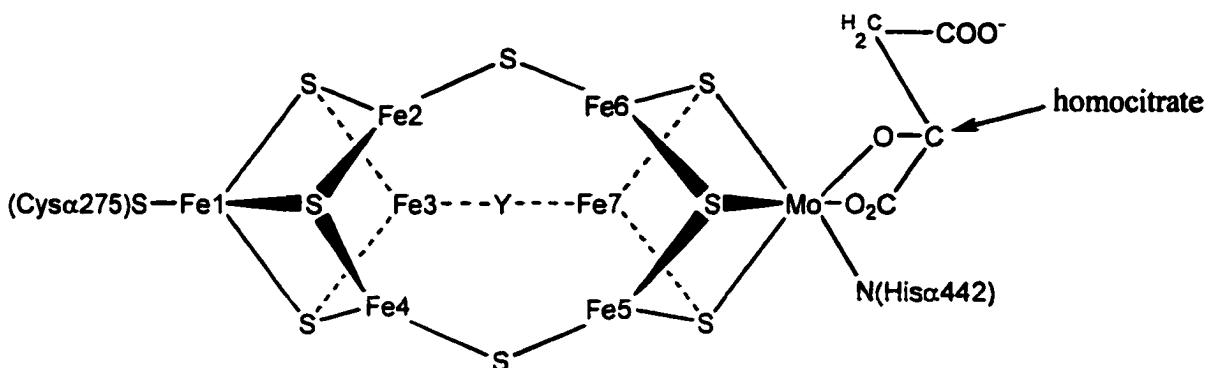


Figure 4.1. Proposed FeMo-cofactor structure in nitrogenase MoFe-proteins where Y is most likely sulfur.⁸

The mechanism by which the reduction of dinitrogen takes place is still under investigation. The first step in the mechanism is the binding of the substrate.⁹ There are three proposed methods of binding the substrate. 1) The nitrogen may bind in an end-on fashion to one of six central three-coordinate iron sites. Such bonding involves synergistic 'back-donation' from the metal to stabilize the metal-N₂ interaction, which can allow reactivity on the N₂ ligand^{10,11} (Figure 4.2). 2) The molecules, N₂ or H₂, could occupy the central cavity in the FeMo-cofactor, thereby replacing weak iron-iron bonds with Fe-substrate bonds. 3) The nitrogen may bind to the Mo center after dissociation of the endogeneous homocitrate ligand.^{8,12}

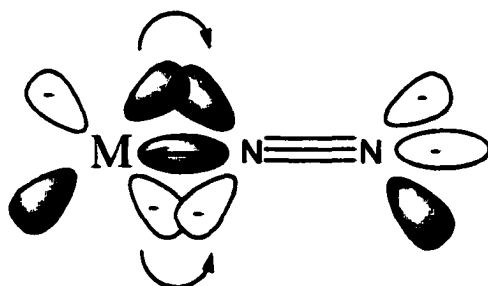


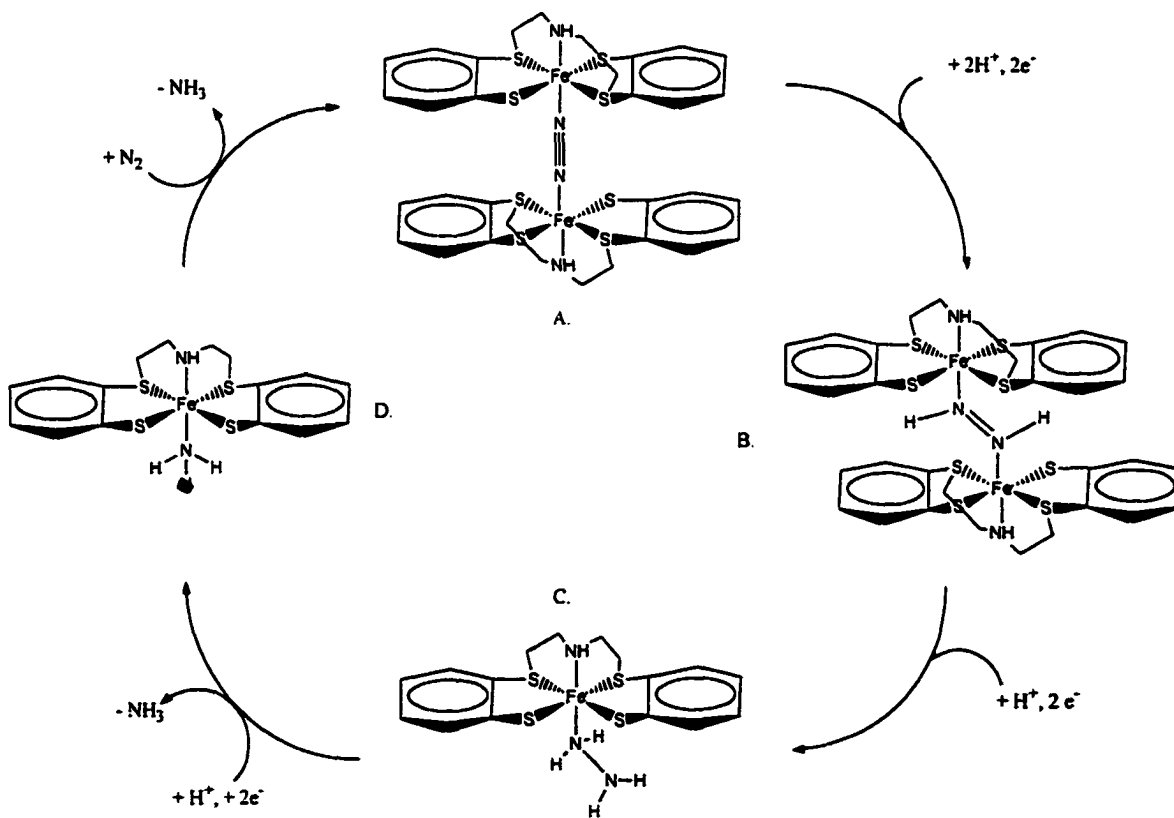
Figure 4.2. End-on metal-dinitrogen bonding.³

A number of model systems have been developed to study the mechanism; however, none of the synthetic chemical systems are truly catalytic.^{12,13} Dinitrogen has been found to be reduced to NH₃ at certain Mo, V, or Fe phosphine-ligated centers but none of the reactions were catalytic.^{9,14} Some models rely on the fact that nitrogenase reduces not only N₂ but a variety of other substrates such as N₂O (to N₂ + H₂O), C₂H₂ (to C₂H₄), H₂NCN (to NH₃ + CH₃NH₂), cyclo-C₃H₄ (to cyclo-C₃H₆), and cyclo-CH₂N₂ (CH₃NH₂ + NH₃).¹⁵ Leigh *et al.* used the compound [FeH(H₂)(dmpe)₂][BPh₄] (dmpe = Me₂PCH₂CH₂PMe₂) as a model system for nitrogenase to reduce 1,1-dimethylallene and allene. The propylene analogues were produced so reduction did take place but the reaction was stoichiometric and not catalytic.¹⁵ A number of other iron-phosphine compounds have been prepared and fully characterized that can either fix or reduce dinitrogen.¹⁴ These include [CpFe(dmpe)((CH₃)₂CO)]BF₄ (dmpe = Me₂PCH₂CH₂PMe₂)¹⁶, which can fix nitrogen under inert conditions, [FeH(THF)(dppe)₂]⁺¹⁷, which can fix atmospheric nitrogen, and (Ph₃P)₂FeCl₃¹⁸, which reduces dinitrogen to hydrazine albeit at very low yields.

Sellmann *et al.* have proposed a mechanism to reduce dinitrogen to ammonia using a model system containing an iron-thiolate complex (Scheme 4.1).¹² They have isolated and obtained an X-ray crystal structure of compound B and have fully characterized compounds C and D; however, compound B formed in very low yields and there were major solubility problems.¹⁹ A number of other metal-thiolate complexes have been synthesized as model systems for nitrogenase and hydrogenase and most of them contain additional phosphine ligands.^{13,20}

Since native FeMo cofactor of FeMo nitrogenase is short-lived in aqueous media and does not catalyze N₂ reduction outside of its native environment, attempts to understand the principles of reduction, instead of using only the

blueprints of the structure, have been used to find a competitive catalyst.¹³ To assist in understanding the mechanism of nitrogenase, each of the "ideal" model systems should produce not only ammonia but also molecular hydrogen since nitrogenase catalyzes one H₂ for every N₂ reduced.^{9,21} The catalytic model should exhibit sulfur-rich ligands, vacant sites, Brønsted acid-base properties, and redox activities.¹³ Obviously, the electronic, reactivity, and structural studies of iron-thiolates are extremely important in finding a suitable model system for nitrogenase.



Scheme 4.1. A model cycle of N₂ fixation by [Fe('N_HS₄')] fragments.

Since hydrogen evolution is a consequence of the activity of nitrogenase, some organisms possess genes for the uptake hydrogenase.⁹ Hydrogenase is

involved in the reduction of H^+ and the oxidation of molecular hydrogen as shown in Equation 4.2.^{22, 23} There are four general types of hydrogenases: 1) [Ni-Fe] hydrogenases, 2) Fe-only hydrogenases, 3) [Ni-Fe-Se] hydrogenases, and 4) one that does not contain transition metals.²⁴⁻²⁷ With the exception of the hydrogenase that does not contain bound transition metals, all of the known general types of the hydrogenases contain iron-sulfur clusters and other metal-thiolate bonds.



The active site of the [NiFe] hydrogenase *Desulfovibrio gigas* contains a bimetallic center comprised of nickel and iron coordinated by two bridging cysteinyl ligands and possibly a bridging oxo or hydroxo ligand (Figure 4.3).²⁸ The [NiFe] hydrogenase also contains two [4Fe-4S] clusters and one [3Fe-4S] cluster as determined by X-ray crystallographic analysis.²⁹

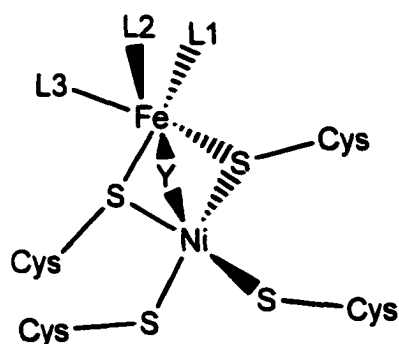


Figure 4.3. The bimetallic center of the [NiFe] hydrogenase *Desulfovibrio gigas*. where Y is possibly oxo or hydroxo ligand, L1 and L2 could be cyanides and L3 is possibly carbon monoxide.²⁸

The three diatomic ligands bound to the iron (L1, L2, and L3) shown in Figure 4.3 could be cyanides and possibly carbon monoxide.³⁰ These diatomic ligands are infrared active and the frequencies shift their position in a concerted fashion depending on the redox state of the enzyme. The frequency shifts suggest a redox role for the Fe center during catalysis.^{29,31}

The Fe-only hydrogenase contains five iron-sulfur clusters. The active-site cluster or H-cluster (HC) (Figure 4.4) contains two subclusters as determined by X-ray crystallographic analysis.³²⁻³⁴ One of the subclusters is a [4Fe-4S] cubane cluster and the other is a [2Fe-2S] cluster which contains one water molecule and five carbon monoxide/cyanide ligands. The other four clusters, which are involved with electron transport, are three [4Fe-4S] clusters and one [2Fe-2S] cluster. All of the iron-sulfur clusters are coordinated to the protein by cysteinate ligands.

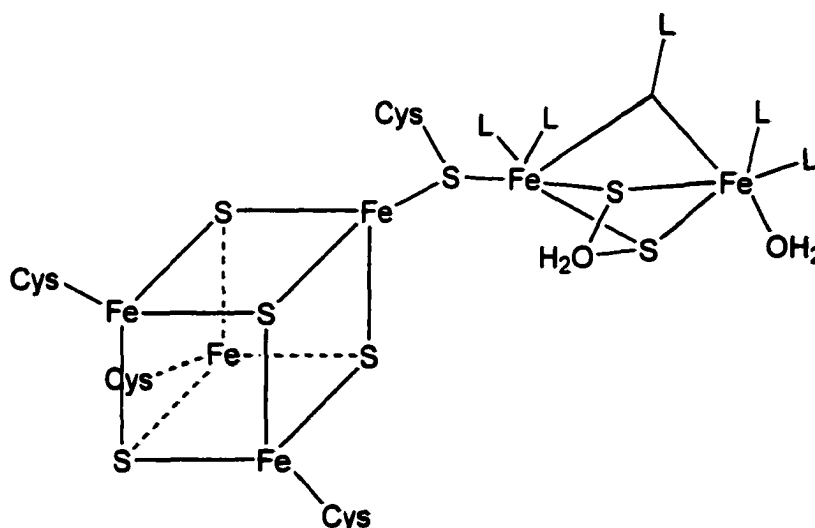


Figure 4.4. The active-site of the Fe-only hydrogenase which contains two subclusters. L represents possible CO and CN ligands.³⁵

A mechanism by which the [NiFe] or Fe-only hydrogenase reduces proton or oxidizes molecular hydrogen is still under investigation.^{24,27} A number of model systems for hydrogenase have been used to study their vibrational spectroscopy, structure, and reactivity to gain insight to the potential mechanisms by which a proton can be reduced or molecular hydrogen can be oxidized.

Darensbourg *et al.* have synthesized $(\text{CO})_3\text{Fe}(\mu\text{-S}_2(\text{CH}_2)_3)\text{Fe}(\text{CO})_3$ as a potential model of the Fe-only hydrogenase active site.³⁶ One of their goals was to develop the background for the use of infrared spectroscopy in the study of hydrogenases. Darensbourg *et al.* have already prepared the potassium salt of $[\text{CpFe}(\text{CO})(\text{CN})_2]^-$ which closely matches the infrared properties to those of the $\text{Fe}(\text{CO})(\text{CN})_2$ site in [NiFe] hydrogenases isolated from *Desulfovibrio vulgaris*.^{37,38}

Liaw *et al.* have synthesized the first dinuclear Fe(II)-thiolate cyanocarbonyl compound, $[\text{PPN}]_2[(\text{CN})(\text{CO})_2\text{Fe}(\mu\text{-S,S-C}_6\text{H}_4)]_2$, which may be regarded as a spectroscopic reference for Fe-only hydrogenase.³⁹ They have determined that the infrared frequencies of this compound are similar in range to the stretching frequencies obtained from the Fe-only hydrogenase³⁰. The compound, $[\text{Fe}^{\text{II}}(\text{PS}_3)(\text{CO})(\text{CN})]^{2-}$ (Figure 4.5.), was prepared by Hsu *et al.* and analyzed by X-ray crystallography and both the Fe(II) and Fe(III) complexes were analyzed by infrared spectroscopy.⁴⁰ They determined that the redox induced shifts in the stretching frequencies of CO ($\nu_{\text{CO}} = 102 \text{ cm}^{-1}$) and CN ($\nu_{\text{CO}} = 29 \text{ cm}^{-1}$) indicates the magnitude of the shifts that could be expected for a redox change in similar $\text{Fe}(\text{CO})(\text{CN})_2$ centers in hydrogenases. Hsu *et al.* have suggested that the changes in the stretching frequencies of [NiFe] hydrogenase could be due to: (a) changes in oxidation states of the iron center, (b) changes in electron density on the iron center caused by changes in the redox state of the

nickel center and/or (c) changes in the ligation of the iron center (i.e., the Y ligand, Figure 4.3).⁴⁰

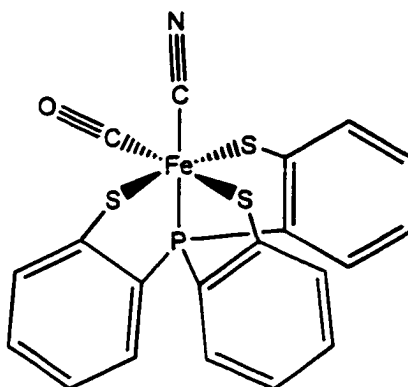
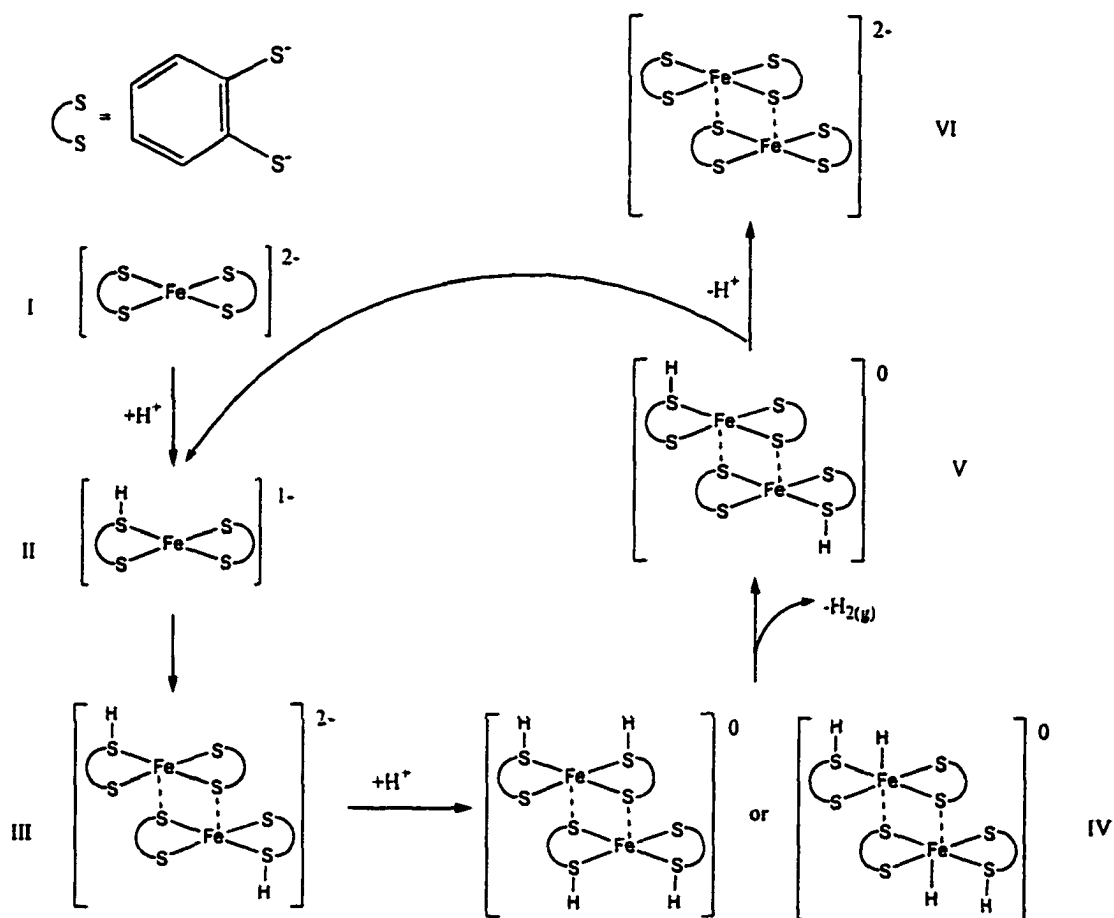


Figure 4.5. Structure of $[\text{Fe}(\text{PS}_3)(\text{CO})(\text{CN})]^{2-}$ synthesized by Hsu *et al.* as a model system for hydrogenase.

An important consideration in the mechanism of hydrogenase is the site of protonation. Sellmann *et al.* have synthesized a model compound to react with proton to obtain molecular hydrogen (Scheme 4.2).⁴¹ Apparently, the HOMO is primarily sulfur in character in complex I as shown in Scheme 4.2 since protonation occurs on a sulfur site forming the coordinated thiol complex II. Going from complex III to complex IV, the electron-rich sulfur or the coordinatively unsaturated iron is a potential site for the second protonation. Theoretical calculations were carried out by Sellmann *et al.* for the evolution of hydrogen at transition-metal sulfur centers for mononuclear bis(dithiolenes) and they showed that elimination of H₂ from a metal hydride species is more favorable than a concerted H₂ elimination from a dithiol species.⁴¹



Scheme 4.2. Potential mechanism for the protonation and formation of molecular hydrogen.

Most model complexes for hydrogenases contain predominantly phosphines in the coordination sphere of the metal with very few exceptions.⁴² These exceptions include the following compounds that exhibit exclusively sulfur ligands such as $[\text{Ir}(\text{H})(1,4,7\text{-trithiacyclononane})_2](\text{PF}_6)_2$ ⁴³, $[\text{Rh}(\text{H})(1,4,8,11\text{-tetrathiacyclotetradecane})](\text{BF}_4)$ ⁴⁴, and $[\text{Li}(\text{THF})_4]_3[\text{Mo}(\text{H})(\text{S}_2\text{C}_6\text{H}_4)_3]$ ⁴⁵; however,

these do not undergo H_2/D^+ exchange through heterolytic cleavage of H_2 as would be expected from a model system for hydrogenase. Notice that none of these complexes contain biologically relevant metals for modeling hydrogenase; however, Sellmann *et al.* have recently synthesized the complex, $[Ni(NHPnPr_3)(S_3)]$ ($S_3 = \text{bis}(2\text{-sulfanylphenyl})\text{sulfide}^{2-}$) shown in Figure 4.6., which does undergo H_2/D^+ exchange when the compound is treated with D_2 at slightly elevated pressures (10 bar).⁴⁶ Using this complex as the model system for $[NiFe]$ hydrogenase, Sellmann has assumed that H_2 activation occurs at the nickel-thiolate site instead of the iron-thiolate site.

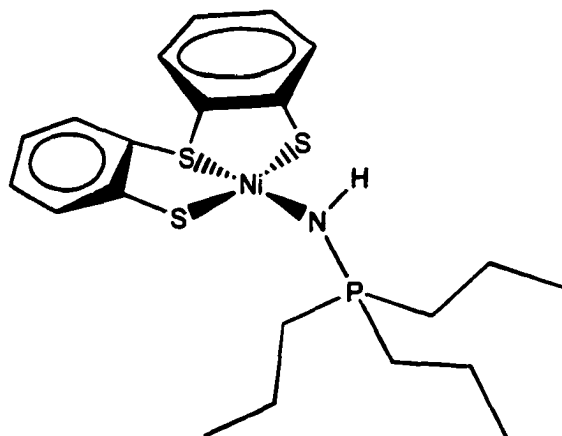


Figure 4.6. The first nickel complex with predominantly sulfur ligands, which serves as a model for $[FeNi]$ hydrogenase, that undergoes H_2/D^+ exchange at the nitrogen site.⁴⁶

This chapter concerns the study of the electron-rich iron-thiolate complexes, $CpFe(dppe)(SC_6H_4-p-Z)$ where $Z = OCH_3, H, Cl, CF_3$ and NO_2 ($dppe = Ph_2PCH_2CH_2PPh_2$). Treichel stated that upon addition of a protic acid to $CpFe(dppe)(SC_6H_5)$ gives an oxidized Fe product and molecular hydrogen.⁴⁷ If

this is the case, then this would provide a model for hydrogenase and a way to determine a possible mechanism for the formation of molecular hydrogen from proton.

In this work, three goals were established to investigate possible mechanisms for H₂(g) production and also to study the electronic effects on the iron and sulfur atoms upon perturbing the sulfur site in electron rich iron-thiolate complexes. The first goal is to determine whether H₂(g) evolution takes place when CpFe(dppe)(SC₆H₅) or CpFe(P₂S) reacts with HBF₄·O(CH₃)₂ and then determine possible mechanisms. The second goal is to determine the oxidation potentials of the compounds, CpFe(dppe)(SC₆H₄-*p*-Z) where Z = OCH₃, H, Cl, CF₃, and NO₂, and also to react these compounds with CH₃I to determine how Z effects the rate of methylation by using cyclic voltammetry and UV-vis spectroscopy, respectively. The third goal is to determine whether the lone electron in the HOMO of [CpFe(dppe)(SC₆H₄-*p*-Z)]BF₄ resides primarily on the metal or sulfur by using electron paramagnetic resonance spectroscopy and running density functional calculations on the following compounds: CpFe(PH₃)₂(SCH₃) and [CpFe(PH₃)₂(SCH₃)]⁺.

4.2 Experimental Section

All reactions were performed under an atmosphere of prepurified nitrogen or argon using Schlenk technique or a MO-40M VAC Dry Box unless stated otherwise. Solvents were distilled from appropriate drying agents under nitrogen and degassed by freeze pump thawing three times prior to use unless stated otherwise: CH₂Cl₂ (CaH₂), pentane (Na), THF(Na), methanol (Mg). [CpFe(dppe)(NCCH₃)]Br,⁴⁸ CpFe(dppe)I,^{48,49} P₂SH (2,2-bis[(diphenylphosphanyl)methyl]-1-propanethiol),⁵⁰ [CpFe(CO)₂(NCCH₃)]PF₆,⁵¹ and CpFe(dppe)(SC₆H₅)⁴⁸ were prepared by literature method. HBF₄·O(CH₃)₂

was purchased from Aldrich Chemical Company and used as received. Infrared spectra were recorded on a Bruker IFS 66/S FTIR spectrometer. ^1H NMR spectra were obtained from a Varian 400MHz spectrometer. UV-vis spectra were recorded on a Hewlett-Packard HP8453 Diode Array instrument. The kinetic data, which was recorded by UV-vis spectroscopy, was analyzed by the SPECFIT/32 computer program.⁵² A Schlenk quartz cell with a 1.0 cm pathlength and a side arm was employed in the UV-vis spectroscopy experiments.

Electron paramagnetic resonance spectra were recorded on a Bruker ESP 300 equipped with a 4102st.cal cavity resonator. Cyclic Voltammetry experiments were performed by the BAS CV-50W Voltammetric Analyzer utilizing glassy carbon working, Ag/AgNO₃ reference, and silver auxiliary electrodes. All kinetic and cyclic voltammetric experiments were conducted under inert atmosphere. Elemental analysis were carried out by Midwest Microlab.

4.2.1 Preparation of CpFe(dppe)(SC₆H₄-*p*-OCH₃).

To dry methanol (60 mL) was added HSC₆H₄-*p*-OCH₃ (4.49 mL, 36.52 mmol) and KOH (0.78 g, 0.013 mol) and the solution was stirred until the KOH dissolved. [CpFe(dppe)(NCCH₃)]Br (2.0 g, 3.12 mmol) was added and the resulting solution was refluxed for 25 minutes under argon. The solution was allowed to cool to room temperature. Dark crystals that precipitated out of solution were filtered off and washed with dry methanol. The olive green compound was dried *in vacuo* overnight to give CpFe(dppe)(SC₆H₄-*p*-OCH₃) (1.80 g, 2.73 mmol, 86% yield). It was stored in a dry box under nitrogen. ^1H NMR (CD₂Cl₂): δ 7.91 – 7.13 (m, Ph), 6.51 (d, C₆H₄), 6.24 (d, C₆H₄), 4.06 (s, Cp), 3.64 (s, CH₃), 2.61 (br.s, CH₂) 2.28 (br.s, CH₂). ^{31}P NMR (CD₂Cl₂): δ 97.44 (br.s, diphos). Anal. Calcd for C₃₈H₃₆FeOP₂S: C, 69.31; H, 5.51. Found: C, 69.13; H, 5.62.

The identity of the product was also confirmed by a single-crystal X-ray crystallographic analysis (Figure 4.29). A suitable crystal for structure determination was obtained by evaporation of a saturated CH₂Cl₂ solution under nitrogen overnight.

4.2.2 Preparation of CpFe(dppe)(SC₆H₄-*p*-Cl).

To dry methanol (60 mL) was added HSC₆H₄-*p*-Cl (1.6 g, 11.07 mmol) and KOH (0.78 g, 0.013 mol) and the solution was stirred until the KOH dissolved. [CpFe(dppe)(NCCH₃)]Br (2.0 g, 3.12 mmol) was added and the resulting solution was refluxed for 25 minutes under argon. The solution was allowed to cool to room temperature. Dark green crystals that precipitated out of solution were filtered off and washed with dry methanol. The brown green compound dried *in vacuo* overnight to give CpFe(dppe)(SC₆H₄-*p*-Cl) (1.34 g, 2.02 mmol, 65% yield). ¹H NMR (CD₂Cl₂): δ 7.82 – 7.14 (m, Ph), 6.53 (m, C₆H₄), 4.15 (s, Cp), 2.63 (br.s, CH₂) 2.24 (br.s, CH₂). ³¹P NMR (CD₂Cl₂): δ 97.56 (br.s, diphos). Anal. Calcd for C₃₇H₃₃ClFeP₂S: C, 67.03; H, 5.02. Found: C, 67.01; H, 5.22.

4.2.3 Preparation of CpFe(dppe)(SC₆H₄-*p*-CF₃).

To dry methanol (60 mL) was added HSC₆H₄-*p*-CF₃ (2.00 g, 11.24 mmol) and KOH (0.78 g, 0.013 mol) and the solution was stirred until the KOH dissolved. [CpFe(dppe)(NCCH₃)]Br (2.0 g, 3.12 mmol) was added and the resulting solution was refluxed for 25 minutes under argon. The solution was allowed to cool to room temperature. Dark green crystals that precipitated out of solution were filtered off and washed with dry methanol. The olive green compound was dried *in vacuo* overnight to give CpFe(dppe)(SC₆H₄-*p*-CF₃) (1.64 g, 2.36 mmol, 75% yield). ¹H NMR (CD₂Cl₂): δ 7.76 – 7.18 (m, Ph), 6.79 (d, C₆H₄), 6.72 (d, C₆H₄), 4.26 (s, Cp), 2.68 (br.s, CH₂) 2.23 (br.s, CH₂). ³¹P NMR (CD₂Cl₂): δ 96.93 (br.s, diphos). Anal. Calcd for C₃₈H₃₃F₃FeP₂S: C, 65.53; H, 4.78. Found: C, 64.82; H, 4.93.

4.2.4 Preparation of CpFe(dppe)(SC₆H₄-p-NO₂).

To dry methanol (60 mL) was added HSC₆H₄-p-NO₂ (1.71 g, 11.02 mmol) and KOH (0.78 g, 0.013 mol) and the solution was stirred until the KOH dissolved. [CpFe(dppe)(NCCH₃)]Br (2.0 g, 3.12 mmol) was added and the resulting solution was refluxed for 25 minutes under argon. The solution was allowed to cool to room temperature. Dark blue crystals that precipitated out of solution were filtered off and washed with dry methanol. The blue compound was dried *in vacuo* overnight to give CpFe(dppe)(SC₆H₄-p-NO₂) (1.96 g, 2.91 mmol, 93% yield). ¹H NMR (CD₂Cl₂): δ 7.68 – 7.21 (m, Ph), 6.80 (m, C₆H₄), 4.32 (s, Cp), 2.63 (br.s, CH₂) 2.21 (br.s, CH₂). ³¹P NMR (CD₂Cl₂): δ 95.09 (br.s, diphos). UV-vis absorption spectrum (CH₂Cl₂); [λ_{max}, nm (ε, M⁻¹ cm⁻¹): 544(9082) Anal. Calcd for C₃₇H₃₃FeNO₂P₂S: C, 65.98; H, 4.94. Found: C, 65.10; H, 4.96.

The identity of the product is confirmed by a single-crystal X-ray crystallographic analysis (Figure 4.33). A suitable crystal for structure determination was obtained by slow vapor diffusion of pentane in a saturated THF solution.

4.2.5 Alternative Preparation of [CpFe(dppe)(SC₆H₅)]BF₄.^{47,53}

To a 20 mL THF solution of CpFe(dppe)(SC₆H₅) (49 mg, 0.08 mmol) was added ferrocenium tetrafluoroborate (22 mg, 0.08 mmol). The color of the solution immediately changed from brown/green to blue. The mixture was stirred for one hour. The product was precipitated by adding dry pentane. The product was filtered using a Schlenk filter frit and washed with dry benzene. The dark blue compound, which was dried *in vacuo* overnight to give [CpFe(dppe)(SC₆H₅)]BF₄ (52 mg, 0.07 mmol, 88% yield), was stored in a dry box under nitrogen. UV-vis absorption spectrum (CH₂Cl₂); [λ_{max}, nm (ε, M⁻¹ cm⁻¹): 580(2050) (Figure 4.8). FAB Mass Spec. 628.

The identity of the product was also confirmed by a single-crystal X-ray crystallographic analysis (Figure 4.35). A suitable crystal for structure determination was obtained by slow vapor diffusion of pentane in a saturated THF solution.

4.2.6 Preparation of [CpFe(dppe)(SC₆H₄-*p*-OCH₃)]BF₄.

To a THF (20 mL) solution of CpFe(dppe)(SC₆H₄-*p*-OCH₃) (79 mg, 0.12 mmol) was added ferrocenium tetrafluoroborate (27 mg, 0.10 mmol). The color of the solution immediately changed from brown/green to red. The mixture was stirred for one hour. The product was precipitated by adding dry pentane. The product was filtered using a Schlenk filter frit and washed with dry benzene. The red compound was dried *in vacuo* overnight to give [CpFe(dppe)(SC₆H₄-*p*-OCH₃)]BF₄ (66 mg, 0.09 mmol, 90% yield). It was stored in a dry box under nitrogen. UV-vis absorption spectrum (CH₂Cl₂); [λ_{\max} , nm (ϵ , M⁻¹ cm⁻¹)]: 644(1754), 578(1757) (Figure 4.8). Anal. Calcd for C₃₈H₃₆FeOP₂SBF₄: C, 61.23; H, 4.87. Found: C, 59.57; H, 4.75.

4.2.7 Preparation of [CpFe(dppe)(SC₆H₄-*p*-Cl)]BF₄.

To a THF (20 mL) solution of CpFe(dppe)(SC₆H₄-*p*-Cl) (80 mg, 0.12 mmol) was added ferrocenium tetrafluoroborate (27 mg, 0.10 mmol). The color of the solution changed from brown/green to blue. The mixture was stirred for one hour. The product was precipitated by adding dry pentane. The product was filtered using a Schlenk filter frit and washed with dry benzene. The blue compound was dried *in vacuo* overnight to give [CpFe(dppe)(SC₆H₄-*p*-Cl)]BF₄ (71 mg, 0.09 mmol, 90% yield). It was stored in a dry box under nitrogen. UV-vis absorption spectrum (CH₂Cl₂); [λ_{\max} , nm (ϵ , M⁻¹ cm⁻¹)]: 580(2099) (Figure 4.8). Anal. Calcd for C₃₇H₃₃ClFeP₂SBF₄: C, 59.21; H, 4.40. Found: C, 59.46; H, 4.52.

4.2.8 Preparation of [CpFe(dppe)(SC₆H₄-*p*-CF₃)]BF₄.

To a THF (20 mL) solution of CpFe(dppe)(SC₆H₄-*p*-CF₃) (84 mg, 0.12 mmol) was added ferrocenium tetrafluoroborate (27 mg, 0.10 mmol). The color of the solution changed from brown/green to blue. The mixture was stirred for one hour. The product was precipitated by adding dry pentane. The product was filtered using a Schlenk filter frit and washed with dry benzene. The blue compound was dried *in vacuo* overnight to give [CpFe(dppe)(SC₆H₄-*p*-CF₃)]BF₄ (71 mg, 0.09 mmol, 90% yield). It was stored in a dry box under nitrogen. UV-vis absorption spectrum (CH₂Cl₂); [λ_{\max} , nm (ϵ , M⁻¹ cm⁻¹)]: 570(2247) (Figure 4.8). Anal. Calcd for C₃₈H₃₃BF₇FeOP₂S: C, 58.27; H, 4.25. Found: C, 58.31; H, 4.29.

4.2.9 Preparation of [CpFe(dppe)(SC₆H₄-*p*-NO₂)]BF₄.

To a THF (20 mL) solution of CpFe(dppe)(SC₆H₄-*p*-NO₂) (81 mg, 0.12 mmol) was added ferrocenium tetrafluoroborate (27 mg, 0.10 mmol). The color of the solution changed from blue to dark blue. The mixture was stirred for one hour. The product was precipitated by adding dry pentane. The product was filtered using a Schlenk filter frit and washed with dry benzene. The dark blue compound was dried *in vacuo* overnight to give [CpFe(dppe)(SC₆H₄-*p*-NO₂)]BF₄ (63 mg, 0.08 mmol, 80% yield). It was stored in a dry box under nitrogen. UV-vis absorption spectrum (CH₂Cl₂); [λ_{\max} , nm (ϵ , M⁻¹ cm⁻¹)]: 570(2521) (Figure 4.8). Anal. Calcd for C₃₇H₃₃FeO₂NP₂SBF₄: C, 58.45; H, 4.37. Found: C, 57.49; H, 4.42.

4.2.10 Preparation of [CpFe(P₂S)]PF₆.

To a THF (50 mL) solution of the tripodal ligand P₂SH (0.410 g, 87 mmol) was slowly added NaH (20.80 mg, 87 mmol) under argon. The mixture stirred for two hours. [CpFe(CO)₂(CH₃CN)]PF₆ (0.315 g, 87 mmol) was added to a 1000 mL photolytic reaction vessel under argon followed by THF (850 mL). The THF

solution of the tripodal ligand (P_2SNa) was slowly added to the reaction vessel. The color changed from yellow to pale brown. Irradiating the solution with a 450 watt Hanovia mercury discharge lamp contained in a water-cooled quartz immersion well for 30 minutes produced a color change from pale brown to green/brown which turned pink upon exposure to air. The solvent was removed from the filtrate under vacuum. The pink residue was chromatographed using THF as eluent. The solvent was reduced and pentane was added to precipitate the corresponding complex $[CpFe(P_2S)]PF_6$. (298 mg, 0.41 mmol, 47% yield) UV-vis absorption spectrum (THF); $[\lambda_{max}, nm (\epsilon, M^{-1} cm^{-1})]$: 530(1520) (Figure 4.8). Anal. Calcd for $C_{34}H_{34}FeP_2SPF_6$: C, 55.37; H, 4.65. Found: C, 55.51; H, 4.75.

The identity of the product was also confirmed by a single-crystal X-ray crystallographic analysis (Figure 4.37). A crystal suitable for structure determination was obtained by slow vapor diffusion of pentane in a saturated 70:30 benzene/THF solution.

4.2.11 Preparation of $CpFe(P_2S)$.

To a 50:1 benzene/THF (20 mL) solution of $CpFe(P_2S)PF_6$ (50 mg, 0.07 mmol) was added cobaltocene (12 mg, 0.06 mmol). The color of the solution changed from pink to green/brown. After allowing the solution to stir for five minutes, it was filtered and the solvent was removed from the filtrate under vacuum. The green/brown compound was dried *in vacuo* overnight to give $CpFe(P_2S)$ (29 mg, 0.05 mmol, 83% yield). 1H NMR (C_6D_6 , δ): 8.31 – 6.98 (m, Ph), 4.00 (s, Cp), 1.91 (m, CH_2), 1.76 (s, CH_2), 1.58 (m, CH_2), 0.64 (s, CH_3). ^{31}P NMR (C_6D_6 , δ): 67.54 (s, diphos). Mass Spec. (FAB) 592. Unfortunately, a small amount of impurity appeared in the 1H and ^{31}P NMR spectra so that a combustion analysis was not possible. Purification by column chromatography

was not possible since the medium (Silica gel or Alumina) oxidizes the compound.

4.2.12 Preparation of CpFe(dppe)(SC₆H₄-p-Z) crystals where Z = H, NO₂ and [CpFe(dppe)(SC₆H₅)]BF₄.

Slow vapor diffusion of pentane into a saturated THF solution of the compound under nitrogen produced X-ray diffraction quality crystals. (Figures 4.31, 4.33, and 4.35, respectively).

4.2.13 Preparation of CpFe(dppe)(SC₆H₄-p-OCH₃) crystals.

Evaporation from a saturated CH₂Cl₂ solution of the compound under nitrogen yielded X-ray diffraction quality crystals (Figure 4.29).

4.2.14 Preparation of [CpFe(P₂S)]PF₆ crystals.

Slow vapor diffusion of pentane into a saturated 70:30 benzene/THF solution of the compound under nitrogen gave crystals that proved suitable for X-ray crystallography (Figure 4.37).

4.2.15 Reaction between CpFe(dppe)(SC₆H₅) with HBF₄ under aerobic and anaerobic conditions.

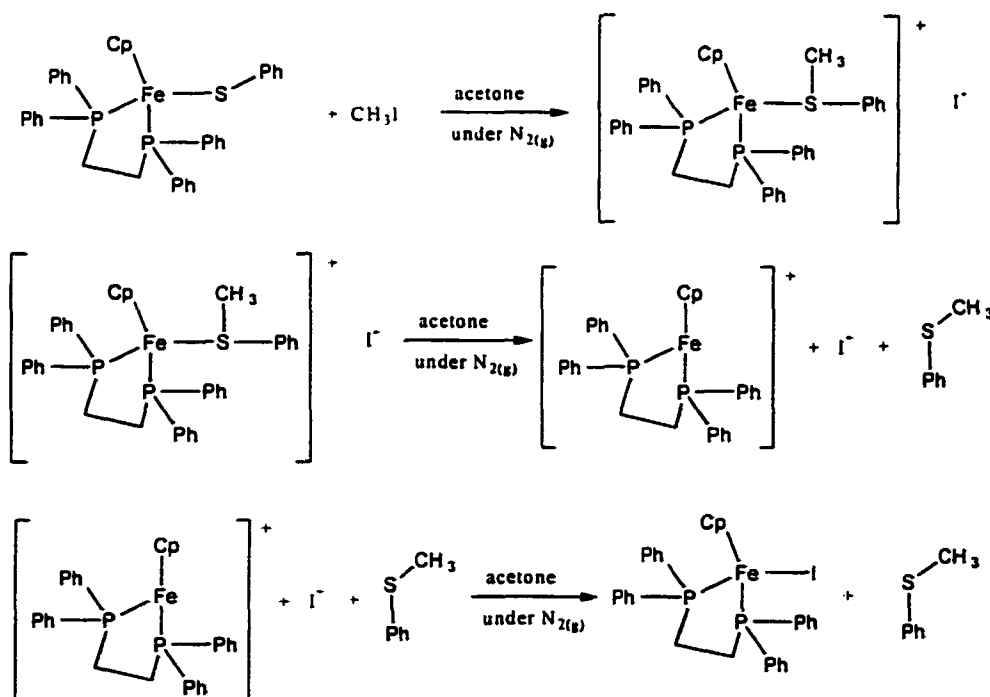
CpFe(dppe)(SC₆H₅) (25 mg) was dissolved in benzene (10 mL) under aerobic conditions and HBF₄·O(CH₃)₂ (5.0 μL) was added. A dark blue compound immediately precipitated out of solution. The product of the reaction is [CpFe(dppe)(SC₆H₅)]BF₄ as confirmed by UV-vis spectroscopy. (CH₂Cl₂); λ_{max} = 580 nm

CpFe(dppe)(SC₆H₅) (25 mg) was dissolved in benzene (10 mL) under argon and HBF₄·O(CH₃)₂ (5.0 μL) was added. A red compound immediately precipitated out of solution and was filtered using Schlenk technique. The protonated species, [CpFe(dppe)(HSC₆H₅)]BF₄ was produced as confirmed by NMR. ¹H NMR (CD₂Cl₂): δ 7.80 – 7.09 (m, Ph), 6.25 (d, C₆H₄), 4.33 (s, Cp), 3.02 (t, 1H), 2.49 (br.m, 2CH₂). ³¹P NMR (CD₂Cl₂): δ 92.02 (s, diphos).

Dissolving $[\text{CpFe}(\text{dppe})(\text{HSC}_6\text{H}_5)]\text{BF}_4$ in dry degassed CH_2Cl_2 and exposing the red solution to air immediately forms the blue oxidized species $[\text{CpFe}(\text{dppe})(\text{SC}_6\text{H}_5)]\text{BF}_4$.

4.2.16 Kinetic experiments: Reaction of $\text{CpFe}(\text{dppe})(\text{SC}_6\text{H}_4\text{-}p\text{-Z})$ (where $Z = \text{OCH}_3, \text{H}, \text{Cl}, \text{CF}_3, \text{NO}_2$) with CH_3I .

Kinetic studies of $\text{CpFe}(\text{dppe})(\text{SC}_6\text{H}_5)$ showed its reaction with iodomethane to be first order in iodomethane, first order in $\text{CpFe}(\text{dppe})(\text{SC}_6\text{H}_5)$ and second order overall. It was determined by UV-vis spectroscopy (Figure 4.10) and ^1H NMR that the final product in the reaction is $\text{CpFe}(\text{dppe})\text{I}$ as shown in Scheme 4.3. In a typical experiment, 0.5 mL of a 0.6 M solution of iodomethane was added to 2.5 mL of a 1.2 mM solution of $\text{CpFe}(\text{dppe})(\text{SC}_6\text{H}_4\text{-}p\text{-Z})$ in a Schlenk cuvette with side arm under nitrogen. After the two reactants were mixed, the resulting solution (0.1 M in iodomethane and 1.0 mM in $\text{CpFe}(\text{dppe})(\text{SC}_6\text{H}_4\text{-}p\text{-Z})$) was observed by UV-vis spectroscopy over time. Figure 4.9 shows a typical example of the UV-vis spectra that are collected during the reaction of $\text{CpFe}(\text{dppe})(\text{SC}_6\text{H}_5)$ and CH_3I . The rate constants and their estimated standard deviations were obtained using the computer program, SPECFIT.⁵²



Scheme 4.3. Proposed mechanism for the methylation of $\text{CpFe}(\text{dppe})(\text{SC}_6\text{H}_5)$.

4.2.17 Reaction of $\text{CpFe}(\text{P}_2\text{S})$ with $\text{HBF}_4 \cdot \text{O}(\text{CH}_3)_2$.

A special Schlenk glass vessel was constructed for the reaction of $\text{CpFe}(\text{P}_2\text{S})$ and HBF_4 as shown in Figure 4.7 so that molecular hydrogen could be detected. The vessel contains two compartments that are relatively deep (volume approximately 30 mL each) that are joined together. Compartment A contains a port on the side for injecting compounds through a septum and an opening at the top for adding compounds which contains a high vacuum valve that can seal off the compartment. The other compartment has an opening at the top that can also be sealed by a high vacuum valve and a side port that contains a greaseless O-ring joint for attachment to a Schlenk manifold.

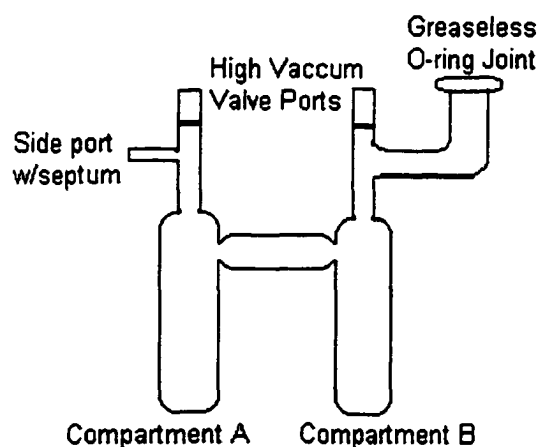


Figure 4.7. Schlenk glassware used for hydrogenation experiments.

In compartment B of the glass vessel, styrene (0.1 mL, 0.87 mmol) was added to dry degassed benzene- d_6 (3.0 mL) along with Wilkinson's catalyst, $[(\text{C}_6\text{H}_5)_3\text{P}]_3\text{RhCl}$, (40 mg, 0.04 mmol) under argon while stirring. In compartment A of the same vessel, $\text{CpFe}(\text{P}_2\text{S})$ (134 mg, 0.23 mmol) was dissolved in dry degassed benzene- d_6 (3.0 mL) and excess $\text{HBF}_4 \cdot \text{O}(\text{CH}_3)_2$ (40 μL , 0.33 mmol) was added through a septum in the side port. Compartments A and B were immediately sealed. As $\text{HBF}_4 \cdot \text{O}(\text{CH}_3)_2$ came in contact with the greenish/brown

solution, an immediate color change to pinkish/violet took place indicating oxidation of CpFe(P₂S). The reaction was allowed to stir for 24 hours; however, no hydrogenation occurred as indicated by ¹H NMR and therefore little to no hydrogen gas was produced.

4.2.18 Reaction of Zinc Powder with HBF₄·O(CH₃)₂.

In compartment B of the glass vessel, styrene (0.1 mL, 0.87 mmol) was added to dry degassed benzene-d₆ (3.0 mL) along with Wilkinson's catalyst, [(C₆H₅)₃P]₃RhCl, (40 mg, 0.04 mmol) under argon while stirring. In compartment A of the same vessel, zinc powder (14 mg, 0.22 mmol) was added to dry degassed benzene-d₆ (3.0 mL) and then excess HBF₄·O(CH₃)₂ (40 μL, 0.33 mmol) was added through a septum in the side port. Compartments A and B were immediately sealed. As HBF₄·O(CH₃) came in contact with the zinc powder, an immediate evolution of hydrogen gas took place. The reaction was allowed to stir for 4 hours. The product, ethyl benzene from compartment B, was detected by ¹H NMR indicating that hydrogenation did take place.

4.2.19 Cyclic Voltammetry experiments.

Cyclic voltammograms were obtained from 0.5 mM analyte concentration in THF using 0.2 M [*t*-Bu₄N][PF₆] (TBAHFP) as supporting electrolyte. The solutions were prepared under nitrogen and a blanket of argon was maintained over the solutions while making the measurements. Potentials were scaled to NHE using ferrocene as an internal standard (Cp₂Fe⁺/Cp₂Fe literature value is E_{1/2}^{NHE} = 400 mV in acetonitrile).⁵⁴ The analytes used were CpFe(dppe)(SC₆H₄-*p*-Z) (Z = OCH₃, H, Cl, CF₃, NO₂) and CpFe(P₂S). The voltammograms are shown in Figures 4.15 – 4.20.

4.2.20 Electron Paramagnetic Resonance experiments.

Electron paramagnetic spectra were collected at room temperature (298 K) on the following solutions which were prepared under nitrogen: 3.1 mM

[CpFe(dppe)(SC₆H₄-*p*-OCH₃)]BF₄, 1.1 mM [CpFe(dppe)(SC₆H₅)]BF₄, 2.1 mM [CpFe(dppe)(SC₆H₄-*p*-Cl)]BF₄, 1.5 mM [CpFe(dppe)(SC₆H₄-*p*-CF₃)]BF₄, and 3.3 mM [CpFe(dppe)(SC₆H₄-*p*-NO₂)]BF₄. The spectral results are shown in Figures 4.22 – 4.26. The microwave frequency was 9.434 GHz and the number of scans collected on each sample were eight. The free radical, DPPH (2,2-di(4-*tert*-octylphenyl)-1-picrylhydrazyl), was used as an external standard which has a *g*-value of 2.0037 ± 0.0002.

4.2.21 X-ray Crystal Structures.

Data for the crystal structures of CpFe(dppe)(SC₆H₅), [CpFe(dppe)(SC₆H₅)]BF₄, CpFe(dppe)(SC₆H₄-*p*-OCH₃), and [CpFe(dppe)(SC₆H₄-*p*-NO₂)] were collected at -85 °C on a Siemens P4 diffractometer using MoK α (λ =0.71073 Å) radiation. The data were corrected for Lorentz and polarization effects and an empirical absorption correction based on ψ -scans was applied.

Structures were solved by the direct atom method using SHELXTL (Siemens) system⁵⁵, and refined by full-matrix least-squares on F^2 using all reflections. All the non-hydrogen atoms were refined anisotropically and all the hydrogen atoms were included in the refinement with idealized parameters for all 4 structures.

For CpFe(dppe)(SC₆H₅), the final $R_1 = 0.036$ is based on 4469 observed reflections [$I > 2\sigma(I)$], and the final $wR_2 = 0.0874$ is based on all reflections (5438 unique data). Figures for the molecule used thermal ellipsoids at 50% level and for the packing diagram at 25% level.

For [CpFe(dppe)(SC₆H₅)]BF₄, the final $R_1 = 0.051$ is based on 5061 observed reflections [$I > 2\sigma(I)$], and the final $wR_2 = 0.139$ is based on all reflections (6527 unique data). Figures for the molecule used thermal ellipsoids at 40% level and for the packing diagram at 20% level.

The asymmetric unit contains a cation, the BF_4^- anion and one $\text{C}_4\text{H}_8\text{O}$ solvent molecule. The $\text{C}_4\text{H}_8\text{O}$ solvent is disordered as evident from the large thermal motion of the carbon atoms (C38-C41) and it displays unrealistic geometry.

For $\text{CpFe}(\text{dppe})(\text{SC}_6\text{H}_4\text{-}p\text{-OCH}_3)$, the final $R1 = 0.063$ is based on 3529 observed reflections [$I > 2\sigma(I)$], and final $wR2 = 0.1623$ is based on all reflections (3970 unique data). Figures for the molecule used thermal ellipsoids at 50% level and the packing diagram at 25% level.

For $\text{CpFe}(\text{dppe})(\text{SC}_6\text{H}_4\text{-}p\text{-NO}_2)$, the final $R1 = 0.045$ is based on 4749 observed reflections [$I > 2\sigma(I)$], and the final $wR2 = 0.121$ is based on all reflections (5510 unique data). Figures for the molecule used thermal ellipsoids at 40% level and the packing diagrams at 20% level.

Data for the crystal structures of $[\text{CpFe}(\text{P}_2\text{S})]\text{PF}_6$ were collected at -120°C on a Norius CAD-4 diffractometer using $\text{CuK}\alpha$ ($\lambda = 1.54178 \text{ \AA}$) radiation. The data were corrected for Lorentz and polarization effects; and an empirical absorption correction based on psi-scans was applied. The structure was solved by the heavy atom method using SHELXTL (Siemens) system⁵⁵, and refined by full-matrix least squares on F^2 using all reflections.

The asymmetric unit contains a cation, the PF_6^- anion, and one benzene solvent molecule in a general position and two halves of a benzene solvent molecule in special positions around the center of symmetry. Thus, each anion-cation pair share two benzene solvent molecules. All of the hydrogen atoms were included in the refinement with idealized parameters. The final $R1 = 0.054$ is based on 2976 observed reflections [$I > 2\sigma(I)$]. Figures are drawn with 50% thermal ellipsoids and the packing diagrams at 20% level.

4.2.22 Molecular Orbital Calculations

Density functional calculations using the DN* basis set, which is a numerical polarization basis set that includes d-type functions on heavy atoms, were carried out using the program SPARTAN 5.0⁴² running on a Silicon Graphics IRIS Indigo 2 Solid Impact with a R10000 processor. The pBP theory was used which introduces non-local corrections according to the method of Becke and Perdew in a perturbative manner.⁴² The compounds used for the computational studies were $\text{CpFe}(\text{CO})_2(\text{SCH}_3)$, $[\text{CpFe}(\text{CO})_2(\text{SCH}_3)]^+$, $\text{CpFe}(\text{PH}_3)_2(\text{SCH}_3)$, and $[\text{CpFe}(\text{PH}_3)_2(\text{SCH}_3)]^+$. These compounds were built and geometrically optimized using molecular mechanics with SYBYL force fields.⁴²

4.3 Results

This section contains results from UV-vis spectroscopy experiments, single-crystal X-ray crystallography, and molecular orbital calculations. Section 4.6.1 contains UV-vis spectra of $[\text{CpFe}(\text{dppe})(\text{SC}_6\text{H}_4\text{-}p\text{-Z})]\text{BF}_4$ ($Z = \text{OCH}_3, \text{H}, \text{Cl}, \text{CF}_3, \text{and NO}_2$) and $[\text{CpFe}(\text{P}_2\text{S})]\text{PF}_6$. Section 4.6.2 contains a sample of the UV-vis spectral results of the kinetic experiments of the reactions between $\text{CpFe}(\text{dppe})(\text{SC}_6\text{H}_4\text{-}p\text{-Z})$ and excess CH_3I and the kinetic data associated with these experiments. This section also contains traces and the curve fit analysis of the traces of the reactions between $\text{CpFe}(\text{dppe})(\text{SC}_6\text{H}_4\text{-}p\text{-Z})$ ($Z = \text{OCH}_3$ and NO_2) and excess CH_3I . The Hammett relationship, $\log[k_x/k_H]$ vs. sigma (σ), is also shown. Section 4.6.3 shows the cyclic voltammograms and cyclic voltammetric data of 0.5 mM solutions of $\text{CpFe}(\text{P}_2\text{S})$ and $\text{CpFe}(\text{dppe})(\text{SC}_6\text{H}_4\text{-}p\text{-Z})$ ($Z = \text{OCH}_3, \text{H}, \text{Cl}, \text{CF}_3, \text{and NO}_2$) in THF. The Hammett relationship, $E_{1/2}$ (mV) vs. sigma (σ), is also shown. Section 4.6.4 contains electron paramagnetic spectra of $[\text{CpFe}(\text{dppe})(\text{SC}_6\text{H}_4\text{-}p\text{-Z})]\text{BF}_4$ in CH_2Cl_2 at room temperature and the associated spectral data. Two Hammett relationships are shown. One of the relationships

shows the g-values vs. sigma (σ) and the other shows the half-width at half-height (HWHH) vs. sigma (σ). Section 4.6.5 contains the results of the solid state experiments. Crystal structures and crystallographic data are shown for the compounds $\text{CpFe}(\text{dppe})(\text{SC}_6\text{H}_4\text{-}p\text{-Z})$ ($Z = \text{OCH}_3, \text{H}, \text{NO}_2$), $[\text{CpFe}(\text{dppe})(\text{C}_6\text{H}_5)]\text{BF}_4$, and $[\text{CpFe}(\text{P}_2\text{S})]\text{PF}_6$. Section 4.6.6 contains the calculated energies of the Highest Occupied Molecular Orbital (HOMO) and Lowest Unoccupied Molecular Orbital (LUMO) using Density Functional Theory (DFT) on the following compounds: $\text{CpFe}(\text{CO})_2\text{SCH}_3$, $[\text{CpFe}(\text{CO})_2\text{SCH}_3]^+$, $\text{CpFe}(\text{PH}_3)_2\text{SCH}_3$, and $[\text{CpFe}(\text{PH}_3)_2\text{SCH}_3]^+$.

4.3.1 UV-vis Spectra of [CpFe(dppe)(SC₆H₄-*p*-Z)]BF₄ and [CpFe(P₂S)]PF₆

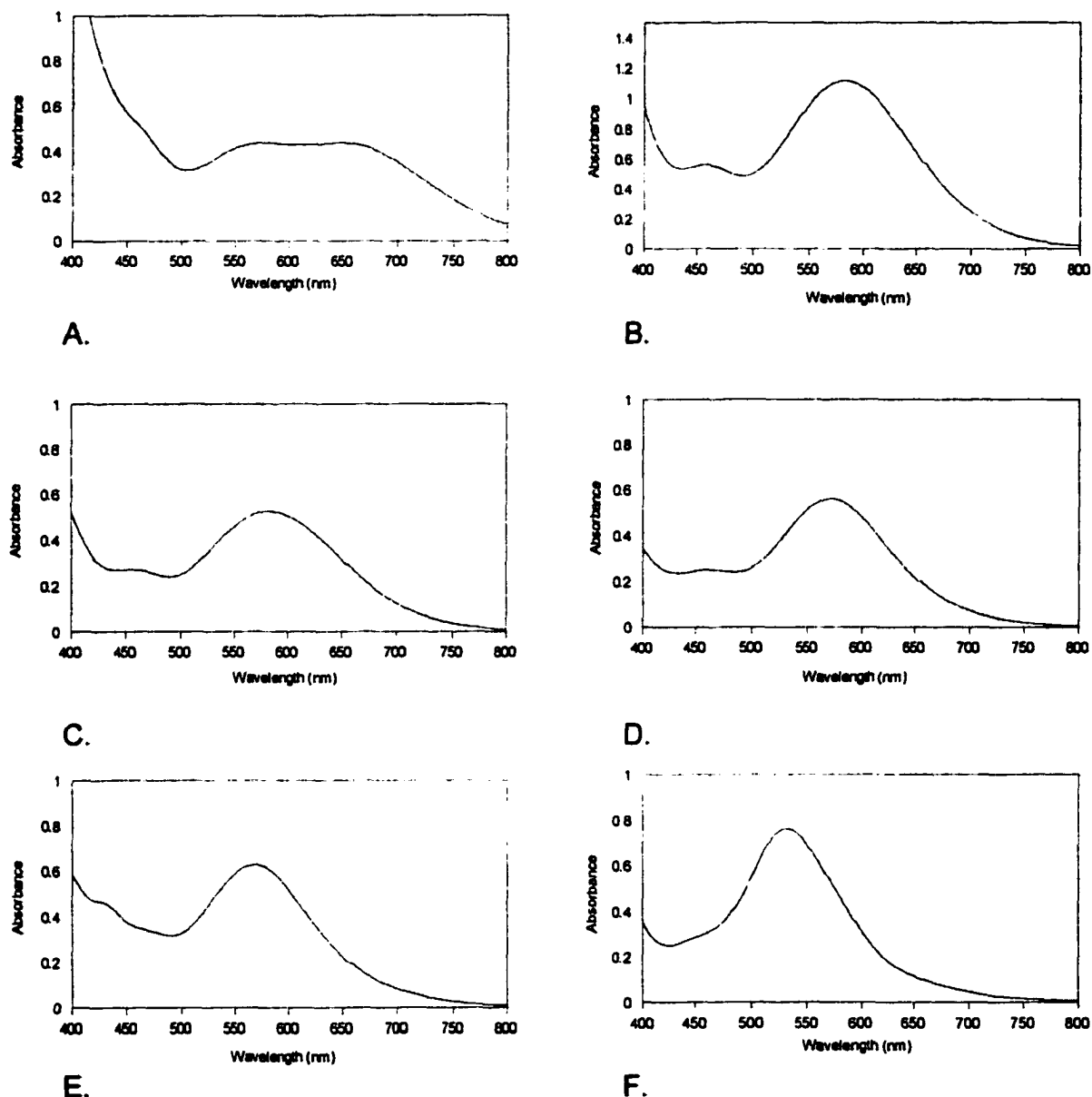
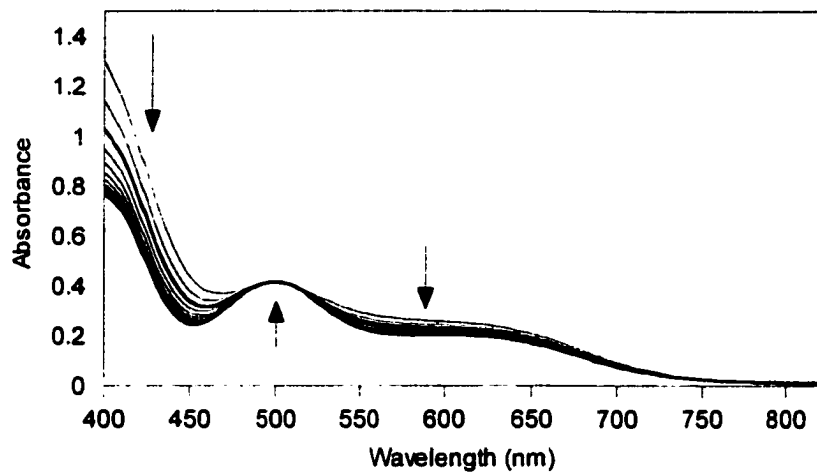
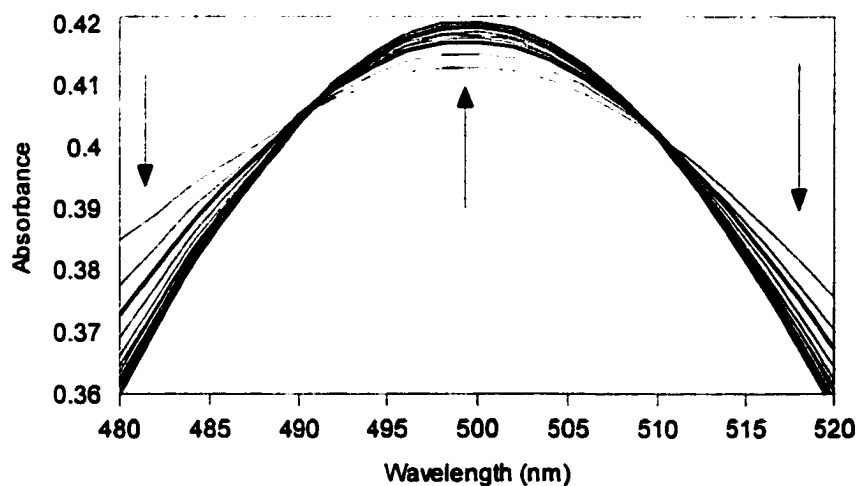


Figure 4.8. UV-vis spectra of: **A.** 1.25 mM solution of [CpFe(dppe)(SC₆H₄-*p*-OCH₃)]BF₄ in a 0.2 cm quartz UV-vis cell. [λ_{max} , nm (ϵ , M⁻¹ cm⁻¹)]: 644(1754), 578(1757). **B.** 0.50 mM solution of [CpFe(dppe)(SC₆H₅)]BF₄ in a 1 cm quartz UV-vis cell. [λ_{max} , nm (ϵ , M⁻¹ cm⁻¹)]: 580(2050). **C.** 1.25 mM solution of [CpFe(dppe)(SC₆H₄-*p*-Cl)]BF₄ in a 0.2 cm quartz UV-vis cell. [λ_{max} , nm (ϵ , M⁻¹ cm⁻¹)]: 580(2099). **D.** 1.25 mM solution of [CpFe(dppe)(SC₆H₄-*p*-CF₃)]BF₄ in a 0.2 cm quartz UV-vis cell. [λ_{max} , nm (ϵ , M⁻¹ cm⁻¹)]: 570(2247). **E.** 1.25 mM solution of [CpFe(dppe)(SC₆H₄-*p*-NO₂)]BF₄ in a 0.2 cm quartz UV-vis cell. [λ_{max} , nm (ϵ , M⁻¹ cm⁻¹)]: 570(2521). **F.** 0.50 mM solution of [CpFe(P₂S)]BF₄ in a 1 cm quartz UV-vis cell. [λ_{max} , nm (ϵ , M⁻¹ cm⁻¹)]: 530(1520).

4.3.2 Results of the kinetic experiments: Reacting $\text{CpFe}(\text{dppe})(\text{SC}_6\text{H}_4\text{-}p\text{-Z})$ where $Z = \text{OCH}_3, \text{H}, \text{Cl}, \text{CF}_3, \text{NO}_2$ with CH_3I .



A.



B.

Figure 4.9. A represents the UV-vis data that was collected over a period of 120 seconds of the reaction between 1.0 mM $\text{CpFe}(\text{dppe})(\text{SC}_6\text{H}_5)$ and 0.1 M CH_3I in dry degassed acetone. B shows two isosbestic points from the reaction represented in A.

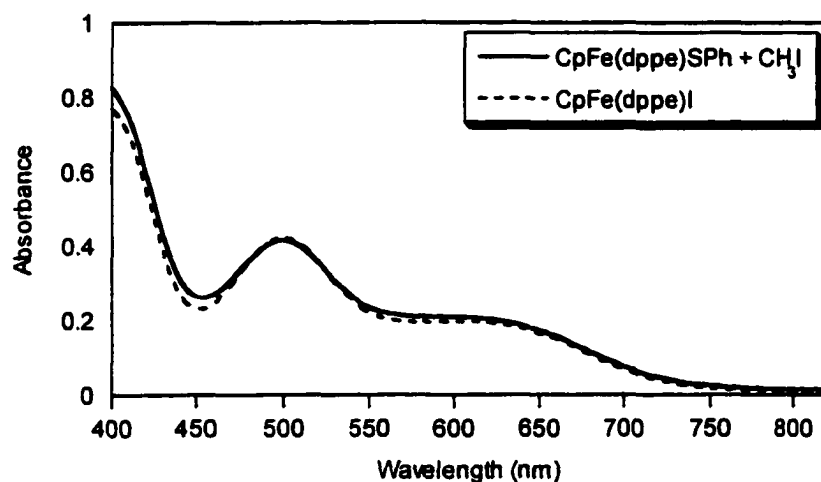


Figure 4.10. The dashed line spectrum represents the absorbance vs. wavelength of 1.0 mM CpFe(dppe)I in acetone. The solid line spectrum represents the absorbance vs. wavelength of the product of the reaction between 1.0 mM CpFe(dppe)(SC₆H₅) and 0.1 M CH₃I in acetone after 120 seconds.

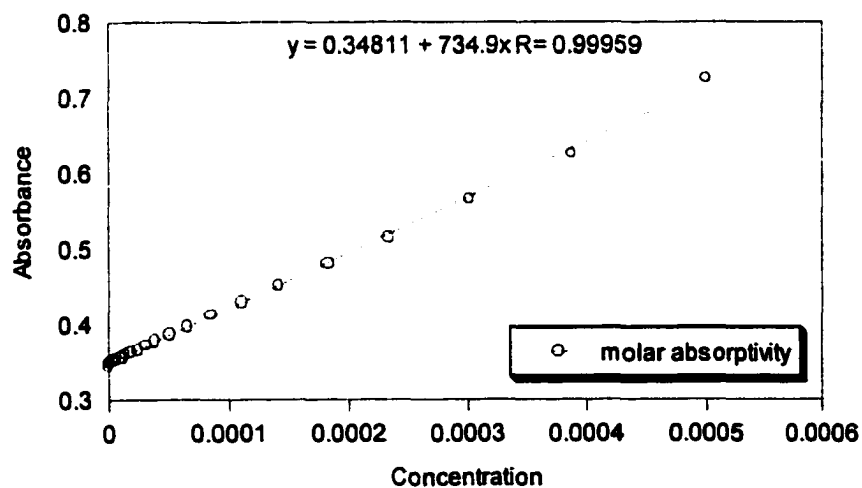


Figure 4.11. Beer's Law plot of 0.5 mM CpFe(dppe)(SC₆H₄-*p*-OCH₃) and 50 mM CH₃I in acetone at 340 nm.

Table 4.1. Represents the kinetic data for the reaction between $\text{CpFe}(\text{dppe})(\text{SC}_6\text{H}_4\text{-}p\text{-Z})$ and excess CH_3I .

Z	[Z] mol L ⁻¹	[CH ₃ I] mol L ⁻¹	k, L M ⁻¹ s ⁻¹	k _{rel}
OCH ₃	0.0005	0.01	2.4817(6)	231.9
H	0.001	0.10	0.3454(2)	32.3
Cl	0.001	0.10	0.1279(6)	12.0
CF ₃	0.001	0.10	0.0562(3)	5.3
NO ₂	0.001	0.10	0.0107(1)	1.0

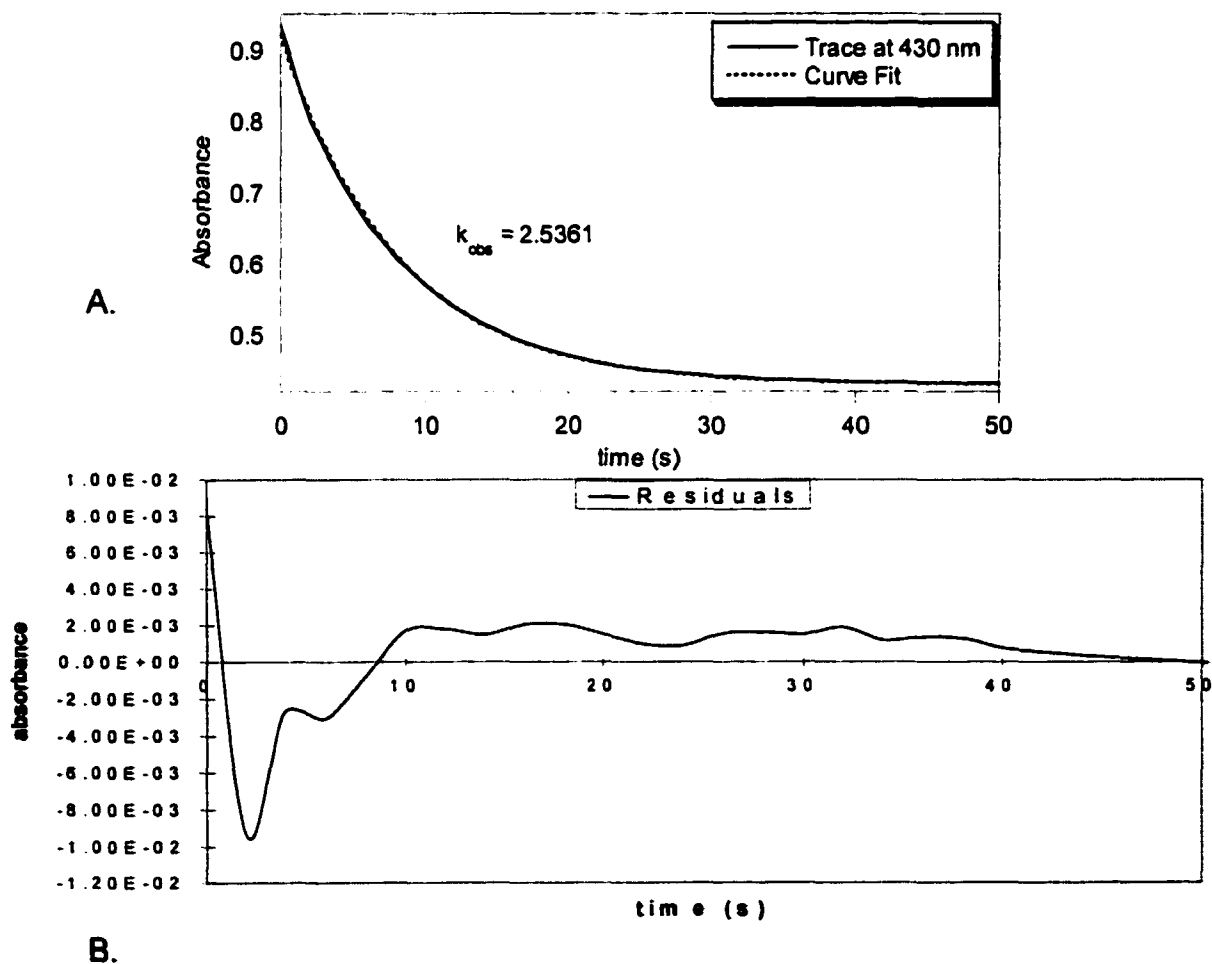


Figure 4.12. A. The plot of absorbance vs. time representing the trace and curve fit at 430 nm of a pseudo-first order reaction of 0.5 mM $\text{CpFe}(\text{dppe})(\text{SC}_6\text{H}_4\text{-}p\text{-OCH}_3)$ and 50 mM CH_3I in acetone. B. Residual plot of the reaction in A.

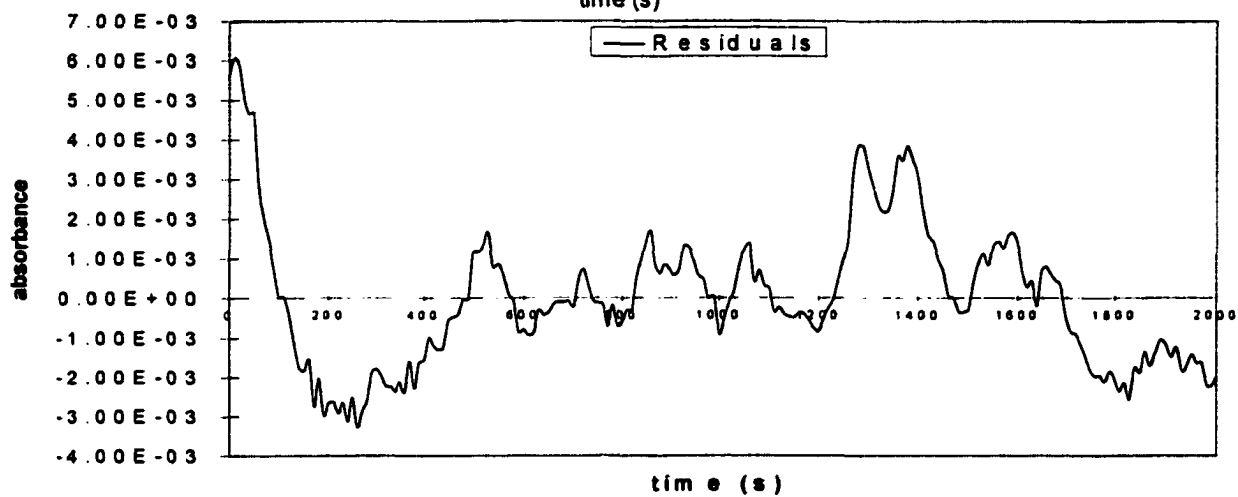
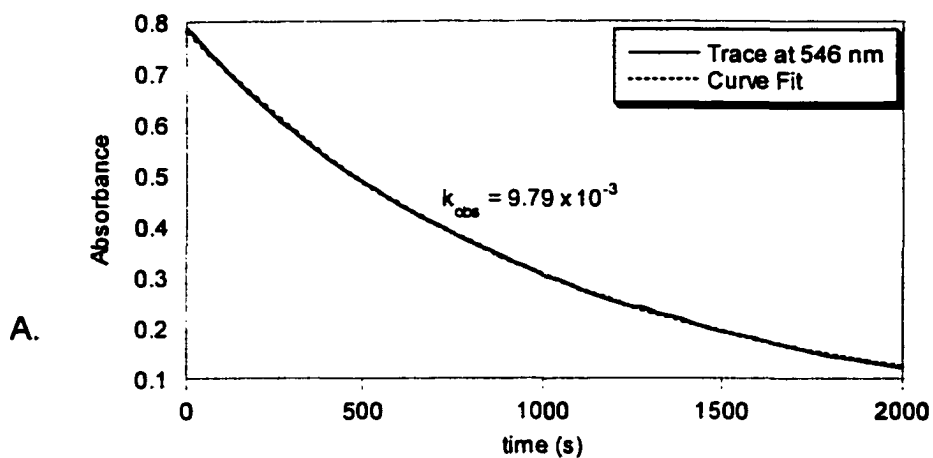


Figure 4.13. A. The plot of absorbance vs. time representing the trace and curve fit at 546 (nm) of a pseudo-first order reaction of 1.0 mM CpFe(dppe)(SC₆H₄-*p*-NO₂) and 100 mM CH₃I in acetone. B. Residual plot of the reaction in A.

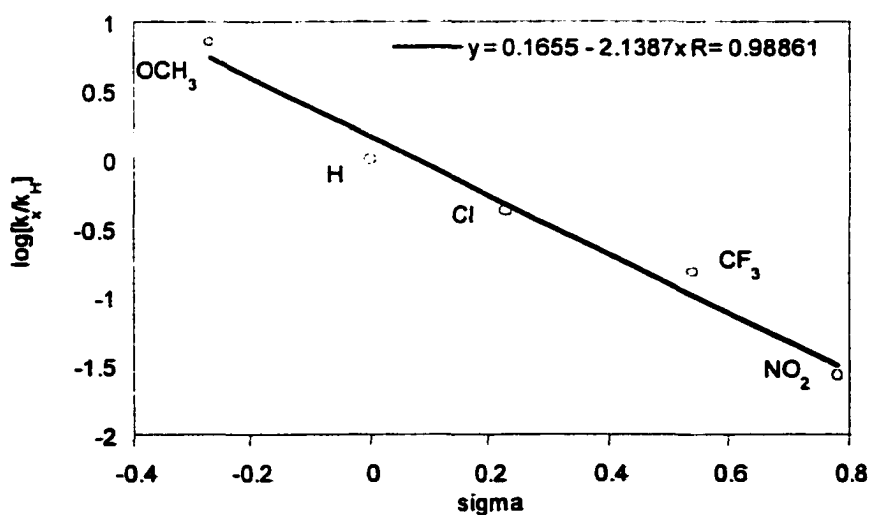


Figure 4.14. Hammett relationship between the rate of reaction of CpFe(dppe)(SC₆H₄-*p*-Z) with iodomethane and the Hammett substituent constant (σ).

4.3.3 Results of the Cyclic Voltammetry experiments.

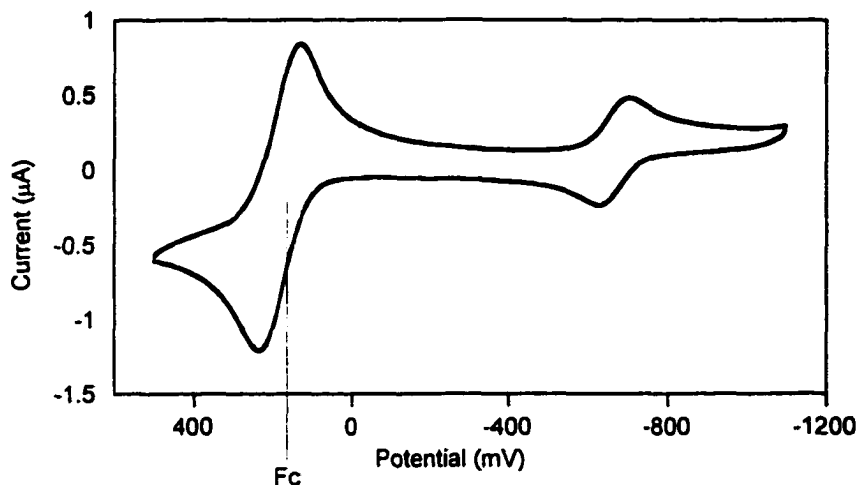


Figure 4.15. Cyclic Voltammogram of a 0.5 mM solution of CpFe(P₂S) in 0.2 M TBAHFP/THF with a glassy carbon working electrode at a scan rate of 100 mV/s. $E_{1/2} = -666$ mV vs. Ag/AgNO₃ reference electrode. (Fc = ferrocene)

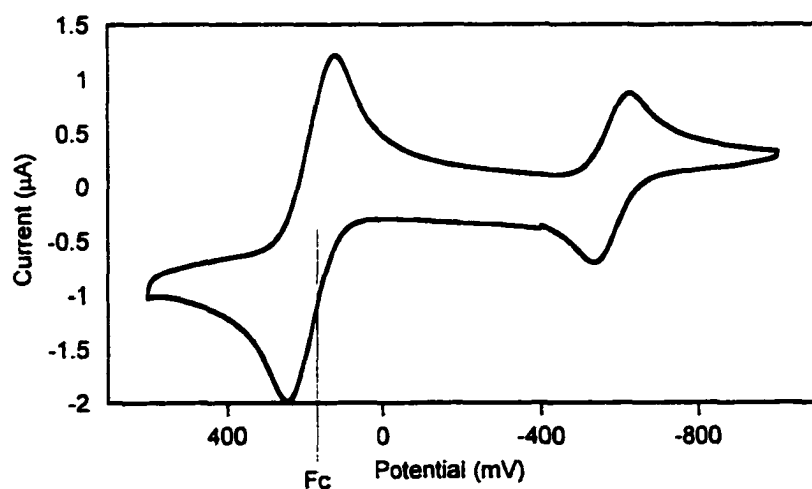


Figure 4.16. Cyclic Voltammogram of a 0.5 mM solution of CpFe(dppe)(SC₆H₄-*p*-OCH₃) in 0.2 M TBAHFP/THF with a glassy carbon working electrode at a scan rate of 100 mV/s. $E_{1/2} = -577$ mV vs. Ag/AgNO₃ reference electrode. (Fc = ferrocene)

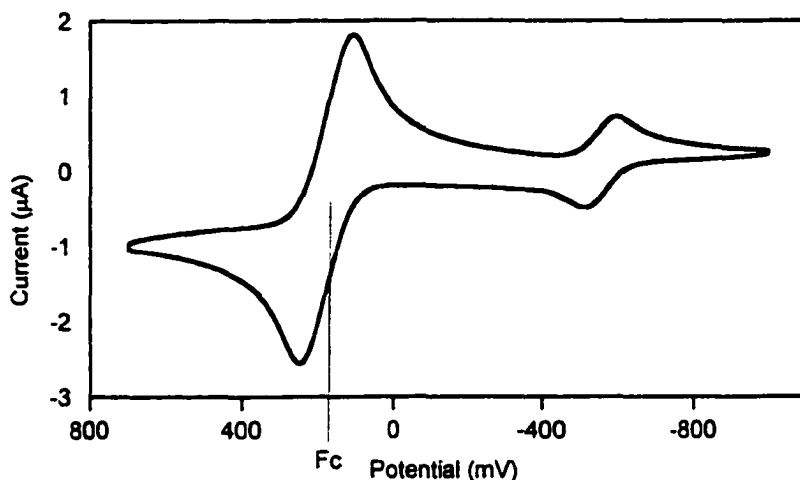


Figure 4.17. Cyclic Voltammogram of a 0.5 mM solution of $\text{CpFe}(\text{dppe})(\text{SC}_6\text{H}_5)$ in 0.2 M TBAHFP/THF with a glassy carbon working electrode at a scan rate of 100 mV/s. $E_{1/2} = -551$ mV vs. Ag/AgNO_3 reference electrode. (Fc = ferrocene)

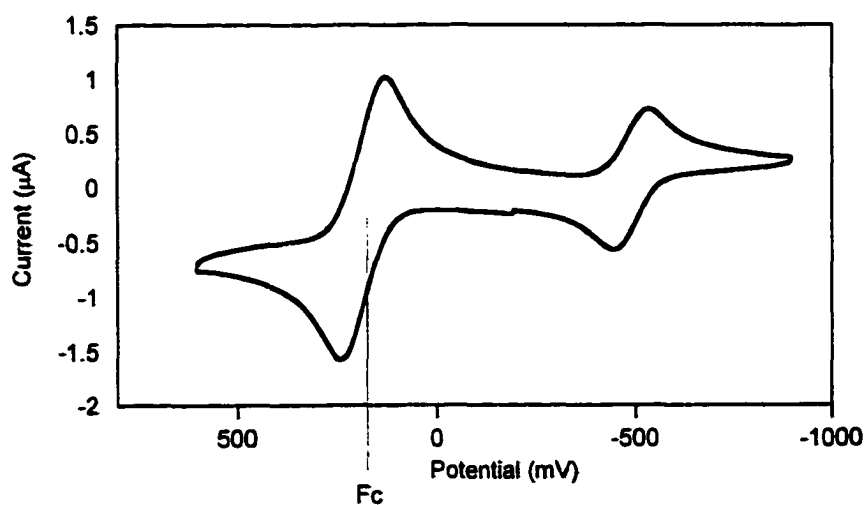


Figure 4.18. Cyclic Voltammogram of a 0.5 mM solution of $\text{CpFe}(\text{dppe})(\text{SC}_6\text{H}_4\text{-}p\text{-Cl})$ in 0.2 M TBAHFP/THF with a glassy carbon working electrode at a scan rate of 100 mV/s. $E_{1/2} = -491$ mV vs. Ag/AgNO_3 reference electrode. (Fc = ferrocene)

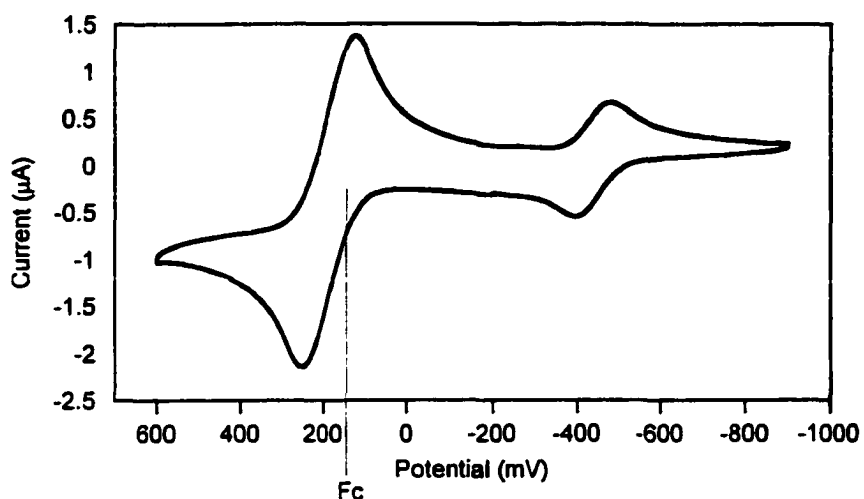


Figure 4.19. Cyclic Voltammogram of a 0.5 mM solution of $\text{CpFe}(\text{dppe})(\text{SC}_6\text{H}_4\text{-}p\text{-CF}_3)$ in 0.2 M TBAHFP/THF with a glassy carbon working electrode at a scan rate of 100 mV/s. $E_{1/2} = -438$ mV vs. Ag/AgNO₃ reference electrode. (Fc = ferrocene)

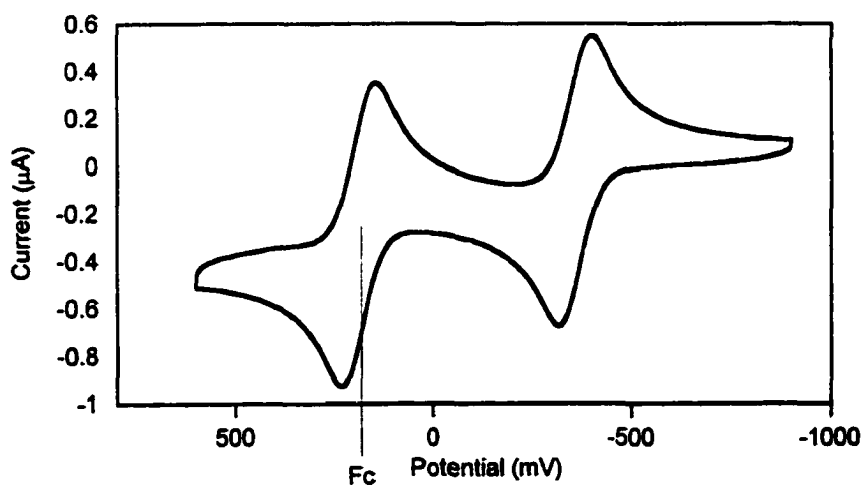


Figure 4.20. Cyclic Voltammogram of a 0.5 mM solution of $\text{CpFe}(\text{dppe})(\text{SC}_6\text{H}_4\text{-}p\text{-NO}_2)$ in 0.2 M TBAHFP/THF with a glassy carbon working electrode at a scan rate of 100 mV/s. $E_{1/2} = -357$ mV vs. Ag/AgNO₃ reference electrode. (Fc = ferrocene)

Table 4.2. Cyclic Voltammetric data for CpFe(dppe)(SC₆H₄-*p*-Z) and CpFe(P₂S) complexes.

Compound	$E_{1/2}$ (mV) ^a	$E_{pa}-E_{pc}$ ^b (mV)	i_{pa}/i_{pc}	Hammett Constant (σ) ^c
CpFe(P ₂ S)	-453	73	0.89	N/A
CpFe(dppe)(SC ₆ H ₄ - <i>p</i> -OCH ₃)	-364	88	1.01	-0.27
CpFe(dppe)(SC ₆ H ₅)	-330	82	1.15	0.00
CpFe(dppe)(SC ₆ H ₄ - <i>p</i> -Cl)	-276	84	1.05	0.23
CpFe(dppe)(SC ₆ H ₄ - <i>p</i> -CF ₃)	-225	1.19	0.54	
CpFe(dppe)(SC ₆ H ₄ - <i>p</i> -NO ₂)	-142	82	1.01	0.78

a. Potentials are versus the National Hydrogen Electrode (NHE), measured at a glassy carbon electrode in THF with 0.2 M [NBu₄][PF₄] as supporting electrolyte.⁵⁴ b. E_{pa} and E_{pc} is the potential for a reversible one-electron oxidation and reduction, respectively, that is measured at a scan rate of 100 mVs⁻¹. c. See reference ⁵⁶

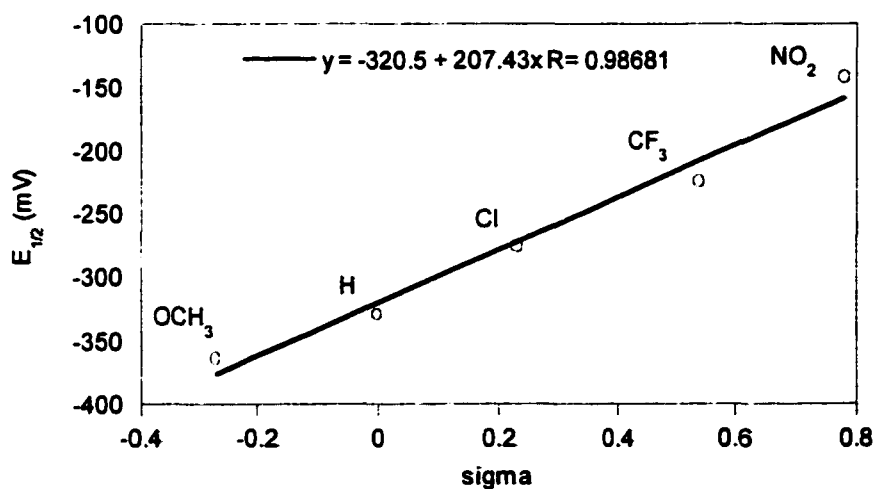


Figure 4.21. Hammett relationship between the half-wave potential of CpFe(dppe)(SC₆H₄-*p*-Z) and sigma. Data from Table 4.2.

4.3.4 Results of EPR experiments.

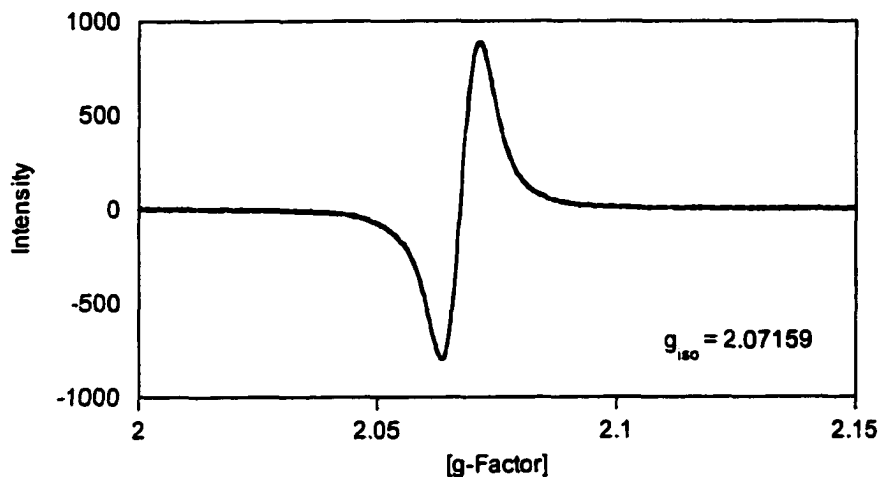


Figure 4.22. EPR spectrum of a 3.1 mM $[\text{CpFe}(\text{dppe})(\text{SC}_6\text{H}_4\text{-}p\text{-OCH}_3)]\text{BF}_4$ in CH_2Cl_2 at 298K referenced to DPPH at 2.0037.

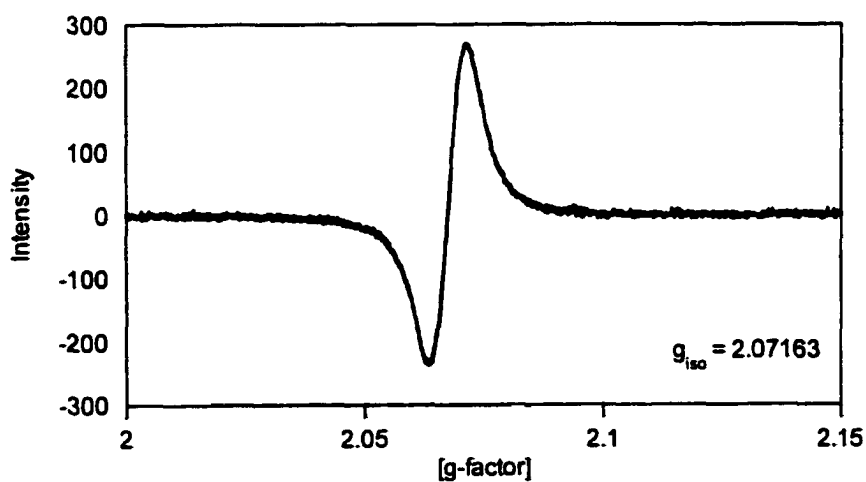


Figure 4.23. EPR spectrum of a 1.1 mM $[\text{CpFe}(\text{dppe})(\text{SC}_6\text{H}_5)]\text{BF}_4$ in CH_2Cl_2 at 298K referenced to DPPH at 2.0037.

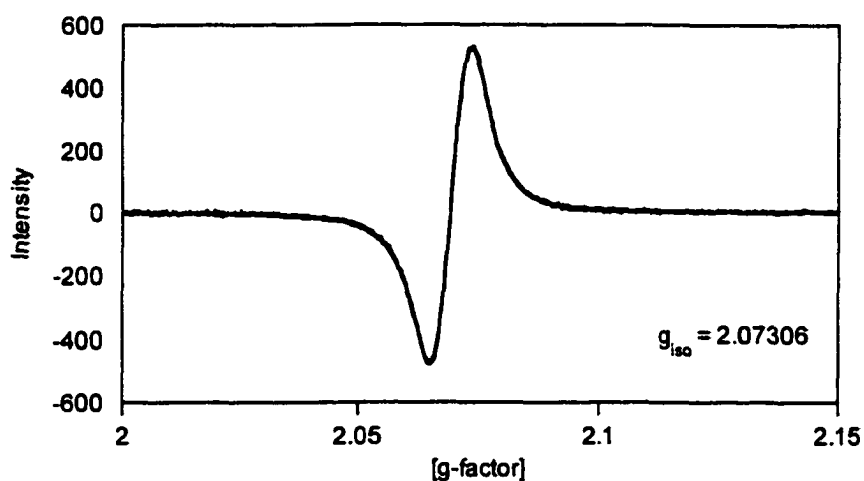


Figure 4.24. EPR spectrum of a 2.1 mM $[\text{CpFe}(\text{dppe})(\text{SC}_6\text{H}_4\text{-}p\text{-Cl})]\text{BF}_4$ in CH_2Cl_2 at 298K referenced to DPPH at 2.0037.

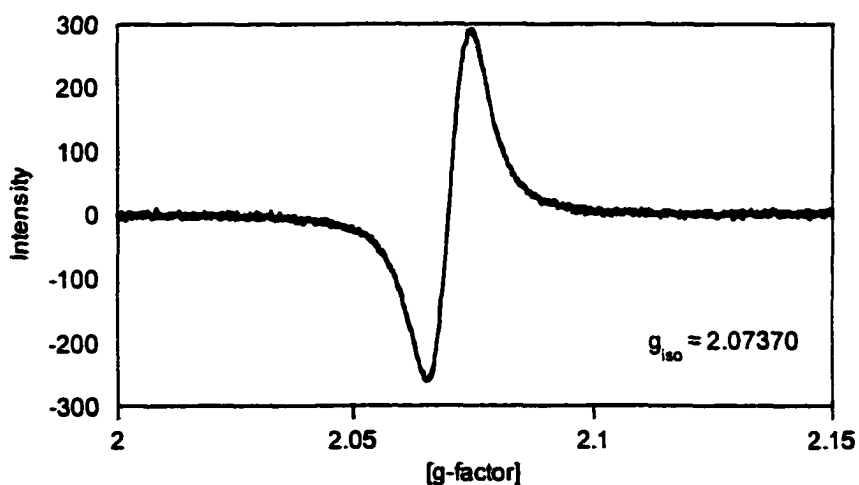


Figure 4.25. EPR spectrum of a 1.5 mM $[\text{CpFe}(\text{dppe})(\text{SC}_6\text{H}_4\text{-}p\text{-CF}_3)]\text{BF}_4$ in CH_2Cl_2 at 298K referenced to DPPH at 2.0037.

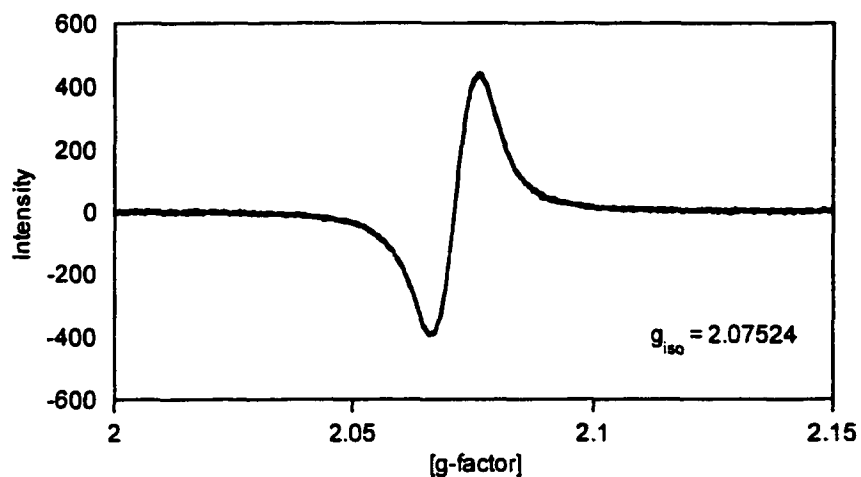


Figure 4.26. EPR spectrum of a 3.3 mM $[\text{CpFe}(\text{dppe})(\text{SC}_6\text{H}_4\text{-}p\text{-NO}_2)]\text{BF}_4$ in CH_2Cl_2 at 298K referenced to DPPH at 2.0037.

Table 4.3. EPR spectra data^a for $[\text{CpFe}(\text{dppe})(\text{SC}_6\text{H}_4\text{-}p\text{-Z})]\text{BF}_4$.

Compound	Concentration (mM)	Solution ^b g_{iso}	HWHH Values ^c
$[\text{CpFe}(\text{dppe})(\text{SC}_6\text{H}_4\text{-}p\text{-OCH}_3)]^+$	3.1	2.07159	0.00568
$[\text{CpFe}(\text{dppe})(\text{SC}_6\text{H}_5)]^+$	1.1	2.07163	0.00569
$[\text{CpFe}(\text{dppe})(\text{SC}_6\text{H}_4\text{-}p\text{-Cl})]^+$	2.1	2.07306	0.00617
$[\text{CpFe}(\text{dppe})(\text{SC}_6\text{H}_4\text{-}p\text{-CF}_3)]^+$	1.5	2.07370	0.00649
$[\text{CpFe}(\text{dppe})(\text{SC}_6\text{H}_4\text{-}p\text{-NO}_2)]^+$	3.3	2.07524	0.00700

a. At 298K; b. CH_2Cl_2 ; c. Half width at half height values.

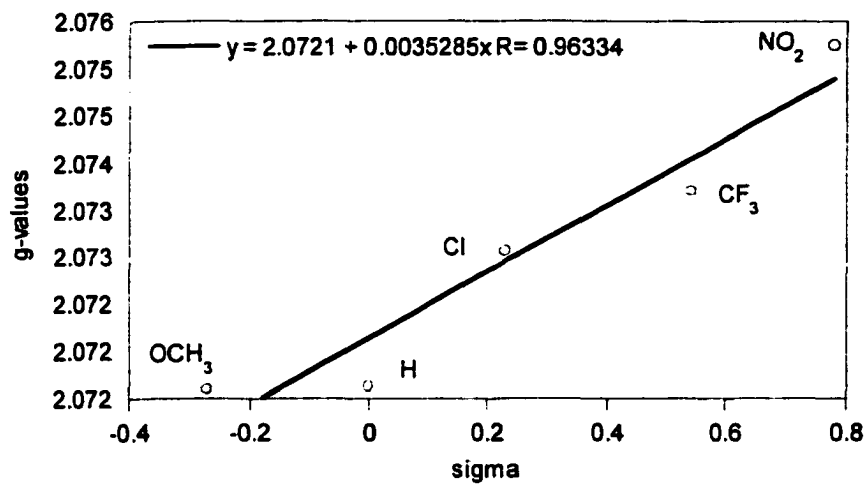


Figure 4.27. Hammett relationship between the g-values of CpFe(dppe)(SC₆H₄-p-Z) in CH₂Cl₂ at 298K and sigma (σ).

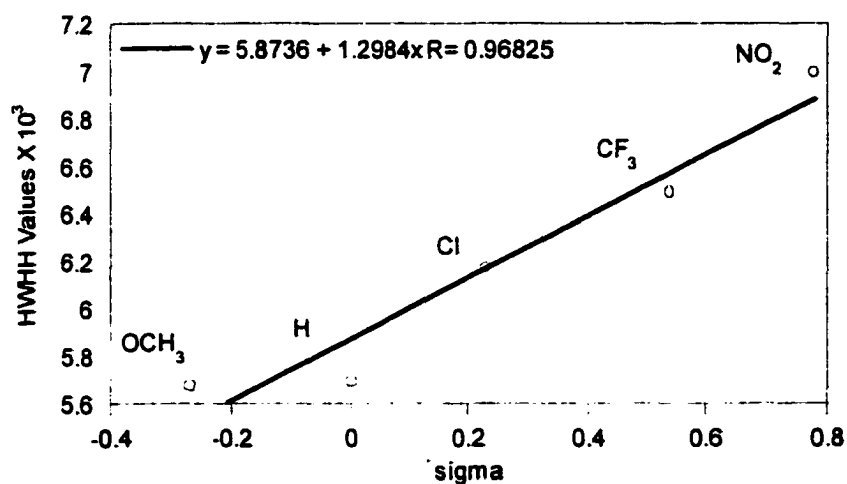


Figure 4.28. Hammett relationship between the half width at half height (HWHH) values of CpFe(dppe)(SC₆H₄-p-Z) in CH₂Cl₂ at 298K and sigma (σ).

4.3.5 Results of the Solid State Experiments

The compound $\text{CpFe}(\text{dppe})(\text{SC}_6\text{H}_4\text{-}p\text{-OCH}_3)$ crystallizes in the $P2_12_12_1$ space group and contains four molecules per unit cell. The thermal ellipsoid drawings of $\text{CpFe}(\text{dppe})(\text{SC}_6\text{H}_4\text{-}p\text{-OCH}_3)$ and crystal packing are located in Figures 4.29 and 4.30. Selected bond lengths and angles for $\text{CpFe}(\text{dppe})(\text{SC}_6\text{H}_4\text{-}p\text{-OCH}_3)$ are located in Table 4.6.

The compound $\text{CpFe}(\text{dppe})(\text{SC}_6\text{H}_5)$ crystallizes in the $P2_1/c$ space group and contains four molecules per unit cell. The thermal ellipsoid drawings of $\text{CpFe}(\text{dppe})(\text{SC}_6\text{H}_5)$ and crystal packing are located in Figures 4.31 and 4.32. Selected bond lengths and angles for $\text{CpFe}(\text{dppe})(\text{SC}_6\text{H}_5)$ are located in Table 4.9.

The compound $\text{CpFe}(\text{dppe})(\text{SC}_6\text{H}_4\text{-}p\text{-NO}_2)$ crystallizes in the $P\bar{1}$ space group and contains two molecules per unit cell. The atoms of the sulfur and C_6H_4 group, and the nitrogen and oxygen atoms from the NO_2 substituent lie in the same plane, which suggests the establishment of a strong conjugated π -system. The $\text{Fe}(1)\text{-S}(1)\text{-C}(6)$ bond angle 121° , which is one of the largest to be published for these type of iron-thiolate complexes, may be due to the stabilizing effect of the conjugated π -system. The thermal ellipsoid drawings of $\text{CpFe}(\text{dppe})(\text{SC}_6\text{H}_4\text{-}p\text{-NO}_2)$ and the crystal packing diagram are located in Figures 4.33 and 4.34. Selected bond lengths and angles for $\text{CpFe}(\text{dppe})(\text{SC}_6\text{H}_4\text{-}p\text{-NO}_2)$ are located in Table 4.12.

The compound $[\text{CpFe}(\text{dppe})(\text{SC}_6\text{H}_5)]\text{BF}_4$ crystallizes in the $P2_1/n$ space group. The asymmetric unit contains a cation, the BF_4^- anion and one solvent molecule (THF). The solvent molecule is disordered as evident from the large thermal motion of the carbon atoms and it displays unrealistic geometry. The thermal ellipsoid drawings of $[\text{CpFe}(\text{dppe})(\text{SC}_6\text{H}_5)]\text{BF}_4$, and the crystal packing diagram are located in Figures 4.35 and 4.36. Selected bond lengths and angles for $[\text{CpFe}(\text{dppe})(\text{SC}_6\text{H}_5)]\text{BF}_4$ are located in Table 4.15.

The compound $[\text{CpFe}(\text{P}_2\text{S})]\text{PF}_6$ crystallizes in the $P\bar{1}$ space group. The asymmetric unit contains a cation, the PF_6^- anion, and one benzene solvent molecule in a general position and two halves of a benzene solvent molecule in

special positions around the center of symmetry. Each anion-cation pair share two benzene solvent molecules. The thermal ellipsoid drawings of $[\text{CpFe}(\text{P}_2\text{S})]\text{PF}_6$ and the crystal packing diagram are located in Figures 4.37 and 4.38. Selected bond lengths and angles for $[\text{CpFe}(\text{P}_2\text{S})]\text{PF}_6$ are located in Table 4.18.

The crystal data and structure refinement for $\text{CpFe}(\text{dppe})(\text{SC}_6\text{H}_4\text{-}p\text{-OCH}_3)$, $\text{CpFe}(\text{dppe})(\text{SC}_6\text{H}_5)$, $\text{CpFe}(\text{dppe})(\text{SC}_6\text{H}_4\text{-}p\text{-NO}_2)$, $[\text{CpFe}(\text{dppe})(\text{SC}_6\text{H}_5)]\text{BF}_4$, and $[\text{CpFe}(\text{P}_2\text{S})]\text{PF}_6$ are located in Tables 4.4, 4.7, 4.10, 4.13, and 4.16, respectively. The atomic coordinates ($\times 10^4$) and equivalent isotropic displacement parameters ($\text{\AA}^2 \times 10^3$) for $\text{CpFe}(\text{dppe})(\text{SC}_6\text{H}_4\text{-}p\text{-OCH}_3)$, $\text{CpFe}(\text{dppe})(\text{SC}_6\text{H}_5)$, $\text{CpFe}(\text{dppe})(\text{SC}_6\text{H}_4\text{-}p\text{-NO}_2)$, $[\text{CpFe}(\text{dppe})(\text{SC}_6\text{H}_5)]\text{BF}_4$, and $[\text{CpFe}(\text{P}_2\text{S})]\text{PF}_6$ are located in Tables 4.5, 4.8, 4.11, 4.14, and 4.17, respectively.

Table 4.4. Crystal data and structure refinement for CpFe(dppe)(SC₆H₄-*p*-OCH₃).

Empirical formula	C ₃₈ H ₃₆ FeOP ₂ S
Formula weight	658.52
Temperature	163(2) K
Wavelength	0.71073 Å
Crystal system	Orthorhombic
Space group	P2 ₁ 2 ₁ 2 ₁
Unit cell dimensions	a = 11.097(2) Å α = 90 deg. b = 15.777(3) Å β = 90 deg. c = 17.841(3) Å γ = 90 deg.
Volume, Z	3123.6(10) Å ³ , 4
Density (calculated)	1.400 mg/m ³
Absorption coefficient	0.683 mm ⁻¹
F(000)	1376
Crystal size	0.56 x 0.42 x 0.22 mm
Theta range for data collection	2.16 to 26.01 deg.
Limiting indices	-13 ≤ h ≤ 3, -17 ≤ k ≤ 19, -8 ≤ l ≤ 22
Reflections collected	4153
Independent reflections	3970 [R(int) = 0.0640]
Absorption correction	Semi-empirical from psi-scans
Max. and min. transmission	0.5792 and 0.4852
Refinement method	Full-matrix least-squares on F ²
Data / restraints / parameters	3970 / 0 / 389

Goodness-of-fit on F^2	1.028
Final R indices [$I > 2\sigma(I)$]	R1 = 0.0630, wR2 = 0.1555
R indices (all data)	R1 = 0.0716, wR2 = 0.1623
Absolute structure parameter	-0.03(4)
Largest diff. peak and hole	0.954 and -0.681 e. \AA^{-3}

Table 4.5. Atomic coordinates ($\times 10^4$) and equivalent isotropic displacement parameters ($\text{\AA}^2 \times 10^3$) for $\text{CpFe(dppe)(SC}_6\text{H}_4\text{-}p\text{-OCH}_3\text{)}$. $U(\text{eq})$ is defined as one third of the trace of the orthogonalized U_{ij} tensor.

	x	y	z	$U(\text{eq})$
Fe(1)	1905(1)	2476(1)	2087(1)	19(1)
S(1)	2206(2)	1088(1)	1678(1)	23(1)
P(1)	2687(1)	2136(1)	3174(1)	19(1)
P(2)	234(1)	1995(1)	2546(1)	18(1)
O(1)	2680(6)	711(3)	-1623(3)	47(2)
C(1)	2664(7)	2958(5)	1100(4)	33(2)
C(2)	1402(7)	3076(4)	1093(4)	29(2)
C(3)	1124(7)	3598(4)	1737(4)	29(2)
C(4)	2209(6)	3770(4)	2122(4)	28(2)
C(5)	3163(7)	3380(4)	1720(4)	33(2)
C(6)	2282(7)	1048(5)	680(4)	36(2)
C(7)	1292(7)	1097(4)	226(4)	36(2)
C(8)	1376(8)	1009(4)	-544(4)	35(2)
C(9)	2522(8)	831(4)	-873(4)	37(2)
C(10)	3472(7)	795(4)	-432(4)	33(2)

C(11)	3415(8)	907(5)	337(5)	39(2)
C(12)	4061(6)	1492(4)	3241(4)	22(1)
C(13)	4789(6)	1371(4)	2603(4)	29(2)
C(14)	5865(6)	918(4)	2678(5)	36(2)
C(15)	6209(6)	591(4)	3371(5)	36(2)
C(16)	5519(6)	725(4)	3986(5)	32(2)
C(17)	4440(6)	1173(4)	3926(4)	29(2)
C(18)	3197(5)	2986(4)	3808(3)	20(1)
C(19)	4147(6)	3491(4)	3550(4)	32(2)
C(20)	4642(6)	4113(5)	4004(4)	33(2)
C(21)	4222(6)	4223(4)	4725(4)	31(2)
C(22)	3292(7)	3745(5)	4979(4)	35(2)
C(23)	2768(7)	3128(4)	4513(4)	30(2)
C(24)	-707(5)	2686(3)	3136(3)	18(1)
C(25)	-233(6)	3423(4)	3453(4)	24(1)
C(26)	-937(6)	3914(4)	3928(4)	28(2)
C(27)	-2104(6)	3698(4)	4076(4)	28(2)
C(28)	-2588(6)	2972(4)	3774(4)	30(2)
C(29)	-1906(5)	2475(4)	3296(4)	26(1)
C(30)	-861(6)	1557(4)	1895(3)	20(1)
C(31)	-965(6)	690(4)	1743(4)	22(1)
C(32)	-1716(6)	411(4)	1182(4)	25(2)
C(33)	-2363(7)	975(4)	756(4)	30(2)

C(34)	-2261(8)	1841(4)	894(4)	35(2)
C(35)	-1518(6)	2114(4)	1464(4)	28(2)
C(36)	1577(6)	1527(4)	3739(4)	24(1)
C(37)	602(5)	1154(4)	3224(3)	19(1)
C(38)	1728(9)	808(5)	-2108(4)	47(2)

Table 4.6. Selected bond lengths (Å) and angles (deg) for CpFe(dppe)(SC₆H₄-*p*-OCH₃).

Fe(1)-S(1)	2.332(2)
Fe(1)-P(1)	2.191(2)
Fe(1)-P(2)	2.164(2)
Fe(1)-X(1)	1.699(6)
S(1)-Fe(1)-P(1)	89.46(7)
S(1)-Fe(1)-P(2)	84.94(7)
S(1)-Fe(1)-X(1)	125.0(2)
P(1)-Fe(1)-P(2)	85.33(7)
P(1)-Fe(1)-X(1)	129.9(2)
P(2)-Fe(1)-X(1)	127.9(2)
Fe(1)-S(1)-C(6)	110.7(2)

X(1) refers to the centroid of C(1)-C(5) ring.

Table 4.7. Crystal data and structure refinement for CpFe(dppe)(SC₆H₅).

Empirical formula	C ₃₇ H ₃₄ FeP ₂ S
Formula weight	628.49
Temperature	188(2) K
Wavelength	0.71073 Å
Crystal system	Monoclinic
Space group	P2 ₁ /c
Unit cell dimensions	a = 11.0560(10) Å α = 90 deg. b = 21.732(2) Å β = 111.530(10) deg. c = 13.875(2) Å γ = 90 deg.
Volume, Z	3101.1(6) Å ³ , 4
Density (calculated)	1.346 mg/m ³
Absorption coefficient	0.682 mm ⁻¹
F(000)	1312
Crystal size	0.24 x 0.46 x 0.52 mm
Theta range for data collection	2.19 to 26.42 deg.
Limiting indices	0 ≤ h ≤ 13, 0 ≤ k ≤ 27, -16 ≤ l ≤ 15
Reflections collected	5737
Independent reflections	5438 [R(int) = 0.0420]
Absorption correction	Semi-empirical from psi-scans
Max. and min. transmission	0.4340 and 0.3615
Refinement method	Full-matrix least-squares on F ²
Data / restraints / parameters	5436 / 0 / 371
Goodness-of-fit on F ²	1.065

Final R indices [$I > 2\sigma(I)$]	R1 = 0.0363, wR2 = 0.0874
R indices (all data)	R1 = 0.0504, wR2 = 0.0974
Extinction coefficient	0.0014(3)
Largest diff. peak and hole	0.301 and -0.283 e. Å ⁻³

Table 4.8. Atomic coordinates ($\times 10^4$) and equivalent isotropic displacement parameters ($\text{Å}^2 \times 10^3$) for CpFe(dppe)(SC₆H₅). U(eq) is defined as one third of the trace of the orthogonalized U_{ij} tensor.

	x	y	z	U(eq)
Fe(1)	2451(1)	1393(1)	5741(1)	26(1)
P(1)	3086(1)	2327(1)	6226(1)	27(1)
P(2)	3703(1)	1110(1)	7302(1)	27(1)
S(1)	834(1)	1590(1)	6402(1)	35(1)
C(1)	1192(3)	849(1)	4545(2)	42(1)
C(2)	1459(3)	1407(1)	4141(2)	42(1)
C(3)	2818(3)	1431(1)	4387(2)	39(1)
C(4)	3382(3)	897(1)	4944(2)	37(1)
C(5)	2363(3)	532(1)	5032(2)	39(1)
C(6)	-721(2)	1596(1)	5395(2)	33(1)
C(7)	-1619(3)	1148(1)	5401(2)	42(1)
C(8)	-2874(3)	1149(2)	4674(3)	55(1)
C(9)	-3237(3)	1586(2)	3918(3)	61(1)
C(10)	-2371(3)	2030(2)	3882(2)	60(1)

C(11)	-1110(3)	2044(2)	4626(2)	46(1)
C(12)	4565(2)	2652(1)	6108(2)	29(1)
C(13)	5500(3)	2269(1)	5973(2)	36(1)
C(14)	6661(3)	2509(2)	5969(2)	45(1)
C(15)	6892(3)	3136(2)	6081(2)	45(1)
C(16)	5970(3)	3521(1)	6209(2)	41(1)
C(17)	4818(3)	3282(1)	6217(2)	35(1)
C(18)	1958(2)	2964(1)	5695(2)	30(1)
C(19)	1375(3)	3289(2)	6264(2)	47(1)
C(20)	524(3)	3762(2)	5811(3)	64(1)
C(21)	241(3)	3915(2)	4791(3)	56(1)
C(22)	793(3)	3589(1)	4205(2)	44(1)
C(23)	1644(3)	3117(1)	4660(2)	36(1)
C(24)	5161(2)	659(1)	7416(2)	32(1)
C(25)	6358(3)	931(2)	7543(2)	43(1)
C(26)	7386(3)	568(2)	7520(2)	55(1)
C(27)	7245(3)	-54(2)	7365(2)	54(1)
C(28)	6073(3)	-327(2)	7238(2)	48(1)
C(29)	5049(3)	25(1)	7269(2)	38(1)
C(30)	3043(2)	614(1)	8062(2)	29(1)
C(31)	3668(3)	557(1)	9131(2)	33(1)
C(32)	3192(3)	166(1)	9689(2)	41(1)
C(33)	2106(3)	-186(1)	9190(2)	45(1)

C(34)	1492(3)	-144(1)	8131(2)	44(1)
C(35)	1949(3)	254(1)	7566(2)	36(1)
C(36)	3506(3)	2361(1)	7640(2)	31(1)
C(37)	4335(3)	1799(1)	8128(2)	36(1)

Table 4.9. Selected bond lengths (Å) and angles (deg) for CpFe(dppe)(SC₆H₅).

Fe(1)-P(1)	2.1721(7)
Fe(1)-P(2)	2.1872(8)
Fe(1)-S(1)	2.3289(8)
Fe(1)-X(1)	1.702(3)
P(1)-Fe(1)-P(2)	86.61(3)
P(1)-Fe(1)-S(1)	85.05(3)
P(1)-Fe(1)-X(1)	130.2(1)
P(2)-Fe(1)-S(1)	87.72(3)
P(2)-Fe(1)-X(1)	127.1(1)
S(1)-Fe(1)-X(1)	125.9(1)
Fe(1)-S(1)-C(6)	110.73(9)

X(1) refers to the centroid of the C(1)-C(5) ring.

Table 4.10. Crystal data and structure refinement for CpFe(dppe)(SC₆H₄-*p*-NO₂).

Empirical formula	C ₃₇ H ₃₃ FeNO ₂ P ₂ S
Formula weight	673.49
Temperature	173(2) K
Wavelength	0.71073 Å
Crystal system	Triclinic
Space group	P $\bar{1}$
Unit cell dimensions	a = 10.1423(8) Å α = 84.147(6) deg. b = 12.5902(11) Å β = 87.572(5) deg. c = 13.0472(10) Å γ = 71.633(6) deg.
Volume, Z	1572.8(2) Å ³ , 2
Density (calculated)	1.422 mg/m ³
Absorption coefficient	0.683 mm ⁻¹
F(000)	700
Crystal size	0.64 x 0.52 x 0.16 mm
Theta range for data collection	2.12 to 24.99 deg.
Limiting indices	-12 ≤ h ≤ 5, -14 ≤ k ≤ 14, -15 ≤ l ≤ 15
Reflections collected	6540
Independent reflections	5510 [R(int) = 0.0341]
Absorption correction	Semi-empirical from psi-scans
Max. and min. transmission	0.7261 and 0.5321
Refinement method	Full-matrix least-squares on F ²
Data / restraints / parameters	5506 / 0 / 397

Goodness-of-fit on F^2	1.018
Final R indices [$I > 2\sigma(I)$]	R1 = 0.0447, wR2 = 0.1129
R indices (all data)	R1 = 0.0534, wR2 = 0.1206
Largest diff. peak and hole	1.044 and -0.452 e. \AA^{-3}

Table 4.11. Atomic coordinates ($\times 10^4$) and equivalent isotropic displacement parameters ($\text{\AA}^2 \times 10^3$) for $\text{CpFe(dppe)(SC}_6\text{H}_4\text{-}i\text{p-NO}_2\text{)}$. $U(\text{eq})$ is defined as one third of the trace of the orthogonalized U_{ij} tensor.

	x	y	z	$U(\text{eq})$
Fe(1)	1424(1)	4103(1)	2573(1)	23(1)
S(1)	2086(1)	3683(1)	4264(1)	31(1)
P(1)	2846(1)	5124(1)	2416(1)	28(1)
P(2)	3188(1)	2750(1)	2066(1)	30(1)
O(1)	2022(4)	-408(2)	7857(2)	81(1)
O(2)	1258(3)	-1039(2)	6603(2)	74(1)
N(1)	1656(3)	-326(2)	6954(2)	54(1)
C(1)	-394(3)	5468(2)	2384(2)	31(1)
C(2)	77(3)	5029(2)	1424(2)	30(1)
C(3)	68(3)	3909(2)	1506(2)	30(1)
C(4)	-395(3)	3642(2)	2512(2)	32(1)
C(5)	-677(3)	4616(2)	3043(2)	32(1)
C(6)	1892(3)	2501(2)	4983(2)	29(1)
C(7)	1427(3)	1670(2)	4626(2)	33(1)
C(8)	1352(3)	753(2)	5267(2)	39(1)

C(9)	1718(3)	648(2)	6288(2)	41(1)
C(10)	2167(3)	1461(2)	6680(2)	41(1)
C(11)	2255(3)	2368(2)	6031(2)	35(1)
C(12)	3093(3)	5826(2)	3525(2)	28(1)
C(13)	1954(3)	6295(2)	4138(2)	33(1)
C(14)	2057(3)	6884(2)	4956(2)	36(1)
C(15)	3324(3)	6973(2)	5191(2)	39(1)
C(16)	4485(3)	6493(2)	4605(2)	39(1)
C(17)	4368(3)	5931(2)	3765(2)	32(1)
C(18)	2384(3)	6316(2)	1417(2)	36(1)
C(19)	1373(4)	7299(3)	1637(2)	50(1)
C(20)	831(4)	8163(3)	873(3)	61(1)
C(21)	1337(4)	8059(3)	-121(3)	60(1)
C(22)	2350(4)	7109(3)	-352(2)	54(1)
C(23)	2873(3)	6228(3)	405(2)	45(1)
C(24)	3615(3)	2611(2)	693(2)	31(1)
C(25)	3014(3)	3463(2)	-57(2)	34(1)
C(26)	3455(3)	3396(3)	-1080(2)	42(1)
C(27)	4480(3)	2453(3)	-1357(2)	47(1)
C(28)	5080(4)	1592(3)	-619(3)	53(1)
C(29)	4660(3)	1661(2)	401(2)	45(1)
C(30)	3277(4)	1296(3)	2503(2)	50(1)
C(31)	2277(5)	897(3)	2119(3)	62(1)

C(32)	2162(5)	-148(3)	2450(3)	77(1)
C(33)	3044(5)	-793(4)	3148(4)	80(1)
C(34)	4082(4)	-495(3)	3557(3)	72(1)
C(35)	4211(4)	625(3)	3224(3)	72(1)
C(36)	4609(3)	4213(3)	2078(2)	43(1)
C(37)	4754(3)	2999(3)	2480(2)	43(1)

Table 4.12. Selected bond lengths (Å) and angles (deg) for CpFe(dppe)(SC₆H₄-*p*-NO₂).

Fe(1)-S(1)	2.2933(7)
Fe(1)-P(1)	2.2051(8)
Fe(1)-P(2)	2.1795(8)
Fe(1)-X(1)	1.712(3)
S(1)-Fe(1)-P(1)	86.65(3)
S(1)-Fe(1)-P(2)	92.46(3)
S(1)-Fe(1)-X(1)	124.25(8)
P(1)-Fe(1)-P(2)	85.62(3)
P(1)-Fe(1)-X(1)	125.84(8)
P(2)-Fe(1)-X(1)	129.12(8)
Fe(1)-S(1)-C(6)	121.23(10)

X(1) refers to the centroid of C(1)-C(5) ring.

Table 4.13. Crystal data and structure refinement for [CpFe(dppe)(SC₆H₅)]BF₄.

Empirical formula	C ₄₁ H ₄₂ BF ₄ FeOP ₂ S
Formula weight	787.41
Temperature	188(2) K
Wavelength	0.71073 Å
Crystal system	Monoclinic
Space group	P2 ₁ /n
Unit cell dimensions	a = 17.236(2) Å α = 90 deg. b = 11.6260(9) Å β = 105.032(8) deg. c = 19.150(2) Å γ = 90 deg.
Volume, Z	3705.9(6) Å ³ , 4
Density (calculated)	1.411 mg/m ³
Absorption coefficient	0.603 mm ⁻¹
F(000)	1636
Crystal size	0.40 x 0.36x 0.24 mm
Theta range for data collection	1.85 to 25.00 deg.
Limiting indices	-20 ≤ h ≤ 0, 0 ≤ k ≤ 13, -21 ≤ l ≤ 22
Reflections collected	6767
Independent reflections	6527 [R(int) = 0.0353]
Absorption correction	Semi-empirical from psi-scans
Max. and min. transmission	0.5713 and 0.5009
Refinement method	Full-matrix least-squares on F ²
Data / restraints / parameters	6525 / 0 / 460
Goodness-of-fit on F ²	1.052

Final R indices [$I > 2\sigma(I)$] R1 = 0.0501, wR2 = 0.1239

R indices (all data) R1 = 0.0710, wR2 = 0.1387

Largest diff. peak and hole 0.708 and -0.374 e. Å⁻³

Table 4.14. Atomic coordinates ($\times 10^4$) and equivalent isotropic displacement parameters ($\text{Å}^2 \times 10^3$) for $[\text{CpFe}(\text{dppe})(\text{SC}_6\text{H}_5)]\text{BF}_4$. $U(\text{eq})$ is defined as one third of the trace of the orthogonalized U_{ij} tensor.

	x	y	z	U(eq)
Fe(1)	3308(1)	1568(1)	1602(1)	28(1)
S(1)	3 333(1)	2885(1)	2426(1)	36(1)
P(1)	2 043(1)	2082(1)	1066(1)	28(1)
P(2)	3 648(1)	2856(1)	864(1)	31(1)
C(1)	3503(2)	76(3)	2266(2)	49(1)
C(2)	4236(2)	439(3)	2168(2)	47(1)
C(3)	4190(3)	428(3)	1430(2)	51(1)
C(4)	3420(3)	46(3)	1058(2)	53(1)
C(5)	3001(2)	-189(3)	1584(3)	53(1)
C(6)	3566(2)	2262(3)	3309(2)	39(1)
C(7)	2955(3)	2134(3)	3654(2)	44(1)
C(8)	3130(4)	1674(4)	4345(2)	62(1)
C(9)	3886(4)	1334(4)	4694(2)	74(2)
C(10)	4486(4)	1455(5)	4354(3)	77(2)
C(11)	4339(3)	1941(5)	3665(2)	61(1)
C(12)	1492(2)	1265(3)	279(2)	38(1)

C(13)	1334(3)	1717(4)	-417(2)	55(1)
C(14)	926(3)	1066(6)	-1007(3)	77(2)
C(15)	687(3)	-32(6)	-903(3)	87(2)
C(16)	824(3)	-489(4)	-219(4)	86(2)
C(17)	1211(2)	169(4)	374(3)	58(1)
C(18)	1328(2)	2097(3)	1622(2)	33(1)
C(19)	687(2)	2850(3)	1471(2)	39(1)
C(20)	130(2)	2854(4)	1882(2)	50(1)
C(21)	207(3)	2080(4)	2437(2)	56(1)
C(22)	834(3)	1312(5)	2584(2)	64(1)
C(23)	1398(2)	1316(4)	2180(2)	55(1)
C(24)	2070(2)	3582(3)	774(2)	36(1)
C(25)	2813(2)	3884(3)	536(3)	53(1)
C(26)	3878(2)	2303(3)	50(2)	34(1)
C(27)	4655(3)	1985(4)	63(2)	53(1)
C(28)	4846(3)	1557(4)	-542(2)	70(1)
C(29)	4272(3)	1434(4)	-1178(2)	62(1)
C(30)	3512(3)	1735(5)	-1207(2)	69(1)
C(31)	3299(3)	2169(5)	-599(2)	60(1)
C(32)	4530(2)	3738(3)	1227(2)	38(1)
C(33)	5123(2)	3397(4)	1829(2)	46(1)
C(34)	5829(3)	4027(5)	2050(2)	63(1)
C(35)	5946(3)	4995(5)	1670(3)	70(2)

C(36)	5363(3)	5338(4)	1080(2)	60(1)
C(37)	4652(3)	4723(3)	849(2)	46(1)
B(1)	8540(3)	5628(4)	1671(2)	44(1)
F(1)	7760(2)	5801(4)	1467(3)	136(2)
F(2)	8819(3)	5365(3)	1085(2)	124(2)
F(3)	8915(2)	6615(3)	1963(2)	106(1)
F(4)	8722(2)	4758(3)	2147(2)	97(1)
O(1)	6854(4)	2171(7)	492(3)	155(2)
C(38)	7443(8)	2778(10)	996(5)	223(7)
C(39)	7640(6)	2106(10)	1657(4)	161(4)
C(40)	7155(10)	1156(11)	1496(6)	223(7)
C(41)	6795(8)	1199(9)	768(5)	194(6)

Table 4.15. Selected bond lengths (Å) and angles (deg) for [CpFe(dppe)(SC₆H₅)]BF₄.

Fe(1)-S(1)	2.1899(10)
Fe(1)-P(1)	2.2367(10)
Fe(1)-P(2)	2.2380(10)
Fe(1)-X(1)	1.745(4)
S(1)-Fe(1)-P(1)	88.82(4)
S(1)-Fe(1)-P(2)	91.60(4)
S(1)-Fe(1)-X(1)	129.6(1)
P(1)-Fe(1)-P(2)	85.10(3)
P(1)-Fe(1)-X(1)	125.4(1)
P(2)-Fe(1)-X(1)	123.5(1)

X(1) refers to the centroid of C(1)-C(5) ring.

Table 4.16. Crystal data and structure refinement for [CpFe(P₂S)]PF₆.

Empirical formula	C ₄₆ H ₄₆ F ₆ FeP ₃ S
Formula weight	893.65
Temperature	153(2) K
Wavelength	1.54178 Å
Crystal system	Triclinic
Space group	P $\bar{1}$
Unit cell dimensions	a = 10.956(2) Å α = 88.51(3) deg. b = 13.828(3) Å β = 86.05(3) deg. c = 14.039(3) Å γ = 81.53(3) deg.
Volume, Z	2098.4(7) Å ³ , 2
Density (calculated)	1.414 mg/m ³
Absorption coefficient	4.934 mm ⁻¹
F(000)	926
Crystal size	0.14 x 0.22 x 0.26 mm
Theta range for data collection	3.16 to 59.93 deg.
Limiting indices	0 ≤ h ≤ 12, -15 ≤ k ≤ 15, -15 ≤ l ≤ 15
Reflections collected	6742
Independent reflections	6221 [R(int) = 0.0574]
Absorption correction	Semi-empirical from psi-scans
Max. and min. transmission	0.3128 and 0.2523
Refinement method	Full-matrix least-squares on F ²
Data / restraints / parameters	6221 / 0 / 514
Goodness-of-fit on F ²	1.033

Final R indices [$I > 2\sigma(I)$]	R1 = 0.0538, wR2 = 0.1082
R indices (all data)	R1 = 0.2201, wR2 = 0.1490
Largest diff. peak and hole	0.574 and -0.351 e. Å ⁻³

Table 4.17. Atomic coordinates ($\times 10^4$) and equivalent isotropic displacement parameters ($\text{Å}^2 \times 10^3$) for $[\text{CpFe}(\text{P}_2\text{S})]\text{PF}_6$. $U(\text{eq})$ is defined as one third of the trace of the orthogonalized U_{ij} tensor.

	x	y	z	U(eq)
Fe(1)	3988(1)	12882(1)	1102(1)	30(1)
S(1)	4058(2)	11607(1)	241(1)	36(1)
P(1)	5120(2)	11984(1)	2133(1)	32(1)
P(2)	2230(2)	12569(1)	1880(1)	31(1)
P(3)	-2002(2)	13039(1)	7328(1)	40(1)
F(1)	-3006(4)	13930(3)	7002(3)	52(1)
F(2)	-997(4)	12161(3)	7659(3)	62(1)
F(3)	-2665(4)	12296(2)	6782(3)	52(1)
F(4)	-1341(4)	13799(3)	7866(3)	57(1)
F(5)	-1148(4)	13185(3)	6386(3)	61(1)
F(6)	-2844(4)	12890(3)	8282(3)	63(1)
C(1)	5265(7)	13875(5)	915(5)	46(2)
C(2)	4203(7)	14306(4)	1449(5)	44(2)
C(3)	3198(7)	14350(4)	888(5)	45(2)
C(4)	3625(7)	13952(4)	-5(5)	42(2)
C(5)	4909(7)	13669(5)	12(5)	44(2)

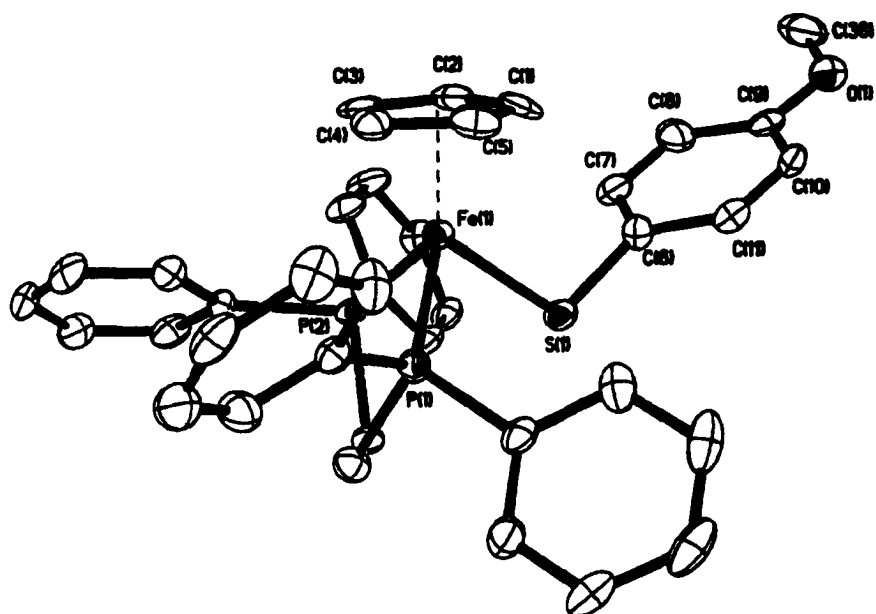
C(6)	4057(6)	10492(4)	972(4)	37(2)
C(7)	3457(6)	10612(4)	1992(4)	35(2)
C(8)	4281(6)	11031(4)	2667(4)	33(2)
C(9)	2185(6)	11256(4)	1957(4)	33(2)
C(10)	3251(6)	9592(4)	2354(5)	43(2)
C(11)	6562(6)	11280(5)	1649(5)	39(2)
C(12)	7082(7)	11461(5)	738(5)	48(2)
C(13)	8150(7)	10911(6)	373(6)	68(3)
C(14)	8742(8)	10169(7)	904(7)	85(3)
C(15)	8263(7)	9975(5)	1820(6)	60(2)
C(16)	7192(7)	10539(5)	2186(5)	46(2)
C(17)	5647(7)	12598(4)	3137(4)	36(2)
C(18)	6887(7)	12709(5)	3169(5)	52(2)
C(19)	7273(8)	13198(6)	3922(6)	66(2)
C(20)	6425(10)	13569(6)	4641(6)	72(3)
C(21)	5216(9)	13478(6)	4597(6)	68(3)
C(22)	4819(7)	12996(5)	3860(5)	50(2)
C(23)	863(6)	13014(5)	1248(5)	38(2)
C(24)	-162(7)	13604(6)	1625(5)	59(2)
C(25)	-1171(8)	13914(6)	1110(7)	76(3)
C(26)	-1195(7)	13617(6)	201(6)	60(2)
C(27)	-205(8)	13024(6)	-195(5)	66(3)
C(28)	811(7)	12719(5)	313(5)	58(2)

C(29)	1827(6)	13026(5)	3087(4)	34(2)
C(30)	1510(7)	12445(5)	3854(5)	47(2)
C(31)	1202(7)	12833(5)	4744(5)	59(2)
C(32)	1195(8)	13803(6)	4895(5)	61(2)
C(33)	1490(7)	14408(5)	4128(5)	61(2)
C(34)	1805(7)	14007(5)	3248(5)	48(2)
C(35)	-7336(12)	14297(8)	7202(7)	95(3)
C(36)	-8232(9)	13742(9)	7452(7)	83(3)
C(37)	-7911(10)	12782(8)	7680(6)	83(3)
C(38)	-6731(11)	12395(8)	7686(7)	90(3)
C(39)	-5831(9)	12929(8)	7436(7)	84(3)
C(40)	-6116(10)	13898(8)	7187(6)	78(3)
C(41)	247(8)	9623(7)	4100(6)	67(3)
C(42)	727(8)	9111(6)	4858(7)	65(2)
C(43)	505(8)	9482(6)	5763(6)	64(2)
C(44)	5556(13)	9120(8)	4657(5)	78(3)
C(45)	4282(13)	9288(9)	4857(6)	82(3)
C(46)	3732(9)	10170(11)	5178(7)	81(3)

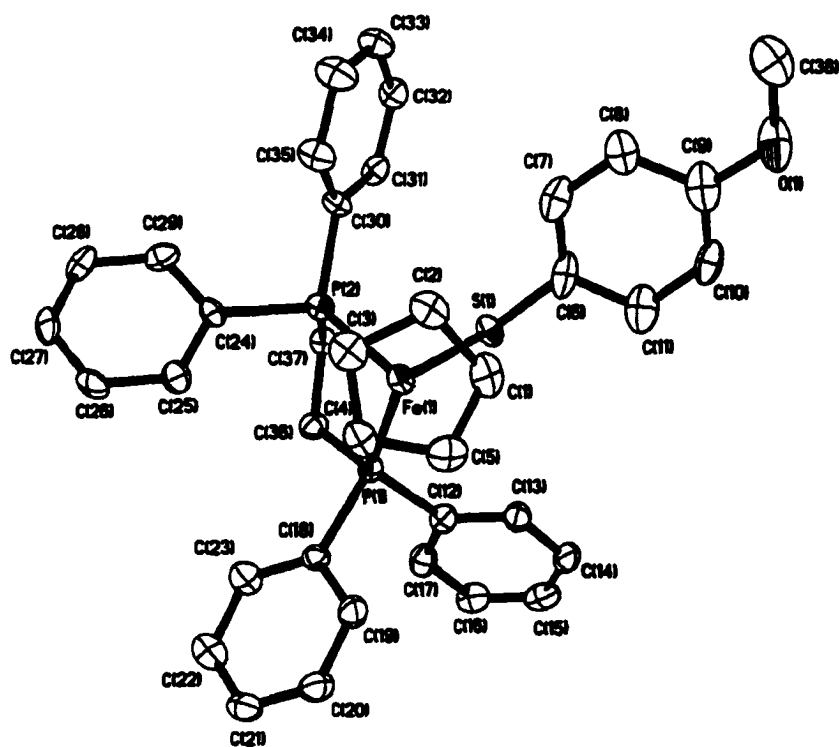
Table 4.18. Selected bond lengths (Å) and angles (deg) for [CpFe(P₂S)]PF₆.

Fe(1)-S(1)	2.153(2)
Fe(1)-P(1)	2.209(2)
Fe(1)-P(2)	2.241(2)
Fe(1)-X(1)	1.746(7)
S(1)-Fe(1)-P(1)	89.10(7)
S(1)-Fe(1)-P(2)	90.95(8)
S(1)-Fe(1)-X(1)	124.3(2)
P(1)-Fe(1)-P(2)	91.69(7)
P(1)-Fe(1)-X(1)	125.7(3)
P(2)-Fe(1)-X(1)	124.6(3)

X(1) refers to the centroid of C(1)-C(5) ring.



A.



B.

Figure 4.29. Thermal ellipsoid drawings of the crystal structure of $\text{CpFe}(\text{dppe})(\text{SC}_6\text{H}_4\text{-}p\text{-OCH}_3)$ at the 50% level with the labeling scheme. The hydrogen atoms are excluded from the figure for the sake of clarity. Drawing A is a side view and B is the top view.

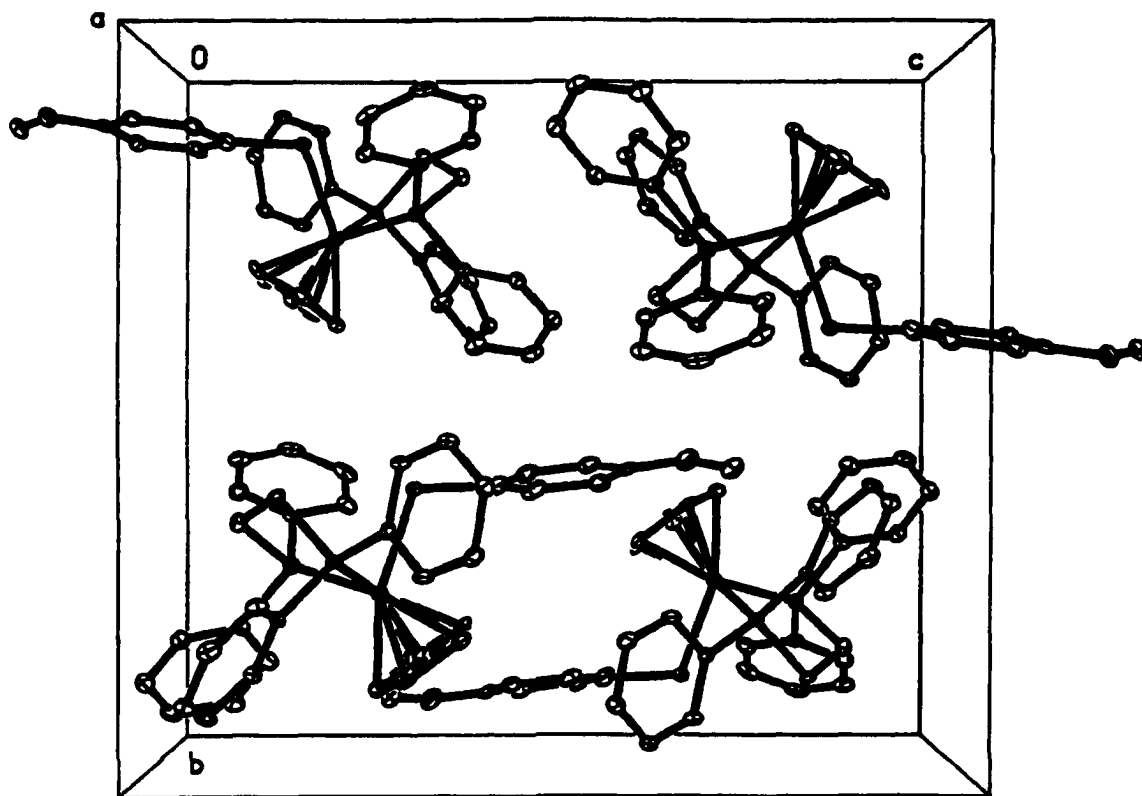
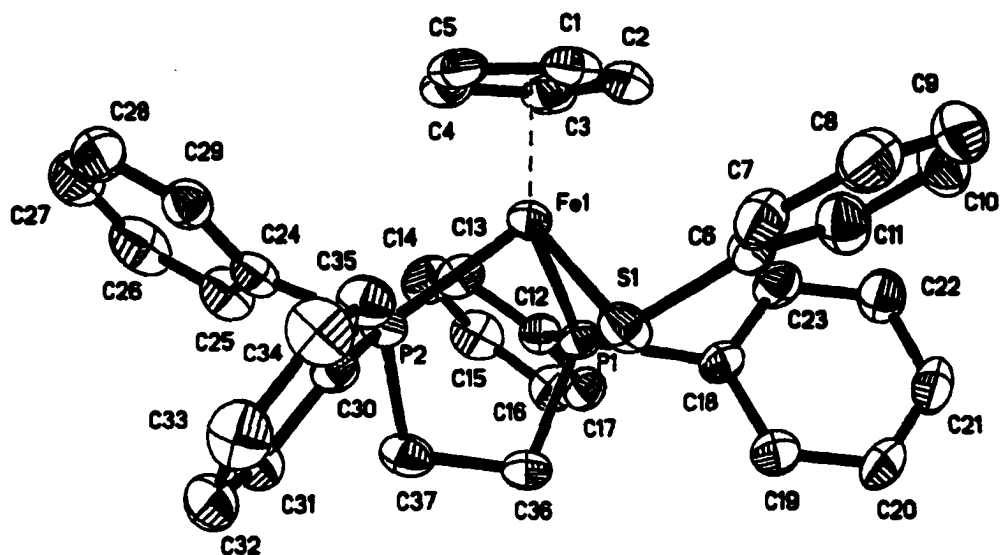
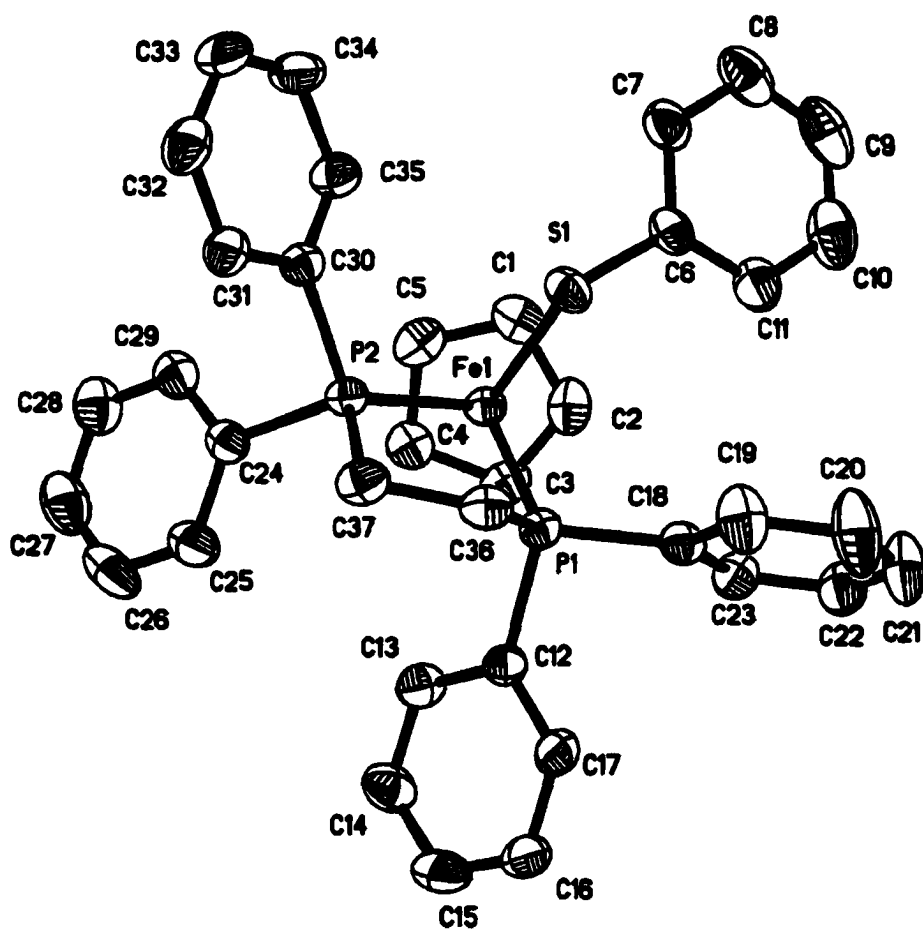


Figure 4.30. Packing diagram of CpFe(dppe)(SC₆H₄-*p*-OCH₃) at the 25% level. The hydrogen atoms are excluded from the figure for the sake of clarity.



A.



B.

Figure 4.31. Thermal ellipsoid drawings of the crystal structure of $\text{CpFe}(\text{dppe})(\text{SC}_6\text{H}_5)$ at the 50% level with the labeling scheme. The hydrogen atoms are excluded from the figure for the sake of clarity.

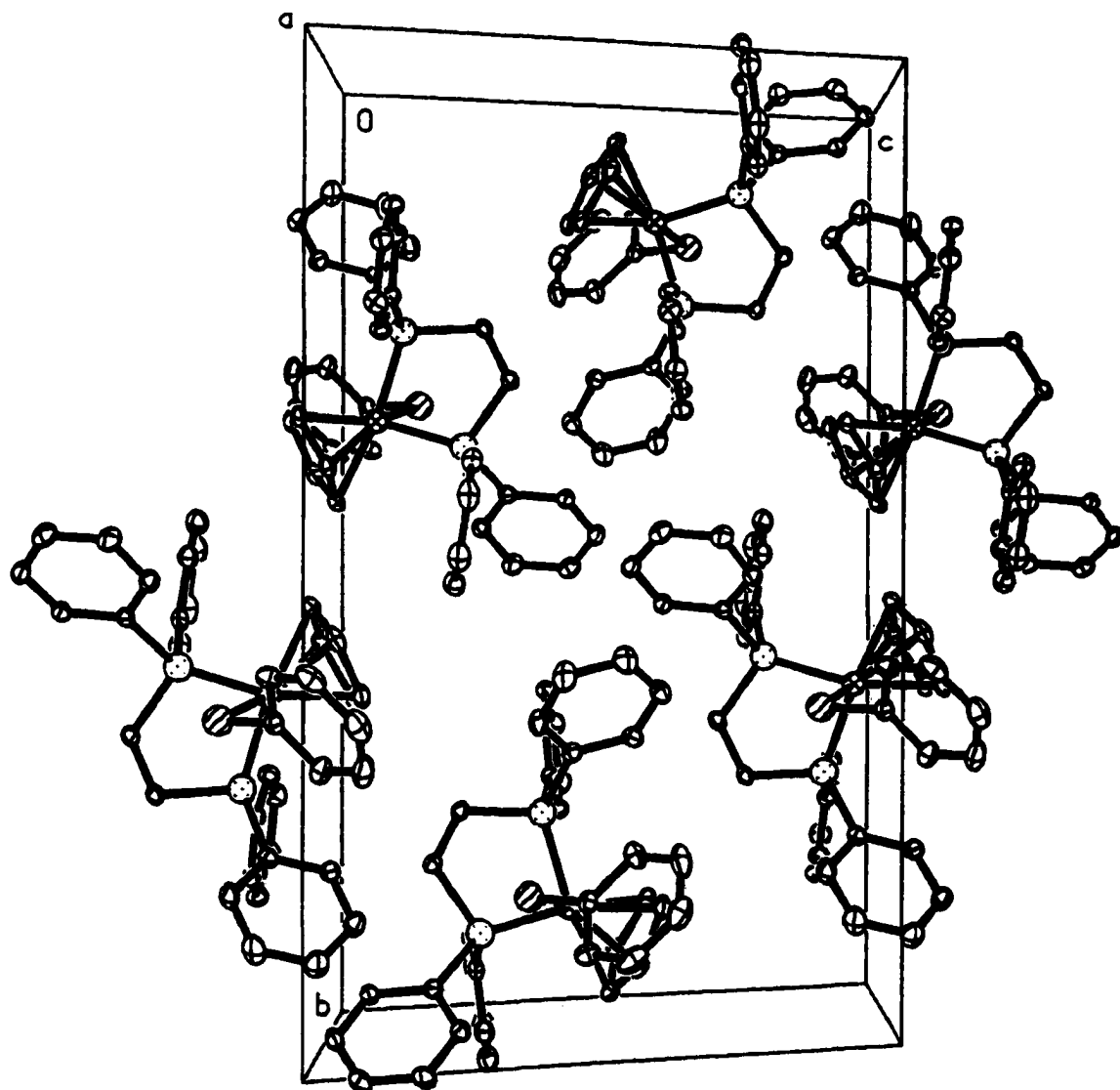


Figure 4.32. Packing diagram of $\text{CpFe}(\text{dppe})(\text{SC}_6\text{H}_5)$ at the 25% level. The hydrogen atoms are excluded from the figure for the sake of clarity.

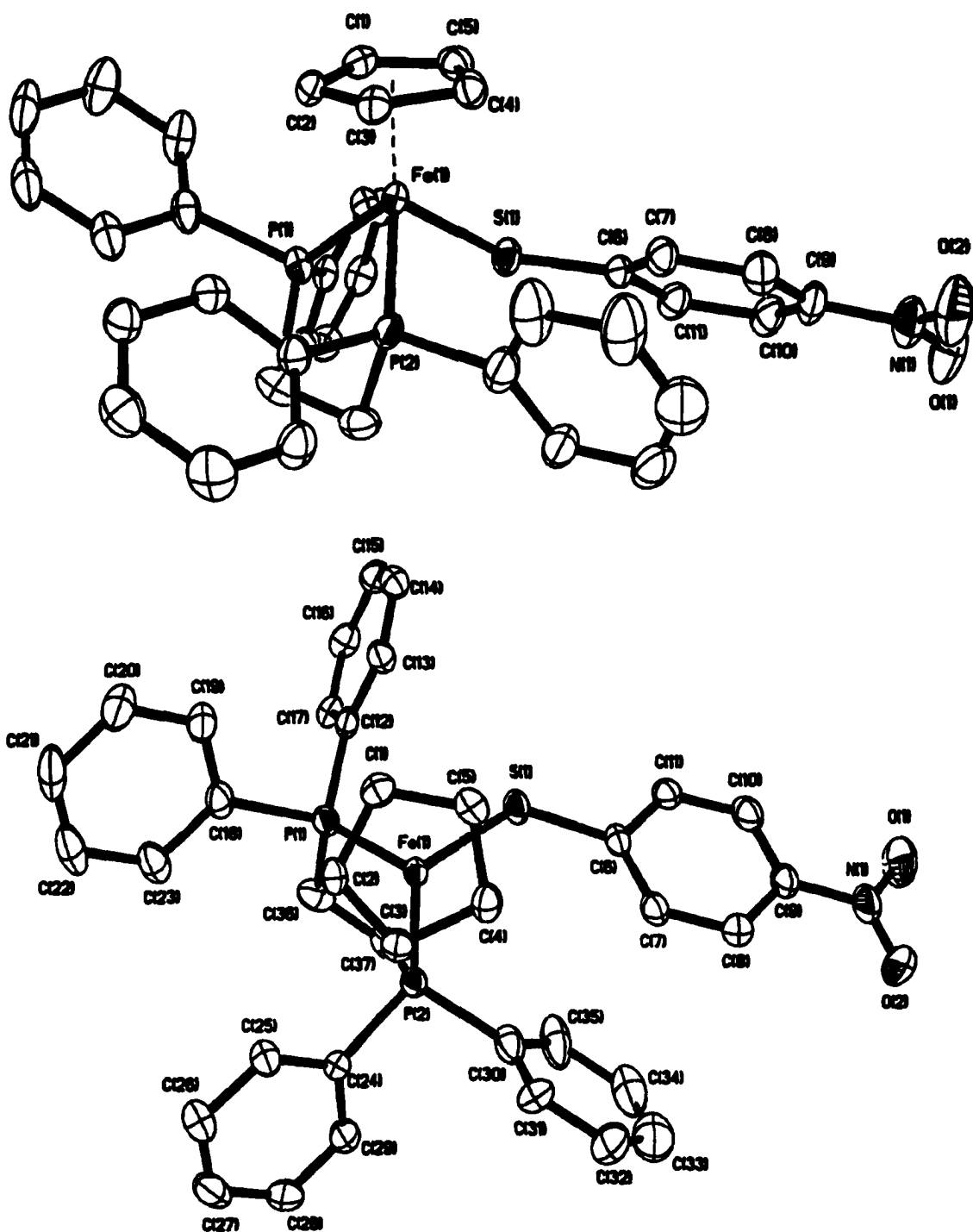


Figure 4.33. Thermal ellipsoid drawing of the crystal structure of $\text{CpFe}(\text{dppe})(\text{SC}_6\text{H}_4\text{-}p\text{-NO}_2)$ at the 40% level with the labeling scheme. The hydrogen atoms are excluded from the figure for the sake of clarity.

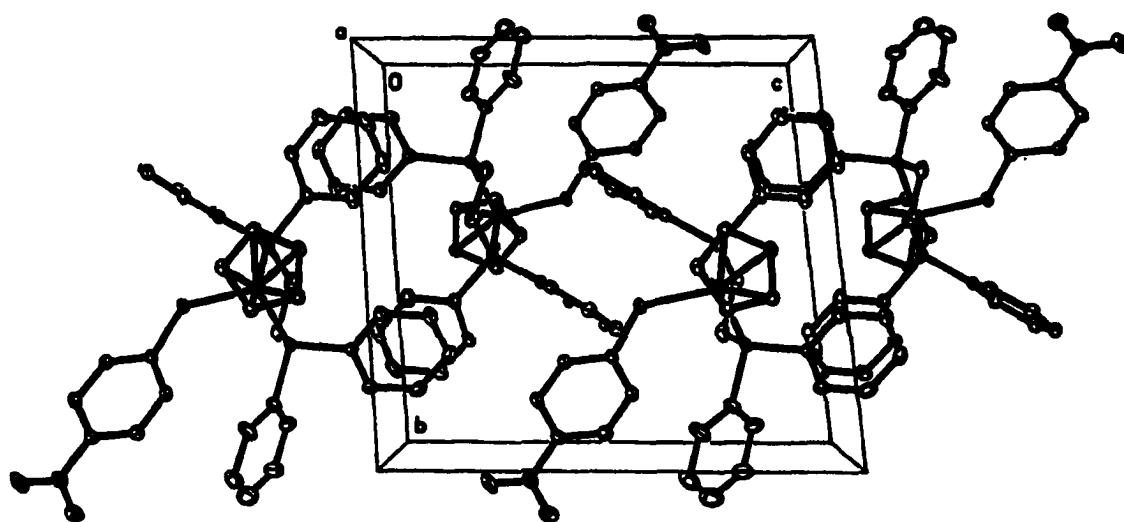
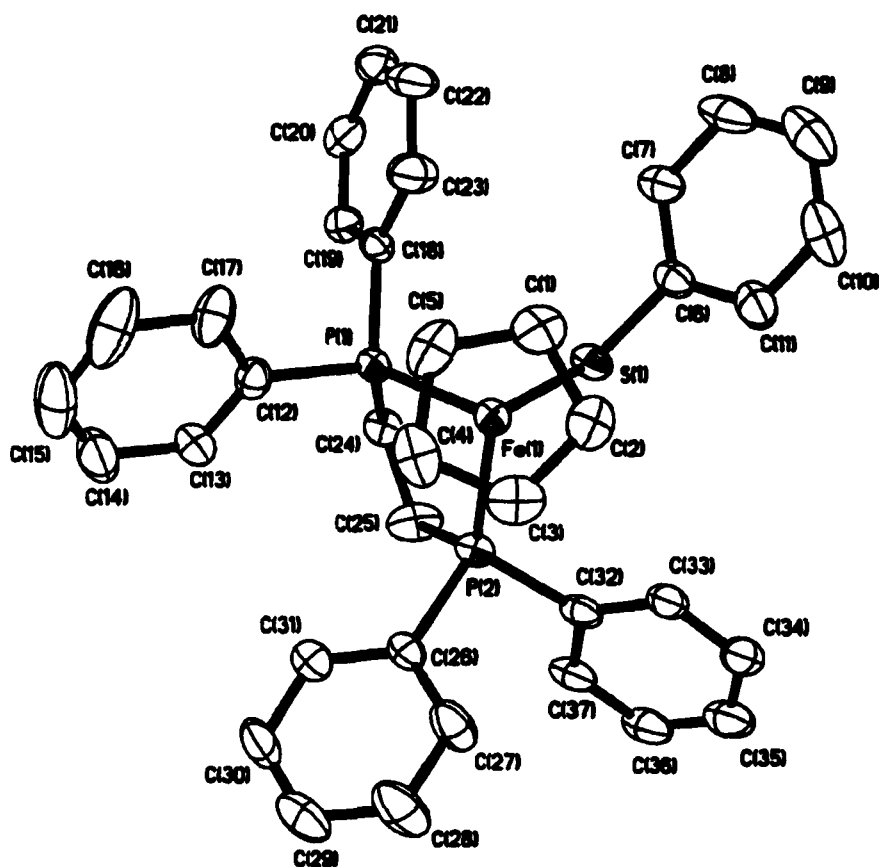
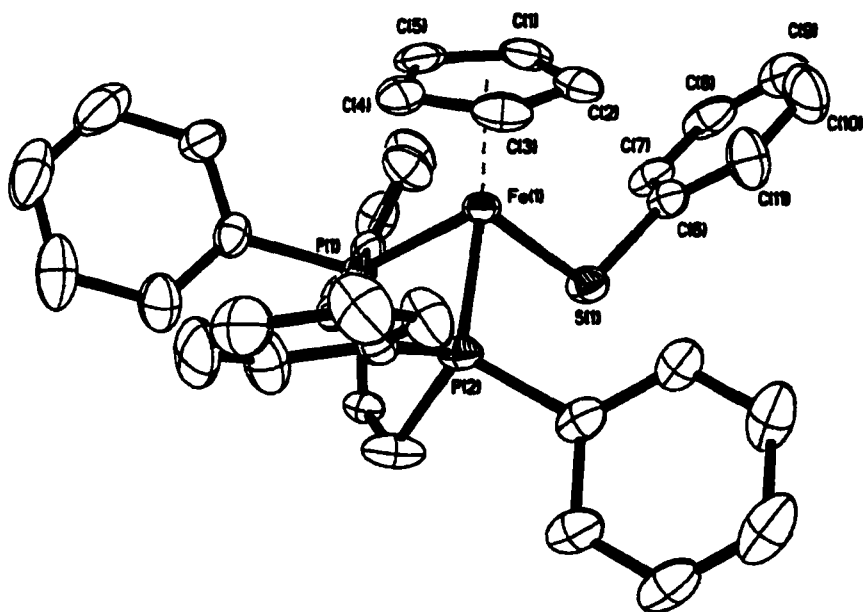


Figure 4.34. Packing diagram of $\text{CpFe}(\text{dppe})(\text{SC}_6\text{H}_4\text{-}p\text{-NO}_2)$ at the 20% level. The hydrogen atoms are excluded from the figure for the sake of clarity.



A.



B.

Figure 4.35. Thermal ellipsoid drawing of the crystal structure of $[\text{CpFe}(\text{dppe})(\text{SC}_6\text{H}_5)]\text{BF}_4$ at the 40% level with the labeling scheme. The hydrogen atoms are excluded from the figure for the sake of clarity.

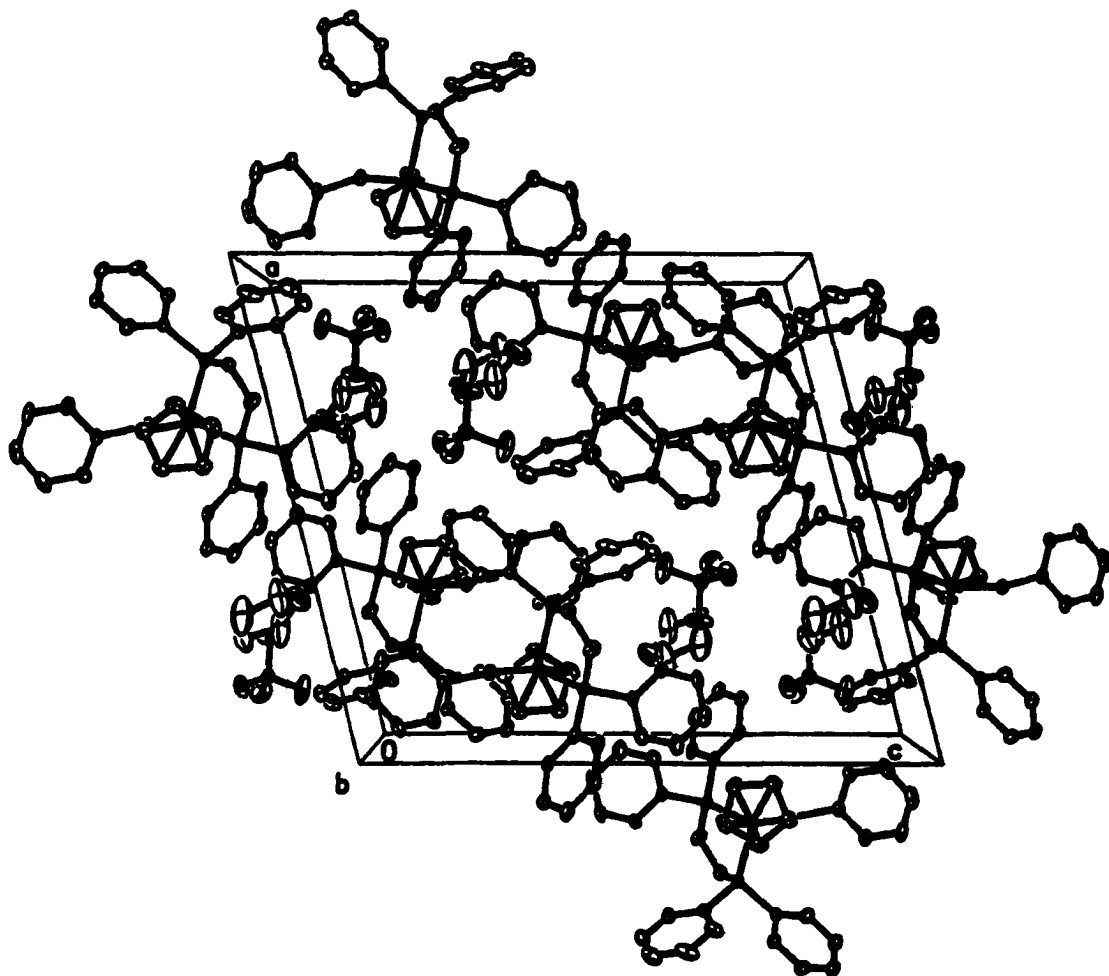


Figure 4.36. Packing diagram of $\text{CpFe}(\text{dppe})(\text{SC}_6\text{H}_5)]\text{BF}_4$ at the 20% level. The hydrogen atoms are excluded from the figure for the sake of clarity

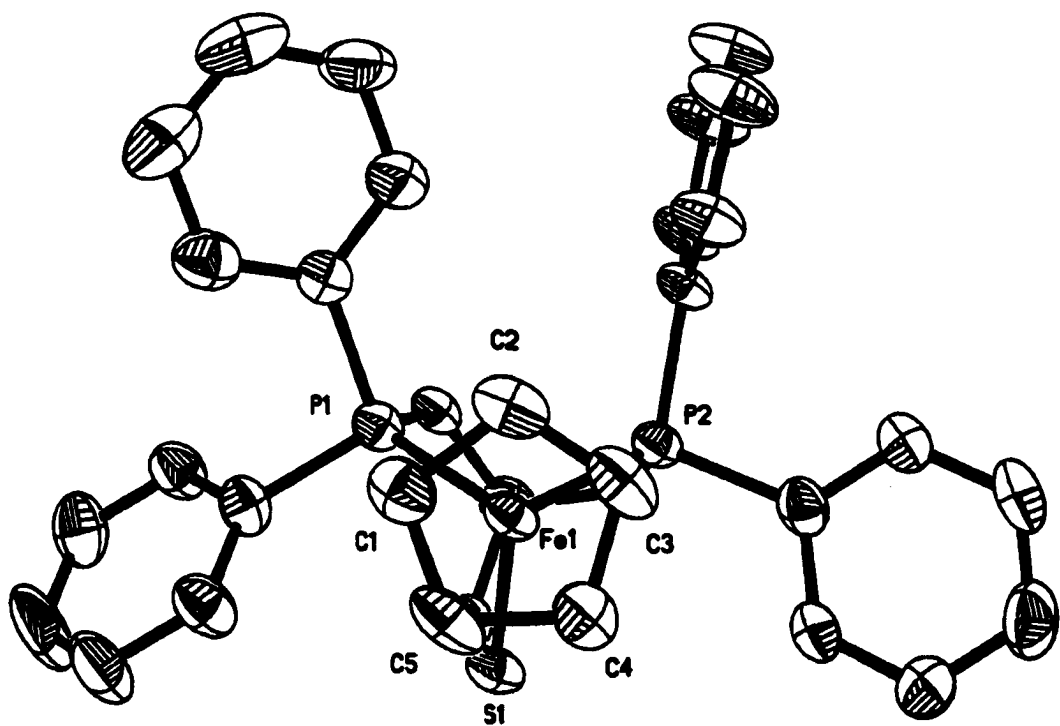
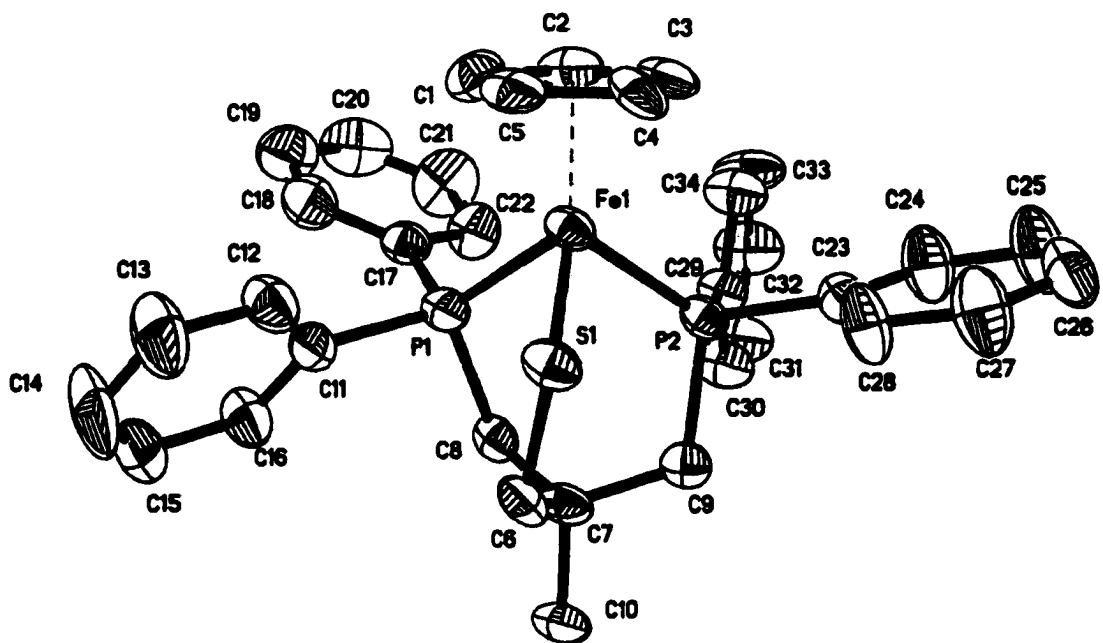


Figure 4.37. Thermal ellipsoid drawing of the crystal structure of $[\text{CpFe}(\text{P}_2\text{S})]\text{PF}_6$ at the 50% level with the labeling scheme. The hydrogen atoms are excluded from the figure for the sake of clarity.

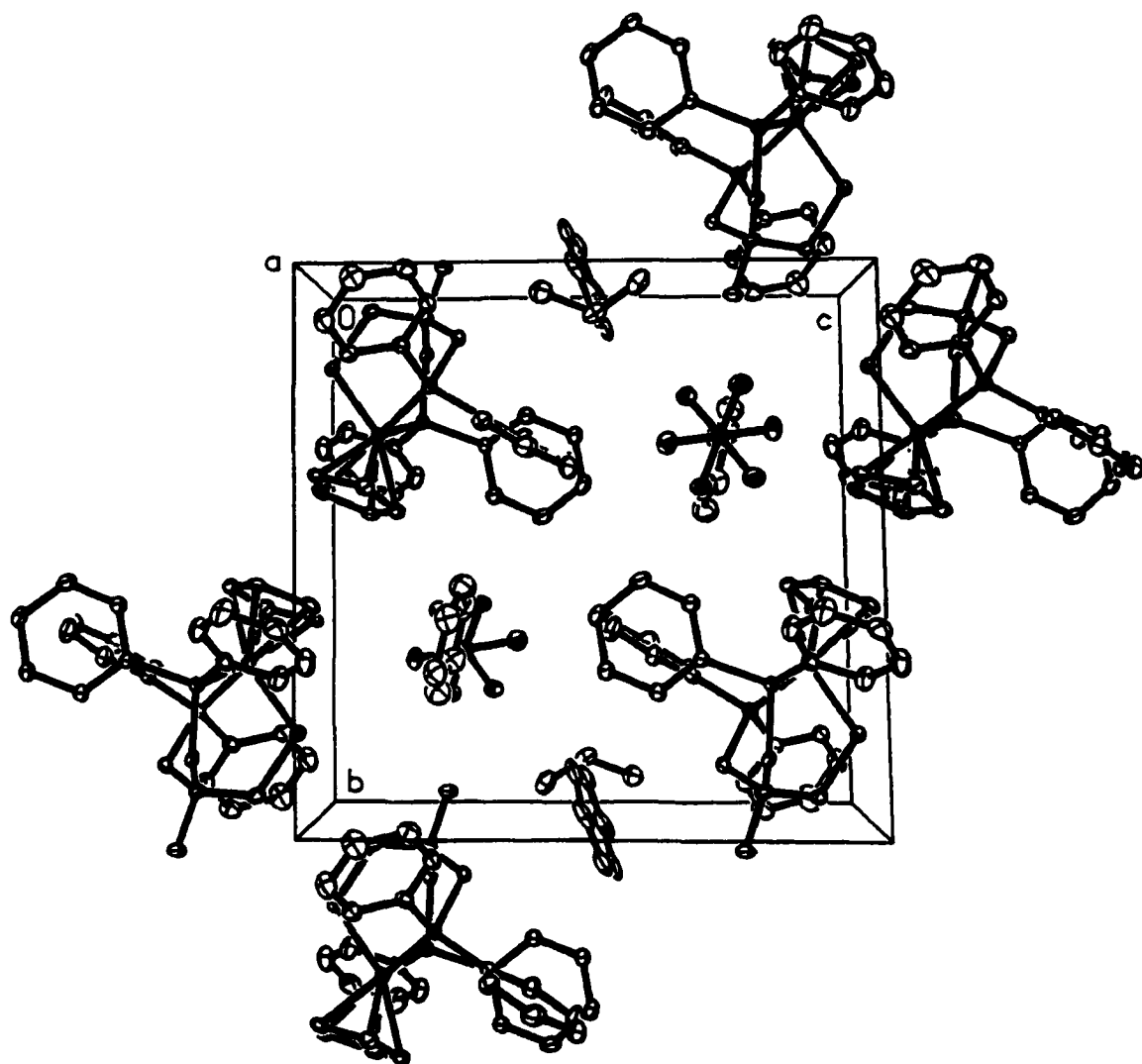


Figure 4.38. Packing diagram of [CpFe(P₂S)]PF₆ at the 20% level. The hydrogen atoms are excluded from the figure for the sake of clarity.

4.3.6 Results of the Molecular Orbital Calculations

Some results of the density functional calculations are presented in Table 4.19. The Highest Occupied Molecular Orbitals (HOMOs) and Lowest Unoccupied Molecular Orbitals (LUMO) of $\text{CpFe}(\text{CO})_2(\text{SCH}_3)$, $[\text{CpFe}(\text{CO})_2(\text{SCH}_3)]^+$, $\text{CpFe}(\text{PH}_3)_2(\text{SCH}_3)$, and $[\text{CpFe}(\text{PH}_3)_2(\text{SCH}_3)]^+$ were calculated by the DFT method.

Table 4.19. Density functional calculations of the HOMO and LUMO in the units of hartrees and electron volts for the following compounds: $\text{CpFe}(\text{CO})_2(\text{SCH}_3)$, $[\text{CpFe}(\text{CO})_2(\text{SCH}_3)]^+$, $\text{CpFe}(\text{PH}_3)_2(\text{SCH}_3)$, and $[\text{CpFe}(\text{PH}_3)_2(\text{SCH}_3)]^+$

Compounds	HOMO (hartrees)	LUMO (hartrees)	HOMO (eV)	LUMO (eV)
$\text{CpFe}(\text{CO})_2(\text{SCH}_3)$	-0.1705	-0.1084	-0.4639	-0.2950
$[\text{CpFe}(\text{CO})_2(\text{SCH}_3)]^+$	-0.3758	-0.2912	-1.0226	-0.7924
$\text{CpFe}(\text{PH}_3)_2(\text{SCH}_3)$	-0.1444	-0.0079	-0.3929	-0.0215
$[\text{CpFe}(\text{PH}_3)_2(\text{SCH}_3)]^+$	-0.3215	-0.2540	-0.8748	-0.6911

4.4 Discussion

This work involves the study of the electron-rich iron-thiolate complexes, $\text{CpFe}(\text{dppe})(\text{SC}_6\text{H}_4\text{-}p\text{-Z})$ where $Z = \text{OCH}_3, \text{H}, \text{Cl}, \text{CF}_3$ and NO_2 ($\text{dppe} = \text{Ph}_2\text{PCH}_2\text{CH}_2\text{PPh}_2$). Part of this work involves using $\text{CpFe}(\text{dppe})(\text{SC}_6\text{H}_5)$ as a potential model system for hydrogenase. Treichel stated that addition of a protic acid to $\text{CpFe}(\text{dppe})(\text{SC}_6\text{H}_5)$ gives the oxidized product and molecular hydrogen.⁴⁷ If this is the case, then this would provide a model for hydrogenase and a way to determine a possible mechanism for the formation of molecular hydrogen from proton. Other parts of this work involves studying how changes in the aryl substituents in the para position from the sulfur phenyl group affect the reactivity, redox potential, and structure of the parent compound, $\text{CpFe}(\text{dppe})(\text{SC}_6\text{H}_5)$.

Sellmann *et al.* have synthesized an iron-thiolate compound that reacts with proton to produce molecular hydrogen.⁴¹ As shown Scheme 4.1, elimination of H₂ from a metal hydride species can take place via a concerted H₂ elimination from a dithiol species (complexes IV). Theoretical calculations have shown that elimination of H₂ from a metal hydride species is the more favorable mechanism (metal-ligand activation).⁶⁰ This reaction occurs stoichiometrically.

Bitterwolf also synthesized a dinuclear chromium complex as a model for hydrogenase (Figure 4.39).⁶¹ Protonation occurs at the metal sites and then reductive elimination of dihydrogen occurs (metal-metal activation) leaving a doubly charged intermediate which then decomposes. This reaction is also non-catalytic.

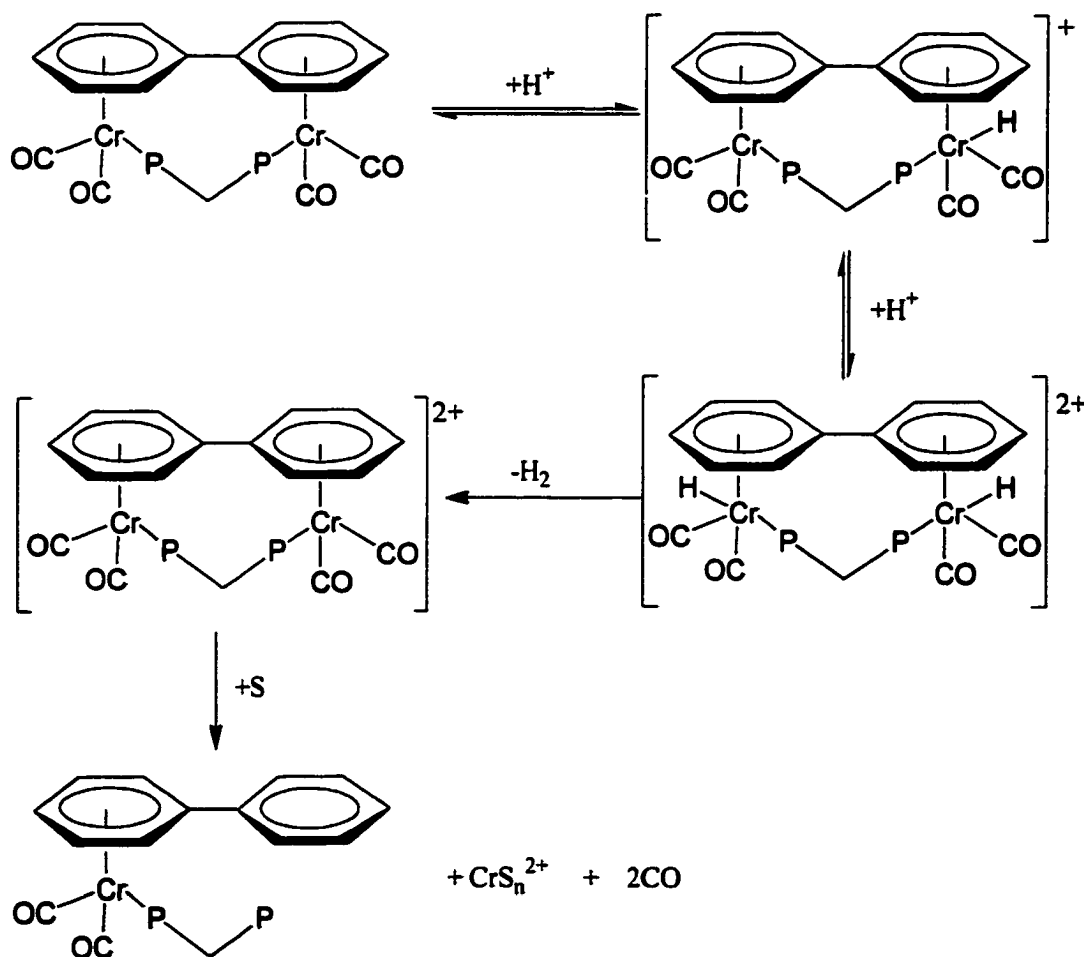


Figure 4.39. Dinuclear model for hydrogenase.⁶¹

Trichel mentioned that $\text{CpFe}(\text{dppe})(\text{SC}_6\text{H}_5)$ could generate dihydrogen upon protonation.⁴⁷ As a prelude to studying the reaction of $\text{CpFe}(\text{dppe})(\text{SC}_6\text{H}_5)$ with proton, we envisaged a possible mechanism for the reaction of H^+ by $\text{CpFe}(\text{dppe})(\text{SC}_6\text{H}_5)$ to give H_2 (Figure 4.40). According to this mechanism, the first step is protonation at the sulfur site. This forms an extremely acidic proton⁶² which can potentially hydrogen bond to a sulfur site on another molecule of $\text{CpFe}(\text{dppe})(\text{SC}_6\text{H}_5)$. The bridging hydrogen becomes hydridic in character and could be susceptible to electrophilic attack by another proton. If this happens, oxidative reduction could occur forming the products, $[\text{CpFe}(\text{dppe})(\text{SC}_6\text{H}_5)]^+$ and dihydrogen.

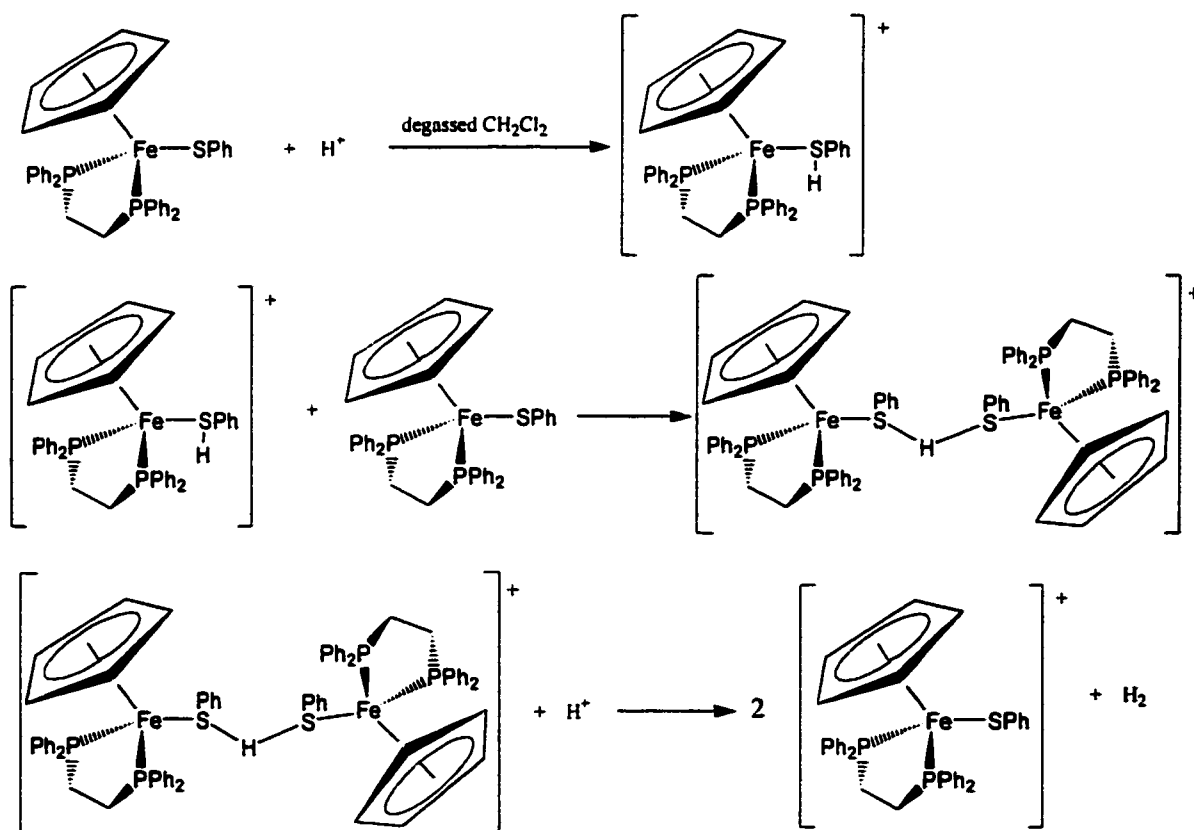


Figure 4.40. Proposed mechanism for ligand-ligand activation for the liberation of dihydrogen.

In testing the proposed mechanism, the first step was to generate dihydrogen by adding $\text{HBF}_4 \cdot \text{O}(\text{CH}_3)_2$ to $\text{CpFe}(\text{dppe})(\text{SC}_6\text{H}_5)$ in dry degassed CH_2Cl_2 under argon. The experiment demonstrated that protonation took place according to ^1H NMR but not oxidation and evolution of dihydrogen. The parent compound, $\text{CpFe}(\text{dppe})(\text{SC}_6\text{H}_5)$ is olive-green when dissolved in CH_2Cl_2 ; however, upon protonation the solution turns red. The oxidized species, $[\text{CpFe}(\text{dppe})(\text{SC}_6\text{H}_5)]\text{BF}_4$, is dark blue in color. When the solvated protonated species is exposed to the air, oxidation occurs. The solution turns from a red color to a dark blue color. Even under the same conditions as Triechel described, using acetone under argon as solvent instead of CH_2Cl_2 , a red color was exhibited upon protonation instead of the dark blue color of the oxidized species. Apparently, the compound, $\text{CpFe}(\text{dppe})(\text{SC}_6\text{H}_5)$, is not a good model for hydrogenases.

By making the iron-thiolate complex more electron rich, there is a better chance for dihydrogen evolution to take place. The tripodal complex, $\text{CpFe}(\text{P}_2\text{S})$, was synthesized (Figure 4.41) to increase the electron environment about the sulfur and also the chelation effect should help to prevent acid solvolysis from taking place. According to cyclic voltammetry experiments, the redox potentials for $\text{CpFe}(\text{P}_2\text{S})$ and $\text{CpFe}(\text{dppe})(\text{SC}_6\text{H}_5)$ are -453 mV and -330 mV vs. NHE, respectively (Table 4.2). Obviously, $\text{CpFe}(\text{P}_2\text{S})$ can be more easily oxidized than $\text{CpFe}(\text{dppe})(\text{SC}_6\text{H}_5)$.

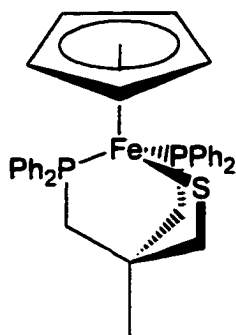


Figure 4.41. The compound, $\text{CpFe}(\text{P}_2\text{S})$, which was synthesized as a potential model system for hydrogenase.

An experiment was set up under argon to test for hydrogen gas evolution using the greenish-brown compound, $\text{CpFe}(\text{P}_2\text{S})$ and excess $\text{HBF}_4 \cdot \text{O}(\text{CH}_3)_2$. A unique Schlenk glass vessel (Figure 4.7) was used to trap hydrogen gas that was, in turn, used for the hydrogenation of styrene to produce ethyl benzene. As $\text{HBF}_4 \cdot \text{O}(\text{CH}_3)_2$ was added to a benzene- d_6 solution of $\text{CpFe}(\text{P}_2\text{S})$, an immediate color change from greenish-brown to violet-pink took place, which is indicative of oxidation. The compound, $[\text{CpFe}(\text{P}_2\text{S})]\text{BF}_4$ is violet-pink when dissolved in benzene. This was allowed to stir for 24 hours to make sure that any hydrogen produced would be trapped in the hydrogenation reaction.

Apparently, no hydrogen gas was produced since ^1H NMR could not detect the product, ethyl benzene. Some spurious oxygen may have been in the solvent or the acid solution to cause the oxidation to occur. This reaction was attempted three times with the same results. The compound, $\text{CpFe}(\text{P}_2\text{S})$, is extremely susceptible to oxidation in the presence of a Brønsted acid and oxygen.

Another experiment was set up under argon to test for hydrogen gas evolution using zinc powder at the same concentration as the compound $\text{CpFe}(\text{P}_2\text{S})$ in the previous experiment and $\text{HBF}_4 \cdot \text{O}(\text{CH}_3)_2$. As $\text{HBF}_4 \cdot \text{O}(\text{CH}_3)_2$ was added to a benzene- d_6 solution of zinc powder, an immediate evolution of hydrogen gas occurred. This was allowed to stir for 4 hours to make sure that any hydrogen gas produced would be available for the hydrogenation reaction. Enough hydrogen gas was produced so that the ^1H NMR was able to detect the hydrogenation product, ethyl benzene.

Not only has protonation been involved in the reactivity study of electron rich iron-thiolates but also methylation. Recently, Lippard *et al.* reported that iron-sulfur clusters $[\text{4Fe-4S}]$ coordinated by a single phenyl thiolate at each metal accepts a methyl group from $(\text{CH}_3\text{O})_3\text{PO}$.⁶³ They also determined that the methylation occurs at the terminal thiolate group; however, ligand exchange occurs between the resulting thioether and the $[(\text{CH}_3\text{O})_2\text{PO}_2]^-$ anion (Figure 4.42).

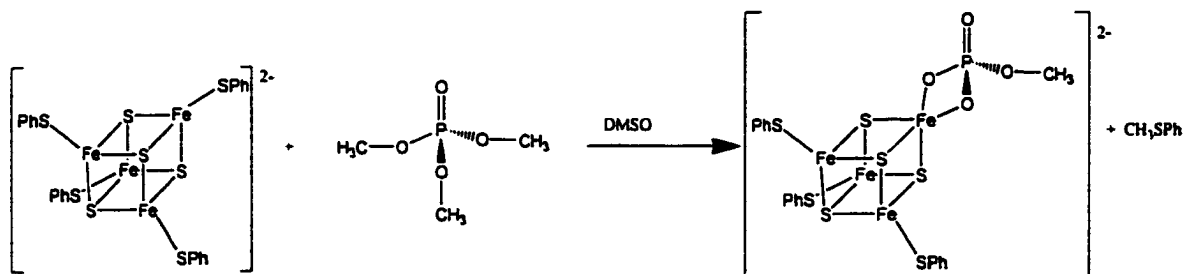


Figure 4.42. Methylation and ligand exchange reaction between $[\text{4Fe-4S}]$ -cluster and $(\text{CH}_3\text{O})_3\text{PO}$.⁶³

A similar ligand exchange process occurs in the pseudo-first order kinetic study involving the reaction between $\text{CpFe}(\text{dppe})(\text{SC}_6\text{H}_4\text{-}p\text{-Z})$ (where $\text{Z} = \text{OCH}_3$,

H, Cl, CF₃, and NO₂) and excess iodomethane in acetone to form the thioether (Figure 4.9). According to Scheme 4.3, methylation takes place first, which is the rate-determining step, and then ligand exchange between the thioether and iodide occurs. Figure 4.10 shows a confirmation of the product by the spectrum representing the absorbance vs. wavelength of the product of the reaction between 1.0 mM CpFe(dppe)(SC₆H₅) and 0.10 M CH₃I and also a spectrum of 1.0 mM CpFe(dppe)I. The results of a kinetic experiment where 1.0 mM CpFe(dppe)(SC₆H₅) reacts with 0.1 M CH₃I is shown in Figure 4.9.A. Notice the two isosbestic points showing the reactants cleanly reacting to form the product (Figure 4.9.B).

The influence of the thiolate ligand substituent Z on the reaction rate is summarized in Table 4.1. The example of a Beer's Law plot that is shown in Figure 4.11 shows the linear change in concentration vs. absorbance from the reaction between CpFe(dppe)(SC₆H₄-*p*-Z) and excess CH₃I. The trace and curve fits (using a nonlinear least-squares program by Specfit)⁵² vs. time (Figures 4.12 and 4.13) show that the reactions are first order in CH₃I since in each case the residuals, $([A]_{t,obs} - [A]_{t,calc})$, contain very small systematic deviations.⁶⁴

Ashby *et al.* accomplished a similar set of experiments using CpFe(CO)₂(SC₆H₄-*p*-Z) and excess iodomethane in acetone.⁶⁵ A linear free energy relationship is observed between the reaction rate and the Hammett substituent constant (σ). A similar correlation is observed in this study between the relative donor ability of the aryl substituent and reaction rate. The calculated Hammett reaction constant using the compound CpFe(CO)₂(SC₆H₄-*p*-Z) is $\rho = -1.82$ which is close to the value of $\rho = -2.14$ that is obtained for the compound CpFe(dppe)(SC₆H₄-*p*-Z) (Figure 4.14). This suggests that the mechanism by which CpFe(dppe)(SC₆H₄-*p*-Z) and CpFe(CO)₂(SC₆H₄-*p*-Z) are methylated is the same. If the mechanism involves frontier orbital control, as is described in the

case of $\text{CpFe}(\text{CO})_2(\text{SC}_6\text{H}_4\text{-}p\text{-Z})$,⁶⁵ or charge control, then the expectation is that the more electron withdrawing substituent should decrease the rate of methylation. The kinetic results obtained from methylating $\text{CpFe}(\text{dppe})(\text{SC}_6\text{H}_4\text{-}p\text{-Z})$ coincides with this expectation.

On average, the reactions of $\text{CpFe}(\text{dppe})(\text{SC}_6\text{H}_4\text{-}p\text{-Z})$ and CH_3I are approximately two hundred times faster than the corresponding reactions of the dicarbonyl analogs. Also, higher oxidation potential values are found in $\text{CpFe}(\text{CO})_2\text{X}$ compared with those for $\text{CpFe}(\text{dppe})\text{X}$ complexes ($\text{X} = \text{Cl}$, or I) which is not surprising, since the diphos derivatives are much more electron rich.^{47,66} According to Hückel molecular orbital calculations and He(I) photoelectron-spectra, the HOMO for the Fe(III) -phosphorus derivatives are primarily metal in character;^{67,68} however, according to reactivity studies⁶⁶, PES studies⁶⁵, and the density functional calculations that were carried out in this work, the HOMO of $\text{CpFe}(\text{CO})_2(\text{SC}_6\text{H}_4\text{-}p\text{-Z})$ and $\text{CpFe}(\text{dppe})(\text{SC}_6\text{H}_4\text{-}p\text{-Z})$ are primarily sulfur in character.

By looking at the relative rates of reaction in Table 4.1, the OCH_3 derivative reacts 232 times faster than the NO_2 derivative. In fact, as the aryl substituent becomes more electron withdrawing, the reaction becomes slower. These data coincide with the cyclic voltammetric data (Table 4.2). The cyclic voltammograms for each complex are shown in Figures 4.15 – 4.20. The electron transfer associated with this redox process can be assigned to the oxidation of the Fe(II) -thiolate complex $\text{CpFe}(\text{dppe})(\text{SC}_6\text{H}_4\text{-}p\text{-Z}) \rightarrow [\text{CpFe}(\text{dppe})(\text{SC}_6\text{H}_4\text{-}p\text{-Z}) + 1e^-$. The compounds, $\text{CpFe}(\text{dppe})(\text{SC}_6\text{H}_5)$ and $[\text{CpFe}(\text{dppe})(\text{SC}_6\text{H}_5)]\text{BF}_4$ (Figures 4.31 and 4.35), have been crystallographically characterized and a comparison of the Fe-S bond distances between the complexes has been carried out. The Fe(II) and Fe(III) derivatives were prepared by slow vapor diffusion of pentane in a saturated THF solution of the

compound under nitrogen. No solvents were trapped in the lattice of the crystal structure of the Fe(II) species but the Fe(III) species contains a THF molecule in its asymmetric unit. The Fe-S bond length for the CpFe(dppe)(SC₆H₅) complex is substantially longer (2.3289(8) Å) as compared with the [CpFe(dppe)(SC₆H₅)]BF₄ complex (2.1899(10) Å). This can be explained by the fact that the orbital from which the electron has been removed is the iron-sulfur π -antibonding HOMO.⁶⁶

According to the CV data, the ratio of anodic to cathodic peak currents are near unity indicating a chemically reversible process with no decomposition of oxidized product; however, $E_{pc}-E_{pa}$ are slightly greater than 59 mV and vary with sweep rate in a manner typical of a quasi-reversible electron transfer process.⁶⁹ The required potentials for oxidation vary from -577 mV for the OCH₃ derivative to -357 mV for the NO₂ derivative versus the Ag/AgNO₃ reference electrode.

A linear free energy relationship is observed in this electrochemical study between the relative donor ability of the aryl substituent and the half-wave potential of the compounds CpFe(dppe)(SC₆H₄-*p*-Z) (Figure 4.21). Notice that the OCH₃ derivative is the most easily oxidizable whereas the NO₂ derivative is the least oxidizable. The NO₂ substituent best stabilizes the complex by withdrawing electron density from the HOMO which is the $d\pi-p\pi$ antibonding orbital.⁶⁵

This can also be corroborated with the solid state evidence. A comparison of the Fe-S bond distances between the complexes, CpFe(dppe)(SC₆H₄-*p*-OCH₃) (Figure 4.29), CpFe(dppe)(SC₆H₅) (Figure 4.31), and CpFe(dppe)(SC₆H₄-*p*-NO₂)(Figure 4.33), was accomplished by single-crystal X-ray crystallographic analysis of a suitable crystal of each compound. The H and NO₂ derivatives were prepared by slow vapor diffusion of pentane in a saturated THF solution of the compound under nitrogen. The OCH₃ derivative was prepared by

evaporation from a saturated CH₂Cl₂ solution of the compound under nitrogen. No solvents were found in the lattice of the crystal structures of any of the Fe(II) complexes. Tables 4.6, 4.9, 4.12, 4.15, and 4.18. list the selected bond distances and angles for each compound. The Fe-S bond length for these compounds are comparable with those of other structurally characterized iron(II)-phenyl thiolate complexes (Table 4.20).

Table 4.20. Fe-S Bond Lengths (Å) and Angles (deg) for Structurally Characterized Iron(II) Aryl Thiolate Complexes.

Fe(II) Compounds	Fe-S-C Angle (deg)	Fe-S Å	Ref.
<i>cis, cis, cis</i> -Fe(CO) ₂ (dppe)(SC ₆ H ₅) ₂	112.4(5)	2.339(5)	57
	109.5(5)	2.343(4)	
<i>cis, cis, cis</i> -Fe(CO) ₂ (dppe)(SC ₆ H ₅) ₂ ^a	114.9(5)	2.350(4)	57
	107.7(5)	2.346(5)	
Fe ₂ (SC ₆ H ₅) ₄ (dppe) ₂	112.7(3)	2.284(2)	58
	108.9(3)	2.293(2)	
FeH(SC ₆ H ₅)(CO) ₂ (P(OC ₆ H ₅) ₃) ₂	113.2(4)	2.343(3)	59
CpFe(dppe)(SC ₆ H ₄ - <i>p</i> -OCH ₃)	110.7(2)	2.332(2)	this study
CpFe(dppe)(SC ₆ H ₅)	110.73(9)	2.3289(8)	this study
CpFe(dppe)(SC ₆ H ₄ - <i>p</i> -NO ₂)	121.23(10)	2.2933(7)	this study

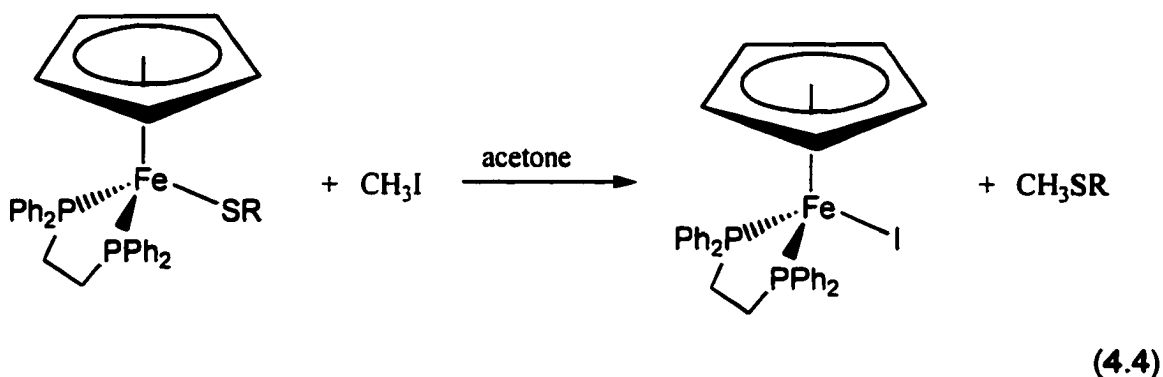
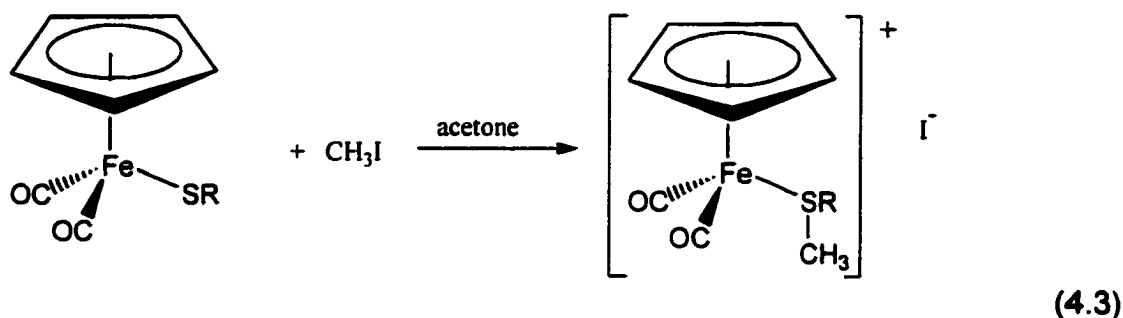
a. The *cis, cis, cis*-Fe(CO)₂(dppe)(SC₆H₅) complex is enantiomeric.

The Fe-S bond distances for the OCH₃, H, and NO₂ derivatives are 2.332(2), 2.3289(8), and 2.2933(7) Å, respectively (Table 4.20). A significant decrease in the Fe-S bond distance occurs as the aryl substituent becomes more electron withdrawing. An explanation for this trend is that the more electron

withdrawing substituent, NO₂, stabilizes the Fe-S bond by removing electron density from the Fed π -Sp π antibonding orbital.⁶⁵

The crystal packing diagrams of the OCH₃, H, and NO₂ derivatives are also shown for comparison (Figures 4.30, 4.32, and 4.34). One of the more interesting features in analyzing the crystal-packing patterns, the NO₂ derivative shows an intermolecular π -stacking arrangement within each pair of molecules. One arene group from each phosphine of one molecule is closely stacked with one arene group from each phosphine of another molecule.

Another major difference between the two reactions, CpFe(dppe)(SC₆H₄-*p*-Z) and CpFe(CO)₂(SC₆H₄-*p*-Z) with excess CH₃I, is shown in equations 4.3 and 4.4. Reaction 4.3 gives the methylated product and reaction 4.4 gives the ligand exchange product. Reaction 4.3 can give the ligand exchange product, CpFe(CO)₂I, but under more vigorous conditions.⁶⁵ Of course, the dicarbonyl fragment, [CpFe(CO)₂]⁺, is a better Lewis acid than [CpFe(dppe)]⁺ due to the back-donation ability of the carbonyl ligand which decreases the electron density from the metal. Since the thioether, CH₃SC₆H₅, is a very weak Lewis base, then it is not surprising that ligand exchange with a stronger Lewis base occurs more readily with the [CpFe(dppe)]⁺ fragment than the [CpFe(CO)₂]⁺ fragment. In fact, it has been demonstrated by Diaz *et al.* that even the Fe-I bond in the compound, CpFe(dppe)I, will undergo dissociation in polar solvents ($\epsilon > 35$) to give the cationic solvated species, [CpFe(dppe)(solvent)]⁺ and solvated iodide anion which speaks to the high ionic nature of the Fe-I bond.^{68,70}



Diaz *et al.* compare the HOMO energies from MO calculations of $[\text{CpFe}(\text{CO})_2]^+$ and $[\text{CpFe}(\text{dppe})]^+$ and find that the carbonyl derivative is lower in energy.⁷¹ The HOMO energies from density functional calculations on the oxidized species, $[\text{CpFe}(\text{CO})_2(\text{SCH}_3)]^+$ and $[\text{CpFe}(\text{dppe})(\text{SCH}_3)]^+$, also shows that the carbonyl derivative is more stable than the phosphine derivative (Figure 4.43); however, the calculations also indicate that the HOMO in the carbonyl derivative is still predominantly sulfur in character while in the phosphine derivative, the HOMO is predominantly metal in character.

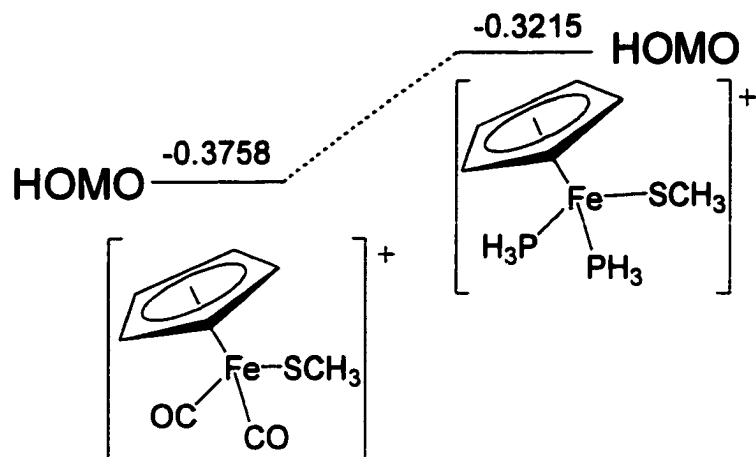


Figure 4.43. Substitution effect on the HOMO's energy (hartrees) in going from carbonyl to phosphine ligands.

There is also indication that the HOMO of the Fe(III) species is primarily metal in character as determined by the electron paramagnetic resonance (EPR) data collected (Table 4.3). Room temperature CH_2Cl_2 solutions of the complex, $[\text{CpFe}(\text{dppe})(\text{SC}_6\text{H}_4\text{-}p\text{-Z})]\text{BF}_4$ where $Z = \text{OCH}_3, \text{H}, \text{Cl}, \text{CF}_3,$ and NO_2 , have a single symmetric peak that indicates pseudooctahedral structures (Figures 4.22 – 4.26) and no phosphorus hyperfine coupling. Diaz has reported EPR results on $[\text{CpFe}(\text{dppe})(\text{SC}_6\text{H}_4\text{-}p\text{-Z})]\text{BF}_4$ where $Z = \text{H}$ and Br .⁷² Diaz indicates that the g -values for these H and Br derivatives are 2.0705(9) and 1.9753(13), respectively and that no phosphorus hyperfine splitting in any of the g components of the spectrum is observed in solution or solid (crushed powder). He also gives no indication that an internal or external reference has been used.

In this work, the free radical, DPPH (2,2-di(4-*tert*-octylphenyl)-1-picrylhydrazyl), was used as an external standard which has a g -value of 2.0037

± 0.0002 . The g-values range from 2.07159 for the OCH₃ derivative to 2.07525 for the NO₂ derivative. From a study by Roger, the g-values higher than those of the free electron value ($g = 2.0023$) are usually observed for 17 electron iron(III) compounds having a single occupied HOMO with a predominant metallic character.⁷³ A linear free energy relationship is observed relative to the g-values and the relative donor ability of the aryl substituent (Figure 4.27). Apparently, when the aryl substituent becomes more electron withdrawing and the g-values increase the HOMO becomes more metal in character.

An apparent linear free energy relationship is also observed relative to the half width at half height (HWHH) and the relative donor ability of the aryl substituent (Figure 4.28). The broadening of an e.p.r. spectrum can be caused by: 1) the relative motion of paramagnets in fluid solutions via dipole-dipole interactions, 2) electron spin exchange whereby unpaired electrons on different paramagnets overlap, 3) rapid tumbling of the paramagnets, and 4) unresolved hyperfine splittings.⁷⁴ An increase in dipole-dipole interactions which can be caused by: 1) increased concentrations of the paramagnetic compound of interest or impurities or; 2) the increase in the dipole moment of the compound can cause peak broadening. In dilute liquid solutions, the exchange effects are removed since the individual molecules are at a much greater distance than in a solid and the rapid tumbling averages away the anisotropic hyperfine effects.⁷⁵

In this work, the concentrations were very dilute but were not kept constant; however, the concentration of [CpFe(dppe)(SC₆H₄-*p*-OCH₃)]BF₄ and [CpFe(dppe)(SC₆H₄-*p*-NO₂)]BF₄ are similar, 3.1 mM and 3.3 mM, respectively. Notice, in Figures 4.22 and 4.26, how the intensities and lineshapes change with respect to the NO₂ and OCH₃ derivatives. The NO₂ derivative is much less intense and much broader than the OCH₃ derivative. The half width at half height (HWHH) values for the NO₂ and OCH₃ derivatives are 0.00700 and

0.00568, respectively (Table 4.3). Apparently, as the more electron donating substituent is replaced with a more electron withdrawing substituent, the more polar the $[\text{CpFe}(\text{dppe})(\text{SC}_6\text{H}_4\text{-}p\text{-Z})]^+$ complex becomes which is indicated by the broadening of the peak.

4.5 Conclusions.

This work has provided reactivity, electrochemical, spectroscopic, and structural information concerning the electron-rich iron-thiolate complexes $\text{CpFe}(\text{dppe})(\text{SC}_6\text{H}_4\text{-}p\text{-Z})$ where $Z = \text{OCH}_3, \text{H}, \text{Cl}, \text{CF}_3,$ and NO_2 and also their respective Fe(III) analogs as well as the more electron rich tripodal compound $\text{CpFe}(\text{P}_2\text{S})$ (Figure 4.41) and its Fe(III) analog (Figure 4.37).

Initially, the use of $\text{CpFe}(\text{dppe})(\text{SC}_6\text{H}_5)$ was to be used as a model system for hydrogenase. Triechel indicated that molecular hydrogen would evolve from a reaction between HBF_4 and $\text{CpFe}(\text{dppe})(\text{SC}_6\text{H}_5)$ under inert conditions.⁴⁷ The results of this experiment was protonation of $\text{CpFe}(\text{dppe})(\text{SC}_6\text{H}_5)$ to form the product $[\text{CpFe}(\text{dppe})(\text{HSC}_6\text{H}_5)]\text{BF}_4$ and no molecular hydrogen was produced. Protonation of $\text{CpFe}(\text{dppe})(\text{SC}_6\text{H}_5)$ was attempted under aerobic conditions to achieve the oxidized product $[\text{CpFe}(\text{dppe})(\text{SC}_6\text{H}_5)]\text{BF}_4$ but no molecular hydrogen was detected. The more electron rich tripodal complex, $\text{CpFe}(\text{P}_2\text{S})$, was synthesized and subsequently reacted with HBF_4 under anaerobic conditions. Oxidation took place to form the product $[\text{CpFe}(\text{P}_2\text{S})]\text{BF}_4$, but no molecular hydrogen was formed. Some spurious oxygen may have been in the reaction vessel during the time of protonation that would cause the oxidation to take place.

Another part of this work involved studies of how changes in the aryl substituents in the para position from the sulfur phenyl group influenced the reactivity, redox potential, and structure of the parent compound,

$\text{CpFe(dppe)(SC}_6\text{H}_5)$. The first study involved observing the kinetics of the pseudo-first order methylation of $\text{CpFe(dppe)(SC}_6\text{H}_4\text{-}p\text{-Z)}$ by CH_3I in acetone to form the products CpFe(dppe)I and $\text{CH}_3\text{S(C}_6\text{H}_5)$ (Scheme 4.3). It was determined that the reaction was first order in CH_3I as expected (Figure 4.12 and 4.13). It was also determined that a correlation exists between the relative donor ability of the aryl substituent and the reaction rate (Figure 4.14). From the Hammett plot, a value of $\rho = -2.14$ was calculated which is similar to the ρ value of -1.82 given for the reaction of $\text{CpFe(CO)}_2(\text{SC}_6\text{H}_4\text{-}p\text{-Z})$ and excess CH_3I in acetone which was accomplished by Ashby et al. in a previous study.⁶⁵ This result suggests that the mechanism by which the compounds $\text{CpFe(dppe)(SC}_6\text{H}_4\text{-}p\text{-Z)}$ and $\text{CpFe(CO)}_2(\text{SC}_6\text{H}_4\text{-}p\text{-Z})$ are methylated are the same. The mechanism appears to be frontier orbital controlled or charge controlled which means that more electron withdrawing substituent should decrease the rate of methylation. This was confirmed by the results of the kinetic experiments.

The second study involved cyclic voltammetry experiments. CV was accomplished on the compounds, $\text{CpFe(dppe)(SC}_6\text{H}_4\text{-}p\text{-Z)}$ solvated in THF (Figures 4.15 – 4.20). A glassy carbon working electrode and a Ag/AgNO_3 reference electrode along with a platinum wire auxiliary electrode were used. According to the CV data, the ratio of anodic to cathodic currents (i_{pa}/i_{pc}) are near unity indicating a chemically reversible process with no decomposition of oxidized product; however, $E_{pc} - E_{pa}$ are slightly greater than 59 mV and vary with a sweep rate typical of a quasi-reversible electron transfer process.⁶⁹ The required potentials for oxidation vary from -577 mV for the OCH_3 derivative to -357 mV for the NO_2 derivative versus the Ag/AgNO_3 reference electrode. A linear free energy relationship is observed between the relative donor ability of the aryl substituent and the half-wave potential of the compounds

$\text{CpFe}(\text{dppe})(\text{SC}_6\text{H}_4\text{-}p\text{-Z})$ (Figure 4.21). Apparently, the NO_2 substituent best stabilizes the complex by withdrawing electron density from the HOMO which is the $d\pi\text{-}p\pi$ antibonding orbital.⁶⁵

The solid state evidence also coincides with the CV data. Single-crystal X-ray crystallographic analysis of $\text{CpFe}(\text{dppe})(\text{SC}_6\text{H}_4\text{-}p\text{-OCH}_3)$, $\text{CpFe}(\text{dppe})(\text{SC}_6\text{H}_5)$ and $\text{CpFe}(\text{dppe})(\text{SC}_6\text{H}_4\text{-}p\text{-NO}_2)$ shows that the Fe-S bond distances decrease in the order of the derivatives: $\text{OCH}_3 > \text{H} > \text{NO}_2$. Their bond distances are 2.332(2), 2.3289(8), and 2.2933(7) Å, respectively. An explanation for this trend is that the more electron withdrawing substituent, NO_2 , stabilizes the Fe-S bond by removing electron density from the $\text{Fe}d\pi\text{-}p\pi$ antibonding orbital.⁶⁵ Another comparison is the Fe-S bond distance between $\text{CpFe}(\text{dppe})(\text{SC}_6\text{H}_5)$ and $[\text{CpFe}(\text{dppe})(\text{SC}_6\text{H}_5)]\text{BF}_4$ which shows that the Fe(II) derivative has the greater bond length of 2.3289(8) Å while the Fe(III) has a bond length of 2.1899(10) Å. This result is due to the removal of an electron from the iron-sulfur π -antibonding HOMO of the Fe(II) species which causes stabilization of the bond.⁶⁶

A major difference between the two reactions, $\text{CpFe}(\text{dppe})(\text{SC}_6\text{H}_4\text{-}p\text{-Z})$ and $\text{CpFe}(\text{CO})_2(\text{SC}_6\text{H}_4\text{-}p\text{-Z})$ with excess CH_3I , is shown in Figure 4.43. Reaction A gives the methylated product and reaction B gives the ligand exchange product. The dicarbonyl fragment, $[\text{CpFe}(\text{CO})_2]^+$, is a better Lewis acid than the fragment, $[\text{CpFe}(\text{dppe})]^+$, due to the back-donation ability of the carbonyl ligand which decreases the electron density from the metal. Since the thioether, $\text{CH}_3\text{SC}_6\text{H}_5$, is a very weak Lewis base, then it is not surprising that ligand exchange with a stronger Lewis base occurs more readily with the $[\text{CpFe}(\text{dppe})]^+$ fragment than the $[\text{CpFe}(\text{CO})_2]^+$ fragment.

The HOMO energies from density functional calculations on the oxidized species, $[\text{CpFe}(\text{CO})_2(\text{SCH}_3)]^+$ and $[\text{CpFe}(\text{dppe})(\text{SCH}_3)]^+$, also show that the

HOMO of the carbonyl derivative is more stable than the phosphine derivative (Figure 4.43); however, the calculations also indicate that the HOMO in the carbonyl derivative is predominantly sulfur in character while in the phosphine derivative, the HOMO is predominantly metal in character.

There is also indication that the HOMO of the Fe(III) species is primarily metal in character as determined by the electron paramagnetic resonance (EPR) data collected (Table 4.3). The free radical, DPPH (2,2-di(4-*tert*-octylphenyl)-1-picrylhydrazyl), which has a g -value of 2.0037 ± 0.0002 , was used as an external standard. The g -values range from 2.07159 for the OCH₃ derivative to 2.07525 for the NO₂ derivative. From a study by Roger, g -values that are higher than those of the free electron value ($g = 2.0023$) are usually observed for 17 electron iron(III) compounds having a single occupied HOMO with predominant metal character.⁷³ A linear free energy relationship is observed relative to the g -values and the relative donor ability of the aryl substituent (Figure 4.27). Apparently, as the aryl substituent becomes more electron withdrawing and the g -values increase, the HOMO becomes more metallic in character.

An apparent linear free energy relationship is also observed relative to the half width at half height (HWHH) and the relative donor ability of the aryl substituent (Figure 4.28). As the more electron donating substituent is replaced with a more electron withdrawing substituent, the [CpFe(dppe)(SC₆H₄-*p*-Z)]⁺ complex becomes more polar as indicated by the broadening of the peak.

4.6 References.

- 1) Smith, B. E. "Structure; Function; and Biosynthesis of the Metallosulfur Clusters in Nitrogenases", *Adv. Inorg. Chem.* **1999**, *47*, 159-218.
- 2) Eady, R. R. "Structure-Function Relationships of Alternative Nitrogenases", *Chem. Rev.* **1996**, *96*, 3013-3030.
- 3) Bazhenova, T. A. and Shilov, A. E. "Nitrogen-Fixation in Solution", *Coord. Chem. Rev.* **1995**, *144*, 69-145.
- 4) Howard, J. B. and Rees, D. C. "Structural Basis of Biological Nitrogen Fixation", *Chem. Rev.* **1996**, *96*, 2965-2982.
- 5) Georgiadis, M. M., Komiya, H., Chakrabarti, P., Woo, D., Kornuc, J. J. and Rees, D. C. "Crystallographic Structure of the Nitrogenase Iron Protein From *Azotobacter-Vinelandii*", *Science* **1992**, *257*, 1653-1659.
- 6) Richards, R. L. "Metal-Sulfur Chemistry and Catalytic Processes", *New J. Chem.* **1997**, *21*, 727-732.
- 7) Richards, R. L. "Reactions of Small Molecules at Transition Metal Sites: Studies Relevant to Nitrogenase ; An Organometallic Enzyme", *Coord. Chem. Rev.* **1996**, *154*, 83-97.
- 8) Kim, J. and Rees, D. C. "Nitrogenase and Biological Nitrogen-Fixation", *Biochemistry* **1994**, *33*, 389-397.
- 9) Dilworth, M. J. *Biology and Biochemistry of Nitrogen Fixation*; Elsevier: New York, 1991; Vol. 1.
- 10) Chatt, J., Dilworth, J. R. and Richards, R. L. "Recent Advances in the Chemistry of Nitrogen Fixation", *Chem. Rev.* **1978**, *78*, 589-625.
- 11) Leigh, G. J. "Protonation of Coordinated Dinitrogen", *Acc. Chem. Res.* **1992**, *25*, 177-181.
- 12) Sellmann, D., Utz, J., Blum, N. and Heinemann, F. W. "On the Function of Nitrogenase FeMo Cofactors and Competitive Catalysts: Chemical

- Principles; Structural Blue-prints; and the Relevance of Iron Sulfur Complexes for N-2 Fixation", *Coord. Chem. Rev.* **1999**, *192*, 607-627.
- 13) Sellmann, D. and Sutter, J. "In Quest of Competitive Catalysts for Nitrogenases and Other Metal Sulfur Enzymes", *Acc. Chem. Res.* **1997**, *30*, 460-469.
 - 14) Chatt, J., Dilworth, J. R. and Richards, R. L. "Recent Advances in Chemistry of Nitrogen-Fixation", *Chem. Rev.* **1978**, *78*, 589-625.
 - 15) Leigh, G. J. and McMahon, C. N. "The Organometallic Chemistry of Nitrogenases", *J. Organomet. Chem.* **1995**, *500*, 219-225.
 - 16) Silverthorn, W. E. "Formation of a Cationic Binuclear Iron-Dinitrogen Compound from Molecular Nitrogen", *J. Chem. Soc., Chem. Commun.* **1971**, 1310-1311.
 - 17) Giannoccaro, P., Rossi, M. and Sacco, A. "New Cationic Hydrido and Hydrodo-Dinitrogen Complexes of Iron", *Coord. Chem. Rev.* **1972**, *8*, 77-79.
 - 18) Borodko, Y. G., Broitman, M. O., Kachapina, L. M., Shilov, A. E. and Ukhin, L. Y. "Reduction of Nitrogen to Hydrazine in a Binuclear Complex of Iron", *J. Chem. Soc., Chem. Commun.* **1971**, 1185-1186.
 - 19) Sellmann, D., Soglowek, W., Knoch, F., Ritter, G. and Dengler, J. "Transition-Metal Complexes With Sulfur Ligands .88. Dependence of Spin State; Structure; and Reactivity of [Fe(II)(L)('NHS₄')] Complexes On the Coligand-L (L = CO; N₂H₂; N₂H₄; NH₃; Pyridine; NHCH₃NH₂; CH₃OH; THF; P(OCH₃)₃; P(OPh)₃): Model Complexes For Iron Nitrogenases ('NHS₄'⁽²⁻⁾=Dianion of 2;2'-Bis[(2-Mercaptophenyl)Thio]Diethylamine)", *Inorg. Chem.* **1992**, *31*, 3711-3717.
 - 20) Krebs, B. and Henkel, G. "Transition-Metal Thiolates : From Molecular Fragments of Sulfidic Solids to Models For Active-Centers in Biomolecules", *Angew. Chem., Int. Ed. Engl.* **1991**, *30*, 769-788.

- 21) Peters, J. W., Fisher, K. and Dean, D. R. "Nitrogenase Structure and Function: a Biochemical-Genetic Perspective", *Annu. Rev. Microbiol.* **1995**, *49*, 335-366.
- 22) Hembre, R. T., McQueen, J. S. and Day, V. W. "Coupling H₂ to Electron Transfer with a 17-Electron Heterobimetallic Hydride: A "Redox Switch" Model for the H₂-Activating Center of Hydrogenase", *J. Am. Chem. Soc.* **1996**, *118*, 798-803.
- 23) Pavlov, M., Siegbahn, P. E. M., Blomberg, M. R. A. and Crabtree, R. H. "Mechanism of H-H Activation by Nickel-Iron Hydrogenase", *J. Am. Chem. Soc.* **1998**, *120*, 548-555.
- 24) Adams, M. W. W. "The Structure and Mechanism of Iron-Hydrogenases", *Biochim. Biophys. Acta* **1990**, *1020*, 115-145.
- 25) Patil, D. S. "Nickel-Iron-Selenium Hydrogenase", *Methods Enzymol.* **1994**, *243*, 68-94.
- 26) Thauer, R. K., Klein, A. R. and Hartmann, G. C. "Reactions with Molecular Hydrogen in Microorganisms: Evidence for a Purely Organic Hydrogenation Catalyst", *Chem. Rev.* **1996**, *96*, 3031-3042.
- 27) Cammack, R. *Bioinorganic Catalysis*; 2nd ed., rev. and expanded ed.; Marcel Dekker, Inc.: New York, 1999.
- 28) Frey, M. "Nickel-Iron Hydrogenases: Structural and Functional Properties", *Struct. Bonding* **1998**, *90*, 97-126.
- 29) Volbeda, A., Garcia, E., Piras, C., deLacey, A. L., Fernandez, V. M., Hatchikian, E. C., Frey, M. and FontecillaCamps, J. C. "Structure of the [NiFe] Hydrogenase Active Site: Evidence for Biologically Uncommon Fe Ligands", *J. Am. Chem. Soc.* **1996**, *118*, 12989-12996.
- 30) deLacey, A. L., Hatchikian, E. C., Volbeda, A., Frey, M., FontecillaCamps, J. C. and Fernandez, V. M. "Infrared Spectroelectrochemical Characterization

- of the [NiFe] Hydrogenase of *Desulfovibrio gigas*", *J. Am. Chem. Soc.* **1997**, *119*, 7181-7189.
- 31) Pierik, A. J., Hulstein, M., Hagen, W. R. and Albracht, S. P. J. "A Low-Spin Iron with CN and CO as Intrinsic Ligands Forms the Core of the Active Site in [Fe]-Hydrogenases", *Eur. J. Biochem.* **1998**, *258*, 572-578.
- 32) Peters, J. W., Lanzilotta, W. N., Lemon, B. J. and Seefeldt, L. C. "X-ray Crystal Structure of the Fe-only Hydrogenase (Cpl) from *Clostridium pasteurianum* to 1.8 Å Resolution", *Science* **1998**, *282*, 1853-1858.
- 33) Peters, J. W. "X-ray Crystal Structure of the Fe-only Hydrogenase (Cpl) from *Clostridium pasteurianum* to 1.8 Å Resolution", *Science* **1999**, *283*, 35-35.
- 34) Peters, J. W. "X-ray Crystal Structure of the Fe-only Hydrogenase (Cpl) from *Clostridium pasteurianum* to 1.8 Å Resolution", *Science* **1999**, *283*, 2102-2102.
- 35) Adams, M. W. W. and Stiefel, E. I. "Biochemistry : Biological Hydrogen Production: Not So Elementary", *Science* **1998**, *282*, 1842-1843.
- 36) Lyon, E. J., Georgakaki, I. and Darensbourg, M. "Sulfur-Containing Bioorganometallic Model Complexes for Fe-only Hydrogenase", *J. Inorg. Biochem.* **1999**, *74*, 215-215.
- 37) Lai, C. H., Lee, W. Z., Miller, M. L., Reibenspies, J. H., Darensbourg, D. J. and Darensbourg, M. Y. "Responses of the Fe(CN)₂(CO) Unit to Electronic Changes as Related to Its Role in [NiFe]-hydrogenase", *J. Am. Chem. Soc.* **1998**, *120*, 10103-10114.
- 38) Darensbourg, D. J., Reibenspies, J. H., Lai, C. H., Lee, W. Z. and Darensbourg, M. Y. "Analysis of an Organometallic Iron Site Model for the Heterodimetallic Unit of [NiFe]-hydrogenase", *J. Am. Chem. Soc.* **1997**, *119*, 7903-7904.

- 39) Liaw, W. F., Lee, N. H., Chen, C. H., Lee, C. M., Lee, G. H. and Peng, S. M. "Dinuclear and Mononuclear Iron(II)-thiolate Complexes with Mixed CO/CN- Ligands: Synthetic Advances for Iron Sites of [Fe]-only Hydrogenases", *J. Am. Chem. Soc.* **2000**, *122*, 488-494.
- 40) Hsu, H. F., Koch, S. A., Popescu, C. V. and Munck, E. "Chemistry of Iron Thiolate Complexes with CN⁻ and CO. Models for the [Fe(CO)(CN)₂] Structural Unit in Ni-Fe Hydrogenase Enzymes", *J. Am. Chem. Soc.* **1997**, *119*, 8371-8372.
- 41) Sellmann, D., Geck, M. and Moll, M. "Transition-Metal Complexes with Sulfur Ligands. 62. Hydrogen Evolution Upon Reaction of Protons with Sulfur-Coordinated Fe(II) Complexes: Investigation of the H⁺; H₂; and H⁻ Interactions with Iron 1; 2-Benzenedithiolate Complexes", *J. Am. Chem. Soc.* **1991**, *113*, 5259-5264.
- 42) Sellmann, D., Kappler, J. and Moll, M. "Transition-Metal Complexes with Sulfur Ligands. 96. Hydrogenase Model Reactions : D₂/H⁺ Exchange at Metal Sulfur Centers Catalyzed by [Rh(H)(CO)(S-Bu₄)] (S-Bu₄²⁻ = 1; 2-Bis((2-Mercapto-3; 5-Di-Tert-Butylphenyl)Thio)Ethanato²⁻)", *J. Am. Chem. Soc.* **1993**, *115*, 1830-1835.
- 43) Blake, A. J., Gould, R. O., Holder, A. J., Hyde, T. I., Reid, G. and Schroder, M. "Iridium Thioether Chemistry : the Synthesis and Structures of [IrI₂][PF₆]₃ and [IrHI₂][PF₆]₂ (L = 1; 4; 7-Trithiacyclononane)", *J. Chem. Soc., Dalton Trans.* **1990**, 1759-1764.
- 44) Lemke, W. D., Travis, K. E., Takvoryan, N. E. and Busch, D. H. "Rhodium(I) Complexes of Macrocyclic Tetradentate Thioethers", *Adv. Chem. Ser.* **1976**, *1976*, 358-378.
- 45) Sellmann, D. and Zapf, L. "Transition-Metal Complexes with Sulfur Ligands. 13. Syntheses and Reactions of the 1; 2-Benzenedithiolato Molybdate

- Complexes $[\text{Mo}(\text{C}_6\text{H}_4\text{S}_2)_3]^0$; $[\text{Mo}(\text{C}_6\text{H}_4\text{S}_2)_3]^{1-}$; $[\text{Mo}(\text{C}_6\text{H}_4\text{S}_2)_3]^{2-}$ and the Hydride Complex $[\text{Mo}(\text{H})(\text{C}_6\text{H}_4\text{S}_2)_3]^{3-}$, *Z. Naturforsch. B: Chem. Sci.* **1985**, *40*, 380-388.
- 46) Sellmann, D., Geipel, F. and Moll, M. "[Ni(NHPNPr₃)(S-3)]; The First Nickel Thiolate Complex Modeling the Nickel Cysteinate Site and Reactivity of [NiFe] Hydrogenase", *Angew. Chem., Int. Ed. Engl.* **2000**, *39*, 561-563.
- 47) Treichel, P. M., Molzahn, D. C. and Wagner, K. P. "New 17 Electron Complexes of Iron", *J. Organomet. Chem.* **1979**, *174*, 191-197.
- 48) Treichel, P. M. and Molzahn, D. C. "Preparation of $[\text{Fe}(\text{C}_5\text{H}_5)(\text{dppe})(\text{NCCH}_3)]\text{Br}$ and Its Conversion to Several $\text{Fe}(\text{C}_5\text{H}_5)(\text{dppe})\text{X}$ Compounds", *Abstracts of Papers of the American Chemical Society* **1979**, *1979*, 45-45.
- 49) Barrado, G., Carriedo, G. A., Diazvalenzuela, C. and Riera, V. "Synthesis and Oxidation of Cationic Heterobinuclear Cyanide-Bridged Complexes of Manganese and Iron", *Inorg. Chem.* **1991**, *30*, 4416-4420.
- 50) Tsai, S. C., Wang, H. E., Huang, C. T., Yiin, L. M. and Liu, S. T. "Study of Effects on the Coordination of Thioether Ligands. 2. Stereospecific Ligand Substitutions in Manganese(I) Complexes", *Chem. Ber.* **1995**, *128*, 151-155.
- 51) Treichel, P. M., Shubkin, R. L., Barnett, K. W. and Reichard, D. "Chemistry of the Cyclopentadienylmetal Carbonyls. II. Cyclopentadienyliron Carbonyl Derivatives", *Inorg. Chem.* **1966**, *5*, 1177-1181.
- 52) Associates, S. S. *SPECFIT/32*; 3.0 ed.; R. A. Binstead & A. D. Zuberbuhler, 2000.
- 53) Diaz, C., Leal, C. and Yutronic, N. "S-S Cleavage in Disulphides by the Fragment $\text{CpFe}(\text{dppe})(+)$ ", *Boletín De La Sociedad Chilena De Química* **1996**, *41*, 99-102.

- 54) Gagne, R. R., Koval, C. A. and Lisensky, G. C. "Ferrocene as an Internal Standard for Electrochemical Measurements", *Inorg. Chem.* **1980**, *19*, 2854-2855.
- 55) Siemens *SHELXTL*; 5.03 ed.; Siemens Analytical X-ray Instruments Inc.: Madison, WI, 1994.
- 56) Roberts, J. D. and Caserio, M. C. *Basic Principles of Organic Chemistry*, 2nd ed.; W. A. Benjamin, Inc.: Reading, MA, 1977.
- 57) Takacs, J., Marko, L. and Parkanyi, L. "Synthesis and Some Reactions of $\text{Fe}(\text{CO})_2(\text{dppe})(\text{SR})_2$ and $\text{Fe}_3(\text{CO})_8(\text{SAr})_6$ Complexes : the Crystal-Structure of $\text{Cis-Cis-Cis-Fe}(\text{CO})_2(\text{dppe})(\text{SPh})_2$ ", *J. Organomet. Chem.* **1989**, *361*, 109-116.
- 58) Pohl, S., Opitz, U., Haase, D. and Saak, W. "Iron(II) Phosphane Complexes : Synthesis and Crystal-Structures of $[\text{Fe}_2\text{I}_4(\text{dppe})_2]$; $[\text{Fe}_2(\text{SR})_4(\text{dppe})_2]$; $[\text{Fe}(\text{SR}')_2(\text{dppp})]$ and $[\text{Fe}(\text{SR})_2(\text{PMePh}_2)_2]$ ($\text{dppe}=\text{Ph}_2\text{P}(\text{CH}_2)_2\text{PPh}_2$ $\text{Dppp}=\text{Ph}_2\text{P}(\text{CH}_2)_3\text{PPh}_2$ $\text{R}=2; 4; 6\text{-Me}_3\text{C}_6\text{H}_2$ $\text{R}'=2; 4\text{-tBuC}_6\text{H}_3$)", *Z. Anorg. Allg. Chem.* **1995**, *621*, 1140-1146.
- 59) Wander, S. A., Reibenspies, J. H., Kim, J. S. and Darensbourg, M. Y. "Synthesis and Characterization of a Stable Iron(II) Hydride Thiolate Complex : $(\text{PhS})\text{Fe}(\text{H})(\text{CO})_2(\text{P}(\text{OPh})_3)_2$ ", *Inorg. Chem.* **1994**, *33*, 1421-1426.
- 60) Alvarez, S. and Hoffmann, R. "The Mechanism of Generation of Hydrogen From Water with the Aid of Transition-Metal Dithiolenes", *Anales De Quimica Serie B-Quimica Inorganica Y Quimica Analytica* **1986**, *82*, 52-56.
- 61) Bitterwolf, T. E. "Reductive Elimination of Dihydrogen From Arenechromium Dimers", *J. Organomet. Chem.* **1983**, *252*, 305-316.
- 62) Treichel, P. M. and Rosenhein, L. D. "Synthesis of a Metal-Complex of Benzenethiol; $[\text{Fe}(\text{C}_5\text{H}_5)(\text{CO})_2(\text{PhSH})]\text{BF}_4$; and Its Characterization as a Strong Acid", *Inorg. Chem.* **1981**, *20*, 942-944.

- 63) Wilker, J. J. and Lippard, S. J. "Methylation of Iron-Sulfur Complexes by Trimethyl Phosphate", *Inorg. Chem.* **1999**, *38*, 3569-3574.
- 64) Espenson, J. H. *Chemical Kinetics and Reaction Mechanisms*; 2nd ed.; McGraw Hill: New York, 1995.
- 65) Ashby, M. T., Enemark, J. H. and Lichtenberger, D. L. "Destabilizing $d\pi-p\pi$ Orbital Interactions and the Alkylation Reactions of Iron(II) Thiolate Complexes", *Inorg. Chem.* **1988**, *27*, 191-197.
- 66) Treichel, P. M. and Rosenhein, L. D. "Radical Coupling of Mercaptide Ligands Upon Oxidation of Organometallic Mercaptide Complexes", *J. Am. Chem. Soc.* **1981**, *103*, 691-692.
- 67) Lichtenberger, D. L., Sellmann, D. and Fenske, R. F. "He (I) Photoelectron-Spectra and Valence Electronic-Structures of $(\eta^5-C_5H_5)Mn(CO)_2N_2$ and $(\eta^5-C_5H_5)Mn(CO)_2NH_3$ ", *J. Organomet. Chem.* **1976**, *117*, 253-264.
- 68) Diaz, C., Yutronic, N. and Weiss, B. "Ionization of the Fe-X Bond in Polar-Solvents: A Spectroscopic Study of CpFe(dppe)X Complexes", *Polyhedron* **1993**, *12*, 1403-1407.
- 69) Nicholson, R. S. "Theory and Application of Cyclic Voltammetry for Measurement of Electrode Reaction Kinetics", *Anal. Chem.* **1965**, *37*, 1351.
- 70) Diaz, C. and Yutronic, N. "Coordinating Properties of Some Solvents Towards the Fragment [CpFe(dppe)]⁺", *Polyhedron* **1996**, *15*, 997-1001.
- 71) Diaz, C., Leal, C. and Yutronic, N. "Oxidative Addition of Disulfides to the Fragment CpFe(dppe)⁺: Steric and Dielectric Medium Control on the Reaction", *J. Organomet. Chem.* **1996**, *516*, 59-64.
- 72) Diaz, C. "Observation of Stable 17 e- Iron(III) Cyclopentadienyl Radical Complexes", *Boletin De La Sociedad Chilena De Quimica* **1999**, *44*, 315-320.

- 73) Roger, C., Hamon, P., Toupet, L., Rabaa, H., Saillard, J. Y., Hamon, J. R. and Lapinte, C. "Halo(Pentamethylcyclopentadienyl)(1,2-Bis(Diphenylphosphino)ethane)iron(III) and Alkyl(Pentamethylcyclopentadienyl)(1,2-Bis(Diphenylphosphino)ethane)Iron(III) 17-electron Complexes: Synthesis, NMR, and Magnetic-Properties, and EHMO Calculations", *Organometallics* **1991**, *10*, 1045-1054.
- 74) Mabbs, F. E. and Collison, D. *Electron Paramagnetic Resonance of d Transition Metal Compounds*; Elsevier: New York, 1992.
- 75) Pake, G. E. and Estle, T. L. *The Physical Principles of Electron Paramagnetic Resonance*; 2nd ed.; W. A. Benjamin, Advanced Book Program: Reading, Mass., 1973.

Iron-sulfur proteins play a significant role in electron transfer and also catalysis in all biological systems. A significant number of these iron-sulfur proteins involve cysteinyl ligands bound to the iron (Figure 2.1). Model systems are often used to study the structural and redox behavior of these proteins.^{1,2} In this research, three major influences on the redox potential have been investigated using electron rich model systems. First, intermolecular hydrogen bonding can influence the redox behavior of the metal as shown in Chapter 2 using the model system, $\text{CpFe}(\text{CO})_2(\text{SC}_6\text{H}_5)$. Second, the local solvent environment effects the electronic and vibrational energies of $\text{CpFe}(\text{CO})_2(\text{SC}_6\text{H}_5)$ and therefore the redox potential as shown in Chapter 3. Third, the reactivity and the redox potential of the complexes, $\text{CpFe}(\text{CO})_2\text{S}(\text{C}_6\text{H}_4\text{-Z})$ and $\text{CpFe}(\text{dppe})\text{S}(\text{C}_6\text{H}_4\text{-Z})$, where $\text{Z} = \text{OCH}_3, \text{H}, \text{Cl}, \text{CF}_3, \text{and NO}_2$, is also influenced by changing the electron environment at the sulfur site as shown in Chapter 4.

5.1 Summary of the Results from Chapter 2.

It has been determined that in the complex, $\text{CpFe}(\text{CO})_2(\text{SC}_6\text{H}_5)$, the HOMO is primarily sulfur in character so that hydrogen bonding as well as protonation occurs at the sulfur site.^{3,4} By titrating CH_2Cl_2 solutions of $\text{CpFe}(\text{CO})_2(\text{SC}_6\text{H}_5)$ with various concentrations of CCl_3COOH , it was determined by the data garnered from the use of UV-vis and infrared spectroscopy that a discrete hydrogen bound species 1-HX does not exist in solution (Scheme 2.1). There are no isosbestic points in the visible spectra (Figures 2.9) and also the curve fit analysis indicates that perhaps there are more than one type of hydrogen bound species in solution at higher concentrations of acid (Figures 2.5-2.8). The hydrogen bound species is part of a continuum, which means that at

low concentrations of weak protic acids, little hydrogen bonding can be detected but as the concentrations or strengths of the protic acids increase, hydrogen bonding becomes more pronounced. The continuum reflects the combined influences of the polarity of the solvent environment and the ability of the acid to hydrogen bond to the thiolate ligand.

By adding less than one equivalent of $\text{HBF}_4 \cdot \text{O}(\text{CH}_3)_2$ to a methylene chloride solution of $\text{CpFe}(\text{CO})_2(\text{SC}_6\text{H}_5)$, a mixture of $\text{CpFe}(\text{CO})_2(\text{SC}_6\text{H}_5)$ and $[\text{CpFe}(\text{CO})_2(\text{HSC}_6\text{H}_5)]\text{BF}_4$ is produced as shown by the carbonyl stretching frequencies (Figure 2.16). By adding more than one equivalent of $\text{HBF}_4 \cdot \text{O}(\text{CH}_3)_2$ to a methylene chloride solution of $\text{CpFe}(\text{CO})_2(\text{SC}_6\text{H}_5)$, only the protonated species, $[\text{CpFe}(\text{CO})_2(\text{HSC}_6\text{H}_5)]\text{BF}_4$, is produced. A comparison between the bond distances between $\text{CpFe}(\text{CO})_2(\text{SC}_6\text{H}_5)$ and $[\text{CpFe}(\text{CO})_2(\text{HSC}_6\text{H}_5)]\text{BF}_4$ was accomplished by single-crystal X-ray crystallographic analysis of a suitable crystal of each compound. It is noteworthy that the bond distance for the protonated species (2.2590(13) Å) is significantly shorter than the parent complex (2.283(2) Å). This can be attributed by the reduction of the 4-electron Fe-S $d\pi$ - $p\pi$ anti-bonding orbital upon protonation of the thiolate ligand.

By increasing the concentration of CCl_3COOH to a 10 mL CH_2Cl_2 solution of $\text{CpFe}(\text{CO})_2(\text{SC}_6\text{H}_5)$, the ligand to metal charge transfer (LMCT) band in the visible region undergoes a blue shift due to an increase in hydrogen bonding and at the same time, the CO stretching frequencies in the infrared region shifted to a higher frequency (Figure 2.9). Not only is hydrogen bonding dependent upon the concentration of a specific acid, but it is also dependent upon the strength of an acid. A series of experiments were carried out using CH_3COOH , CH_2ClCOOH , CHCl_2COOH , CCl_3COOH , and CF_3COOH at the same concentration (150 mM in CH_2Cl_2). To each acid solution was added enough $\text{CpFe}(\text{CO})_2(\text{SC}_6\text{H}_5)$ to form a 10 mM solution. Once again, a blue shift occurred in the LMCT band and the

carbonyl stretching frequencies increased in frequency as stronger acids were used (Figure 2.15). The carbonyl stretching frequencies (ν_{CO}) shifting to higher frequencies is an indirect indication of the existence of hydrogen bonding to a ligand or metal. As electron density is decreased at the metal center as a result of hydrogen bonding to the metal or a ligand, there is less back donation from the metal to the CO π^* antibonding orbitals.

A correlation is shown between the redox potentials and force constants by the empirical formula that was derived from other equations:⁴⁻⁹

$$\Delta E_{1/2} = \lambda \Delta F_{\text{CO}} \text{ (i.e., for } 1.6 \leq \lambda \leq 2.1 \text{ and the observed } \Delta F_{\text{CO}} = 0.65 \text{ mdyn/ \AA).}$$

We predict a shift of the oxidation potential of $\text{CpFe}(\text{CO})_2(\text{SC}_6\text{H}_5)$ by 1.0 – 1.3 V upon protonation. Using the value of $F_{\text{CO}} = 16.42 \text{ mdyn/\AA}$ that is observed for the hydrogen bound species **1-TFA** (TFA is trifluoroacetic acid), we estimate a maximal effect of $300 \leq \Delta E_{1/2} \leq 400 \text{ mV}$ for H-bonding to $\text{CpFe}(\text{CO})_2(\text{SC}_6\text{H}_5)$. Based on this information, there is a substantially smaller affect for hydrogen bonding, which is about 30% of that observed upon protonation.

Density functional calculations were carried for $\text{CpFe}(\text{CO})_2(\text{SCH}_3)$, two hydrogen bound species with CF_3COOH and HBF_4 as the hydrogen bound donors and the protonated species $[\text{CpFe}(\text{CO})_2(\text{HSCH}_3)]^+$ as shown in Figure 2.2. The data from the calculations on $\text{CpFe}(\text{CO})_2(\text{SCH}_3)$ show that the HOMO is primarily sulfur in character, as expected, but upon protonation, becomes primarily metal in character (Figure 2.25). The complex that contains the weaker acid, CF_3COOH , that is hydrogen bound to $\text{CpFe}(\text{CO})_2(\text{SCH}_3)$ shows more of the HOMO as primarily sulfur in character but the complex that contains the stronger acid, HBF_4 , hydrogen bound to $\text{CpFe}(\text{CO})_2(\text{SCH}_3)$ shows a decrease in sulfur character and an increase in metal character.

Another trend to observe is from the carbonyl stretching frequencies that were calculated. The stretching frequencies for $\text{CpFe}(\text{CO})_2(\text{SCH}_3)$ are 1980 and 2024 cm^{-1} and the frequencies for $\text{CpFe}(\text{CO})_2\text{SCH}_3\text{-HBF}_4$ and $\text{CpFe}(\text{CO})_2(\text{HSCH}_3)^+$ are 1998, 2043 cm^{-1} and 2042, 2078 cm^{-1} respectively. The trend is an increase in carbonyl stretching frequencies as FpSCH_3 undergoes hydrogen bonding and then protonation. This reflects the decreased electron density backbonding from the metal to the $\text{CO } \pi^*$ antibonding orbital.

The carbonyl stretching frequencies that were calculated using the density functional method follows the same trend as those that were observed experimentally. An increase in the stretching frequencies occurs as hydrogen bonding to the compound, $\text{CpFe}(\text{CO})_2(\text{SC}_6\text{H}_5)$, takes place and even more so when protonation occurs. These results indicate only a small perturbation of the donor ability of the thiolate ligand during hydrogen bonding as compared with the more significant change that results from protonation. Based on the free-energy relationships that relate redox potentials and ν_{CO} , there is a substantially smaller affect for hydrogen bonding, which is about 30% of that observed upon protonation.

5.2 Summary of the Results from Chapter 3.

The compound, $\text{CpFe}(\text{CO})_2(\text{SC}_6\text{H}_5)$ exhibits solvatochromic behavior as well as other solvent effects based on carbonyl stretching frequencies. The solutions of $\text{CpFe}(\text{CO})_2(\text{SC}_6\text{H}_5)$ in pentane, benzene, and acetone are colored green, greenish/brown, and red, respectively. The wavelength of the LMCT band was correlated to several solvent polarity scales, which includes the Dimroth-Reichardt's normalized energy of transition scale, Gutmann's Acceptor Number scale, and Kosower's Z-scale (Figures 3.45-3.48). As $\text{CpFe}(\text{CO})_2(\text{SC}_6\text{H}_5)$ is dissolved in more polar solvents, a blue shift occurs in the visible region. This is

evidence that the ground-state dipole moment is greater than the excited-state dipole moment, $\mu_g > \mu_e$ as illustrated in Figure 3.2.¹⁰ This means that the ground-state will become more stable in polar solvents than the excited-state, which will produce a hypsochromic or blue shift. By using the Dimroth-Reichardt's normalized energy of transition scale, it was also shown that the ground-state energy of $\text{CpFe}(\text{CO})_2(\text{SC}_6\text{H}_5)$ is less stable than the ground-state energy of $\text{CpFe}(\text{CO})_2(\text{SC}_6\text{H}_4\text{-}p\text{-CF}_3)$ (Figure 3.46). By adding an electron withdrawing substituent in the para position of the phenyl thiolate group makes it a weaker π donating ligand. Since it has been determined that the HOMO for each of the compounds is a $d\pi\text{-}p\pi$ antibonding orbital, which is primarily sulfur in character, the electron withdrawing group better stabilizes the compound as demonstrated by gas phase photoelectron spectroscopy.⁴

Other solvent effects at the vibrational level are observed in the infrared region which are more difficult to correlate. A plot of the antisymmetric stretching versus the symmetric stretching frequencies of $\text{CpFe}(\text{CO})_2(\text{SC}_6\text{H}_5)$ in various solvents show two lines (Figure 3.50). One line represents the less polar hydrocarbon solvents with the exception of diethyl ether, and the other line represents the more polar non-hydrocarbon solvents.

As indicated in Figure 3.51, there seems to be similar solvent influences for the compounds $\text{CpFe}(\text{CO})_2\text{Cl}$, $\text{CpFe}(\text{CO})_2\text{I}$, and $\text{CpFe}(\text{CO})_2(\text{SC}_6\text{H}_5)$. Since the phenyl thiolate ligand is the strongest π donor and certainly the largest of the three ligands, it should be less sensitive to solvent interactions than the chloride or the iodide anions. This means that a competition between the carbonyl-solvent interaction and the iron-thiolate-solvent interaction is occurring to determine whether the carbonyl stretching frequency is going to increase or decrease. The Bellamy plot, Figure 3.50, shows that less polar hydrocarbon solvents have less influence on the carbonyl ligands of $\text{CpFe}(\text{CO})_2(\text{SC}_6\text{H}_5)$ and

so the carbonyl antisymmetric stretching frequencies, which seem to be more sensitive to the solvent effects¹¹, are higher than in the more polar solvents. Within the more polar solvents, tetrahydrofuran seems to effectively interact with the carbonyl ligands enough to significantly lower the carbonyl stretching frequency, however, as the polarity of the solvent increases, the iron-thiolate-solvent interaction becomes more effective and increases the carbonyl stretching frequency.

The last solvent interaction to be mentioned is the hydrogen bonding effect between the protic solvents and $\text{CpFe}(\text{CO})_2(\text{SC}_6\text{H}_5)$. Figures 3.14-3.17 show a decrease in intensity and wavelength which is indicative of hydrogen bonding. The solvent, 2,2,2-trifluoroethanol, shows substantial hydrogen bonding according to the UV-vis and infrared spectra. The carbonyl stretching frequencies closely matches those of the hydrogen bound species that was made by reaction 10 mM $\text{CpFe}(\text{CO})_2(\text{SC}_6\text{H}_5)$ with 500 mM CCl_3COOH in methylene chloride which is discussed in Chapter 2 of this dissertation.

5.3 Summary of the Results of Chapter 4.

Part of this project involved using $\text{CpFe}(\text{dppe})(\text{SC}_6\text{H}_5)$ as a potential model system for hydrogenase. Figure 4.40 shows a potential mechanism for the ligand-ligand activation for the liberation of dihydrogen using $\text{CpFe}(\text{dppe})(\text{SC}_6\text{H}_5)$. In testing the proposed mechanism, the first step was to generate dihydrogen by adding $\text{HBF}_4 \cdot \text{O}(\text{CH}_3)_2$ to $\text{CpFe}(\text{dppe})(\text{SC}_6\text{H}_5)$ in dry degassed CH_2Cl_2 under argon. The experiment demonstrated that protonation took place according to ^1H NMR but not oxidation and evolution of dihydrogen. The parent compound, $\text{CpFe}(\text{dppe})(\text{SC}_6\text{H}_5)$ is olive-green when dissolved in CH_2Cl_2 ; however, upon protonation the solution turns red. The oxidized species, $[\text{CpFe}(\text{dppe})(\text{SC}_6\text{H}_5)]\text{BF}_4$, is dark blue in color. When the solvated protonated

species is exposed to the air, oxidation occurs. The solution turns from a red color to a dark blue color. Even under the same conditions as Triechel described¹², using acetone under argon as solvent instead of CH_2Cl_2 , a red color was exhibited upon protonation instead of the dark blue color of the oxidized species. Apparently, the compound $\text{CpFe}(\text{dppe})(\text{SC}_6\text{H}_5)$ is not a good model for hydrogenases.

By making the iron-thiolate complex more electron rich, there is a better chance for dihydrogen evolution to take place. The tripodal complex, $\text{CpFe}(\text{P}_2\text{S})$, was synthesized (Figure 4.41) to increase the electron environment about the sulfur and also the chelation effect should help to prevent acid solvolysis from taking place. As $\text{HBF}_4 \cdot \text{O}(\text{CH}_3)_2$ was added to a benzene- d_6 solution of $\text{CpFe}(\text{P}_2\text{S})$, an immediate color change from greenish-brown to violet-pink took place, which is indicative of oxidation; however, hydrogen gas was not detected.

Other parts of this project involved studying the reactivity, redox potential, and structure of the compounds $\text{CpFe}(\text{dppe})(\text{SC}_6\text{H}_4\text{-}p\text{-Z})$ where $\text{Z} = \text{OCH}_3, \text{H}, \text{Cl}, \text{CF}_3, \text{and } \text{NO}_2$. By reacting $\text{CpFe}(\text{dppe})(\text{SC}_6\text{H}_4\text{-}p\text{-Z})$ with excess CH_3I in acetone, a ligand exchange process occurs forming the final products as $\text{CpFe}(\text{dppe})\text{I}$ and $\text{CH}_3\text{SC}_6\text{H}_5$ (Figure 4.9). The influence of the thiolate ligand substituent Z on the reaction rate is summarized in Table 4.1. The plots of the $\ln([\text{A}_0]/[\text{A}])$ vs. time (Figures 4.12 and 4.13) shows that the reaction is first order in CH_3I since in each case, by increasing the concentration of CH_3I by a multiple of five, the rate also increases by a multiple of five.¹³

Ashby *et al.* accomplished a similar set of experiments using $\text{CpFe}(\text{CO})_2(\text{SC}_6\text{H}_4\text{-}p\text{-Z})$ and excess iodomethane in acetone.⁴ A linear free energy relationship is observed between the reaction rate and the Hammett substituent constant (σ). A similar correlation is observed in this study between the relative donor ability of the aryl substituent and reaction rate. The calculated

Hammett reaction constant using the compound $\text{CpFe}(\text{CO})_2(\text{SC}_6\text{H}_4\text{-}p\text{-Z})$ is $\rho = -1.82$ which is close to the value of $\rho = -2.14$ that is obtained for the compound $\text{CpFe}(\text{dppe})(\text{SC}_6\text{H}_4\text{-}p\text{-Z})$ (Figure 4.14). This suggests that the mechanism by which $\text{CpFe}(\text{dppe})(\text{SC}_6\text{H}_4\text{-}p\text{-Z})$ and $\text{CpFe}(\text{CO})_2(\text{SC}_6\text{H}_4\text{-}p\text{-Z})$ are methylated is the same. If the mechanism involves frontier orbital control, as is described in the case of $\text{CpFe}(\text{CO})_2(\text{SC}_6\text{H}_4\text{-}p\text{-Z})$,⁴ then the expectation is that the more electron withdrawing substituent should decrease the rate of methylation. The kinetic results obtained from methylating $\text{CpFe}(\text{dppe})(\text{SC}_6\text{H}_4\text{-}p\text{-Z})$ coincides with this expectation. By looking at the relative rates of reaction in Table 4.1, the OCH_3 derivative reacts 232 times faster than the NO_2 derivative. In fact, as the aryl substituent becomes more electron withdrawing, the reaction becomes slower. These data coincides with the cyclic voltammetric data (Table 4.2).

A linear free energy relationship is observed in this electrochemical study between the relative donor ability of the aryl substituent and the half-wave potential of the compounds $\text{CpFe}(\text{dppe})(\text{SC}_6\text{H}_4\text{-}p\text{-Z})$ (Figure 4.21). Notice that the OCH_3 derivative is the most easily oxidizable whereas the NO_2 derivative is the least oxidizable. The NO_2 substituent best stabilizes the complex by withdrawing electron density from the HOMO which is the $d\pi\text{-}p\pi$ antibonding orbital.⁴

This can also be corroborated with the solid-state evidence. A comparison of the Fe-S bond distances between the complexes, $\text{CpFe}(\text{dppe})(\text{SC}_6\text{H}_4\text{-}p\text{-OCH}_3)$ (Figure 4.29), $\text{CpFe}(\text{dppe})(\text{SC}_6\text{H}_5)$ (Figure 4.31), and $\text{CpFe}(\text{dppe})(\text{SC}_6\text{H}_4\text{-}p\text{-NO}_2)$ (Figure 4.33), was accomplished by single-crystal X-ray crystallographic analysis of a suitable crystal of each compound. Tables 4.6, 4.9, 4.12, 4.15, and 4.18. list the selected bond distances and angles for each compound. The Fe-S bond length for these compounds are comparable

with those of other structurally characterized iron(II)-phenyl thiolate complexes (Table 4.19).

By observing the Fe-S bond distances, a significant decrease occurs. The Fe-S bond distances for the OCH₃, H, and NO₂ derivatives are 2.332(2), 2.3289(8), and 2.2933(7) Å, respectively (Table 4.19). Explanation for this trend is that the more electron withdrawing substituent, NO₂, stabilizes the Fe-S bond by removing electron density from the Fe d π -S p π antibonding orbital.⁴

Diaz *et al.* compares the HOMO energies from MO calculations of [CpFe(CO)₂]⁺ and [CpFe(dppe)]⁺ and finds that the carbonyl derivative is lower in energy.¹⁴ The HOMO energies from density functional calculations on the oxidized species, [CpFe(CO)₂(SCH₃)]⁺ and [CpFe(dppe)(SCH₃)]⁺, also shows that the carbonyl derivative is more stable than the phosphine derivative (Figure 4.44); however, the calculations also indicate that the HOMO in the carbonyl derivative is still predominantly sulfur in character while in the phosphine derivative, the HOMO is predominantly metal in character.

There is also indication that the HOMO of the Fe(III) species is primarily metal in character as determined by the electron paramagnetic resonance (EPR) data collected (Table 4.3). Room temperature CH₂Cl₂ solutions of the complex, [CpFe(dppe)(SC₆H₄-*p*-Z)]BF₄, have a single symmetric peak that indicates pseudooctahedral structures (Figures 4.22 – 4.26) and no phosphorus hyperfine coupling. The g-values range from 2.07159 for the OCH₃ derivative to 2.07525 for the NO₂ derivative. From a study by Roger, the g-values higher than those of the free electron value (g = 2.0023) are usually observed for 17 electron iron(III) compounds having a single occupied HOMO with a predominant metallic character.¹⁵

A linear free energy relationship is observed relative to the g-values and the relative donor ability of the aryl substituent (Figure 4.27). Apparently, when

the aryl substituent becomes more electron withdrawing and the g-values increase the HOMO becomes more metal in character. An apparent linear free energy relationship is also observed relative to the half width at half height (HWHH) and the relative donor ability of the aryl substituent (Figure 4.28). The NO₂ derivative is much less intense and much broader than the OCH₃ derivative. The half width at half height (HWHH) values for the NO₂ and OCH₃ derivatives are 0.00700 and 0.00568, respectively (Table 4.3). Apparently, as the more electron donating substituent is replaced with a more electron withdrawing substituent, the more polar the [CpFe(dppe)(SC₆H₄-*p*-Z)]⁺ complex becomes which is indicated by the broadening of the peak.

5.4 Future Work.

5.4.1 Project 1

A specific correlation between the broadening effect on the carbonyl stretching frequency and any physical properties of the solvent has yet to be found. It seems that the compounds, CpFe(CO)₂(SC₆H₅-*p*-Z) where Z = OCH₃, H, Cl, CF₃, and NO₂, CpFe(CO)₂I, CpFe(CO)₂Br, and CpFe(CO)₂Cl would provide excellent opportunity to study the broadening effect using line shape analysis and to correlate it to some physical property of the solvent. These compounds are soluble in many types of solvents and are easily synthesized.

5.4.2 Project 2

The tripodal complex, CpFe(P₂S), is an interesting compound. When this compound reacts with HBF₄·O(CH₃), why does oxidation take place and no hydrogen gas evolve? It may have been due to some spurious oxygen associated with the solvent or acid. This needs to be investigated further. Also, by making the pentamethylcyclopentadienyl derivative of CpFe(P₂S) would make the compound even more electron rich. Perhaps this might achieve the goal of

producing hydrogen *via* the proposed mechanism (Figure 4.40). A comparison of redox behavior as well as rate of methylation could be achieved between $\text{Cp}^*\text{Fe}(\text{P}_2\text{S})$ and $\text{CpFe}(\text{P}_2\text{S})$ to see the affect of the additional methyl groups.

References

- 1) Chakrabarti, P. and Pal, D. "An Electrophile-Nucleophile Interaction in Metalloprotein Structures", *Protein Sci.* **1997**, *6*, 851-859.
- 2) Sweeney, W. V. and Rabinowitz, J. C. "Proteins Containing 4Fe-4S Clusters : an Overview", *Annu. Rev. Biochem.* **1980**, *49*, 139-161.
- 3) Treichel, P. M., Schmidt, M. S. and Koehler, S. D. "Alkylation of Organoiron Thiolate Complexes", *J. Organom. Chem.* **1983**, *258*, 209-216.
- 4) Ashby, M. T., Enemark, J. H. and Lichtenberger, D. L. "Destabilizing $d\pi-p\pi$ Orbital Interactions and the Alkylation Reactions of Iron(II) Thiolate Complexes", *Inorg. Chem.* **1988**, *27*, 191-197.
- 5) Byers, B. P. and Hall, M. B. "Comparison of Isolobal Fragments: Photoelectron-Spectra and Molecular-Orbital Calculations of (Arene)Tricarbonylchromium; (arene)Tricarbonylmolybdenum; and (arene)Tricarbonyltungsten complexes", *Organometallics* **1987**, *6*, 2319-2325.
- 6) Gower, M., Kane-Maguire, L. A., Maier, J. P. and Sweigart, D. A. "Ultraviolet Photoelectron-Spectra of Cyclohepta-1; 3; 5-Triene and Mesitylene Tricarbonyl Complexes of Group-6A Metals", *J. Chem. Soc., Dalton Trans.* **1977**, 316-318.
- 7) Hubbard, J. L. and Lichtenberger, D. L. "The Jahn-Teller Effect in the Photoelectron-Spectrum of Iron Pentacarbonyl", *J. Chem. Phys.* **1981**, *75*, 2560-2568.
- 8) Lichtenberger, D. L., Sellmann, D. and Fenske, R. F. "He (I) Photoelectron-Spectra and Valence Electronic-Structures of $\eta^5\text{-C}_5\text{H}_5\text{Mn}(\text{CO})_2\text{N}_2$ and $\eta^5\text{-C}_5\text{H}_5\text{Mn}(\text{CO})_2\text{NH}_3$ ", *J. Organomet. Chem.* **1976**, *117*, 253-264.
- 9) Lichtenberger, D. L., Elkadi, Y., Gruhn, N. E., Hughers, R. P., Cumow, O. J. and Zheng, X. M. "Electronic Structure Perturbations of Substituted

Ruthenocenes: The First Photoelectron Spectra of Perchloro- and Perfluorocyclopentadienyl Complexes", *Organometallics* **1997**, *16*, 5209-5217.

- 10) Reichardt, C. *Solvent and Solvent Effects in Organic Chemistry*, 2nd ed.; VCH Publishers: New York, 1988.
- 11) Foffani, A., Poletti, A. and Cataliotti, R. "Solvent effect on C-O and N-O Stretching Modes of Different Symmetry in Transition-Metal Carbonyl-Nitrosyls", *Spectrochim. Acta* **1968**, *24A*, 1437-1447.
- 12) Treichel, P. M., Molzahn, D. C. and Wagner, K. P. "New 17 Electron Complexes of Iron", *J. Organomet. Chem.* **1979**, *174*, 191-197.
- 13) Espenson, J. H. *Chemical Kinetics and Reaction Mechanisms*; 2nd ed.; McGraw Hill: New York, 1995.
- 14) Diaz, C., Leal, C. and Yutronic, N. "Oxidative Addition of Disulfides to the Fragment $\text{CpFe}(\text{dppe})^+$: Steric and Dielectric Medium Control on the Reaction", *J. Organomet. Chem.* **1996**, *516*, 59-64.
- 15) Roger, C., Hamon, P., Toupet, L., Rabaa, H., Saillard, J. Y., Hamon, J. R. and Lapinte, C. "Halo(Pentamethylcyclopentadienyl)(1,2-Bis(Diphenylphosphino)ethane)iron(III) and Alkyl(Pentamethylcyclopentadienyl)(1,2-Bis(Diphenylphosphino)-ethane)Iron(III) 17-electron Complexes: Synthesis, NMR, and Magnetic-Properties, and EHMO Calculations", *Organometallics* **1991**, *10*, 1045-1054.